INDIRECT DETECTION OF DARK MATTER AT INO

By
DEEPAK TIWARI
PHYS01201204003

Bhabha Atomic Research Centre, Mumbai

A thesis submitted to the
Board of Studies in Physical Sciences
In partial fulfillment of requirements
for the Degree of
DOCTOR OF PHILOSOPHY
of
HOMI BHABHA NATIONAL INSTITUTE

July, 2018

Homi Bhabha National Institute[1]

Recommendations of the Viva Voce Committee

As members of the Viva Voce Committee, we certify that we have read the dissertation prepared by Deepak Tiwari entitled "Indirect Detection of Dark Matter at INO" and recommend that it may be accepted as fulfilling the thesis requirement for the award of Degree of Doctor of Philosophy.

Chairman – Prof. Satchitananda Naik	S. Naik	21/6/19
Guide / Convener – Prof. Sandhya Choubey	Sandhya Choubey	21/6/19
Co-guide - Name & Signature with date (if any)		
Examiner - Prof. James Libby	JFL	21/6/19
Member 1- Prof. Raj Gandhi	Raj Gandhi	21/6/19
Member 2- Prof. Amol Dighe	Amol Dighe	21/6/19
Member 3- Prof. L M Pant	L M Pant	21/6/19
Technology Adviser - < Name & Signature with date > (if any)		

Final approval and acceptance of this thesis is contingent upon the candidate's submission of the final copies of the thesis to HBNI.

I/We hereby certify that I/we have read this thesis prepared under my/our direction and recommend that it may be accepted as fulfilling the thesis requirement.

Date: 21 June, 2019

Sandhya Choubey

Place: Prayagraj (Allahabad)

Prof. Sandhya Choubey

Guide

[1] This page is to be included only for final submission after successful completion of viva voce.

STATEMENT BY AUTHOR

This dissertation has been submitted in partial fulfillment of requirements for an advanced degree at Homi Bhabha National Institute (HBNI) and is deposited in the Library to be made available to borrowers under rules of the HBNI.

Brief quotations from this dissertation are allowable without special permission, provided that accurate acknowledgement of source is made. Requests for permission for extended quotation from or reproduction of this manuscript in whole or in part may be granted by the Competent Authority of HBNI when in his or her judgment the proposed use of the material is in the interests of scholarship. In all other instances, however, permission must be obtained from the author.

Deepak Tiwari

DECLARATION

I, hereby declare that the investigation presented in the thesis has been carried out by me. The work is original and has not been submitted earlier as a whole or in part for a degree / diploma at this or any other Institution / University.

Deepak Tiwari

List of Publications arising from the thesis

Journal

1. "Neutrino Physics with Non-Standard Interactions at INO", Sandhya Choubey, Anushree Ghosh, Tommy Ohlsson and Deepak Tiwari, *Journal of High Energy Physics*, **2015**, JHEP 1512 (2015) 126 [arXiv:1507.02211][hep-ph]].
2. "Prospects of Indirect Searches for Dark Matter at INO", Sandhya Choubey, Anushree Ghosh and Deepak Tiwari, *Journal of Cosmology and Astroparticle Physics*, **2018**, JCAP 1805 (2018) no.05, 006 [arXiv:1711.02546][hep-ex]].
3. "Prospects of indirect searches for dark matter annihilations in the earth with ICAL@INO", Deepak Tiwari, Sandhya Choubey and Anushree Ghosh, *Journal of High Energy Physics*, **2019**, JHEP 1905 (2019) 039 [arXiv:1806.05058][hep-ph]].

Other publication (not included in thesis)

1. "Physics Potential of the ICAL detector at the India-based Neutrino Observatory (INO)", ICAL collaboration, Shakeel Ahmed et al., *Pramana*, **2017**, Pramana 88 (2017) no. 5, 79 [arxiv:1505.07380][phyiscs.ins-det]]

Conferences

1. Searches for Dark Matter annihilation with ICAL [poster], **Advanced Workshop on Physics of Atmospheric Neutrinos- PANE 2018,** 28 May-1 June 2018, ICTP Trieste, Italy.
2. Indirect searches for Dark Matter signatures with ICAL@INO [poster], **NuHoRIzons VII**, 21-23 February 2018, Harish-Chandra Research Institute, India.
3. Indirect searches for Dark Matter with neutrinos as a probe [talk], **Workshop in High Energy Physics Phenomenology (WHEPP) XV**, 14-23 December 2017, IISER Bhopal, India.
4. Indirect searches for Dark Matter Signatures at INO [poster], **NSPDI-2017 National Symposium on Particles, Detectors and Instrumentation**, 4-7 October 2017, Tata Institute of Fundamental Research (TIFR), Mumbai.
5. Indirect detection of Dark Matter at INO [talk], **TAUP 2017-XV International Conference on Topics in Astroparticle and Underground Physics**, 24-28 July 2017, Laurentian University, Sudbury, Canada.

6. Neutrino Physics with Non-standard Interactions at INO [talk], **NuHoRIzons VI**, 17-19 March 2016, Harish-Chandra Research Institute, India.
7. Indirect Searches for Dark Matter Signatures at INO [talk], **XXI DAE-BRNS High Energy Physics Symposium 2014**, 8-12 December 2014, Indian Institute of Technology, Guwahati, India.
8. Indirect Searches for Dark Matter Signatures at INO [poster], **Invisibles Workshop 2014**, 14-18 July 2014, Institut des Cordeliers, Paris, France.

Deepak Tiwari

Dedicated to

Ma & Papa

ACKNOWLEDGEMENTS

Seven years ago, a confused engineer was endowed with an opportunity to purse Ph.D. in the field of fundamental physics. An email from Dr. Satyanarayana Bheesette, TIFR was the first step in that direction. He warmly welcomed me into the INO Graduate Training Programme, and ever since, has been a source of constant support and guidance. I am, and will always remain, grateful to him for the kind support and affection throughout. This thesis would have been impossible without the support of my supervisor Prof. Sandhya Choubey. I am very grateful to her for the incessant guidance and encouragement. Her patience and confidence in me, particularly when I slowed down, boosted me and kept me going. My heartfelt thanks to Prof. Amol Dighe for being a source of constant support and learning. During my coursework at TIFR Mumbai, I was fortunate to have experts in the field of experimental high energy physics. In particular, I have learned a great deal of experimental approach, techniques, and simulation tools from Prof. Gobinda Majumdar and Prof. Vandana Nanal and I am very grateful to them.

I am sincerely thankful to Prof. Raj Gandhi for the inspiring discussions and guidance. He is a constant source of motivation for learning new things. I express my sincere thanks to Prof. Pinaki Majumdar, Prof. Jayant Kumar Bhattacharjee and Prof. Satchitananda Naik. I am grateful to Prof. Uma Shankar for the wonderful classes on neutrino physics. I would like to thank Prof. D. Indumathi and Prof. Srubabati Goswami for valuable discussions. My heartfelt gratitude goes to Naba Mondal and Prof. Vivek Datar for their help and wonderful suggestions at various stages for last seven years. I am also thankful to Prof. Deborah Harris, Prof. Brajesh Choudhary and Tommy Ohlsson for their support.

During my PhD tenure, I have attended several workshops and conferences. I am indebted to the organisers for giving me a chance to present my work which enriched my understanding of the subject. Specially, I am thankful to Invisibles 2014 School and Workshop organisers- Prof. Belen Gavela and Prof. Asmaa Abada. I am thankful to Prof. Silvia Pascoli for providing financial

support to attend SUSSP70/INSS 2014. I am also thankful to TAUP 2017 organisers for providing me with an opportunity to present my work. I thank Prof. Sanjib Kumar Agarwalla for supporting me to attend PANE 2018.

The projects in my thesis made use of several softwares. Without the support from the developers, life would have been very difficult. I would like to thank Prof. Joakim Edsjö for help related to WIMPSIM installation and responding to queries whenever I had any doubt. Céline Combet and David Maurin have provided support with CLUMPY installation and I am very grateful to them for the same. I thank Prof. Constantinos Andreopoulos for responding to my queries related GENIE. I am grateful to Prof. Gobinda Majumdar and Ali Ajmi for modifying the GENIE for ICAL. My cheers to the Geant4 and ROOT team, for the two wonderful packages! This thesis has made use of "Aladin sky atlas" developed at CDS, Strasbourg Observatory, France and PyAstronomy packages. I am very grateful to the developers.

I gratefully acknowledge the HRI HPSC cluster facilities. While I ran codes, several people were there to support. In particular, Amit Khulve, Chandan Kannaujia and Rajeev kumar are the people who have helped me the most. I would like to extend my thanks to Sanjay Verma for support related to HRI computing facilities. I am also thankful to Mr. Nagaraj Panyam and Mr. Pawan Gupta, who have supported me with the TIFR computing facilities. I am grateful to the administrative staff at HRI Allahabad and TIFR Mumbai. I am specially thankful to Raachna Pareek and Shweta Srivastava for being so wonderful and supportive throughout and were always there to help. I gratefully acknowledge Mr. R. Shinde and Mr. M. Bhuyan of TIFR for their assistance during the course work at TIFR.

I would like to acknowledge the INO Collaboration for bestowing me with a wonderful opportunity, so that I could be a part of lively particle physics community. I gratefully acknowledge the funding from the Department of Atomic Energy (DAE) and the Department of Science and Technology (DST), Government of India without which this thesis would not have been possible.

I would like to thank my colleagues and friends Sarif Khan, Dipyaman Pramanik, Abhik Jash, Mrityunjay Verma, Sitender Kashyap, Kasinath Das and Ruchi Saxena for their love and

support. And, among other things, I thank them for both academic and nonacademic discussions which widened my horizon. Thanks to Meghna, Moon Moon Devi, Apoorva Bhatt and Kolahal Bhattacharya for helping me with the Geant4 simulation and related analysis. My sincere thanks to Lakshmi S Mohan, Neha Dokania, Varchaswi Kashyap, Asmita Redij, Shiba Behera, Sudeshna Dasgupta, Deepak Samuel, Amina Khatun, Neha Panchal, Jim John, Deepak Raikwal and Dhruv Mulmule who have helped me at various stages of PhD life.

I would like to extend my healtfelt thanks to my colleagues at Universite de Montreal for all the support and cooperation during the last phase of thesis writing. Especially I wish to thank Dr. Alan Robinson, Prof. Viktor Zacek and Arthur Plante for the useful discussions which enriched my understanding of the subject.

Thank you Ibrahim Mughal for making Allahabad a lively place. I learned a deal from you and continue to do so. I am also thankful to my friends Ankita Verma and Namrata Shukla for their love and support. Finally, with all my heart, I would like to thank my parents and my other family members for their love, trust, continuous support and patience.

Contents

SUMMARY 1

List of Figures 3

List of Tables 19

List of Abbreviations 21

1 Introduction 23

2 Dark Matter 31

2.1 Dark matter evidence 32

2.2 Candidates for dark matter 36

2.3 Weakly Interacting Massive Particles 38

2.4 Interaction between WIMP and nucleon 41

2.4.1 Spin dependent (axial-vector) interaction 41

2.4.2 Spin-independent (scalar) interactions 42

2.5 Detection of dark matter 42

2.5.1 Direct searches 44

2.5.2 Indirect searches 46

2.5.3 Collider searches 48

2.6 Complementarity of direct, indirect and collider searches 50

3 Neutrino fluxes due to WIMP annihilation 55

3.1 Neutrinos from WIMP annihilation in the sun . . . 55
3.2 Neutrino flux from WIMP annihilation in the earth . . . 62
3.3 Neutrino fluxes due to WIMP annihilation in the galactic centre . . . 67
3.3.1 DM density profiles and J-Factor calculations . . . 69

4 Atmospheric neutrino fluxes 77
4.1 Introduction . . . 77
4.2 Calculation of atmospheric neutrino fluxes . . . 79
4.3 Characteristics of atmospheric neutrino fluxes . . . 80
4.4 Comparison of Theni and Kamioka Fluxes . . . 85
4.5 Atmospheric neutrinos as a background to indirect detection . . . 87

5 ICAL detector and simulation framework 91
5.1 India-based Neutrino Observatory . . . 91
5.2 The Iron Calorimeter . . . 93
5.2.1 The detector geometry . . . 93
5.2.2 The Magnetic Field . . . 94
5.2.3 Resistive Plate Chambers . . . 97
5.3 Event generation at ICAL . . . 99
5.3.1 Neutrino interactions and event generation . . . 99
5.3.2 Event Reweighting . . . 102
5.4 ICAL Simulation Framework . . . 103
5.4.1 Event simulation and digitisation . . . 103
5.4.2 Event reconstruction . . . 105
5.5 ICAL response to muons . . . 107
5.5.1 Reconstruction efficiency . . . 107
5.5.2 Charge Identification efficiency . . . 108
5.5.3 Muon momentum resolution . . . 109

5.5.4 Muon zenith angle resolution . . . 112
5.6 Folding events with detector efficiency and resolution functions . . . 115

6 Searches for DM annihilations in the sun 117
6.1 Atmospheric neutrino background suppression . . . 118
6.2 The statistical analysis . . . 124
6.3 Results . . . 125
6.4 Conclusions . . . 136

7 Searches for DM annihilations in the earth 139
7.1 Atmospheric neutrino background suppression . . . 140
7.2 Statistical Analysis . . . 145
7.3 Results . . . 145
7.4 Summary . . . 151

8 Searches for DM in the galactic centre 153
8.1 Signal and the background . . . 154
8.2 Atmospheric neutrino background suppression . . . 156
8.3 Statistical Analysis . . . 160
8.4 Expected sensitivity for ICAL . . . 161
8.5 Conclusions . . . 166

9 Neutrino Physics with Non-Standard Interactions at INO 167
9.1 Introduction . . . 167
9.2 Impact of NSI on Oscillation Probabilities . . . 168
9.3 Event Spectrum at INO . . . 174
9.4 Expected Results from INO . . . 177
9.4.1 Impact of NSI on Mass Hierarchy Sensitivity . . . 177
9.4.2 Expected Bounds on NSI . . . 181

9.4.3 Discovery Reach for NSI Parameters 183
9.4.4 Precision on NSI Parameters 184
9.5 Conclusions 186

10 Summary and outlook **189**

References **197**

SUMMARY

In this thesis, we present prospects of indirect detection of dark matter with the proposed Iron Calorimeter (ICAL) detector at upcoming India-based Neutrino (INO) facility. Firstly, we study the prospects of searching for neutrinos at ICAL due to WIMP annihilation in the centre of the sun [1]. We perform ICAL dedicated detector simulations on Geant4.9.4.p02 [2] framework to obtain the detector efficiencies and resolutions in order to simulate muon events in ICAL due to neutrinos coming from annihilation of WIMP in the mass range $m_\chi = (3 - 100)$ GeV. The atmospheric neutrinos pose a major background for these indirect detection studies. Fortunately, using the fact that the signal comes only from the direction of the sun whereas the atmospheric background has dependence in zenith and azimuthal directions, the background can be suppressed considerably. For a given WIMP mass, we find the opening angle θ_{90} such that 90 % of the signal events are contained within this angle and use this cone-cut criteria to reduce the atmospheric neutrino background. Thereafter, the reduced background is weighted by the solar exposure function at INO to obtain the final background spectrum for a given WIMP mass. We perform a χ^2 analysis and present expected exclusion regions in the $\sigma_{SD} - m_\chi$ and $\sigma_{SI} - m_\chi$, where σ_{SD} and σ_{SI} are the WIMP-nucleon Spin-Dependent (SD) and Spin-Independent (SI) scattering cross-section, respectively. For a 50×10 kt-years of exposure and $m_\chi = 25$ GeV, the expected 90 % C.L. exclusion limit is found to be $\sigma_{SD} < 6.87 \times 10^{-41}$ cm^2 and $\sigma_{SI} < 7.75 \times 10^{-43}$ cm^2 for the $\tau^+\tau^-$ annihilation channel and $\sigma_{SD} < 1.14 \times 10^{-39}$ cm^2 and $\sigma_{SI} < 1.30 \times 10^{-41}$ cm^2 for the $b\,\bar{b}$ channel, assuming 100 % branching ratio for each of the WIMP annihilation channel.

Thereafter, we look for WIMP annihilation in the centre of the earth [3]. For a given m_χ and annihilation channel, we define θ_{90} to be the half angle of the cone that contains 90% of the signal muons, the axis of the cone being in the direction of the earth's centre. We accept muons events due to signal and background neutrinos within this cone. The atmospheric neutrinos coming from

the direction of earth core presents an irreducible background. We consider 50kt $\times$ 10 years of ICAL running and WIMP masses between 10-100 GeV and present 90 % C.L. exclusion sensitivity limits on σ_{SI} which is the WIMP-nucleon Spin Independent (SI) interaction cross-section. The expected sensitivity limits calculated for ICAL for the WIMP annihilation in the earth are more stringent than the limits obtained by any other indirect detection experiment. The SI capture of WIMP in the earth interior is significantly enhanced if m_χ is close to that of one of the nuclear species in the earth. For a WIMP mass of 52.14 GeV, where the signal fluxes are significantly enhanced due to resonance capture of WIMP due to Fe nuclei which has the largest abundance in the earth, the expected 90% sensitivity limits, assuming 100% branching ratio for each channel, are : $\sigma_{SI} = 1.02 \times 10^{-44}\ cm^2$ for the $\tau^+\tau^-$ channel and $\sigma_{SI} = 5.36 \times 10^{-44}\ cm^2$ for the $b\,\bar{b}$ channel.

Subsequently, we study prospects of detecting events at ICAL due to WIMP annihilation in the GC region [4]. The neutrino flux from DM annihilation in the GC is proportional to velocity averaged annihilation cross-section $\langle \sigma_A v \rangle$ and the line-of-sight integral over the DM density profile J_Ψ factor [5] which is a function of the angular separation (Ψ) of reconstructed muon track at ICAL with the GC. We exploit the difference in directional dependence of the signal and background neutrinos to suppress the background. We accept muon events in a cone of half angle Ψ, the axis of the cone being in the direction of GC. We consider WIMP masses between (5-100) GeV and several annihilation channels. The expected 90 % C.L. sensitivity limits for a 30 GeV WIMP, assuming NFW [6] DM profile, neutrino spectra from [7] and assuming 100% branching ratio for each channel are: $\langle \sigma_A v \rangle \leq 1.19 \times 10^{-22}\ cm^3 s^{-1}$ for the $\mu^+\mu^-$ channel and $\langle \sigma_A v \rangle \leq 6.35 \times 10^{-23} cm^3 s^{-1}$ for the $\nu\ \bar{\nu}$ channel.

Finally, we look at the impact of Non Standard Interactions (NSI) on the signal at the ICAL detector [8]. The mass hierarchy sensitivity is shown to be rather sensitive to the NSI parameters $\epsilon_{e\mu}$ and $\epsilon_{e\tau}$, while the dependence on $\epsilon_{\mu\tau}$ and $\epsilon_{\tau\tau}$ is seen to be very mild, once the χ^2 is marginalised over oscillation and NSI parameters.

List of Figures

2.1 The measured rotational curve for NGC 6503 (data taken from [9, 10]) shown in blue crosses. Also shown are the combined rotational curve (cyan line) obtained by adding contribution from different mass components of the galaxy. The galactic rotation curves due to disk (light orange), dark matter halo (red), gas (green) is also shown. The data points are shown without error bars. 32

2.2 A Horseshoe Einstein ring from Hubble [Image Credit: ESA/Hubble &NASA]. This is an example of a gravitational lens mirage. The gravity of a luminous red galaxy (LRG) has gravitationally distorted the light from a farther blue galaxy. . . . 34

2.3 Planck's power spectrum [11] of temperature fluctuations in the cosmic microwave background. The fluctuation are plotted for different angular scales on the sky. The Planck data are marked by red dots with corresponding error bars whereas the green curve represents the standard model of cosmology, ΛCDM. The first peak at 1° is the evidence for a flat geometry of universe, the height of the second peak indicates that ordinary matter is just 5% of the total and from the second and third peaks give the DM contribution to be approximately 26%. 34

2.4 Comoving number density evolution as a function of the ratio x in the context of the thermal freeze-out. The value of the annihilation cross section determines the DM abundance since $\Omega_\chi h^2 \propto 1/\langle\sigma_{\rm A} v\rangle$. 39

2.5 An interaction diagram of standard model particle q and dark matter χ. The three categories of dark matter detection *viz.*, direct, indirect and collider searches are shown. 43

2.6 Schematic of possible signals that can be measured in direct detection experiments depending on the technology in use. The detectors marked in black are sensitive to either charge, light or phonon/heat signals. For better particle discrimination, many detectors combine these techniques to be sensitive to more than one kind of signal. These are shown in magenta color. Here TPC stands for Time Projection Chamber. The recoil image (at the centre of the figure) has been taken from https://indico.fnal.gov/event/6661/session/2/contribution/22/material/slides/0.pdf. . 43

2.7 Worldwide hunt for the dark matter, including the terrestrial and satellite experiments. Gamma ray telescopes (black circle) and neutrino telescopes (green box) are examples of indirect searches. The underground labs housing direct detection experiments (blue pyramids) and collider (yellow diamond) production searches are also shown. Some of these experiments have now stopped operation. The figure has been taken from Ref. [12]. 52

3.1 SI and SD capture rates for WIMP in the core of the sun as a function of WIMP mass m_χ. 58

3.2 The ν (solid) and $\bar{\nu}$ (dashed) fluxes at ICAL due to annihilation of 25 GeV WIMPs in the sun for channels for various annihilation channels with $\sigma_{\rm SD} = 10^{-39}$ cm^2. The fluxes due to SI interactions in the sun are similar and scaled by the appropriate $\sigma_{\rm SI}$. 61

3.3 The dependence of the time required for equilibrium to reach between annihilation and capture rate for WIMP in the earth as a function of WIMP mass m_χ. It can be seen that for the parameters chosen in this analysis, we can see that equilibrium is never achieved. This has been calculated by fixed value of $C_{\rm A}$ by choosing $\langle \sigma_{\rm A} v \rangle = 3 \times 10^{-26} {\rm cm}^3 {\rm s}^{-1}$. A scattering cross-section of $\sigma_{\rm SI} = 10^{-44} {\rm cm}^2$ has been assumed while calculating C using Eq. 3.12. 63

3.4 SI capture rate for WIMP in the earth as a function of WIMP mass m_χ. The enhanced capture rate due to resonance scattering on various nuclei is also shown. A scattering cross-section of $\sigma_{\rm SI} = 10^{-44}{\rm cm}^2$ has been assumed. 65

3.5 The ν and $\bar{\nu}$ fluxes at ICAL due to annihilation of 25 GeV WIMPs in the earth for various WIMP annihilation channels with $\sigma_{\rm SI} = 10^{-38}$ cm^2 and $\langle\sigma_A v\rangle = 3\times10^{-26}$ cm^3 s^{-1} 66

3.6 The definition of Ψ, $\Delta\Omega$ and other factors involved in J_Ψ and $\mathcal{J}(\Delta\Omega)$ calculation. Ψ is the angular separation between the line joining the earth and GC and the line joining the earth and point P. R_{SC} is the solar radius, R_{MW} is the radius of the Milky Way galaxy and l_{max} is the maximum distance between the earth and the farthest point in the galaxy. $\Delta\Omega$ is the solid angle subtended at the earth due to cone half angle Ψ. 67

3.7 The ν_μ spectra at the surface of the earth due to WIMP annihilation in the galactic centre. The ν_μ spectra is similar and not shown here. We used the spectra at the point of production [7] and propagate it to the earth surface taking care of vacuum oscillations. The shown spectra is for a 30 GeV WIMP and for several annihilation channels. Electroweak corrections have been included [13]. 70

3.8 The effect of oscillation on the neutrinos propagating from the G.C. to the surface of the earth. 70

3.9 $M(r)$ of DM density profiles as a function of radial distance r. 73

3.10 $\rho(r)$ of DM density profiles as a function of radial distance r. 74

3.11 The line-of-sight integral $J(\Psi)$ as a function of angular separation Ψ for NFW (orange), Burkert (blue) and Einasto (green) DM density profiles. 75

3.12 $\mathcal{J}(\Delta\Omega)$ as a function of angular separation Ψ for NFW (orange), Burkert (blue) and Einasto (green) DM density profiles. 76

3.13 ν fluxes (${\rm cm}^{-2}{\rm s}^{-1}$) for 50 GeV WIMP annihilating in GC through $\tau^+\tau^-$ channel for a NFW profile, $\langle\sigma_{\rm A} v\rangle = 3\times10^{-26}{\rm cm}^3{\rm s}^{-1}$, calculated using PPPC4DMID [7]. . 76

4.1 A schematic illustration of the production of atmospheric neutrinos due to cosmic ray interactions with the air molecules in the atmosphere. 78

4.2 The variation of atmospheric neutrino fluxes with the neutrino energy E_ν. The fluxes have been averaged over all directions and shown for Theni site. The ν_μ fluxes (red solid) are more than ν_e (blue solid) fluxes. Also, the fluxes from the antiparticles are lower than their respective particles and are shown in lighter shade dotted lines. 81

4.3 Neutrino flavour ratio for all direction averaged atmospheric neutrinos fluxes at Theni. 81

4.4 The dependence of atmospheric neutrino fluxes on cosine of the zenith angle $\cos\theta$ for different neutrino flavours and types. The fluxes have been averaged over all azimuthal bins and summed over entire energy range $E_\nu \in [0.1, 10000]$ GeV. $\cos\theta = 1$ represents down going neutrinos. 82

4.5 The azimuthal angle dependence of the atmospheric neutrino fluxes, averaged over zenith angle bins and summed over entire energy range. In this convention, $\phi = 0$ indicates South, $\phi = 90$ is East and so on. 82

4.6 Atmospheric ν fluxes, averaged over all directions, as a function of neutrino energy E_ν for Kamioka and Theni sites. The difference between the fluxes at two sites decreases with the increase in E_ν. 87

4.7 The zenith angle dependence of atmospheric neutrino fluxes averaged over all azmiuthal angles (ϕ) and summed over all energy range $E_\nu \in [0.1, 10000]$ GeV. The ν_μ fluxes for Theni (magenta) and Kamioka (azure) are shown. The corresponding $\bar{\nu}_\mu$ fluxes are shown in a lighter shade and dotted lines. 88

4.8 The azimuthal angle dependence of atmospheric neutrino fluxes averaged over all zenith angles ($\cos\theta$) and summed over all energy range $E_\nu \in [0.1, 10000]$ GeV. The ν_μ fluxes for Theni (magenta) and Kamioka (azure) are shown. The corresponding $\bar{\nu}_\mu$ fluxes are shown in a lighter shade and dotted lines. 88

4.9 Atmospheric neutrinos act as a severe background to the signal neutrinos coming from the WIMP annihilation. The background ν_μ fluxes are shown in azure for the $E_\nu \in [1, 25]$ GeV. The ν_μ fluxes due to WIMP annihilation in the sun for a 25 GeV WIMP and assuming 100% branching ratio for $\tau^+\tau^-$ channel and $\sigma_{SD} = 10^{-39}\mathrm{cm}^2$ and is also shown (red). The signal fluxes are several orders of magnitude lower than the background neutrino fluxes. The signal and the background fluxes have been averaged over all directions. 89

5.1 The Bodi West Hills (BWH) and the layout of INO facilities. Figure taken from Ref. [14]. 92

5.2 The three modules of ICAL detector. Each module dimension is 16 m (L) $\times$ 16 m (W) $\times$ 14.5 m (H). The axis along which the modules will be placed is defined as x-axis in ICAL coordinate system. The remaining traverse axis is labelled as y-axis. The vertical direction is labelled as z-axis. Each of the modules contain two vertical slots cut into it so as to enable the current carrying copper coils to be wound around them. Figure taken from Ref. [14]. 92

5.3 Magnetic field map in the central plate of the central module ($z = 0$). The length and the direction of the arrows indicate the strength and the direction of the field respectively. The magnitude is also shown in T in the colour palette. This map is generated using the MAGNET6 [15] software. Figure taken from Ref. [14]. 95

5.4 Schematic representation of an RPC. Figures taken from Ref. [14] 97

5.5 NC and CC events. 99

5.6 Sample track of a neutrino event with a muon track and hadron shower in the ICAL detector, where z = 0 indicates the central layer of the detector. Figure taken from Ref. [14]. 101

5.7 The INO simulation and analysis framework. 104

5.8 LEFT: Reconstruction Efficiency for μ^- at ICAL. RIGHT: Reconstruction efficiency for μ^+ at ICAL 108

5.9 LEFT: Charge identification reconstruction efficiency for μ^- at ICAL RIGHT: Charge identification reconstruction efficiency for μ^+ at ICAL 109

5.10 Schematic showing tracks for two muons (μ^+) in the $x - z$ plane for the same values of incident muon energy and muon zenith angle, but with $\phi < \pi/2$ (shown in red and has a momentum component in the positive x direction) and other with $\phi > \pi/2$ (shown in green and has a momentum component in the negative x direction). The difference in bending causes the muons to traverse different layers will results in difference in their track reconstruction accuracy, thereby resulting in a ϕ dependence of muon response to the detector. 111

5.11 LEFT: Reconstructed momentum distribution for μ^- at ICAL. RIGHT: Reconstructed cosine of zenith angle distribution for μ^- at ICAL. Both the distributions are for μ^- with true $E_\mu = 1$ GeV and $\cos\theta = 0.65$. 112

5.12 LEFT: Reconstructed momentum distribution for μ^- at ICAL. RIGHT: Reconstructed cosine of zenith angle distribution for μ^- at ICAL. Both the distributions are for μ^- with true $E_\mu = 10$ GeV and $\cos\theta = 0.65$. 113

5.13 LEFT: Reconstructed momentum distribution for μ^- at ICAL. RIGHT: Reconstructed cosine of zenith angle distribution for μ^- at ICAL. Both the distributions are for μ^- with true $E_\mu = 100$ GeV and $\cos\theta = 0.65$. 113

5.14 LEFT: Reconstructed momentum distribution for μ^- at ICAL. The energy resolution(σ_E) is given by σ'_E/E, where σ'_E is the width obtained by fitting this with Gaussian probability distribution functions. RIGHT: Reconstructed cosine of zenith angle distribution for μ^- at ICAL. Angular resolution is given by $\sigma_{cos\theta}$ which is the width obtained by fitting it with Gaussian probability distribution functions. Both the distributions are for μ^- with true $E_\mu = 25$ GeV and $\cos\theta = 0.85$. 114

5.15 LEFT: RMS width for μ^-. RIGHT: RMS width for μ^+ at ICAL 114

5.16 LEFT: Momentum resolution for μ^-. RIGHT: Momentum resolution for μ^+ at ICAL 114

5.17 LEFT: $\cos\theta$ resolution for μ^- at ICAL. RIGHT: $\cos\theta$ resolution for μ^+ at ICAL . . 115

6.1 The μ^- event distribution at ICAL due to atmospheric neutrino background for 500 kt-years of ICAL exposure. ICAL has zero efficiency for horizontal tracks which is reflected in the bins around $\cos\theta = 0$. Note that $\cos\theta = 1$ represents upward going muons in ICAL convention. 118

6.2 The cone regions where signal from the WIMP annihilations are expected for the sun. 119

6.3 90 % cone-cut values obtained for the sun for neutrinos (LEFT) and antineutrinos (RIGHT) as a function of the WIMP mass m_χ. 121

6.4 The figure shows the probability of solar exposure for each zenith (θ) and azimuthal (ϕ) angle bin for INO's geographical coordinates. Here, $\theta = 180^\circ$ represents zenith. The plot has been obtained through SLALIB routine of WIMPSIM. 121

6.5 The μ^- event distribution at ICAL due to atmospheric background after applying the angular suppression corresponding to a 100 GeV WIMP. $\cos\theta = 1$ represents upward going muons. The plot is for 10 years of ICAL running. 122

6.6 The μ^- (red solid lines) and μ^+ (orange dotted lines) event distribution at ICAL due to signal neutrinos arising out of WIMP annihilations in the sun through various annihilation channels. The signal events correspond to neutrino fluxes arising due to SD capture rate. A cross-section of $\sigma_{SD} = 10^{-39}\mathrm{cm}^2$ has been assumed for the signal neutrinos and m_χ is taken as 25 GeV. Also shown are μ^- (blue solid lines) and μ^+ (azure dotted lines) event distributions due the reduced atmospheric neutrino background after applying the cone-cut angular suppression and the solar exposure function suppression. 123

6.7 The expected 90 % C.L. sensitivity limit on the WIMP-nucleon spin-dependent cross-sections as a function of the WIMP mass. The ICAL expected sensitivity are shown for $\nu\bar{\nu}$ (red solid line), $\tau^+\tau^-$ (red dashed line) and $b\bar{b}$ (red dashed line) channels and for 10 years of running of ICAL. Current 90 % C.L. limits from other indirect detection and direct detection experiments have been shown. Also shown is the region compatible with the claimed signal seen by DAMA/LIBRA. 126

6.8 The expected 90 % C.L. sensitivity limit on the WIMP-nucleon spin-independent cross-sections as a function of WIMP mass. The expected ICAL sensitivity are shown for $\nu\bar{\nu}$ (red solid line), $\tau^+\tau^-$ (red dashed line) and $b\bar{b}$ (red dashed line) channels and for 10 years of running of ICAL. Current 90 % C.L. limits from other indirect detection and direct detection experiments have been shown. Also shown is the region compatible with the claimed signal seen by DAMA/LIBRA, CoGeNT, CRESSTII and CDMS II Si. 127

6.9 The expected 90 % C.L. sensitivity limit for ICAL on the WIMP-nucleon spin-dependent cross-sections as a function of the WIMP mass and for different annihilation channels. 128

6.10 The expected 90 % C.L. sensitivity limit for ICAL on the WIMP-nucleon spin-independent cross-sections as a function of the WIMP mass and for different annihilation channels. 128

6.11 The expected 95% C.L. ICAL sensitivity limits in the mediator mass M_{med} vs DM mass m_χ plane for WIMP proton SD scattering. It has been generated following the prescription given by LHCDMWG [16] and using the recommended values of the universal coupling to quarks $g_q = 0.25$ and the mediator coupling to DM $g_\chi = 1.0$ in Eq. 2.19. The red shaded region represents the expected exclusion parameter space at 95 % C.L. for 500kt-years of ICAL exposure and assuming $\chi\chi \rightarrow \nu_\tau\bar{\nu}_\tau$ annihilation channel. Exclusion regions at 95 % C.L. are shown from other experiments for comparison: PICO-60 [17] (blue-gray shaded region), XENON-1T [18] (light blue shaded region), ATLAS [19] (orange shaded region) and CMS [20](green shaded region). 129

6.12 The expected 90 % C.L. sensitivity limit for ICAL on the WIMP-nucleon spin-dependent and spin-independent cross-sections as a function of the WIMP mass and for different annihilation channels. The solid lines are the sensitivity limits calculated using detector systematics as described in Sec 6.2. The corresponding dotted lines are without systematics. 130

6.13 Impact of varying branching ratios on the expected 90 % C.L. sensitivity limit at ICAL. The shown limits are for WIMP-nucleon spin-dependent cross-sections as a function of the WIMP mass and for three annihilation channels (same as in Fig. 6.7). Detector systematics have been included. The expected 90 % C.L. sensitivity limit due to toy Models A (red line) and B (violet line) have been shown. . . 131

7.1 The cone regions where signal from the WIMP annihilations are expected for the earth. 141

7.2 90 % cone cut values obtained for the earth. This is obtained using WIMPSIM and GENIE. A cone angle is estimated such that it contains 90% of the signal events. The solid lines correspond to neutrinos and dashed lines correspond to anti-neutrinos for each of the annihilation channel. 142

7.3 Angular probability distribution of reconstructed μ^- at ICAL due to WIMP annihilations in the earth. A comparison for three WIMP masses has been shown and the region where signal is expected is marked. The probability distribution for the unsuppressed atmospheric background is also shown. 143

7.4 Muon event distribution at ICAL due to atmospheric neutrinos and signal neutrinos arising out of a WIMP annihilations in the earth. The plots are for fluxes arising due to SI capture rate. A cross-section of $\sigma_{\rm SI} = 10^{-44}{\rm cm}^2$ has been assumed for the signal neutrinos. The left plot is for the WIMPs annihilating into the channel $b\bar{b}$ while the right plot is for the annihilation channel $\tau^+\tau^-$. A 100 % branching ratio has been assumed for each of the channels. Also shown are the corresponding events coming from the atmospheric background after applying the suppression scheme as described in 7.1. Atmospheric events have been simulated using Honda fluxes at Theni [21]. The softer channel $b\bar{b}$ has more background than the harder channel $\tau^+\tau^-$. 143

7.5 Muon event distribution at ICAL due to atmospheric neutrinos and signal neutrinos arising out of a WIMP annihilations in the earth. The plots are for fluxes arising due to SI capture rate. A cross-section of $\sigma_{\rm SI} = 10^{-44}{\rm cm}^2$ has been assumed for the signal neutrinos. The plot is for the WIMPs annihilating into the channel $\nu_\mu\bar{\nu}_\mu$, assuming a 100 % branching ratio. The corresponding events coming from the atmospheric background after applying the suppression scheme as described in 7.1 are also shown. It can be seen that events in this case are more than the $b\bar{b}$ and $\tau^+\tau^-$ channels. 144

7.6 The expected 90 % C.L. sensitivity limits on $\sigma_{\rm SI}$ for ICAL as a function of annihilation cross-section $\langle\sigma_{\rm A}v\rangle$ for a 52.14 GeV WIMP annihilating through $\nu_\mu\bar{\nu}_\mu$ (dark orange solid), τ^+ and τ^- (red solid) and $b\,\bar{b}$ (red dashed). Also shown are upper limits at 90 % C.L obtained by various experiments IceCube [22] τ^+ and τ^- (green), ANTARES [23] τ^+ and τ^- (black), $b\,\bar{b}$ (cyan), $\nu_\mu\bar{\nu}_\mu$ (azure), LUX [24] (blue-dashed) and XENON-1T [25] (dark brown solid) have been shown for comparison. For ICAL, systematics have been included. 146

7.7 The expected 90% C.L. sensitivity limits on $\sigma_{\rm SI}$ as a function of WIMP mass, assuming a WIMP annihilation cross section $\langle\sigma_{\rm A}v\rangle = 3\times10^{-26}$ cm^3 s^{-1}. The displayed sensitivity limits are for the local dark matter density $\rho = 0.3$ GeVcm^{-3}. Among the indirect detection experiments, using neutrinos as a probe, ICAL provides the most stringent bound. The dip around 50 GeV in the limits obtained for Earth WIMP annihilation is a prominent feature in all experiments and is due to resonant capture of WIMPs on Fe. ICAL 90% C.L. sensitivity limits for $\nu_\mu\bar{\nu}_\mu$ (dark orange solid), $\tau^+\tau^-$ (red solid) and $b\,\bar{b}$ (red dashed) channels for WIMP annihilation in the Earth are shown; 90% C.L. upper limits from SK [26] for τ^+ and τ^- (brown), IceCube [22] τ^+ and τ^- (green) and ANTARES [23] τ^+ and τ^- (black). Also, shown are the limits obtained from DARKSIDE [27] (dark green dotted), LUX (blue), XENON-1T [25] (brown solid) and PANDA [28] (cyan dotted). 147

7.8 The expected 90% C.L. sensitivity limits on the annihilation rate ($\Gamma_{\rm A}$) as function of WIMP mass (m_χ) due to WIMPS annihilating into $\nu_\mu\bar{\nu}_\mu$ (dark orange), $\tau^+\,\tau^-$ (red solid) and $b\,\bar{b}$ (red dashed) with 100% branching ratio each. The limits are for 10 years of ICAL running. For comparison limits from various other experiments have been shown: ANATARES [23] $\tau^+\,\tau^-$ (black), $b\,\bar{b}$ (cyan), $\nu_\mu\bar{\nu}_\mu$ (azure) , and IceCube [22] τ^+ and τ^- for $m_\chi < 50$ GeV and W^+W^- for $m_\chi > 50$ GeV (green). We show these limits for a fixed $\langle\sigma_{\rm A}v\rangle = 3\times10^{-26}$cm^{3}s^{-1}. 148

7.9 The expected 90% C.L. sensitivity limits for WIMP annihilation for different masses and two annihilation channels for WIMP annihilation in the earth are shown. The solid lines are the sensitivity limits calculated using detector systematics as described in Sec 6.2. The corresponding dotted lines are without systematics. The expected sensitivity limits are shown for $\nu_\mu\bar{\nu}_\mu$ in red solid (with systematics) and orange-dotted lines (without systematics), for τ^+ and τ^- are shown in blue solid (with systematics) and azure-dotted lines (without systematics) and for $b\,\bar{b}$ in dark green solid (with systematics) and light green-dotted lines (without systematics). The effect of systematics, as we expect, is to worsen the limits as expected. It can be seen that for the harder channels, the impact of systematics is seen to decrease and for $\nu_\mu\bar{\nu}_\mu$ channel it becomes almost non-negligible. 149

7.10 The expected 90% C.L. ICAL sensitivity limits on $\sigma_{\rm SI}$ as a function of m_χ for WIMP annihilation in the sun and earth. The expected sensitivity limits for the annihilation in the sun is shown for $\tau^+\,\tau^-$ (light blue dashed), $b\,\bar{b}$ (green dashed), and $\nu_\mu\bar{\nu}_\mu$ (dark orange dashed) with 100% branching ratio each. The expected sensitivity due to WIMP annihilation in the earth for channels $\tau^+\,\tau^-$ (blue solid), $b\,\bar{b}$ (dark green solid) and $\nu_\mu\bar{\nu}_\mu$ (red solid) are shown for comparison. For calculating earth's sensitivity, a WIMP annihilation cross section $\langle\sigma_{\rm A}v\rangle = 3\times10^{-26}{\rm cm}^3{\rm s}^{-1}$ has been assumed. 150

8.1 The signal search region for the WIMP annihilation in the galactic centre. The figure is not to scale. The angular separation Ψ has to be optimised so as to maximise the ICAL sensitivity to this search. 155

8.2 The Ψ_μ values as a function of m_χ used for the analysis in this work. 157

8.3 The galactic centre exposure function in terms of horizontal coordinates θ and ϕ. . 158

8.4 μ^- event distribution at ICAL due to annihilation of 30 GeV WIMP in GC and the corresponding suppressed atmospheric neutrino background. The signal μ^- events corresponding to channels $b\bar{b}$ (LEFT) and $\mu^+\mu^-$ (RIGHT) have been shown in red. The μ^+ events for the channels are shown in dotted orange lines. μ^- and μ^- events for the suppressed atmospheric background is shown in solid blue and light blue dotted lines for both the channels. These events are for 50 $\times$ 10 kt-years of ICAL exposure and signal expectation is assuming $\langle\sigma_A\, v\rangle = 5 \times 10^{-21}\mathrm{cm}^3\mathrm{s}^{-1}$ and NFW density profile. 159

8.5 μ^- event distribution at ICAL due to annihilation of 30 GeV WIMP for $\tau^+\tau^-$ (LEFT) and $\nu_\mu\bar{\nu}_\mu$ (RIGHT) channels. The colour convention, detector exposure parameter values are same as in Fig. 8.4. 160

8.6 The 90% C.L. expected ICAL sensitivity for $\langle\sigma_A v\rangle$ as a function of m_χ for $b\bar{b}$ (light blue), $\mu^+\mu^-$ (black), $\tau^+\tau^-$ (green) and $\nu_\mu\bar{\nu_\mu}$ (red) annihilation channels. The shown result is assuming 100 % branching ratio for each annihilation channel and NFW DM density profile. This is for 50 $\times$ 10 kt-years of ICAL exposure and systematic uncertainties have been considered. 161

8.7 The 90% C.L. expected ICAL sensitivity for $\langle\sigma_A v\rangle$ as a function of m_χ assuming 100% branching ratio each for the channels $\mu^+\mu^-$ (black solid line) and $\nu_\mu\bar{\nu_\mu}$ (red solid) for 50 $\times$ 10 kt-years of ICAL exposure and assuming NFW density profile. The 90 % C.L. upper limit obtained by other experiments are also shown : SK [29] are shown for $\mu^+\mu^-$ (black dashed line) and $\nu_\mu\bar{\nu_\mu}$ (red dashed), IceCube [30] for channel $\tau^+\tau^-$ (green) and ANTARES [31] for $\tau^+\tau^-$ (brownish yellow) channel. The observed e^+ e^- excesses and the interpretations of them as dark matter self annihilations, limit obtained by FERMI-LAT [32] (blue) is also shown. The thick cyan line represents the natural scale for which WIMP is a thermal relic from the early universe. 162

8.8 The 90% C.L. expected ICAL sensitivity for $\langle \sigma_A v \rangle$ as a function of m_χ assuming 100% branching ratio for $\nu_\mu \bar{\nu_\mu}$ channel and for 50 $\times$ 10 kt-years of detector exposure are shown for NFW (blue). EINASTO (red) and BURKERT (green) dark matter density density profiles. 163

8.9 The 90% C.L. expected ICAL sensitivity for $\langle \sigma_A v \rangle$ as a function of m_χ assuming 100% branching ratio for $\nu_\mu \bar{\nu_\mu}$ channel, for 50 $\times$ 10 kt-years of detector exposure and EINASTO dark matter density density profile. The result considering systematic uncertainties (red solid line) and with only statistical uncertainties (black solid line) are shown and the area in the between has been shaded for visual clarity. . . . 163

9.1 The relative probability difference $A^{\rm MH}_{\mu\mu}$ as a function of the NSI parameters $\epsilon_{\mu\tau}$ and $\epsilon_{\tau\tau}$ for $\cos\theta = -1$ (left panel) and $\cos\theta = -0.55$ (right panel). Please note the scale of the colorbars to the right of each panel. The following values of the neutrino parameters have been used: $\theta_{12} = 34^\circ$, $\theta_{13} = 9.2^\circ$, $\theta_{23} = 45^\circ$, $\delta = 0$ (no leptonic CP-violation), $\Delta m^2_{21} = 7.5 \cdot 10^{-5}\,{\rm eV}^2$, and $\Delta m^2_{31} = +2.4 \cdot 10^{-3}\,{\rm eV}^2$ (normal neutrino mass hierachy). All NSI parameters, except $\epsilon_{\mu\tau}$ and $\epsilon_{\tau\tau}$, have been set to zero. 171

9.2 The relative probability difference $A^{\rm MH}_{\mu e}$ as a function of the NSI parameters $\epsilon_{e\mu}$ and $\epsilon_{e\tau}$ for $\cos\theta = -1$ (left panel) and $\cos\theta = -0.55$ (right panel). The neutrino parameter values used are the same as in Fig. 9.1, except that $\epsilon_{e\mu}$ and $\epsilon_{e\tau}$ are non-zero, while all other NSI parameter values have been set to zero. 171

9.3 The $\Delta\chi^2_{\rm MH}$, giving the expected mass hierarchy sensitivity from 10 years of running of ICAL, as a function of the true value of NSI parameters. We keep only one $\epsilon_{\alpha\beta}$(true) to be non-zero at a time, while others are set to zero. The $\Delta\chi^2$ is obtained as explained in the text. However, the resultant $\Delta\chi^2$ is *not* marginalised over the oscillation parameters as well as NSI parameters. 178

9.4 The $\Delta\chi^2_{\rm MH}$, giving the expected mass hierarchy sensitivity from 10 years of running of ICAL, as a function of the true value of NSI parameters. We keep only one $\epsilon_{\alpha\beta}$(true) to be non-zero at a time, while others are set to zero. The $\Delta\chi^2$ is obtained after marginalisation over the oscillation parameters as well as NSI parameters as explained in the text. 179

9.5 The $\Delta\chi^2_{\rm S}$, giving the sensitivity reach of 10 years of ICAL data in constraining the NSI parameters in the event that the data show no signal of any new physics, as a function of the fit value of NSI parameters. We keep only one $\epsilon_{\alpha\beta}$(true) to be non-zero at a time, while others are set to zero. The $\Delta\chi^2_{\rm S}$ has been marginalised over the oscillation parameters and NSI parameters as explained in the text. 181

9.6 The improvement in the expected bounds on NSI from increasing the considered muon energy range from 20 GeV to 100 GeV in the analysis. We show this only for the NSI parameters $\epsilon_{\mu\tau}$. 182

9.7 The $\Delta\chi^2_{\rm D}$, giving the discovery potential of 10 years of ICAL data in observing NSI, as a function of the true value of NSI parameters. We keep only one NSI parameter to be non-zero at a time, while others are set to zero. The $\Delta\chi^2_{\rm D}$ has been marginalised over the oscillation parameters as explained in the text. 183

9.8 The expected C.L. contours in the given NSI parameter plane. The other NSI parameters are set to zero. The NH has been assumed to be true. The black dots show the points where the data were generated, which are for no NSI in this case. . 185

9.9 The expected C.L. contours in the given NSI parameter plane. The other NSI parameters are set to zero. The upper panels are drawn in the $\epsilon_{\mu\tau} - \epsilon_{\tau\tau}$ plane, while the lower panels are drawn in the $\epsilon_{e\tau} - \epsilon_{e\mu}$ plane. The black dots show the points where the data were generated. 185

10.1 The simulation and analysis involved in the indirect searches for WIMP annihilation with ICAL. 193

List of Tables

3.1 Oscillation parameters used in the simulations related to dark matter searches in the sun and the earth. 60

3.2 Oscillation parameters used in the GC WIMP annihilation analysis [33] [www.nu-fit.org]. 69

3.3 Parameter values for different density profiles. 73

5.1 ICAL at a glance 94

List of Abbreviations

CC	Charged Current
CDM	Cold Dark Matter
DM	Dark Matter
ICAL	Iron Calorimeter
INO	India-based Neutrino Observatory
GC	Galactic Centre
LSP	Lighest Supersymmetric Particle
NC	Neutral Current
NSI	Non-Standard Interactions
RPC	Resistive Plate Chamber
SD	Spin Dependent
SI	Spin Independent
SM	Standard Model
SUSY	Supersymmetry
WIMP	Weakly Interacting Massive Particle

Chapter 1

Introduction

The major composition of our universe still evades our comprehension. Based on evidence from various astrophysical and cosmological observations, a standard cosmological model has emerged wherein the ordinary matter constitutes only about 5% of the universe and the nature of the remaining 95% remains 'dark' or unknown to us. Around 68% of the global energy budget is in form of dark energy, which has been hypothesised to explain the current acceleration of the expanding universe, and other than that, its nature is completely unknown to us. The remaining $\sim$ 27% is in form of dark matter (DM) which is a non-baryonic, non-luminous, non-relativistic and yet-to-be discovered form of matter and constituting about 85% of the matter content of the universe. While the gravitational evidence for dark matter's existence is overwhelming, the particle nature of DM remains a mystery. Unravelling the nature of DM is one of the most fundamental and challenging goal of the contemporary particle physics and astrophysics.

The Standard Model (SM) of particle physics does not explain the origin of DM or its properties and the existence of dark energy in the universe. It also fails to convincingly explain data from neutrino oscillation experiments and other fundamental physical phenomena in nature [34]. Although there has been no signal of physics beyond the Standard Model in any of the accelerator-based experiments including LHC, we have unambiguous evidence from complementary experiments that the SM of elementary particles is at best a low-energy effective theory and that calls for

theories beyond the SM. Although little is known about DM as a particle, any candidate for (most of) the DM must be consistent with the constraints from observations. The relic abundance of the candidate particle should account for the observed cold dark matter (CDM) abundance, it should be non-relativistic to form structures in the early universe, and among others, must be cosmologically stable implying that its lifetime is larger than the age of the universe. Among the various particles that have been put forth as candidates for DM, Weakly Interacting Massive Particles (WIMPs) are of particular interest and have been widely considered theoretically which has motivated enormous experimental endeavours to detect them. WIMPs naturally arise in several extensions of the SM, such as the minimal supersymmeteric standard model (MSSM). Among others, perhaps the well motivated and theoretically well developed candidate is the lightest supersymmetric particle (LSP). The new weak scale physics beyond SM embodies an entire class of theories and hence within the context of supersymmetry (SUSY), exact identity of WIMP is not certain. In most SUSY theories, LSP could be the neutralino which is a linear combination of supersymmetric partners of photons, Z and Higgs bosons. In the SUSY theories where R-parity is conserved, LSP has to be stable and electrically neutral and interact only weakly with the SM particles, which are the exact characteristics expected of a dark matter candidate [35]. Then there are modern theories of extra dimension, such as universal extra-dimensions (UED) which put forth lightest Kaluza Klein particle (LKP) as viable WIMP candidates.

For WIMP to be the dark matter particle, it should have small but finite coupling to ordinary matter. This arises from the requirement for WIMPs to have present cosmological density of order unity, or otherwise WIMPs would not have annihilated in the early universe and its present abundance would not conform to the observational value. Therefore, we expect a small, but non-zero, coupling to nuclei (through the coupling to quarks) and it results in a small detection rates. The cross-section for WIMP nucleon elastic scattering is very crucial when it comes to detection of WIMPs. For it is this cross section that determines the detection rate at direct detection experiments as well as accounts for the accretion of galactic halo WIMPs in the celestial bodies like

the sun and the earth which, as we will see later in this thesis, is important for indirect searches. WIMPs could have weak scale masses ranging from a few GeVs to several TeV [35] implying a similar energy scale for the prompt observable products of annihilation and decay.

An extension of the SM could include addition to its gauge or particle sector, or both. It is therefore pertinent to envisage that such an extended theory[1] would also have new (effective) interactions between the particles, beyond what is included in the Standard Model. Such interactions are expected to change the predicted outcome of experiments and existing data can be used to put limits on the strength of these interactions. Therefore, NSI can, in principle, affect the sensitivity to direct and indirect detection of dark matter.

There has been a worldwide endeavour for detecting WIMPs and the hunt is still on, employing many direct, indirect and collider searches. Unfortunately, there is no conclusive WIMP detection signature so far. DAMA/LIBRA collaboration [37, 38], has reported a long standing annual modulation at its detector, which can be interpreted as due to the modification in the relative velocity of the galactic WIMPs with respect to the earth due to latter's revolution around the sun. DAMA uses NaI(Tl) crystals for measuring scattering of WIMPs and the detected signal corresponds to a WIMP mass of $\sim$ 10 GeV, if the scattering from Na ions is considered[2]. The combined significance of DAMA phase 1 and phase 2 [40] data sets, corresponding to 2.46 ton $\times$ exposure, stands at 12.9 σ C.L. [39]. CRESST [41] collaboration has reported an excess over expected background which point to WIMP masses 10-60 GeV region with a WIMP nucleon scattering cross section of order $10^{-43} - 10^{-40}\mathrm{cm}^2$. CoGENT [42] has reported event excess and also seen an annual modulation, similar to DAMA experiment, and at 2.8 σ C.L.. The results are in cacophony for the DAMA[3], CoGENT and CRESST results are difficult to be explained in terms of simplest

[1] For discussion on NSIs at one loop in the R-parity conserving MSSM with generic lepton flavour violation sources in the soft sector, please see Ref. [36]

[2] Scattering from iodine atom would correspond to WIMP mass of around 80 GeV but has been, however, ruled out by null result from KIMS [39] which uses CsI(Tl) crystals.

[3] DAMA data is not available publicly and hence is a matter of much debate and experimental scrutiny.

dark matter models [43, 44] and the parameter space favoured by them in the WIMP mass-WIMP nucleon scattering cross section plane seems to be inconsistent. These positive signals are also in severe conflict with the null results from other experiments such as LUX [24], XENON-1T [25] and PANDA [28] which have put the most stringent limits on WIMP nucleon spin independent cross cross section constraining to below $10^{-45}\mathrm{cm}^2$ for the light dark matter *i.e.*, WIMP masses below 100 GeV. Therefore, it is worth considering to explore the WIMP nucleon cross-section for the lighter WIMPs, especially through complementary techniques such as indirect detection or searches at collider.

WIMPs could be produced as a result of proton–proton collisions at the Large Hadron Collider (LHC), and in association with one or more QCD (Quantum Chromodynamics) jets, photons as well as other detectable SM debris. However, the dark matter thus produced would escape the detector because of its very weak interaction cross section. Thus, these experiments are looking for missing transverse energy (E_T) signals which could be a signature of dark matter. In the dark matter production searches, usually one looks for SUSY particles wherein unstable and heavy SUSY particles can further decay to dark matter candidates. Thus searches at the collider involve looking for E_T and specific SM particles predicted final states. Such a signature has not been found yet and the results obtained from collider searches are so far consistent with the SM expectations leading to very strong limits from the ATLAS [19], CMS [45] and LHCb [46] experiments at the LHC. Sub-GeV DM candidates are also constrained by the MiniBooNE experiment at Fermilab [47]. Endeavours to detect dark matter in the sub-GeV mass range has also been actively pursued at fixed target experiments and with high intensity, low-energy colliders. Specifically, search for dark photons decaying into light dark matter at e^+e^- colliders such as BaBar has been done (see Chapter 16 of Ref. [48]). It should be noted, however, that the limits from the colliders are highly model dependent and hence the interpretation of these limits should be done carefully taking into consideration the underlying mechanisms that couple DM to the SM particles. We will discuss this further in Chapter 2.

Indirect searches often complement the direct detection and collider-based searches and look for the annihilation and decay products of the WIMPs in the region of high DM accumulations such as centre of the sun, earth and galaxy. The annihilation or decay of WIMP into standard model particle antiparticle pairs which could, among other products, finally give rise to neutrino-antineutrino fluxes. Neutrino detectors/ telescopes have been extensively searching for such signals. The atmospheric neutrinos pose a severe background to such indirect searches and has to be suppressed using a suitable suppression scheme. Since no excess has been found over the expected background, the neutrino experiments like SK [49], ANATRES [23] and IceCube [22, 50] have put upper exclusion limits on the WIMP-nucleon cross section. In particular, very strong limit for light WIMPs (below 100 GeV) comes from SK for spin-dependent WIMP nucleon cross sections[4].

Neutrino experiments have also looked for possible presence of NSI in their event sample and have found the data to be completely consistent with the SM. Through a statistical analysis, the SK collaboration converts this into an upper bound on the relevant NSI parameters [51]. Strong constraints on the NSI parameters come from IceCube/DeepCore data [52]. Expected constraints from other (future) atmospheric neutrino experiments have been studied previously in the literature, see *e.g.* Refs. [53–58] (see Ref. [59–64] for earlier works).

There is a proposal to build India-based Neutrino Observatory (INO) which will be an underground neutrino observatory in the southern part of India in the state of Tamil Nadu. It will house a 50 kt magnetised iron detector. The main physics goals of the ICAL detector are to observe neutrino oscillations and do precision measurements of the neutrino oscillation parameters. In particular, it aims to study the effect of matter on propagation of neutrinos through the earth and use to determine neutrino mass hierarchy *i.e.*, the sign of Δm^2_{32}. The difference in probabilities of ν and $\bar{\nu}$ depends on the sign of Δm^2_{32} and θ_{13}. ICAL with its capability of charge identification

[4]The limits on spin dependent WIMP nucleon cross sections from direct detection experiments, in general, are weaker than those from the indirect detection experiments for all ranges of WIMP masses with the exception of the limit obtained by PICO-60 [17]

can distinguish between μ^+ and μ^- and hence is greatly suited to study of neutrino mass hierarchy. Besides MH, ICAL can be used to probe signatures of sterile neutrinos, probe CPT violation using atmospheric neutrinos and look for the non-standard interactions of neutrinos. It can also be used to study the high energy cosmic rays. The main physics goal of this detector would be to use atmospheric neutrino events to determine the neutrino mass hierarchy [65–67] and atmospheric neutrino parameters [68–71] with good precision. However, it has been shown that one could use this detector to obtain competitive sensitivity to new physics scenarios such as sterile neutrinos [72], CPT violation in neutrinos [73], non-standard neutrino interactions [8], and magnetic monopoles [74] and decaying dark matter [75], among others. We attempt to use the upcoming ICAL detector at proposed INO facility to probe signatures of WIMP annihilation. We simulate prospective ICAL data and estimate expected sensitivity of the ICAL detector to such indirect searches. Specifically, in this thesis prospects of WIMP annihilation searches in the sun, earth and the galactic centre will be presented.

Besides indirect detection of dark matter, ICAL's sensitivity to explore new physics such as non-standard interactions will also be discussed. NSI, if present in nature, would not only affect the production mechanism of neutrinos at the source but would also modify the transport of atmospheric neutrinos inside the solar and earth matter, and hence alter the signal at ICAL. In this thesis, however, we are primarily interested in non-standard interactions (NSI) affecting neutrino oscillations as neutrinos propagate inside earth matter. NSI can have an impact on dark matter searches in multi-ton direct detection experiments [76] and as well can affect sensitivity of indirect seaches [77]. In this thesis, however, we do not consider impact of NSI on indirect detection of dark matter at INO. We defer such analysis to future projects.

This thesis is organised as follows. In Chapter 2, which is an introductory chapter on dark matter, we will discuss the evidence for the existence of dark matter, various particles proposed as DM candidates and why WIMP has been so widely considered as one of the most compelling

candidate. Thereafter, we will look at WIMP detection techniques of the dark matter and elaborate on the indirect searches with neutrinos as a probe which constitutes the central part of this thesis. In Chapter 3, we will focus on the neutrino fluxes arising at ICAL due to WIMP annihilation in the sun, earth and galactic centre (GC). The annihilation rates in the celestial bodies like the sun and earth are related to the capture rate of WIMPs for that body and it will be discussed in detail. The annihilation rates and the corresponding neutrino fluxes from GC depends on the distribution of WIMPs in the core region. A few benchmark DM profile will be taken up and corresponding neutrino fluxes will be compared. As mentioned earlier, ICAL will primarily study atmospheric neutrinos, which are, however, a serious background to the indirect searches. In Chapter 4, we discuss the production of atmospheric neutrinos, their spectral features and dependence of polar and horizontal coordinates. Previously, ICAL collaboration made use of atmospheric fluxes at Kamioka for doing simulations and physics analysis. However, recently fluxes at Theni have been calculated [21] and made available to us. Therefore, for the background estimation (for the indirect detection projects) Theni fluxes have been used. This is for the first time that Theni fluxes have been used in conjunction with GENIE event generator. A comparison of fluxes at Kamioka and Theni have been done in one of the sections. Finally, we briefly indicate how atmospheric neutrinos act as a background to the indirect detection work. After having described the signal and the background fluxes, we will describe the ICAL detector and its features in detail in Chapter 5. Detector geometry will be discussed with special focus on resistive plate chambers (RPCs) which are the active detection units of ICAL. Much of the chapter is devoted to ICAL response to muons for the energy range upto 100 GeV and it is an extension of the previous work [78]. For the work presented in this thesis, the muon response has been obtained through dedicated Geant4 simulation and this has enabled us to carry out the simulation and physics analysis in the muon range upto 100 GeV, which has not been done previously by the ICAL collaboration. At the end of the chapter, the simulation and analysis framework has been shown in the form of a flowchart. After having set up the simulation framework, we take up the issue of background suppression, statistical analysis and expected sensitivity to the WIMP annihilation in the sun, the earth and GC in the following

chapters. The WIMP masses considered will be up to 100 GeV and several annihilation channels. In an attempt to be as generic [5] as possible, the analysis with will be presented for 100 % branching ratio for each of the channels. In Chapter 6, searches in the sun has been discussed in detail and the calculated expected sensitivity for ICAL is compared with the existing limits from latest neutrino and direct detection experiments. In Chapter 7, the searches in the earth have been discussed and the corresponding reach of ICAL in comparison with the current limits from experiments discussed. In Chapter 8, we extend our search for WIMP annihilation to the galactic centre and derive expected sensitivity limits. A comparison of sensitivity studies dependent on profile and different annihilation channel will also be presented. All the interactions considered in the indirect detection work are for standard neutrino interactions. In Chapter 9, we will present a study of prospects of detecting signatures of non-standard interaction with ICAL and in case detected how well ICAL can discover or constrain NSI parameters. This study will be discussed in the context of only atmospheric neutrinos only. Finally, in Chapter 10, we conclude the findings in this thesis with a brief outlook.

[5]The signal strength in case of indirect detection depends on the model of DM considered which dictates the branching ratio of annihilation channels. Therefore, indirect detection experiments customarily quote results in terms of 100% branching ratio for each annihilation channel. These limits can be easily scaled within the framework of a specific model.

Chapter 2

Dark Matter

There is mounting evidence that the ordinary baryonic matter constitutes only $\sim$5% of the known universe. The rest comprises some unknown components such as dark energy $\sim$68% and dark matter $\sim$27% [11]. Dark matter is an elusive substance that seem to be all pervading, exerts many detectable gravitational influences throughout the universe and yet it eludes direct detection. It is known as 'dark' for it does not have any visible signatures- does not emit or absorb electromagnetic radiation at any known wavelengths, yet its gravitational interactions dominate on scales from tiny dwarf galaxies, to large spirals such as our galaxy and to the largest scales known [34, 35].

While the evidence for the existence of dark matter via its gravitational interactions is pretty strong, its particle nature remains largely unknown. The organisation of this chapter is as follows. In Section 2.1 the evidence for dark matter's gravitational interactions have been discussed. Section 2.2 is where we enumerate the most widely considered candidates for cold dark matter. This is followed by Section 2.3 where we discus WIMP in some details for we consider WIMP dark matter in this thesis. Section 2.4 describes the dark matter interactions and Section 2.5 discusses dark matter search techniques. Finally, we briefly summarise in Section 2.6 and conclude.

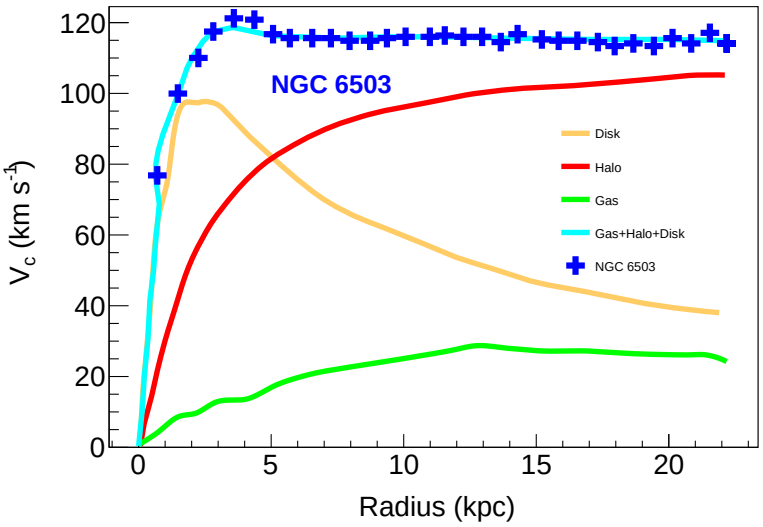

Figure 2.1: The measured rotational curve for NGC 6503 (data taken from [9, 10]) shown in blue crosses. Also shown are the combined rotational curve (cyan line) obtained by adding contribution from different mass components of the galaxy. The galactic rotation curves due to disk (light orange), dark matter halo (red), gas (green) is also shown. The data points are shown without error bars.

2.1 Dark matter evidence

The presence of dark matter is known so far only through the observations of gravitational interactions. The evidence is overwhelming and comes from a wide variety of astrophysical and cosmological observations [10, 79]. These observations can be enumerated as follows :

- **Earliest evidence from the motion of galaxies** The earliest evidence for existence of DM was postulated by Fritz Zwicky [80] who in an attempt to explain the dynamics of galaxies in the Coma galaxy cluster concluded that the most of the mass in the cluster must be invisible. Missing mass of spiral galaxies were reported by Jan Oort and later confirmed by Vera Rubin (see [81] for a more recent discussion) from the observation of flat galactic rotation curves which demanded that most of the matter of the galaxy is non-luminous and existed in the form of dark haloes [79, 82].

- **Rotational curve of galaxies** The observation of the rotational curves of the spiral galaxies i.e. the rotation speed in regard to the radial distance of the object, give us an indirect

evidence of missing matter in the form of 'dark matter'. This observation implies that that the mass of galaxy increases significantly with the distance r to its centre. From the Newtonian dynamics we know that

$$\frac{mv^2}{r} = \frac{mM(r)G}{r^2}, \tag{2.1}$$

where $M(r)$ is the mass contained within the radius r and G is the gravitational constant. For galaxies like ours, the luminous matter is concentrated in the core where we expect $M(r) \propto r^3$ and hence $v \propto r$. For the region outside the hub, we expect $M(r) =$ constant and hence $v \propto r^{-1/2}$. Therefore, we expect the galactic rotation to decrease for high r values. Instead, we see that the velocities remain constant. This can be explained by invoking the presence of dark matter reaching beyond galactic disks. Fig. 2.1 shows the circular velocity V_c of the galaxy NGC 6503 as a function of radial distance r from the galactic centre [10]. The baryonic matter comprising the disk and the gas are not enough to explain the galactic rotation curve. However, adding the contribution of the dark matter halo fits the data very well.

- **Gravitational lensing** From Einstein's theory of general relativity we know that mass bends, or in other words lenses, light. This effect can be used to look for the existence of mass even when it has no visible signature. Lensing measurements have strongly confirmed the existence of dark matter in galaxies and galaxy clusters. There is evidence from weak [83,84] and strong [85] gravitational lensing data. A beautiful example of this effect can be seen in Fig. 2.2 which shows lensing of a distant blue galaxy by the gravity of a luminous red galaxy (LRG), making it to form a horseshoe ring which are called 'Einstein Rings'. LRG 3-757 was first discovered by Sloan Digital Sky Survey (SDSS), but this image was taken with Hubble Space Telescope. The evidence provided by lensing of dark matter has an advantage over the rotational curves for the former technique can probe dark matter signatures to a much larger distances $\sim$200 kpc from the centre of galaxies.

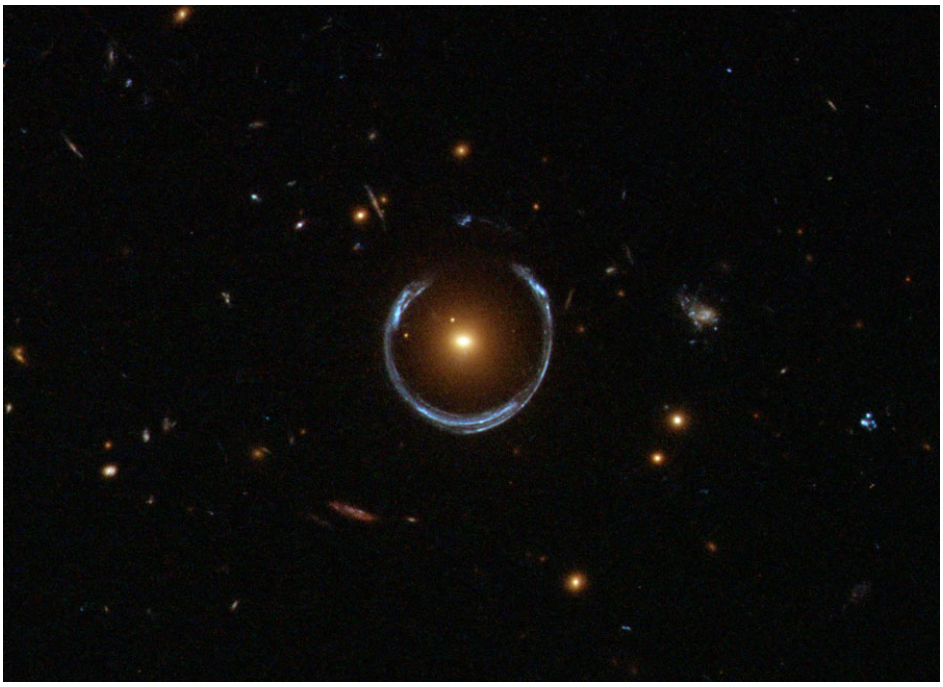

Figure 2.2: A Horseshoe Einstein ring from Hubble [Image Credit: ESA/Hubble &NASA]. This is an example of a gravitational lens mirage. The gravity of a luminous red galaxy (LRG) has gravitationally distorted the light from a farther blue galaxy.

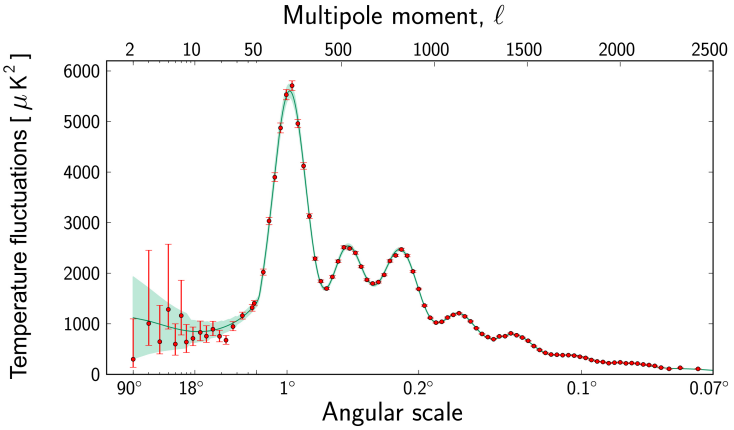

Figure 2.3: Planck's power spectrum [11] of temperature fluctuations in the cosmic microwave background. The fluctuation are plotted for different angular scales on the sky. The Planck data are marked by red dots with corresponding error bars whereas the green curve represents the standard model of cosmology, ΛCDM. The first peak at 1° is the evidence for a flat geometry of universe, the height of the second peak indicates that ordinary matter is just 5% of the total and from the second and third peaks give the DM contribution to be approximately 26%.

- **Bullet cluster** Observations of the bullet cluster by the Chandra satellite [86] further reinforced the idea of existence of a dark non-baryonic component of matter in the universe. Bullet cluster was formed out of collision of two smaller galaxies and observations in X-ray, visible light and lensing data clearly show two different types of matter by observing that in the process of merging of the two smaller clusters, the dark matter passed through the collision point whereas the baryonic matter coalesced to a form a single region in the centre of the bullet cluster.

- **Cosmic microwave background** The most precise measurement of the dark matter abundance of the universe comes from the measurements of the anisotropies of the cosmic microwave background spectra (CMB) [87]. The CMB is the remnant radiation of the early universe and marks the epoch when the photons underwent oscillations that froze in just before decoupling from the baryonic matter at a redshift $z \sim 1100$. Through measurements of the angular scale and height of the peaks (and troughs) of these oscillations, cosmological parameters such as total energy density of universe (Ω), the baryonic energy density (Ω_b) and the dark matter density contribution (Ω_χ) can be determined. For a flat universe, the light travels in a straight line and the angular scale of the first Doppler peak is expected to be at 1° and the sound horizon of the last scattering surface shows that it is indeed the case thereby proving that the universe geometry is indeed flat corresponding to an energy density of $\sim 10^{-29}\mathrm{gcm}^{-3}$. The height of the second peak implies that 5% of the global energy budget is ordinary matter, while comparing all peaks we conclude that around 26% of the global energy budget of universe is dark matter. Fig. 2.3 shows the power spectrum of the temperature fluctuations in the CMB as measure by Planck satellite [11]. The most recent analysis of the data from the Planck satellite [11] gives a dark matter abundance of $0.1172 \leq \Omega_{\mathrm{DM}} h^2 \leq 0.1226$ at 67 % C.L..

- **Primordial nucleosynthesis model** At an age of a few hundred seconds, the universe had a temperature of around 10^{10} degrees, deuterium became stable : $p + n \rightarrow D + \gamma$. With the formation of deuterium, the elements helium and lithium could form as well. After billion

of years when the stars formed, the synthesis of the heavier elements like C, N and O started only when the high enough density conditions were available for fusion of three helium atoms into a single carbon atom. The Big Bang predicts the abundance of 25 % ^{4}He, 10^{-5} % deuterium and, 10^{-7} % ^{7}Li by mass which matches exactly with the data, provided the ordinary matter constitutes only 5% of the total universe.

- **Evolution of large cosmic structures** The existence of dark matter is crucial for the large structure formation. The dark matter must be 'cold' or non-relativistic as a hot dark matter particle would be freely streaming and would not form clumps which are essential for initiating the structure formation process. DM initiates the process, because before recombination at $z \sim 1100$, baryons and photons are coupled and are freely streaming through universe. It is the DM clumps that provides the potential wells for the ordinary matter to get trapped and form structures. The requirement for non-relativistic cold dark matter rules out neutrinos as a dark matter candidate.

2.2 Candidates for dark matter

Several candidates for dark matter has been proposed and they have to conform to the various observations of the gravitational interactions described in the previous section. Dark matter must be cold for the structure formation requirement. From primordial nucleosynthesis and microwave background data the nature of the dark matter has to be non-baryonic.

- **MACHOs** Various observations that indicated the existence of dark matter based on high M/L values i.e. a discrepancy between gravitationally measured and visible mass, led to a class of dark matter candidates generally termed as MaCHOs (Massive Compact Halo Objects). MaCHOs includes a range of objects like brown dwarves, stellar remnants, black holes and other low luminous objects. However, a combination of theory and observations have ruled out low mass stars, substellar objects or brown dwarfs and stellar remnants (white dwarfs) to be the convincing solution to the dark matter problem in the milky way (see

Ref. [10] and the references therein for further details). However,a few MACHO candidates could still be viable dark matter candidates: primordial black holes [88], particularly in light of the LIGO (Laser Interferometer Gravitational-Wave Observatory) [89] observation of black hole mergers where the black holes are very massive.

- **Axions** One of the popular candidates for cold dark matter (CDM) is the axions. The axions were proposed to address what is known as "strong CP problem", as proposed by Peccei and Quinn [90]. Axion mass $m_{\rm A} \sim eV(10^7/f_{\rm A})$ where $f_{\rm A}$ is the axion mass scale as a theoretical free parameter. The axion strength of coupling to ordinary matter is $\propto f_{\rm A}^{-1}$. These are considered suitable CDM candidates if their masses lie in the range $m_{\rm A} \sim 10^{-3} - 10^{-6}$ eV. Astrophysical considerations places an upper bound on axion mass $m_{\rm A} < 15$ meV, while a lower bound comes from cosmology. Microwave cavity searches allow for direct detection of axions such as ADMX (ADark MatterX cavity experiment) [91] which has provided exclusion limits in the axion mass range and currently looking for axion mass $\sim 10^{-5}$ eV. Several other experiments based on novel techniques are carrying out axion searches.

- **WIMPs** WIMPs comprise a broad category of dark matter candidates. Their couplings to the SM is via weak interactions, they do not couple to photons directly and are thermally produced in the early universe with their relic density fixed by their abundance at the time of freeze-out *i.e.*, when the WIMP interaction rate is sufficiently small that they fall out of the equilibrium with the other particles. They are discussed further in section 2.3.

- **Sterile Neutrinos** Ordinary neutrinos are too light to provide for the structure formation and hence were ruled out to be DM candidate. Sterile (or right-handed) neutrinos could be dark matter candidates and this idea was was first proposed by Dodelson and Widrow [92]. It has been shown to be a viable as cold or warm dark matter candidate in different scenarios [93]. Sterile neutrino is predominantly composed of heavier neutrino mass eigen states and, in some scenarios, its decay into a lower mass eigen states is often described as a sterile neutrino

decaying into an active neutrino. This gives a photon line corresponding to the half of the sterile neutrino mass, which for the most viable DM candidates is in the KeV-MeV energy range. Line emission could be used to indirectly detect sterile neutrino dark matter.

Although the cold dark matter paradigm has been successful in explaining the galactic motion and the structure formation in the galaxies, the modelling and predicting the dark matter haloes around the galaxies is a challenging task. The framework such as MOND (MOdified Newtonian Dynamics), tackles this issue by modifying the gravitational effect on matter rather than the matter content itself. This is achieved by modifying Newtonian dynamics at a vary small accelerations which are present at galaxy length scales [94]. Although, the MOND theory has been successful in predicting the galactic rotation curves considering the baryonic mass distribution, it fails to explain the observations from global clusters or the bullet cluster. Apart from these, several candidates like asymmetric dark matter, non-thermal WIMPzillas, Q-balls, and many others have been proposed. In the next section, we discuss WIMP in detail which is the candidate under consideration in this thesis.

2.3 Weakly Interacting Massive Particles

Weakly Interacting Massive Particle (WIMP) is one of the most widely studied candidate for cold dark matter. WIMP refers to a class of neutral stable particles which are predicted to have masses ranging from a few GeVs to tens of TeV [35] and their interactions with standard matter, apart from gravitational interactions, are weak in nature. The main reason behind WIMP's popularity is that these appear in several extensions of the SM in an attempt to solve unrelated problems. As mentioned in Chapter 1, the most popular candidates for WIMP are the neutralino, that arise in minimal supersymmetric standard model (MSSM) and the lightest Kaluza-Klein particle (LKP) which are predicted in theories of universal extra dimension [95, 96].

DM particles have to be sufficiently massive to solve the problems brought on by a baryons-only universe. Also, they should be long-lived or decay with a decay lifetimes of more than the

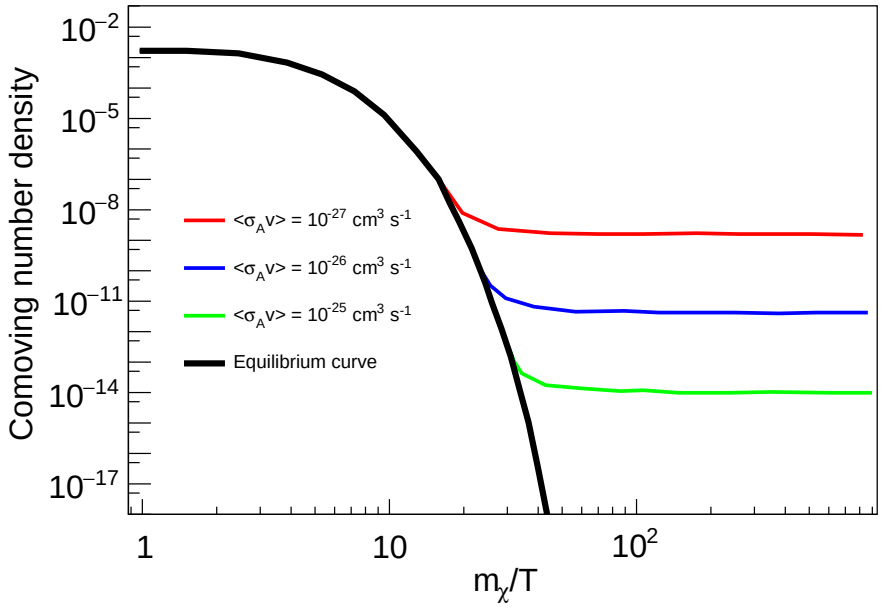

Figure 2.4: Comoving number density evolution as a function of the ratio x in the context of the thermal freeze-out. The value of the annihilation cross section determines the DM abundance since $\Omega_\chi h^2 \propto 1/\langle\sigma_{\rm A} v\rangle$.

age of the universe and WIMP seem to fit these criteria. Supposing that there is such a yet-to-be discovered particle χ[1], in thermal equilibrium we can write its the number density n_χ as [35]

$$n_\chi^{eq} = \frac{g}{(2\pi)^3}\int f(p)\mathrm{d}^3p, \tag{2.2}$$

where g is the number of internal degrees of freedom of the particle and $f(p)$ is the Fermi-Dirac or Bose-Einstein distribution depending on whether WIMP is fermion or a boson. At high temperatures *i.e.*, $T \gg m_\chi$, where m_χ is WIMP mass, χ are in abundance such that $n_\chi \propto T^3$. At this temperature, they are rapidly undergoing the following conversion process: $\chi\chi \to l\bar{l}$, where $l\bar{l}$ are particle-antiparticle pairs. These could be quark-antiquark pairs, lepton-antilepton pairs or even gauge-and/or Higgs-boson pairs for kinematically allowed WIMP masses. For $T \ll m_\chi$, there is an exponential drop in their number density such that $n_\chi^{eq} \approx g(m_\chi T/2\pi)^{3/2}\mathrm{e}^{-\frac{m_\chi}{T}}$. Soon after T drops below m_χ, the rate of WIMP annihilation Γ drops below the expansion rate of the universe

[1]At many places in this thesis, WIMP has been indicated by notation χ. This notation includes all the class of WIMP and not just neutralino.

and we have $\Gamma = \langle\sigma_{\rm A} v\rangle n_\chi$, where $\langle\sigma_{\rm A} v\rangle$ is the velocity averaged WIMP annihilation cross section[2] and for a colder universe ($T \ll m_\chi$), $\Gamma \leq H$, where H is the Hubble expansion rate related to the scale factor of the universe by relation $H = \frac{1}{a}\frac{\mathrm{d}a}{\mathrm{d}t}$. At this point, WIMPs "freeze out" *i.e.*, fall out of the equilibrium and their relic cosmological abundance is set constant.

The time evolution of n_χ is described by the Boltzmann equation [97]

$$\frac{\mathrm{dn}_\chi}{\mathrm{dt}} + 3n_\chi H = -\langle\sigma_{\rm A} v\rangle\big(n_\chi^2 - (n_\chi^{eq})^2\big). \tag{2.3}$$

The total comoving number density of WIMP is denoted as Y and is related to n_χ as follow

$$Y = \frac{n_\chi}{n_s}, x = \frac{m_\chi}{T}, \tag{2.4}$$

where n_s is the entropy density of the universe. The Boltzmann equation describing the time evolution of Y can now be written as [97, 98]

$$\frac{\mathrm{d}Y}{\mathrm{d}x} = -\frac{1}{2}\sqrt{\frac{\pi}{45G}}\frac{m_\chi\sqrt{g_*}}{x^2}\langle\sigma_{\rm A} v\rangle\big(Y^2 - (Y^{eq})^2\big), \tag{2.5}$$

where $x = m_\chi/T$, G is the Newton's gravitational constant and g_* is a function of effective degrees of freedom and has a dependence on both energy and entropy densities of the universe [97]. Y^{eq} is the equilibrium value of the comoving energy density. Solving Eq. 2.5, we can get the value of total number density Y at the present temperature ($T_0 \sim 10^{-13}$ GeV) which can be used to compute the total relic abundance of WIMP Ω_χ and is given by the following equation [99]

$$\Omega_\chi h^2 = 2.755 \times 10^8 \left(\frac{m_\chi}{\mathrm{GeV}}\right) Y(T_0), \tag{2.6}$$

where h is the Hubble constant in units of 100 km $\mathrm{s}^{-1}\mathrm{Mpc}^{-1}$. Fig 2.4 shows the numerical solution to the Boltzmann equation. The equilibrium abundance per comoving volume as a function of $x = m_\chi/T$ (which increases with the increase in time) is shown by a thick black line. The coloured

[2] In indirect detection literature, the quantity $\langle\sigma_{\rm A} v\rangle$ is often referred to as simply the annihilation cross-section.

lines are for actual abundance for varying values of $\langle\sigma_{\rm A}v\rangle$. $\Omega_\chi h^2 \propto 1/\langle\sigma_{\rm A}v\rangle$ *i.e.*, as the annihilation cross section increase the WIMPs stay in equilibrium longer, resulting in a smaller relic abundance. We can re-write Eq. 2.6 in the form

$$\Omega_\chi h^2 \sim \frac{3\times10^{-27}{\rm cm}^3{\rm s}^{-1}}{\langle\sigma_{\rm A}v\rangle}, \tag{2.7}$$

From the measured dark matter abundance, Eq. 2.8 implies that if WIMPs indeed constitute all of dark matter, then it should have a total pair annihilation cross-section of $\langle\sigma_{\rm A}v\rangle \sim 3\times10^{-27}{\rm cm}^3{\rm s}^{-1}$. This value is often used as a benchmark and is referred to as the thermal relic cross-section[3] For a massive particle interacting via weak force, this cross section value is a suitable choice and hence the term WIMP is applicable to this category of thermal relic dark matter candidate. Nevertheless, it should be mentioned that in some scenarios the annihilation cross section value required to produce the observe relic density can vary significantly from the canonical thermal relic value [34].

2.4 Interaction between WIMP and nucleon

There could be several effective interactions between WIMPs and SM nucleons. Considering WIMPs to be Majorana neutralinos and their interactions under non-relativistic conditions, their effective interactions could be either spin-dependent (SD) or spin-independent (SI) [35].

2.4.1 Spin dependent (axial-vector) interaction

In SD interactions WIMP couple to the spin of the target nucleus. The WIMP-nucleon SD scattering cross-section ($\sigma_{\rm SD}$) can be written as :

$$\sigma_{\rm SD} = 32\frac{G_F^2\mu^2}{\pi}(a_pS_{p(N)} + a_nS_{n(N)})^2\frac{J+1}{J}, \tag{2.8}$$

[3] Also see Ref. [100] for more precise calculations.

where G_F is the Fermi constant, $\mu = m_\chi m_N/(m_\chi + m_N)$ is the reduced mass with m_χ being the WIMP mass and m_N being the mass of the target, a_p and a_n are the coupling constants for proton and neutron, respectively, and $S_{p(N)}$ and $S_{n(N)}$ are the spin of the proton and neutron in the nucleus N. J is the coupled angular momentum of the nucleus. From Eq. 2.8, we can see that the SD interaction is effective when WIMPs interact with a nucleus having large number of unpaired protons and neutrons.

2.4.2 Spin-independent (scalar) interactions

In the SI scattering the WIMP coherently scatter on the target nuclei. The WIMP nucleon SI scattering cross section ($\sigma_{\rm SI}$) can be written as :

$$\sigma_{\rm SI} = \frac{4\mu^2}{\pi}(Zf_p + (A-Z)f_n)^2, \tag{2.9}$$

where f_p and f_n are the coupling constants for the proton and the neutron respectively. A and Z are the mass number and the atomic number of the target, respectively. From Eq. 2.9, we can see that $\sigma_{\rm SI}$ is proportional to square of the mass number of the target nucleus *i.e.*, $\propto A^2$. Therefore, this interaction becomes dominant for the case of WIMP interacting with heavier nuclei.

2.5 Detection of dark matter

The particle dark matter hypothesis can be tested via three processes: the production at particle accelerators, directly via scattering on target nuclei, or indirectly by searching for DM's annihilation and decay products. The three main strategies as shown in Fig. 2.5. In the coming following subsections, we briefly summarise each technique.

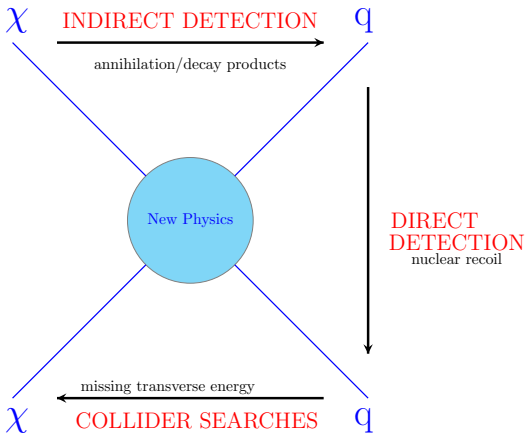

Figure 2.5: An interaction diagram of standard model particle q and dark matter χ. The three categories of dark matter detection *viz.*, direct, indirect and collider searches are shown.

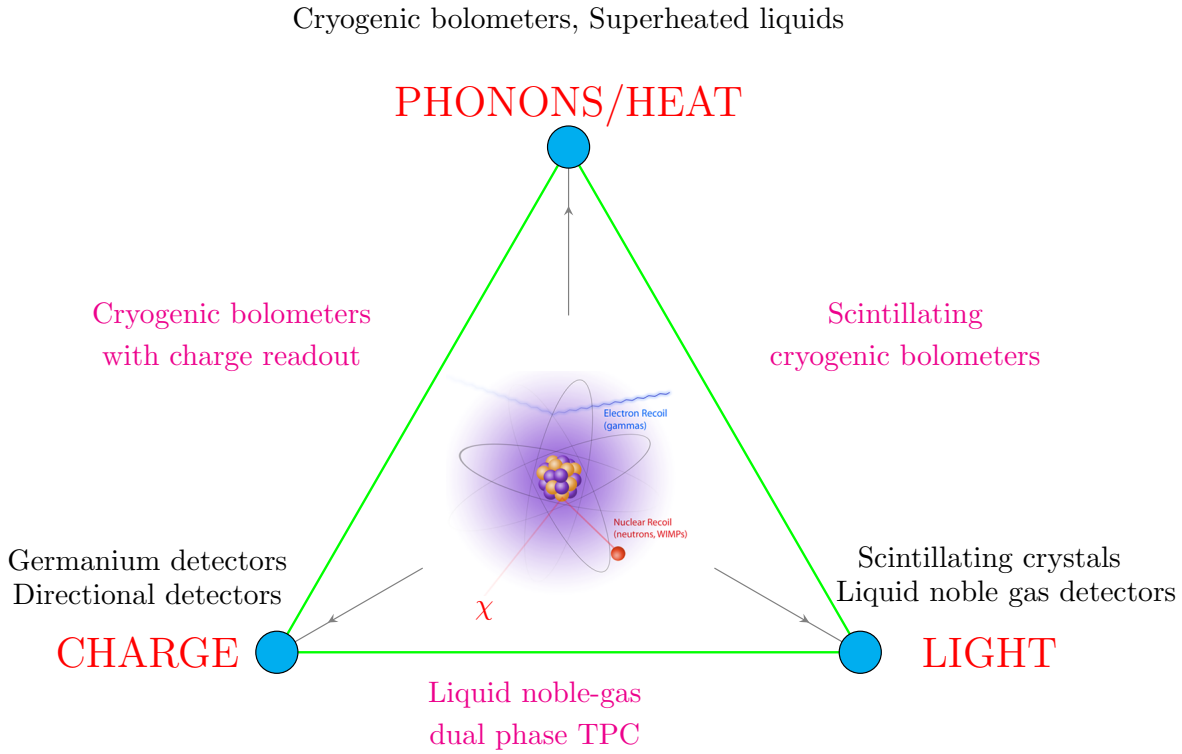

Figure 2.6: Schematic of possible signals that can be measured in direct detection experiments depending on the technology in use. The detectors marked in black are sensitive to either charge, light or phonon/heat signals. For better particle discrimination, many detectors combine these techniques to be sensitive to more than one kind of signal. These are shown in magenta color. Here TPC stands for Time Projection Chamber. The recoil image (at the centre of the figure) has been taken from https://indico.fnal.gov/event/6661/session/2/contribution/22/material/slides/0.pdf.

2.5.1 Direct searches

WIMP in the local galactic halo could scatter on nuclei and cause it to recoil. The direct detection experiments aim to measure this recoil energy of the target nuclei. The WIMP-nuclei differential scattering rate can be written as,

$$\frac{dR(E,t)}{dE} = \frac{N_T \rho_\chi}{m_\chi m_N} \int_{v_{min}}^{v_{esc}} v f_E(v,t) \frac{d\sigma(v,E)}{dE} d^3v, \tag{2.10}$$

where E is the recoil energy associated with the scattering events, m_N is the mass and N_T is the number of the target nuclei (per kg) of the detector, m_χ is the WIMP mass, ρ_χ is the local DM density, v is the velocity of the DM particle relative to the earth, $f_E(v,t)$ is the velocity distribution of WIMP in the frame of the earth. v_{min} is the minimum velocity required by a WIMP to produce a detectable event at energy E and is given by $v_{min} = \sqrt{m_N E/(2\mu^2)}$, where $\mu = m_N m_\chi/(m_N + m_\chi)$ is the DM-nucleus reduced mass. The WIMP-nucleus differential cross-section $\frac{d\sigma(v,E)}{dE}$ for WIMP-nucleus scattering is

$$\frac{d\sigma(v,E)}{dE} = \frac{m_N}{2\mu^2 v^2}(\sigma_{\rm SI} F^2(q) + \sigma_{\rm SD} S(q)), \tag{2.11}$$

where q is the momentum transfer, $\sigma_{\rm SD}$ and $\sigma_{\rm SI}$ are WIMP-nucleon interaction cross section and are given by Eq. 2.8 and Eq. 2.9, respectively. $F(q)$ and $S(q)$ are the SI and SD form factors as described in Refs. [35, 101–103].

The recoil energy of the target can be measured in the recoil energy ranges from a few keV to hundreds of keV and depends on m_χ and the mass of the target nuclei. Since WIMP induced events are very rare due to the low WIMP nucleon scattering cross section, direct detection experiments are background limited. After measuring the scattering rate, the background is separated by using the detector response to electron and nuclear scattering. WIMPs being very weakly interacting are expected to produce single scattered events unlike the dominant background neutrons that could produce multiple scattering. The actual technique used to discriminate signal from

background depends on a particular experiment. For example, in Germanium detectors ionization yield is used to discriminate signal from background, whereas in experiments that use Xenon, the ionization/scintillation ratio is the discriminating variable.

The sensitivity to WIMP detection for a particular experiment is a cumulative consequence of the following factors [104]:

- **Energy threshold** drives an experiment's sensitivity to low WIMP masses, and consequently the sharpening of the direct detection limits on the WIMP nucleon scattering cross-section at low masses.

- **Background control and exposure** determine the overall sensitivity of the experiment and pushes the limits to lower scattering cross-sections assuming that they are statistically dominated. In general, an experiment's sensitivity to probe lower WIMP nucleon scattering cross-section increases with the better background discrimination and increasing the exposure.

- **Target** material decides an experiment's sensitivity to detect low and heavy WIMP masses. The target nucleus determines where the strongest limit on the scattering cross-section lies as well as its sensitivity to lower and larger WIMP masses. The choice of target nuclei also determines which scattering process dominates i.e. spin dependent or spin independent. The experimental sensitivity appears to be very different between SI and SD interactions. In case of SI interactions, SI WIMP-nucleus cross-section is a result of coherent sum of the contributions from the interactions of the WIMP with the single nucleons. Therefore, targets like Xe, with atomic number of the order 100 result in an enhanced sensitivity to SI interactions. However, for the case of SD interactions, the contribution to the different nucleons tend to interfere destructively, so that SD WIMP nucleon cross section is appreciable only for targets with an unpaired nucleon,

The main source of background for direct DM searches are mostly due to the radioactivity of the materials of and around the detector and cosmic rays muons and products of their interactions.

DM detectors need to be installed underground so as to cut down the cosmic ray fluxes and various other sources of radioactivity. Therefore, several layers of further shielding and vetoing is required to further make the detector environment to be background free as far as possible.

The energy of recoils can be measured in a detector in several ways and depending on the measurement technique, there are different types of direct detection experiments (see Ref. [104] for a detailed review). The recoil energy can manifest itself in the form of phonons which can be detected in cryogenic bolometers or superheated liquids. The signal can also be in form of scintillation light for which scintillation crystals and liquid noble-gas detectors are the most appropriate. The recoil can also cause ionisation which can be measured by semi-conductor detectors such as CoGENT. Fig. 2.6 shows the possible signal due to WIMP scattering on the target nuclei and various experiments based on the detection techniques.

Due to rotation of the sun around GC, the earth-based detectors are effectively moving into a "wind" of WIMPs. In addition to this, the earth is rotating around the sun which results in a relative velocity of the earth with respect to the WIMP wind. This is expected to give rise to an annual modulation signal at the direct detection detectors. However, as mentioned in Chapter 1, that despite the fact that DAMA has seen the annual modulation, for all the known theoretical assumptions it is hard to reconcile the positive results with the null results given by other experiments such as LUX, XENON and PANDA. In fact, they have placed strong upper bounds on the WIMP nucleon elastic scattering cross-sections. This tension demands more careful searches, especially for low mass WIMP region. In this context, WIMP indirect detection methods an attractive complementary probe.

2.5.2 Indirect searches

The indirect searches of dark matter look for the flux of final state SM particles like neutrinos, positrons, gamma rays, anti protons, arising out of WIMP annihilations or decay. WIMP annihilation rate is proportional to the square of the dark matter density (see Chapter 3 for details). Hence, indirect search involves searching for WIMP annihilation or decay products at the core of celestial

bodies, like the sun and earth, or galactic centre/halo or in general where we expect high WIMP concentration. WIMP could annihilate to various SM model particles like quark-antiquark pairs and lepton-anti-lepton pairs. These SM products then can subsequently decay to give rise to final state particles such as neutrino-antineutrino pairs and gamma photons. Depending on the WIMP model, they could also decay directly into neutrinos[4] and photons. Now, we briefly summarise various experimental techniques classified as per their search for the end product.

- γ **rays** The photons produced from an annihilating or decaying dark matter would not be significantly affected by the magnetic field. They could be, however, weakly attenuated over large galactic distances, yet their energy spectra at the point of detection at earth should be close to the spectra at the point of production at the source. The photons are therefore a good probe to measure angular position of the source and other energy related information. There are several experiments that are conducting searches for gamma rays arising out of WIMP annihilation in the galactic centre/ halo. Some of these are space based such as Fermi-LAT [32] and others are ground based like HAWC [105, 106] and MAGIC [107].

- **Antimatter** Annihilation of WIMPs into proton-antiproton, electron positron and deutron anti-deutron pairs offers a unique way of probing dark matter signatures. The flux of particles like protons, electons are copiously being produced in the cosmos. Their antiparticles, however, are limited by known production mechanism. Therefore, an excess in the anti matter content such as positron and antideutron can be inferred to be coming from WIMP annihilation. Different experiments worldwide are looking for different antiparticles. PAMELA [108] is conducting a search for antiprotons and positrons whereas GAPS [109] is a planned experiment specifically being designed to detect antideutrons.

  These charged particles, unlike gamma rays or neutrinos, gets affected by the galactic and the earth's magnetic field and appear as a diffuse spectrum. Also, in order to distinguish these particles from the antiparticles produced in the electromagnetic showers due to the

[4] Some models of extra-dimensions predict WIMP annihilating directly into $\nu_e\bar{\nu}_e, \nu_\mu\bar{\nu}_\mu, \nu_\tau\bar{\nu}_\tau$ [95, 96].

action of cosmic rays in the upper atmosphere (see Chapter 4), the searches for dark matter through this scheme have to be conducted at high altitudes or in the space.

- **Neutrinos** Neutrinos are a very powerful probes for searches for WIMP annihilation as they can propagate through space, unaffected by magnetic field. Since they are weakly interacting they can also escape the interiors of the celestial bodies without being modified significantly. The indirect detection with neutrinos as a probe is the theme of this thesis. Specifically, we will look at the prospects of detecting neutrino with ICAL in the sun, earth and galactic centre.

Indirect searches complement the direct searches, since unlike them, they not only aim to provide a measurement of WIMP mass and scattering cross-section, but also information on the different annihilation branching ratios.

2.5.3 Collider searches

As mentioned in the previous chapter, being electrically neutral and cosmologically stable massive particles, WIMPs would manifest at colliders as missing transverse momentum E_T. Therefore, colliders searches of DM are based on the observation of the visible counterpart of an event such as charged leptons, jets or a photon, and are generally referred to as mono-X searches. In order to disentangle DM signal from large SM background, events with large E_T are selected. However, since colliders identify missing energy, they cannot uniquely determine the presence of DM in a signal event. All they can do is to confirm the presence of a neutral and "stable" particle, that might have even decayed outside the detector. Nevertheless, the strategy to identify WIMPs at colliders is quite exciting and complementary to direct and indirect dark matter searches. Assuming that the production of WIMPs at colliders is uniquely connected to the WIMP-nucleon scatterings at underground laboratories, one can use the non-observation signals with large E_T to derive limits on the WIMP-nucleon scattering cross-section.

Since the interpretation of dark matter requires that one assumes a model leading to the signal under consideration, LHC DM working group (LHCDMWG) has given recommendations (see

Ref. [16, 110]) while comparing LHC results in context of a specified model with results from direct and indirect detection experiments. Based on Ref. [16], we discuss below one such model where the DM particle has been assumed as a Dirac fermion χ and that the particle mediating the interaction (the "mediator") is exchanged in the s-channel. Several simplifying assumptions are considered leading to a model characterised by four parameters: the DM mass m_χ, the mediator mass M_{med}, the universal coupling to quarks g_q and the mediator coupling to DM g_χ. Due to strong LHC bounds from di-lepton searches, mediator couplings to leptons are always set to zero in such models.

In general, the SI WIMP-nucleon scattering cross section takes the form

$$\sigma_{\rm SI} = \frac{f^2(g_q) g_\chi^2 \mu_{n\chi}^2}{\pi M_{med}^4}, \tag{2.12}$$

where $\mu_{n\chi}^2 = m_n m_\chi/(m_n + m_\chi)$ is the DM-nucleon reduced mass with $m_n \simeq 0.939$ GeV the nucleon mass. The mediator-nucleon coupling $f(g_q)$ is a function of mediator-quark coupling and hence depends on the scattering considered *viz.* scalar, vector or axial vector. For the interactions involving vector and scalar mediators (and for recommended choice of couplings), the difference between the proton and neutron cross section is negligible. For the vector mediator,

$$f(g_q) = 3 g_q, \tag{2.13}$$

and hence we have

$$\sigma_{\rm SI} \simeq 6.9 \times 10^{-41} {\rm cm}^2 . \left(\frac{g_q g_\chi}{0.25}\right)^2 \left(\frac{1{\rm TeV}}{M_{\rm med}}\right)^4 \left(\frac{\mu_{n\chi}}{1{\rm GeV}}\right)^2, \tag{2.14}$$

Using the values from Ref. [16], for the scalar mediator

$$f(g_q) = 1.16 \times 10^3 g_q, \tag{2.15}$$

and therefore, the SI WIMP nucleon cross section can be written as

$$\sigma_{\rm SI} \simeq 6.9 \times 10^{-43}{\rm cm}^2 . \left(\frac{g_q g_\chi}{1}\right)^2 \left(\frac{125{\rm GeV}}{M_{\rm med}}\right)^4 \left(\frac{\mu_{n\chi}}{1{\rm GeV}}\right)^2 . \tag{2.16}$$

For the axial-vector mediator, the SD scattering cross-section can be written as

$$\sigma_{\rm SD} = \frac{3 f^2(g_q) g_\chi^2 \mu_{n\chi}^2}{\pi M_{med}^4}, \tag{2.17}$$

and under the assumption that the coupling to all quarks is of equal strength,

$$f(g_q) = 0.32 g_q, \tag{2.18}$$

and hence

$$\sigma_{\rm SD} \simeq 2.4 \times 10^{-42}{\rm cm}^2 . \left(\frac{g_q g_\chi}{0.25}\right)^2 \left(\frac{1{\rm TeV}}{M_{\rm med}}\right)^4 \left(\frac{\mu_{n\chi}}{1{\rm GeV}}\right)^2 . \tag{2.19}$$

While the searches at collider are not completely model independent, as they assume production channels within context of specific WIMP models, they do offer an advantage of being independent of any astrophysical uncertainties. Further searches in future with high centre-of-mass energy[5] could provide further insight into the particle nature of dark matter.

2.6 Complementarity of direct, indirect and collider searches

The dark matter searches relying on different approaches complement each other and are needed to completely reconstruct and understand the nature of dark matter. The complementarity may be seen at several levels [111]. Firstly, these strategies are qualitatively complementary *i.e.* they differ in essential characteristics, and rely on different dark matter properties to see a signal. Di-

[5]Future Circular Collider (FCC) is one such proposal to extend the existing LHC facility to centre of mass energies up to 100 TeV.

rect detection searches attempt at measuring the tiny energy deposited by a WIMP scattering on target nuclei, in ultra-low background conditions, whereas indirect detection involves search for the products of WIMP annihilation and decay and then there are collider searches hunting for DM production signals. Therefore, it is essential to have these complementary set of approaches, sensitive to viable and well-motivated dark matter possibilities. Secondly, the approaches are also quantitatively complementary: for a given class of dark matter possibilities, these approaches are sensitive to different DM interactions and mass ranges. Lastly, in the event of the discovery of a compelling dark matter signal, complementary experiments are not only required to verify the initial discovery but also to confirm answers to several questions: whether the particle makes up all of dark matter or only a portion of it, what are its essential properties such as its interactions, spin, and mass, and also to determine its role in the large scale structures formation of the universe that we see today. It is imperative, therefore, to push for a balanced dark matter program comprising these complementary searches to discover and understand the dark matter. Fig. 2.7 shows the worldwide hunt for the dark matter, including the terrestrial and satellite experiments. In the rest of this section we look into the complementarity between these approaches in some detail.

In order to compare sensitivity of different approaches, interpret results and appreciate the extent of complementarity between approaches, we should be careful regarding the assumptions involved in the signal rate calculation in different experiments. We also need to understand the various source of uncertainties affecting the reconstruction of WIMP parameters related to the WIMP velocity distribution, nuclear form factor, type of WIMP-nucleon scattering, and the local DM density which suffers from large uncertainties [112]. Generally, for the case of direct and indirect experiments, the common assumptions involved in the signal calculation are the following: there is a smooth halo of DM particles in our galaxy wich is well described by a Maxwellian velocity distribution [113]; the nucleus can be treated as a hard sphere as indicated by the Helm form factor [103], and that the WIMP-nucleon scattering is elastic.

The scenario in which a large class of even the most natural WIMP candidates, may have too small WIMP nucleon cross sections, and hence evade detection in the currently running direct

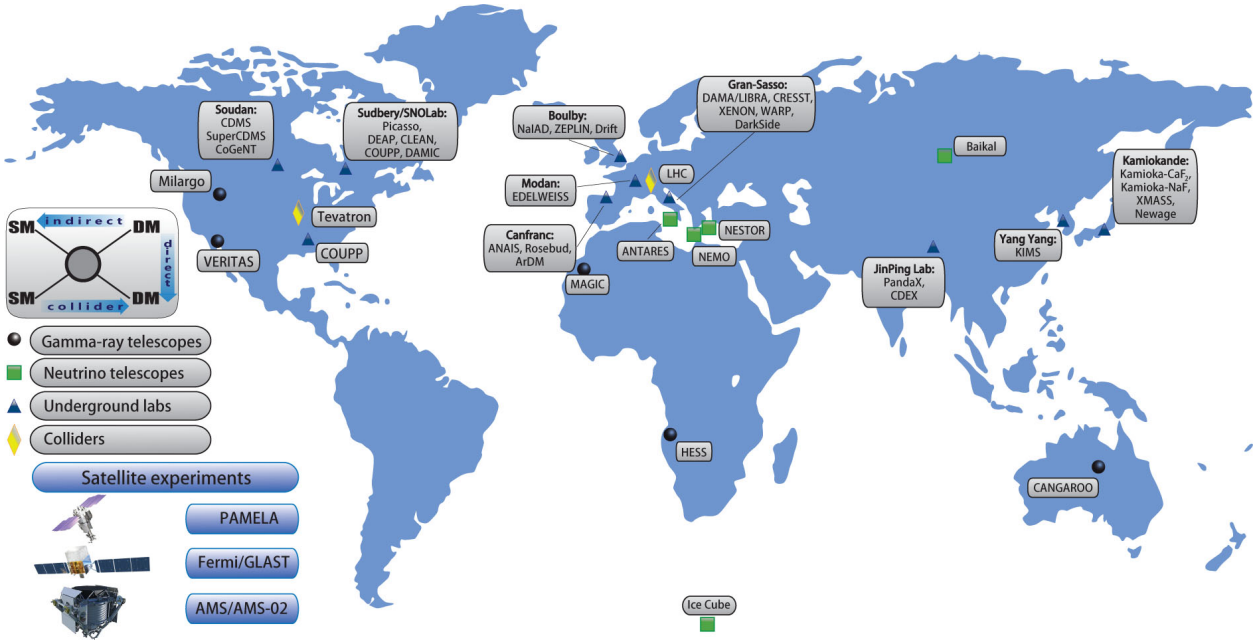

Figure 2.7: Worldwide hunt for the dark matter, including the terrestrial and satellite experiments. Gamma ray telescopes (black circle) and neutrino telescopes (green box) are examples of indirect searches. The underground labs housing direct detection experiments (blue pyramids) and collider (yellow diamond) production searches are also shown. Some of these experiments have now stopped operation. The figure has been taken from Ref. [12].

detection experiments. A study of such models has been done in Ref. [114]. For these models, associated with low WIMP nucleon cross sections, the background becomes the principal limitation and hence DM can escape detection even in the future large scale direct detection experiments. Should we have very massive neutralinos as a DM candidate, it will be beyond collider searches. However, in that scenario indirect detection in terms of gamma rays provides an interesting and unique search window [114]. For the parameters favouring direct detection, the possibility of seeing a signal in at least two independent types of experiments will be interesting and crucial to make a convincing case that the dark matter problem has been resolved. See Ref. [114] for the details of model wise complementarity of direct detection techniques and gamma ray searches in $\sigma_{\rm SI}$ vs $\langle\sigma\, v\rangle/m_\chi^2$ plane.

Similarly, while reconstructing the mass, spin-independent and spin-dependent WIMP nucleon cross sections of dark matter particles with a combined data set of direct and indirect detection experiments can help break the degeneracies in the dark matter cross section parameter space,

even in the unfortunate scenario when there is no signal at the indirect detection experiment. Combined analysis of XENON1T and IceCube is one such promising scenario and has been described in Ref. [115].

The DM velocity distribution impacts the direct and indirect detection methods in a different manner. Direct detection experiments are more sensitive to the nuclear recoils from high velocity WIMPs whereas indirect detection (when depends on the capture rate of WIMPs in the sun or earth) are more likely to be from the slower portion of the WIMP velocity distribution. One can combine null results from direct detection experiments with neutrino telescopes/detectors and derive an upper limit on the scattering cross-section which is independent of velocity of dark matter in the halo (See for e.g. Ref. [116]). Similarly, using a positive direct detection signal, a halo-independent lower bound on the dark matter capture rate in the sun can be obtained [117].

Collider searches offer an advantage over direct and indirect approaches in the sense that they do not suffer from astrophysical uncertainties [118]. By combining data from accelerator and direct-detection experiments, a better reconstruction of the DM properties can be obtained (see for instance Ref. [119]). Then there can be complementarity of indirect and collider searches, such as the case where the exclusion limits from indirect detection experiments can help break degeneracies in the phenomenological parameter space of DM that would be present even in accelerator data (see for example, Ref. [120]). Similarly, complementarity can arise between direct detection and fixed target experiments [121]. Thus, in conjunction with direct and collider searches, indirect detection techniques emphasize the importance of multi-pronged approach to the dark matter identification. In this thesis, we present the prospects of indirect detection with ICAL detector. In the next chapter, we calculate the neutrino fluxes at the ICAL detector due to WIMP annihilation in the sun, the earth and the galactic centre.

Chapter 3

Neutrino fluxes due to WIMP annihilation

Neutrinos offer a unique way of probing dark matter signatures, for they retain the spectral information and point back to the source, making them a powerful astroparticle tool for indirect searches. In this chapter, we will calculate the neutrino fluxes arising due to WIMP annihilation in the sun, the earth and the galactic centre.

In Section 3.1, we calculate the capture and annihilation rate of WIMPs in the sun, the subsequent production of neutrino fluxes and propagation from the sun core to the ICAL detector. This is followed by 3.2 where the capture rate calculations and the corresponding neutrino fluxes due to WIMP annihilation in the earth core have been described. Finally, in Section 3.3, we describe the signal flux calculation due to WIMP annihilation in the galactic centre region. This involves knowledge of DM distribution in the galaxy, which are also discussed in the subsections.

3.1 Neutrinos from WIMP annihilation in the sun

The number of WIMPs inside the sun as a function of time is given by the following differential equation [35],

$$\frac{\mathrm{d}N}{\mathrm{d}t} = C - C_{\mathrm{A}} N^2 - C_E N \,, \tag{3.1}$$

where the three terms on the right-hand side correspond to capture of WIMPs inside the sun, their self annihilation inside the sun's core and evaporation from its surface, respectively. The effect of

evaporation from the sun is seen to be important only for very light WIMP [122–125]. Since we will be working with WIMP masses above 3 GeV[1] we will neglect the last term of Eq. (3.1) in this thesis. Since each annihilation reduces the number of WIMP by two units, the rate of depletion of WIMP ($\Gamma_{\rm A}$) is twice the annihilation rate in the sun and hence

$$\Gamma_{\rm A} = \frac{1}{2} C_{\rm A} N^2. \tag{3.2}$$

The quantity $C_{\rm A}$ is a function of total WIMP annihilation cross-section times the relative velocity of the WIMP ($\langle \sigma_{\rm A} v \rangle$) and the distribution of WIMP in the sun and can be written as,

$$C_{\rm A} = \langle \sigma_{\rm A} v \rangle \frac{V_2}{V_1^2}, \tag{3.3}$$

where V_j is the effective volume of the sun and is given by $V_j = 6.5 \times 10^{28} (j\ m_\chi^{10})^{3/2}$, and m_χ^{10} being WIMP mass in the units of 10 GeV [35]. Solving Eq. (3.1) for N, we find the annihilation rate at any given time as

$$\Gamma_{\rm A} = \frac{1}{2} C \tanh^2(t/\tau)\,, \tag{3.4}$$

where $\tau = (C C_{\rm A})^{-1/2}$ is the time required for equilibrium to be established between the capture and annihilation of WIMP in the sun. If the age of the sun is greater than the equilibrium time scale ($t_\odot = 1.5 \times 10^{17}$ s $>> \tau$), which is indeed the case, and hence we have $\Gamma_{\rm A} = \frac{1}{2} C$.

The WIMP capture rate due to spin independent interactions ($C_{\rm SI}$) in the sun is given by [35, 126],

$$C_{\rm SI} = c \left(\frac{1\ \text{GeV}}{m_\chi} \right) \left(\frac{\rho_{\rm local}}{0.3\ \text{GeV/cm}^3} \right) \left(\frac{270\ \text{km/s}}{\bar{v}_{\rm local}} \right) \sum_i F_i(m_\chi) \sigma_{\rm SI}^i f_i \phi_i \frac{S(m_\chi/m_{Ni})}{m_{Ni}/(1\ \text{GeV})}\,, \tag{3.5}$$

where $c = 4.8 \times 10^{24}$ s^{-1}, m_χ is the mass of DM, $\rho_{\rm local}$ is the local DM density and $\bar{v}_{\rm local}$ is the

[1]The lower m_χ considered for the WIMP annihilation in the sun, the earth and the galactic centre is 3 GeV, 10 GeV and 5 GeV, respectively.

DM velocity dispersion in the halo, the summation has to be carried out over all the nuclei in the sun, $F_i(m_\chi)$ is the form-factor suppression for the capture of a WIMP of mass m_χ with the i^{th} nuclei, m_{N_i} is the mass (in GeV) of the i^{th} nuclear species, f_i is the mass fraction of the i^{th} element, and $\sigma^i_{\rm SI}$ is the cross-section for elastic scattering of the WIMP from the i^{th} nucleus via SI interaction in units of 10^{-40} cm^2. The normalised average "potential energy" ϕ_i depends on the spatial distribution of the i^{th} element in the sun and is expressed as

$$\phi_i = \langle v^2 \rangle_i / v_0 \tag{3.6}$$

where $\langle v^2 \rangle_i$ being the escape velocity square of WIMP, averaged over the distribution of the element i and v_0 is the escape velocity at the surface of the sun [127]. The quantity $S(m_\chi/m_{N_i})$ is the kinematic suppression factor for the capture of the WIMP from a nucleus and is given by:

$$S(x) = (A^b/(1+A^b))^{1/b}, \tag{3.7}$$

where $x = m_\chi/m_{N_i}$, b = 1.5 and A is written as,

$$A = \frac{3}{2}\frac{x}{(x-1)^2}\left(\frac{\langle v^2_{\rm esc}\rangle}{\bar{v}^2}\right). \tag{3.8}$$

The quantity $\langle v^2_{\rm esc}\rangle$ is a mean escape velocity and for the sun we have $\langle v^2_{\rm esc}\rangle = 1156 {\rm kms}^{-1}$. $\bar{v}$ = $\bar{v}_{\rm local}$ is the local dark matter velocity dispersion mentioned earlier. It can easily seen that for $x \to 1$, $S(x) \to 1$ and for the case $x \to \infty$, $S(x) \to \frac{\langle v_{\rm esc}{}^2\rangle}{\bar{v}^2} x^{-1}$; for $x \to 1$, $S(x) \propto \frac{\langle v^2_{\rm esc}\rangle}{\bar{v}^2} x^{-1}$. This implies that the kinetic suppression factor is zero for WIMP mass close to nuclear mass and resulting in an enhancement in the capture rate. The capture is, however, kinematically suppressed for WIMP mass differing from nuclear mass. $\sigma^i_{\rm SI}$ can be related to $\sigma_{\rm SI}$ by the equation

$$\sigma^i_{\rm SI} = \sigma_{\rm SI} A_i^2 \left(\frac{\mu_{\chi N_i}}{\mu_{\chi p}}\right)^2 \tag{3.9}$$

where A is the atomic number, μ is the reduced mass and in approximation $m_{N_i} = A_i m_p$, where

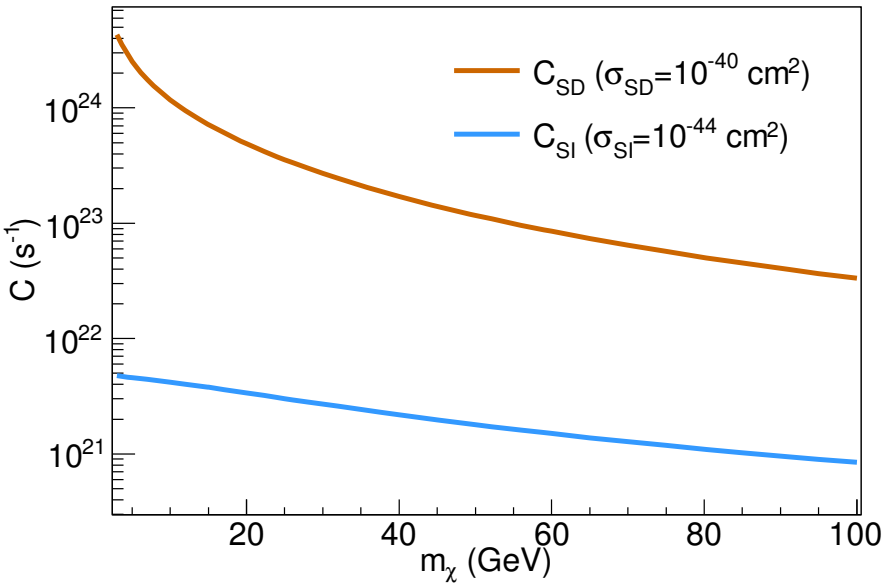

Figure 3.1: SI and SD capture rates for WIMP in the core of the sun as a function of WIMP mass m_χ.

m_p is the proton's mass.

The spin dependent capture rate ($C_{\rm SD}$) of WIMP due to elastic scattering off sun's nuclei is given by [128],

$$C_{\rm SD} = 9 \times 10^{24}\ {\rm s}^{-1} \left(\frac{\sigma_{\rm SD}}{10^{-2}\ {\rm pb}}\right) \left(\frac{50\ {\rm GeV}}{m_\chi}\right)^2 \left(\frac{\rho_{\rm local}}{0.3\ {\rm GeV/cm^3}}\right) \left(\frac{270\ {\rm km/s}}{\bar{v}_{\rm local}}\right) , \qquad (3.10)$$

where as before, m_χ is the DM mass, $\rho_{\rm local}$ is the local DM density, $v_{\rm local}$ is the DM velocity dispersion in the halo and $\sigma_{\rm SD}$ is the SD WIMP-nucleon cross- section. The WIMP capture in the sun due to SD scattering is mainly due to hydrogen. Figure 3.1 shows the SD and SI capture rates for the sun for an assumed WIMP-nucleon cross-section for each case.

The WIMP annihilate into pairs of standard model leptons, quarks, gauge and Higgs bosons. Their subsequent hadronisation and/or decay give rise to neutrinos. We will also consider the situation where the WIMP annihilate directly into neutrino-antineutrino pairs. The differential

neutrino flux at the detector coming from WIMP annihilations in the sun is given by

$$\frac{dN'_\nu}{d\Omega dt dE_\nu} = \frac{\Gamma_{\rm A}}{4\pi R^2} \sum_{j=1} {\rm BR}_j \frac{dN_j}{dE_\nu}\,, \tag{3.11}$$

where Γ_A is defined above in terms of $C_{\rm SI}$ or $C_{\rm SD}$, R is the distance travelled by the neutrinos and dN_j/dE_ν is the differential flux for a given annihilation channel j, where j could be W^+W^-, $b\bar{b}$, $c\bar{c}$, $\tau^+\tau^-$ and so on. The sum in Eq. 3.11 is over all possible channels j and the sum has to be weighted with the branching ratio (BR_j) of the particular channel j. These branching ratios can be calculated within the framework of specific models. Since we consider a generic WIMP scenario, we will take only one annihilation channel at a time and assume 100% branching ratio for that channel. The expected sensitivity limit calculated for each channel for 100 % branching ratio indicates the limit expected for that particular channel alone. A given WIMP model will predict a mixture of these channels with varying branching ratios, and hence the corresponding sensitivity limit will lie somewhere in the region bounded by the best and worst limit expected from these various channels. For instance, the expected sensitivity limit for a DM model that predicts annihilation of WIMPs into $\tau^+\tau^-$ with 20 % BR and into $b\bar{b}$ with 80 % BR, will lie in a region between the expected sensitivity for these two channels with 100% BR, and closer to the latter channel. It should be noted, however, that this example model explicitly assumes only two annihilation channels. In case WIMP annihilate to less competitive annihilation channels such as $d\bar{d}$, $u\bar{u}$ and $s\bar{s}$, the sensitivity limits would decrease proportionately. Similarly, WIMP annihilation to channels like $e^+\ e^-$, which do not contribute to neutrino fluxes, would weaken the sensitivity. The annihilation of WIMP can occur through various channels : $c\bar{c}$, $b\bar{b}$, $t\bar{t}$, e^+e^-, $\mu^+\mu^-$, $\tau^+\tau^-$, W^+W^-, Z^0Z^0, $g\ g$, $d\bar{d}$, $u\bar{u}$ and $s\bar{s}$. Among these channels, electrons are stable and the muons would interact and get absorbed inside the sun before they could produce high energy neutrinos. Hence these are not relevant to our analysis. Annihilation of DM into particles like protons, anti-deutrons, gamma rays will also not produce neutrino fluxes and hence not considered in our work. The quark-antiquark annihilation channels like $u\bar{u}$, $d\bar{d}$ and $s\bar{s}$ will produce a weaker neutrino spectra, in fact a few order of magnitude smaller than the $g\ g$ annihilation channel and hence we do not consider them in our

Paramter	Best-Fit Value
θ_{12}	34°
θ_{13}	9.2°
θ_{23}	45°
δ	0
Δm^2_{21}	$7.5 \times 10^{-5}\text{eV}^2$
Δm^2_{31}	$2.4 \times 10^{-3}\text{eV}^2$

Table 3.1: Oscillation parameters used in the simulations related to dark matter searches in the sun and the earth.

analysis. The $g\ g$ annihilation channel is not competitive, but we quote the sensitivity limits for this channel. We will work with WIMP masses between a few GeVs to up to 100 GeV, and hence the channels W^+W^-, Z^0Z^0, $t\bar{t}$ are not kinematically relevant as they open up from masses 80.4 GeV, 91.2 GeV and 173 GeV, respectively. The annihilation to Higgs boson has also not been considered for the same reason. In WIMP models like Kaluza-Klein (KK) dark matter, WIMP could directly undergo annihilation into neutrinos $\nu_{\text{E}}\bar{\nu}_{\text{E}}, \nu_\mu\bar{\nu}_\mu, \nu_\tau\bar{\nu}_\tau$. We have considered these channels in our analysis.

The spectra of neutrino fluxes due to WIMP annihilation in the sun have been calculated in detail in [129, 130]. In this work, for simulating the WIMP annihilations into standard model particle-antiparticle pairs in the centre of the sun, the subsequent propagation of the daughter particles and finally the neutrinos, we use WIMPSIM [131] package. WIMPSIM uses Nusigma [132] for simulation of neutrino-nucleon interactions and PYTHIA [133] for the hadronisation, decay and production of neutrinos. The upper WIMP mass considered for all the annihilation channels is 100 GeV and the lower mass considered is 3 GeV with the exception of $b\bar{b}$ whose lower mass limit has been taken to be 7 GeV. The propagation of neutrinos includes full three flavour neutrino oscillations with the oscillation parameters given in Table 3.1. We consider normal mass hierarchy for the neutrinos in our analysis. Neutrino mass hierarchy and oscillation parameters may influence the signal neutrino flux calculations [130] and hence detector's indirect detection sensitivity. We defer such sensitivity studies to future projects..

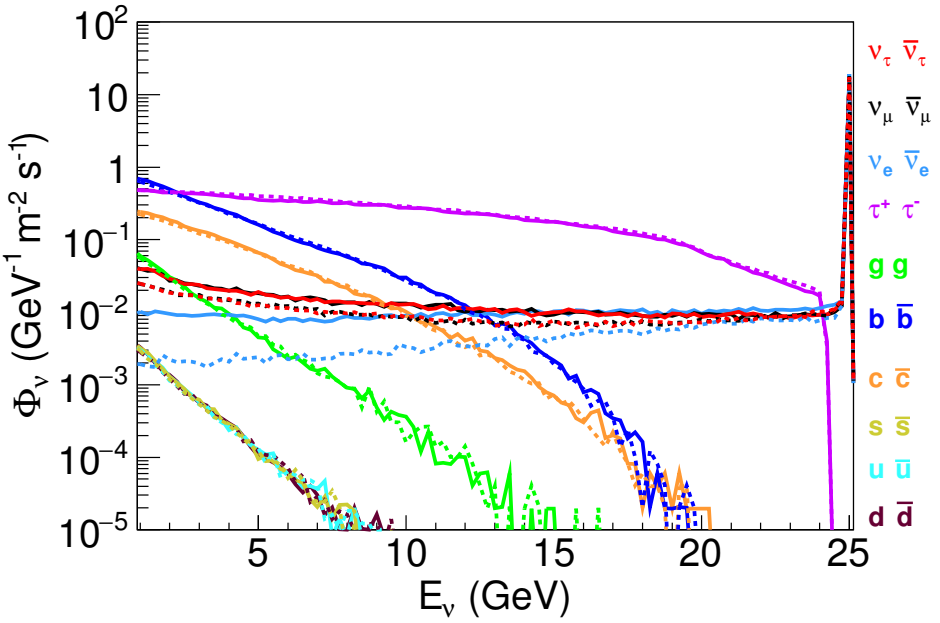

Figure 3.2: The ν (solid) and $\bar{\nu}$ (dashed) fluxes at ICAL due to annihilation of 25 GeV WIMPs in the sun for channels for various annihilation channels with $\sigma_{\rm SD} = 10^{-39}$ cm^2. The fluxes due to SI interactions in the sun are similar and scaled by the appropriate $\sigma_{\rm SI}$.

The neutrino and antineutrino fluxes (in units of GeV^{-1}m$^{-2}\Omega^{-1}$s^{-1}) at ICAL due to WIMP annihilations in the sun is shown in Fig. 3.2. We use the following values: $\rho_{\rm local} = 0.3\,{\rm GeV/cm^3}$, $v_{\rm local} = 270$ km sec^{-1} and 100 % BR for each of the channels. We show the fluxes for WIMP mass of 25 GeV and WIMP-nucleon scattering cross-sections of $\sigma_{\rm SD} = 10^{-39}$ cm^2. Note from Fig. 3.2 that for WIMP mass of 25 GeV, the fluxes for both neutrinos as well as antineutrinos are nearly same. The above feature is seen to be true for nearly all WIMP masses. Also note that for the $\tau^+\tau^-$ channel, the neutrino fluxes fall by only about 1 order of magnitude between neutrino energies 0 and 25 GeV, which is the maximum possible neutrino energy from a 25 GeV WIMP. For the $b\bar{b}$ channel on the other hand, the fluxes are lower than those for the $\tau^+\tau^-$ channel to begin with, and subsequently fall sharply by many orders of magnitude by $E_\nu = 15$ GeV. For higher energies, the neutrino flux from the $b\bar{b}$ channel is relatively negligible. The fluxes due to $c\bar{c}$ channel are lower than $b\bar{b}$ for all neutrino energies but follow a similar trend. The contribution from gg channel is an order less than $b\bar{b}$. The fluxes due to $u\bar{u}$, $d\bar{d}$ and $s\bar{s}$ channels are pretty indistinguishable from each other and are several orders of magnitude lower than $b\bar{b}$ making them least competitive. The KK

channels give rise to monoenergetic neutrino fluxes at high energies and hence will give the most sensitive limits. The tail associated with KK channel fluxes is as a result of pile-up of events at low energies coming from secondary decays of $\tau^{\pm}$ that have been created in ν_τ $\bar{\nu}_\tau$ charge current (CC) interactions inside the sun and as well as from energy losses due to neutral current (NC) interactions. The interactions also create a loss at higher energies (both due to absorption via CC interactions of electron and muon neutrinos and due to energy losses). Therefore, it is evident that the indirect detection bounds from observation of these neutrinos and antineutrinos will be stronger when one considers the $\nu\bar{\nu}$ or $\tau^+\tau^-$ channels compared to when one takes the softer channels such as $b\bar{b}$ and $c\bar{c}$. As mentioned above, we do not consider the other channels with weaker neutrino flux strength in our discussion on the expected sensitivity to indirect detection of dark matter in ICAL. Within the context of specific WIMP models, of course, the individual BR for each of the channels can be calculated and then one can find the expected sensitivity of ICAL to indirect detection within that given model. For illustration, however, we give the expected sensitivity limits for the $\tau^+\tau^-$, $b\bar{b}$, $c\bar{c}$ and gg channels with 100 % BR as mentioned above, and also consider WIMP annihilation channels $\nu_{\rm E}\bar{\nu}_{\rm E}, \nu_\mu\bar{\nu}_\mu, \nu_\tau\bar{\nu}_\tau$ in our analysis and calculate the corresponding expected sensitivities. The Fig. 3.2 is shown for benchmark values of WIMP mass and cross-sections. The fluxes for other values of $\sigma_{\rm SD}$ simply scale with the value of the cross-section, however, for other values of WIMP masses the spectral shape changes. Nevertheless, the above mentioned features regarding the fluxes from different annihilation channels remain true for all WIMP masses.

3.2 Neutrino flux from WIMP annihilation in the earth

The time evolution of WIMPs inside the earth also follows Eq. 3.1. As we did for the case of solar WIMP analysis, we neglect the effect of evaporation from the earth assuming that it is not significant for reasonably heavy WIMPs [122–125]. For the lighter WIMPs *i.e.*, for $m_\chi < 10$ GeV, this assumption may not be valid. However, for the WIMP annihilation searches in the earth, we consider $m_\chi \geq 10$ GeV and evaporation has been neglected. The quantity $C_{\rm A}$ in Eq. 3.2, depends on the velocity averaged WIMP self-annihilation cross-section $\langle \sigma_A v \rangle$ and the effective volume of

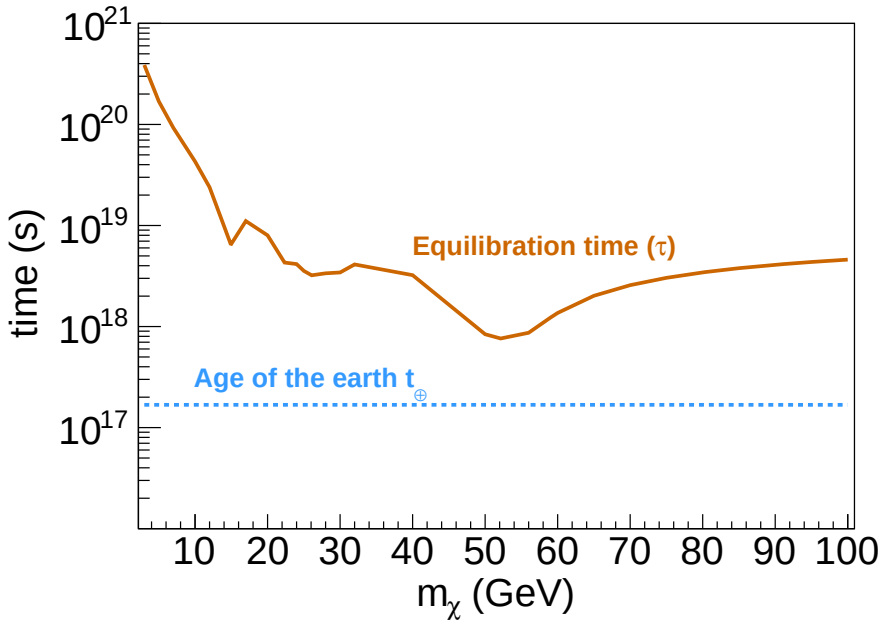

Figure 3.3: The dependence of the time required for equilibrium to reach between annihilation and capture rate for WIMP in the earth as a function of WIMP mass m_χ. It can be seen that for the parameters chosen in this analysis, we can see that equilibrium is never achieved. This has been calculated by fixed value of $C_{\rm A}$ by choosing $\langle\sigma_{\rm A} v\rangle = 3\times10^{-26}{\rm cm}^3{\rm s}^{-1}$. A scattering cross-section of $\sigma_{\rm SI} = 10^{-44}{\rm cm}^2$ has been assumed while calculating C using Eq. 3.12.

the earth $V_j = 2\times10^{25}(j\, m_\chi^{10})^{3/2}$ [134]. Unlike sun, it is seen that equilibrium between the capture and annihilation of WIMP has not reached in the earth and hence there is no simple proportionality between the annihilation rate and WIMP-nucleon scattering cross-section. Nevertheless, t/τ can be related to the capture rate C and annihilation cross-section $\langle\sigma_A v\rangle$ through the following relation:

$$\frac{t_\oplus}{\tau_\oplus} = 1.9\times10^4\left(\frac{C}{{\rm s}^{-1}}\right)^{1/2}\left(\frac{\langle\sigma_A v\rangle}{{\rm cm}^3{\rm s}^{-1}}\right)^{1/2}\left(\frac{m_\chi}{10{\rm GeV}}\right)^{3/4}, \tag{3.12}$$

where $t = t_\oplus \sim 4.5\times10^9$ years is the age of the earth. We can see that the equilibration time $\tau_\oplus$ in equation Eq. 3.12 depends on the capture rate (Eq. 3.5) and the quantity $C_{\rm A}$ (Eq. 3.3) and has a dependence on WIMP mass. From Fig. 3.3, we can see that for a 50 GeV WIMP mass, τ is the order of $\sim 10^{18}$ s, whereas the age of the earth is of the order of $\sim 10^{17}$ s. For WIMP masses less than 50 GeV, the value of τ increases by a few orders while for WIMP masses greater than 50 GeV it goes up by up to 1 order of magnitude. Therefore, we see that equilibrium between the

annihilation and capture rate is never achieved. This implies that the ratio $t/\tau \ll 1$, and hence the tanh contribution in the Eq. 3.4 remains. For a fixed value of $\langle \sigma_A v \rangle$, $C_{\rm A}$ is constant and a direct proportionality between $\Gamma_{\rm A}$ and C can be established. Hence, the annihilation of WIMP in the earth can be related to the WIMP-nucleon scattering cross-section. The scattering of the WIMP could proceed via both Spin Dependent (SD) and Spin Independent (SI) processes. As mentioned earlier in chapter 2, WIMP nucleon scattering cross-section depends on the number and spin of nucleons present in the nucleus. Since the earth comprises mainly heavy nuclei with negligible fraction of nuclei with spin, the SI WIMP-nucleon scattering is dominant and is given by Eq. 3.5, where the constant c has a value of 4.8×10^{15} s^{-1} for earth. The summation in Eq. 3.5 has to be carried out over all the nuclei in the earth and f_i and ϕ_i are the quantities as defined in the previous section with the relevant values for the earth taken from [35, 126]. Fig. 3.4 shows the rate at which WIMPs are captured in the interior of the earth for a scattering cross-section of $\sigma_{\rm SI} = 10^{-44}{\rm cm}^2$. From Eq. 3.5 and Eq. 3.7 we can see that when m_χ is close to the mass of one of the abundant nuclei in the earth, there is a resonant capture leading to an enhanced capture rate which is shown as peaks in Fig. 3.4.

The differential neutrino flux arising at the ICAL detector, due to WIMP annihilation in the earth, is given by Eq. 3.11, where Γ_A and C are related as discussed above in this section, R is the distance travelled by the neutrinos between the point of creation in the earth's core and detection at the detector. The differential neutrino flux dN_j/dE_ν for a given WIMP annihilation channel j is calculated using WIMPSIM. In fact, the neutrino spectra at the point of production for the case of the WIMP annihilation in the sun and earth are identical. The final fluxes reaching the detector, however, are modified due to different normalisation factors in Eq. 3.5. The neutrinos from solar and terrestrial WIMP annihilations also encounter different propagation length through matter, thereby resulting in different neutrino interactions and oscillations. For earth WIMP analysis, we consider WIMP mass in the range $(10 - 100)$ GeV and only $b\,\bar{b}$ and $\tau^+\tau^-$ annihilation channels. The neutrino oscillations involved in the propagation of neutrinos through earth matter has been incorporated in a full three flavour neutrino framework with the oscillation parameters given in

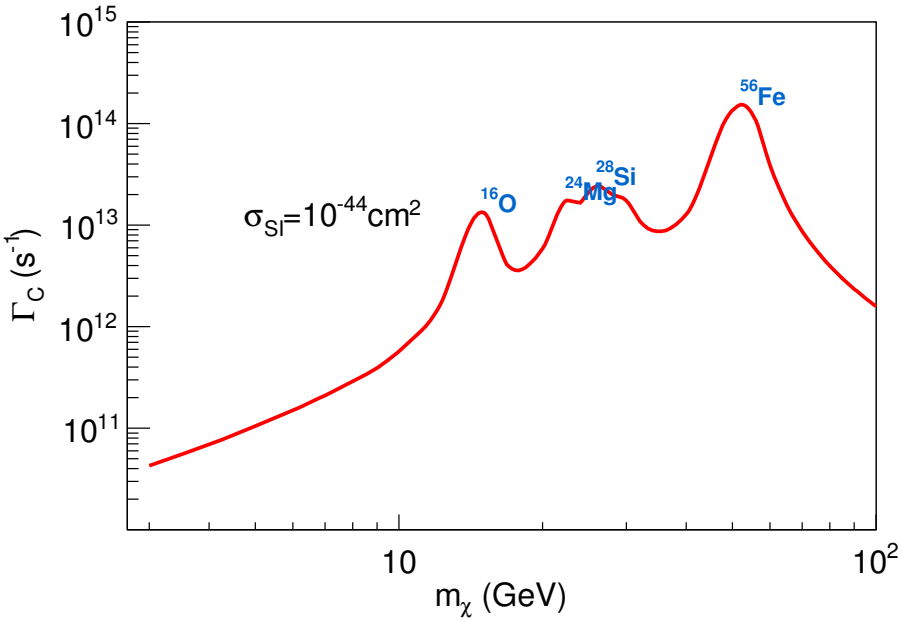

Figure 3.4: SI capture rate for WIMP in the earth as a function of WIMP mass m_χ. The enhanced capture rate due to resonance scattering on various nuclei is also shown. A scattering cross-section of $\sigma_{\rm SI} = 10^{-44}{\rm cm}^2$ has been assumed.

Table 3.1. Throughout our analysis related to dark matter searches, we consider normal mass hierarchy.

Fig. 3.5 shows the neutrino and antineutrino fluxes (in units of GeV^{-1}m$^{-2}\Omega^{-1}$s^{-1}) at ICAL due to WIMP annihilations in the earth. For each of the annihilation channels, we assume 100 % BR. We take $\rho_{\rm local} = 0.3$ GeV/cm^3 and $v_{\rm local} = 270$ km sec^{-1} in our flux calculations. The fluxes shown in Fig. 3.5 are for a 25 GeV WIMP assuming a WIMP-nucleon scattering cross-section $\sigma_{\rm SI} = 10^{-38}$ cm^2. We can see from the figure that the fluxes for both neutrinos as well as antineutrinos are nearly same, with antineutrino fluxes being slightly higher than the neutrino fluxes because their interactions with the matter in the earth are helicity suppressed. This feature seems to hold for nearly all WIMP masses. The fluxes follow the same trend as for the case of solar WIMP annihilation. For the $\tau^+\tau^-$ channel, the neutrino fluxes fall by about 1 order of magnitude in the above range. However, for the $b\bar{b}$ channel, the fluxes fall sharply by many orders of magnitude and well before $E_\nu = 20$ GeV it becomes negligible. Therefore, stronger indirect detection bounds are expected with neutrino fluxes from $\tau^+\tau^-$ channel in comparison to $b\ \bar{b}$ channel. As discussed

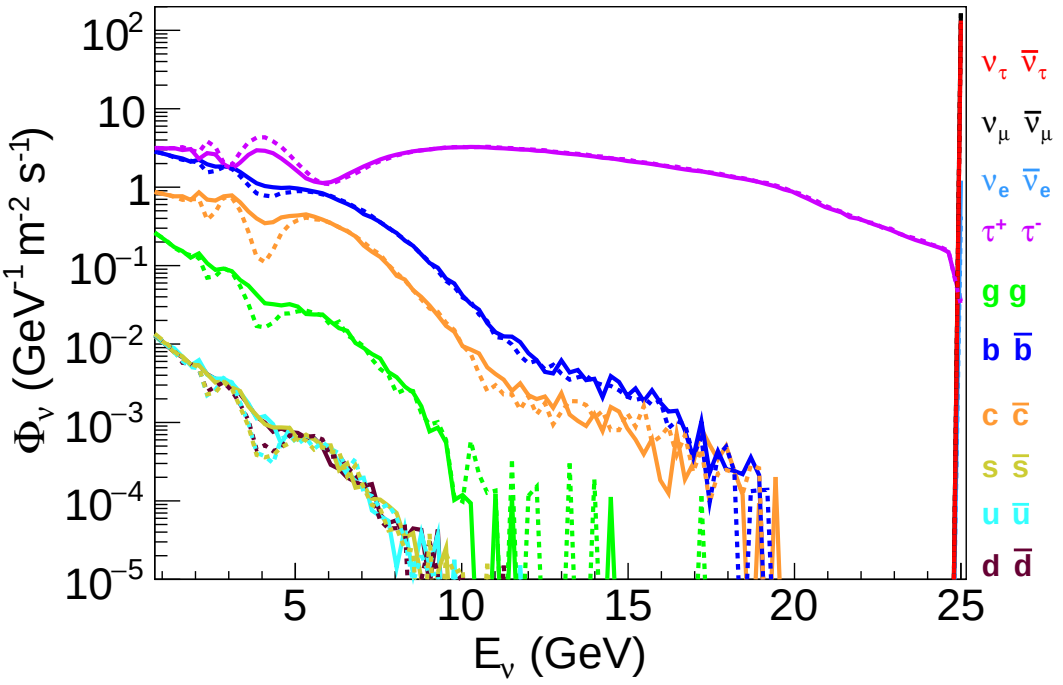

Figure 3.5: The ν and $\bar{\nu}$ fluxes at ICAL due to annihilation of 25 GeV WIMPs in the earth for various WIMP annihilation channels with $\sigma_{\rm SI} = 10^{-38}$ cm^2 and $\langle \sigma_A v \rangle = 3 \times 10^{-26}$ cm^3 s^{-1}

in the previous section, the fluxes arising due to annihilation channels involving the other quark-antiquark pairs are even weaker. The Fig. 3.5 shows fluxes for benchmark values of WIMP mass and cross-sections. The fluxes for other values of $\sigma_{\rm SI}$ can be obtained by simply scaling the value of the cross-section. The above mentioned features of fluxes from various annihilation channels hold for all WIMP masses.

For WIMP searches, the dark matter phase distribution is a large source of uncertainty. Such study has not been done in this thesis but one could see Ref. [135] where the impact of dark matter velocity distribution on the WIMP capture rate calculations have been discussed. Detailed studies of the individual uncertainties on the dark matter capture rate shows that the overall uncertainties in indirect searches are moderate. An existence of dark disc enriching low-velocity population could result in a significant increase in capture rate especially for heavy WIMPs. It will, however, enhance the capture rate and therefore allow the interpretation of current limits from indirect searches to be more conservative. There could also be uncertainties in the capture rate calculations due to form factor contributions [35].

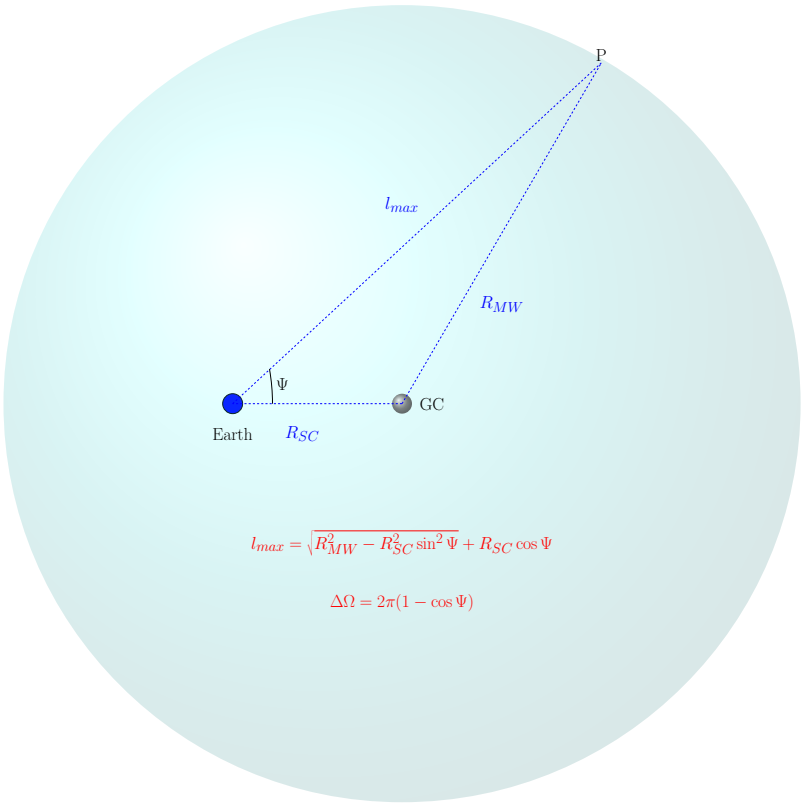

Figure 3.6: The definition of Ψ, $\Delta\Omega$ and other factors involved in J_Ψ and $\mathcal{J}(\Delta\Omega)$ calculation. Ψ is the angular separation between the line joining the earth and GC and the line joining the earth and point P. R_{SC} is the solar radius, R_{MW} is the radius of the Milky Way galaxy and l_{max} is the maximum distance between the earth and the farthest point in the galaxy. $\Delta\Omega$ is the solid angle subtended at the earth due to cone half angle Ψ.

3.3 Neutrino fluxes due to WIMP annihilation in the galactic centre

The ν fluxes $\frac{\mathrm{d}\Phi_\nu}{\mathrm{d}E_\nu}(E, \Psi)$ (in units of $\mathrm{GeV}^{-1}\mathrm{m}^{-2}\Omega^{-1}\mathrm{s}^{-1}$) from dark matter annihilating in the galactic centre is expressed as the product of a particle physics term $\frac{\mathrm{d}\Phi_\nu}{\mathrm{d}E_\nu}(E)$ and an astrophysical term $\mathcal{J}(\Delta\Omega)$. Ψ is the angular separation between the line connecting the detector and the GC and the line connecting the detector and point P in the halo as shown in Fig. 3.6. At neutrino energy E and in the direction of the GC, the flux integrated over the solid angle $\Delta\Omega = 2\pi(1 - \cos\Psi)$ is given

by the following equation :

$$\frac{\mathrm{d}\Phi_\nu}{\mathrm{d}E_\nu}(E,\Psi) \ = \frac{\mathrm{d}\Phi_\nu}{\mathrm{d}E_\nu}(E) \ \times \mathcal{J}(\Delta\Omega). \tag{3.13}$$

The term $\frac{\mathrm{d}\Phi_\nu}{\mathrm{d}E_\nu}(E)$ is a function of velocity averaged WIMP annihilation cross section $\langle\sigma_{\mathrm{A}}v\rangle$ and WIMP mass m_χ and can be written as:

$$\frac{\mathrm{d}\Phi_\nu}{\mathrm{d}E_\nu}(E) = \frac{1}{4\pi}\frac{\langle\sigma_{\mathrm{A}}\ v\rangle}{m_\chi^2\delta}\sum_f BR_f\frac{\mathrm{d}N_\nu}{\mathrm{d}E_\nu}\Big|_\oplus. \tag{3.14}$$

where δ is a factor which is 2 for Majorana fermion and 4 for Dirac fermion. We consider WIMP to be Majorana fermions in our analysisBR_f is the branching ratio as described in the previous sections. $\frac{\mathrm{d}N_\nu}{\mathrm{d}E_\nu}\big|_\oplus$ is the neutrino spectra at the surface of earth. The neutrino (and anti-neutrino) spectra at the point of production $\frac{\mathrm{d}N_\nu}{\mathrm{d}E_\nu}\big|_\ominus$ have been calculated [2] [7] including the electroweak corrections [13]. The neutrinos undergo vacuum oscillation while propagating from the GC to the surface of the earth as given by,

$$\frac{\mathrm{d}N_\nu}{\mathrm{d}E_\nu}\Big|_\oplus = \sum_\alpha P(\nu_\alpha\to\nu_\beta)\frac{\mathrm{d}N_\nu}{\mathrm{d}E_\nu}\Big|_\ominus, \tag{3.15}$$

where $P(\nu_\alpha \to \nu_\beta)$ is the probability of transition of ν_α neutrino into ν_β. These probabilities average out since the baselines are very long and are given by the following expression:

$$P(\nu_\alpha\to\nu_\beta) = P(\bar\nu_\alpha\to\bar\nu_\beta) = \sum_{i=1}^{3}|V_{\alpha i}V_{\beta i}|^2 \approx \begin{pmatrix} 0.52 & 0.32 & 0.17 \\ 0.32 & 0.34 & 0.35 \\ 0.17 & 0.35 & 0.48 \end{pmatrix} \tag{3.16}$$

[2]It can be noted that the neutrinos spectra at the point of production calculated using WIMPSIM and PPPC 4 DM ID are different mainly because the latter group incorporates electroweak corrections in their spectra calculation. The channels like $\nu\bar\nu$ which are almost monoenergetic for the case of WIMPSIM, are broader for the latter case. This is because the primary neutrinos start to radiate gamma rays and the charged leptons due to radiative weak corrections. This effect is significant for m_χ above electroweak scale ~ 250 GeV, but could be observed (although less significant) even for low WIMP masses [7].

Paramter	Best-Fit Value
θ_{12}	33.62°
θ_{13}	8.54°
θ_{23}	47.2°
δ	234°
Δm^2_{21}	$7.40 \times 10^{-5}\text{eV}^2$
Δm^2_{31}	$2.49 \times 10^{-3}\text{eV}^2$

Table 3.2: Oscillation parameters used in the GC WIMP annihilation analysis [33] [www.nu-fit.org].

where the index i runs over the neutrino mass eignestates, $(\alpha, \beta) = (e, \mu, \tau)$ flavour states, and the elements of $|V_{\alpha i}|$ of the neutrino matrix can depend on its unknown CP-violating phase. The oscillation parameters used for calculating the fluxes for this work are different than those used in the previous sections and are given in Table 3.2. Fig. 3.7 shows the muon neutrino spectra at the surface of earth due to annihilation of 30 GeV WIMP in the galactic centre. The ν_μ spectra for various annihilation channels have been shown. One can see that $\tau^+\tau^-$, $\mu^+\mu^-$ and $\nu\bar{\nu}$ channels give a harder spectra. One can see the effect of vacuum oscillations on different neutrino flavours as they propagate from the GC to the surface of the earth. Fig. 3.8 shows the comparison of the oscillated and the unoscillated neutrino fluxes arising out of 30 GeV WIMP at the CC.

3.3.1 DM density profiles and J-Factor calculations

The astrophysical contribution $\mathcal{J}(\Delta\Omega)$ or J-Factor as given in the Eq. 3.17 is a function of the line-of-sight integral $J(\Psi)$ of the DM distribution profile and is discussed in detail in the following subsection. Since there is an uncertainty in the distribution of DM in the galaxy, especially in the galactic core, generally a standard DM density profile is assumed and results are quoted for the DM profile.

$$\mathcal{J}(\Delta\Omega) = \int_0^{\Delta\Omega} J(\Psi)\mathrm{d}\Omega = \int_0^{\Delta\Omega}\int_{l.o.s} \rho^2 \mathrm{d}l\mathrm{d}\Omega, \tag{3.17}$$

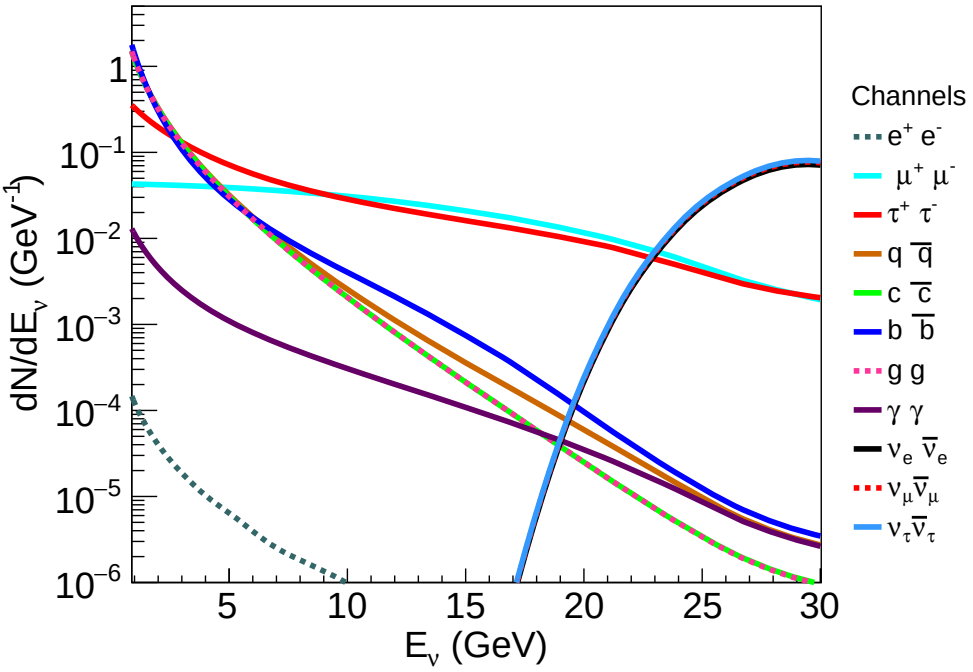

Figure 3.7: The ν_μ spectra at the surface of the earth due to WIMP annihilation in the galactic centre. The ν_μ spectra is similar and not shown here. We used the spectra at the point of production [7] and propagate it to the earth surface taking care of vacuum oscillations. The shown spectra is for a 30 GeV WIMP and for several annihilation channels. Electroweak corrections have been included [13].

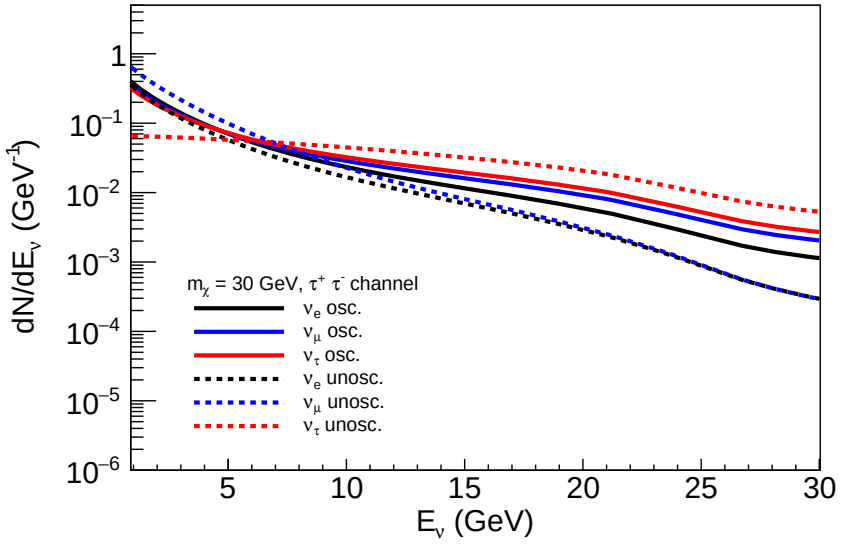

Figure 3.8: The effect of oscillation on the neutrinos propagating from the G.C. to the surface of the earth.

where $J(\Psi)$ = line of sight integration of DM-density squared and is given by:

$$J(\Psi) = \int_0^{l_{max}} dl\ \rho^2 \left(\sqrt{R_{sc}^2 - 2lR_{sc}\cos\Psi + l^2}\right). \tag{3.18}$$

In Eq. 3.18, ρ_{sc} is the local dark matter density, R_{sc} is the solar radius whose value is taken to be 8.5 kpc. The parameter l is the distance between a point and the earth and shown in the Fig. 3.6. $\mathcal{J}(\Omega)$ is the integral radius of $J(\Psi)$ over a solid cone $\Delta\Omega = 0.5\pi(1-cos\Psi)$ and we call it J-Factor.

There is a tension between the halo profile models which describe the DM density distribution in galaxies, especially in the region around their centre. While the N-body simulations tend to favour highly steeped concentration of DM in the centre (a cuspy profile), the DM halo profile fits to the observation data rather favours a flat central core region. This disagreement between the observational data and the expectations from numerical simulations is known as the cusp-core problem [136].

A DM profile can be described in terms of a density normalisation ρ_s, scale radius r_s, the physical size of the DM halo and several shape parameters $\mathcal{S}$ [137]. The radius R_Δ at overdensity Δ is usually taken to be the physical size of the halo[3]. Thus for a spherically symmetric DM halo, DM density $\rho(r)$ as a function of radial distance r, we have :

$$\rho(r) = f(\rho_s, r_s, \mathcal{S}). \tag{3.19}$$

The DM concentration in a halo is also a function of r_{-2} which is the radius at which the slope becomes -2.

$$\left.\frac{\mathrm{d}\left[r^2\rho(r)\right]}{\mathrm{d}r}\right|_{r=r_{-2}} = 0 \Leftrightarrow \left.\frac{\mathrm{d}\log\rho}{\mathrm{d}\log r}\right|_{r=r_{-2}} = -2. \tag{3.20}$$

Generally, the DM profiles that can be parametrised in terms of three parameters $\mathcal{S} = (\alpha, \beta, \gamma)$ are collectively known as Zhao's (or Zhao-Hernquist) profile. Here α is transition slope of the density profile that regulates the sharpness of the transition between the inner and the outer slopes, β is

[3]Please refer http://lpsc.in2p3.fr/clumpy/ for more details.

outer slope and γ is inner slope of the density profile [138].

$$\rho^{ZHAO}(r) = \frac{2^{\frac{\beta-\gamma}{\alpha}} \times \rho_s}{(r/r_s)^{\gamma}[1+(r/r_s)^{\alpha}]^{\frac{\beta-\gamma}{\alpha}}}, \tag{3.21}$$

where r_s is the scale radius in kpc and ρ_s is the density at $r = r_s$ and acts as a density normalisation factor. The most popular of Zhao-Hernquist profile are NFW (Navarro, Frenk & White) [139] with (α, β, γ)=(1,3,1) and Modified Isothermal (MI) [82] with (α, β, γ)=(2,2,0).

The Burkert profile [140] is a phenomenological density distribution that resembles an isothermal profile in the inner regions ($r \ll r_0$), and with an outer slope -3 as in a NFW profile:

$$\rho^{BURKERT}(r) = \frac{\rho_0}{(1+r/r_0)[1+(r/r_s)^2]}, \tag{3.22}$$

where r_0 is the scale (or core radius) in units of kpc and ρ_0 is the core density in units of $M_{\odot} kpc^{-3}$. It is to be noted that for this profile $\rho(r_0) = \rho/4$ and r_{-2} is the root of $R^3 - R - 2 = 0$, where $R = r_{-2}/r_0$, *i.e.*, $r_{-2} \approx 1.5213797068 r_0$.

Recently dark matter only simulations tend to favour EINASTO profile [141, 142] in which the inner slope of the DM halo decrease as r decrease, *i.e.*,

$$\rho(r) \propto \exp\big(-Ar^{\alpha}\big) \Leftrightarrow \frac{\mathrm{d}\log\rho}{\mathrm{d}\log r} = -\alpha A r^{\alpha}. \tag{3.23}$$

The standard Einasto profile is used in [141] where $A = \frac{2}{\alpha} r_{-2}^{-\alpha}$ and that implies :

$$\rho^{EINASTO}(r) = \rho_{-2} \exp\left[-\frac{2}{\alpha}\left[\left(\frac{r}{r-2}\right)^{\alpha} - 1\right]\right], \tag{3.24}$$

where $\alpha = 0.17$, r_{-2} is the radius for which the profile slope becomes -2 and ρ_{-2} is the associated normalisation. Table 3.3 shows the parameters used for various density profiles [137].

The scale parameters for each of the profiles are chosen in such a manner that they yield the DM density [4] of $0.4\ \mathrm{GeVcm}^{-3}$ at $R_{\odot} = 8.33$ kpc and the total dark matter contained in the galaxy

[4]For the case of the solar/earth signal calculation we have used $\rho_{\odot,\oplus} = 0.3\mathrm{GeV\ cm}^{-3}$

PROFILE	α	β	γ	r_s (kpc)
NFW	1	3	1	21.7
BURKERT	-	-	-	9.26
EINASTO	0.17	-	-	21.7

Table 3.3: Parameter values for different density profiles.

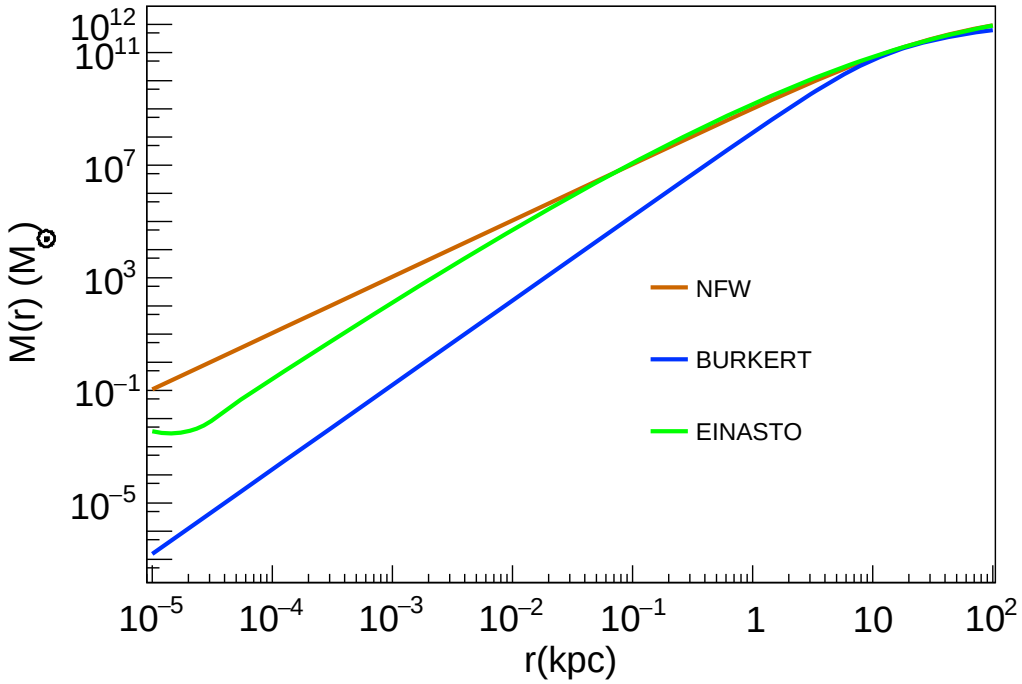

Figure 3.9: $M(r)$ of DM density profiles as a function of radial distance r.

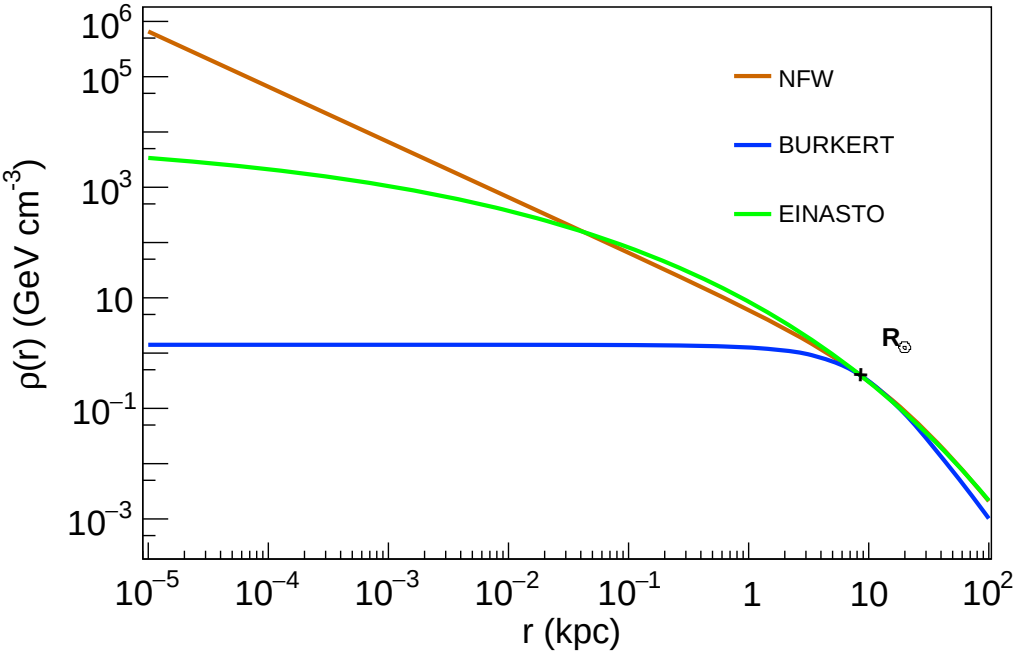

Figure 3.10: $\rho(r)$ of DM density profiles as a function of radial distance r.

of radius 60 kpc to be $4.7 \times 10^{11} M_{\odot}$ [143].

The DM mass distribution (M_r) and density distribution ($\rho(r)$) for various DM density profiles is shown in Fig 3.9 and Fig. 3.10, respectively. It can be seen that for the position of the solar system, all the density profiles predict roughly the same DM density which is expected. All these density profiles discussed here are spherically symmetric with respect to the radial distance r. In Fig. 3.11, we show the $J(\Psi)$ as a function of angular separation from the galactic centre. Fig. 3.12 shows the integral of $J(\Psi)$ over a solid angle cone of Ψ for three different DM density profiles. Among the three profiles, the integral $\mathcal{J}(\Delta\Omega)$ is maximum for NFW (orange) and lowest for BURKERT (blue) for low angular separation. For calculating the J-Factors, we have used the CLUMPY package [137], assuming the contribution of DM clumps to be negligible and hence turned off while generating the values shown in Fig. 3.9, Fig. 3.10, Fig. 3.11 and Fig. 3.12.

Finally, in Fig. 3.13, we show the neutrino fluxes due to annihilation of a 50 GeV WIMP in the galactic centre, assuming NFW profile. The colour coding on the left hand side palette shows the strength of the neutrino fluxes. The red dot represents the galactic centre where the flux strength is maximum. The skymap has been plotted in terms of the equatorial coordinates using ALADIN

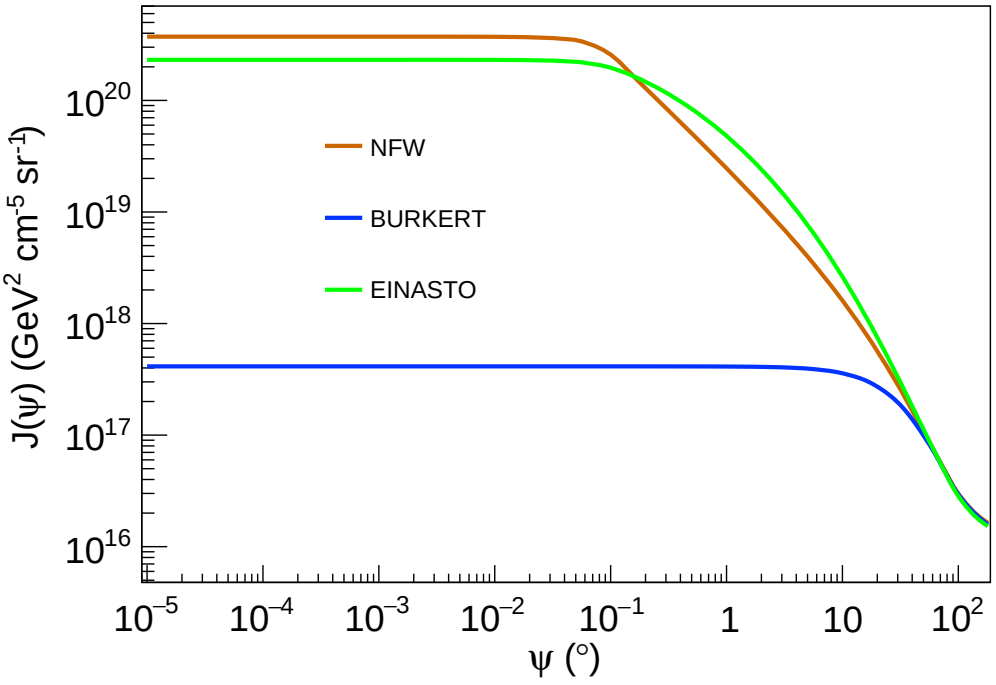

Figure 3.11: The line-of-sight integral $J(\Psi)$ as a function of angular separation Ψ for NFW (orange), Burkert (blue) and Einasto (green) DM density profiles.

package [144].

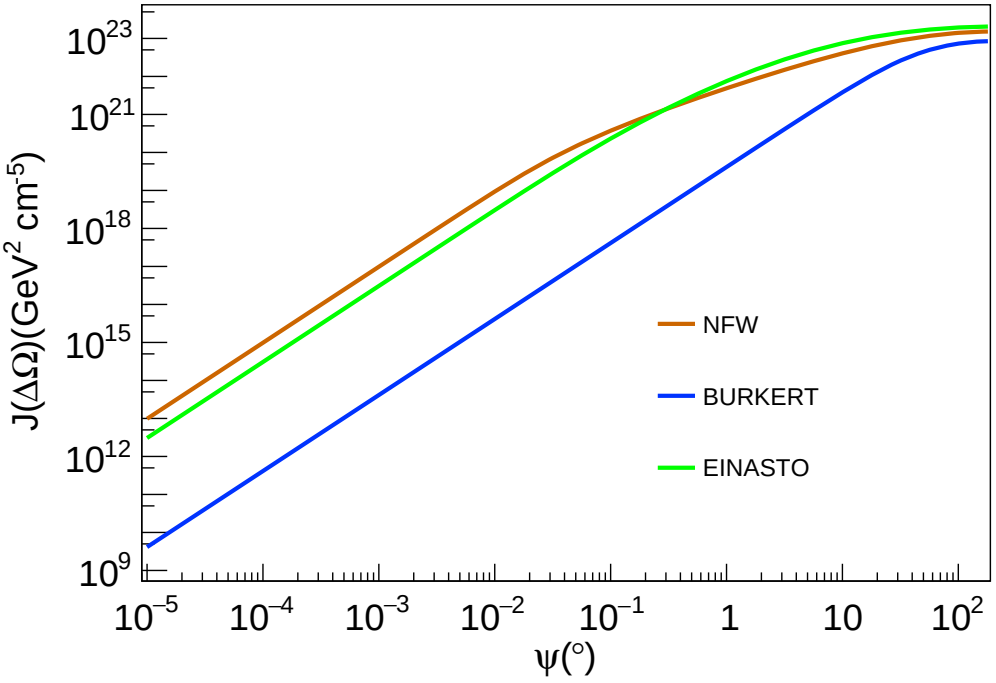

Figure 3.12: $\mathcal{J}(\Delta\Omega)$ as a function of angular separation Ψ for NFW (orange), Burkert (blue) and Einasto (green) DM density profiles.

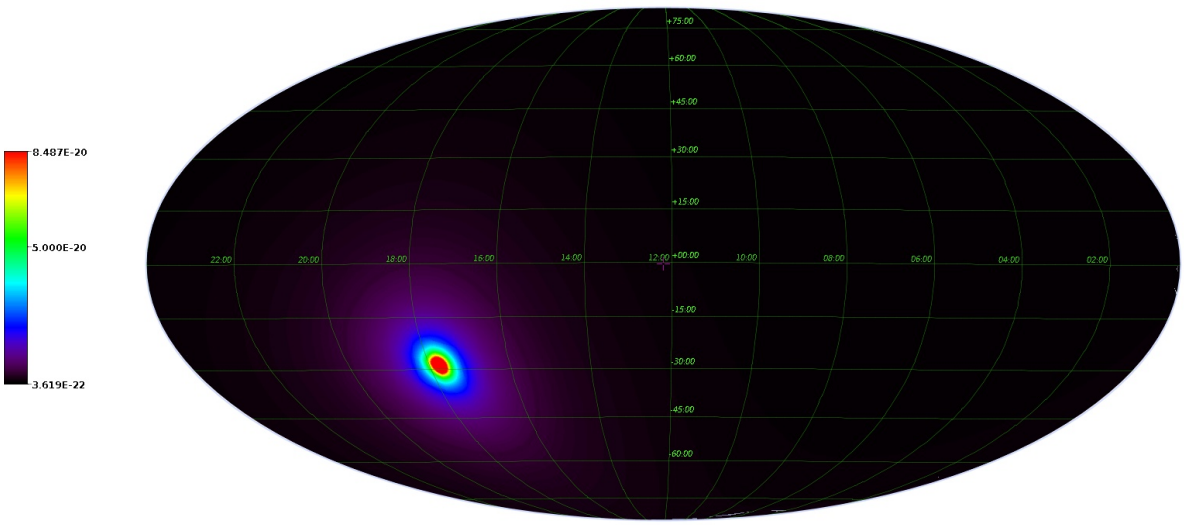

Figure 3.13: ν fluxes ($\mathrm{cm}^{-2}\mathrm{s}^{-1}$) for 50 GeV WIMP annihilating in GC through $\tau^+\tau^-$ channel for a NFW profile, $\langle\sigma_{\mathrm{A}}v\rangle = 3 \times 10^{-26}\mathrm{cm}^3\mathrm{s}^{-1}$, calculated using PPPC4DMID [7].

Chapter 4

Atmospheric neutrino fluxes

4.1 Introduction

Atmospheric neutrinos arise due to interaction of the cosmic ray with the nuclei in the air molecules in the atmosphere Fig. 4.1. Primary cosmic rays are high energy particles of galactic and extra-galactic origin and whose exact origin is still unknown. They comprise mostly protons $\sim$ 89%, around 9% helium nuclei and a small fraction $\sim$ 1% of heavier nuclei, all the way up to uranium [145, 146]. The cosmic rays incessantly bombard the earth's atmosphere. The interactions of cosmic rays with the nuclei in the atmosphere produces secondary particles, mostly pions and a small mixture of kaons. These mesons decay mainly to muons and through the following decay chain neutrinos are produced:

$$\pi^{\pm} \rightarrow \mu^{\pm} + \nu_{\mu}(\bar{\nu}_{\mu}),$$

$$\mu^{\pm} \rightarrow e^{\pm} + \bar{\nu}_{\mu}(\nu_{\mu}) + \nu_{e}(\bar{\nu}_{e}). \tag{4.1}$$

Kaons follow a similar decay chain and produce neutrinos of the above two flavours. However, their contribution to the atmospheric neutrinos flux is quite small in comparison to the neutrino fluxes produced by decay of pions. The decay of pions and kaons give "conventional" atmospheric neutrino fluxes comprising only ν_{μ} and ν_{e} flavour neutrinos and their antiparticles. The decay of heavier mesons typically containing a charm quark produce "prompt" atmospheric neutrinos and

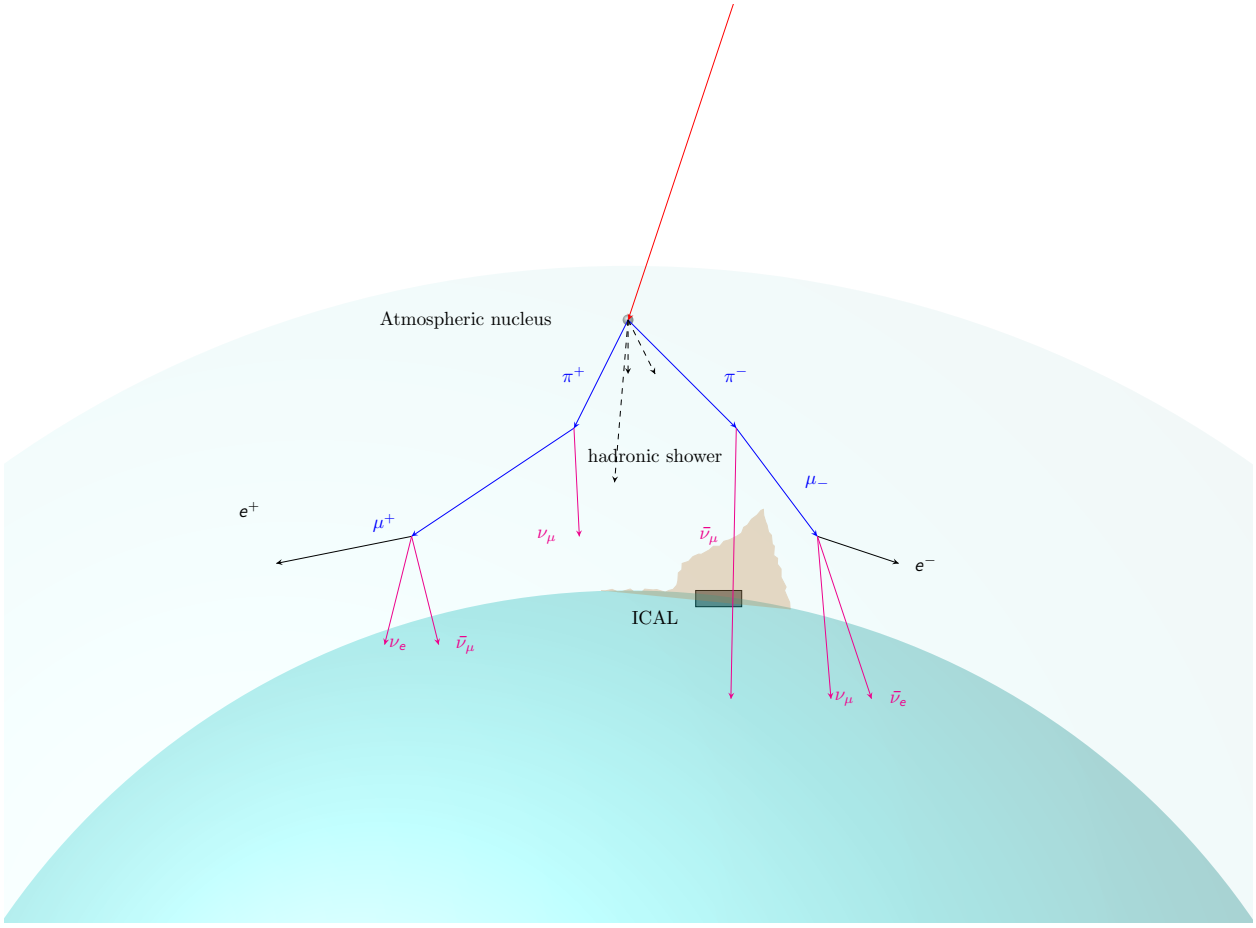

Figure 4.1: A schematic illustration of the production of atmospheric neutrinos due to cosmic ray interactions with the air molecules in the atmosphere.

are expected to exhibit a harder energy spectrum. They can produce $\nu_\tau/\bar{\nu}_\tau$ fluxes, however, their production is strongly suppressed and is expected to dominate the atmospheric neutrino fluxes at energies above $\sim$ 100 TeV and hence are not relevant to our analysis.

The atmospheric neutrino fluxes used in this thesis have been calculated by Honda et. al as discussed in Ref. [21]. The original work [21] discusses the flux calculation in great detail. In this Chapter, we include a qualitative details of the flux calculations, and discuss the reasons responsible for the difference among the fluxes at various locations in Section 4.2. Thereafter, the features of atmospheric neutrino fluxes such as their dependence on neutrino energy and direction and their flavour ratios in Section 4.3. This is followed by Section 4.4, where we compare the fluxes at Theni and Kamioka. Finally, the fact that atmospheric neutrinos act as a major background to indirect detection is discussed in Section 4.5.

4.2 Calculation of atmospheric neutrino fluxes

The 3D-calculations of the atmospheric neutrino flux as done in Ref. [21] involve tracing the motion of the cosmic rays and carefully recording the fraction which would penetrate the rigidity cut off (a quantitative measure of the shielding provided by the earth's magnetic field), and their associated secondaries. This is followed by examining all the neutrinos produced during their propagation in the atmosphere, and registering the neutrinos which hit the virtual detector, assumed around the target neutrino observation site. Several factors have to be taken into account for accurately modelling atmospheric neutrino fluxes for a specified location on the earth: empirical, global models of the earth's atmosphere from surface to space, including details of the temperatures and densities of the atmosphere's components, and a detailed knowledge of earth's geomagnetic field.

The most important quantity involved in the calculation of the fluxes is the air density. The seasonal variation in the air density (for a production height above sea level) becomes more and more prominent as we move from the tropical regions to the poles. Therefore, we expect less seasonal variation in the atmospheric fluxes for the INO site (which is in the tropical region) in comparison to mid altitude sites such as Kamioka (see Figure 1 of Ref. [21] for further details).

Another quantity affecting the neutrino fluxes is the value of the geomagnetic field for the geographical site considered and involves the following two processes: rigidity cut off and muon bending. Rigidity cut off (or more precisely geomagnetic rigidity cut off) is a quantitative measure of the shielding provided by the earth's magnetic field and is a function of the horizontal component of the geomagnetic field (B_h) near the earth which guides the gyroscopic motion of the cosmic rays. The cosmic rays need to have a large gyro-radius in order to arrive at a point very close to the earth. However, for large gyro-radius the earth acts as a slant shield thereby limiting the arrival azimuth angle of cosmic rays. For radius sufficiently large enough, the earth becomes a flat shield and then just limits the upward going cosmic rays, and in that scenario the limitation on the arrival azimuth angle disappears. This mechanism is known as rigidity cut off.

The muons, before decaying into neutrinos, could bend due to the geomagnetic field thereby affecting the arrival zenith angle of atmospheric neutrino fluxes. Let us call the difference between the arrival zenith angles of the neutrino fluxes with and without muon bending as θ_{MB}. Since the atmospheric neutrino flux (above a few GeV) has a large arrival zenith angle dependence, even a small θ_{MB} results in a significant difference of the flux (among different geographical sites) and this effect is distinguishable from the effect due the rigidity cut off at these energies. Again, it is B_h which regulates the difference of the arrival zenith angle of neutrinos and, therefore, is a crucial parameter to understand the effects of rigidity cut off and muon bending. Figure 2 of Ref. [21] shows the strength of B_h for various geographical sites.

Having mentioned the quantities governing the flux calculations, we can now discuss the characteristics of atmospheric neutrino fluxes, followed by the differences in fluxes for Theni and Kamioka site in subsequent section in some detail.

4.3 Characteristics of atmospheric neutrino fluxes

The spectra of primary cosmic rays has the dependence on energy E as $\sim E^{-2.7}$ in the 10 GeV-TeV range. Therefore, the atmospheric neutrino fluxes follow a similar dependence on neutrino energy E_ν as shown in Fig. 4.2. The figure shows all direction averaged fluxes as a function of neutrino

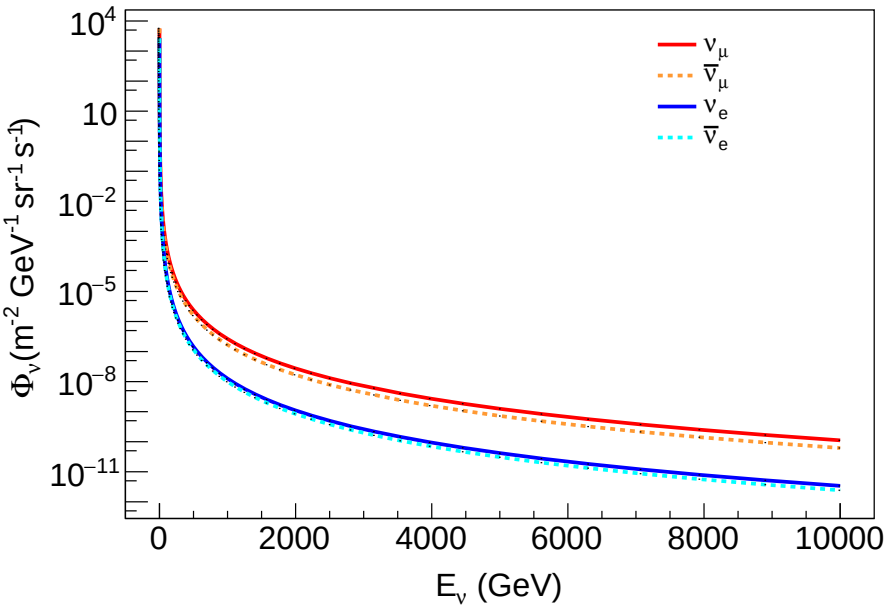

Figure 4.2: The variation of atmospheric neutrino fluxes with the neutrino energy E_ν. The fluxes have been averaged over all directions and shown for Theni site. The ν_μ fluxes (red solid) are more than ν_e (blue solid) fluxes. Also, the fluxes from the antiparticles are lower than their respective particles and are shown in lighter shade dotted lines.

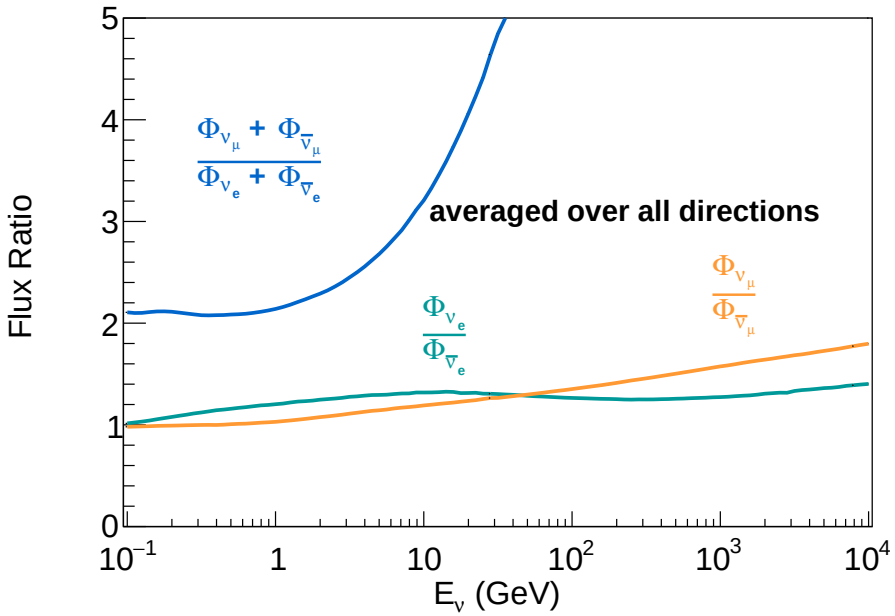

Figure 4.3: Neutrino flavour ratio for all direction averaged atmospheric neutrinos fluxes at Theni.

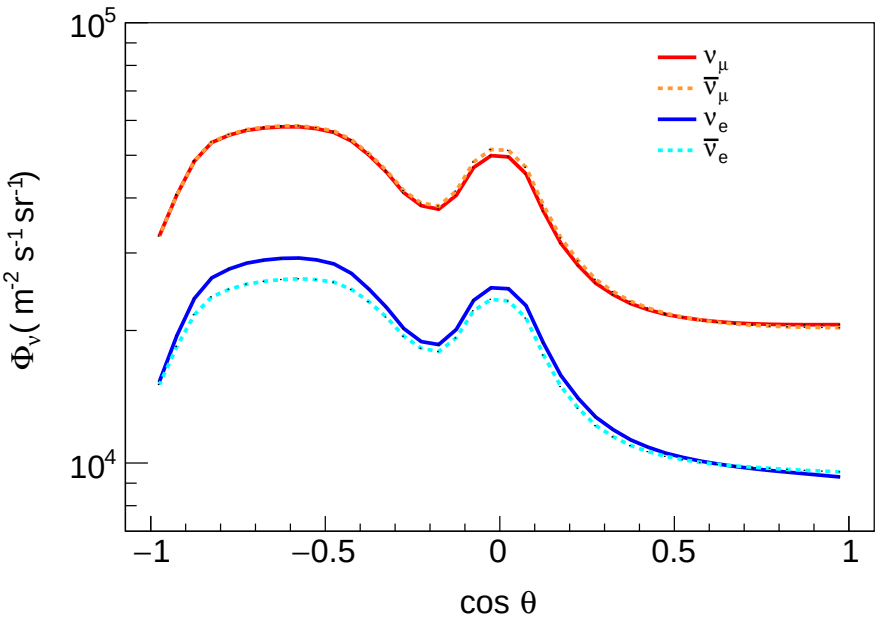

Figure 4.4: The dependence of atmospheric neutrino fluxes on cosine of the zenith angle $\cos\theta$ for different neutrino flavours and types. The fluxes have been averaged over all azimuthal bins and summed over entire energy range $E_\nu \in [0.1, 10000]$ GeV. $\cos\theta = 1$ represents down going neutrinos.

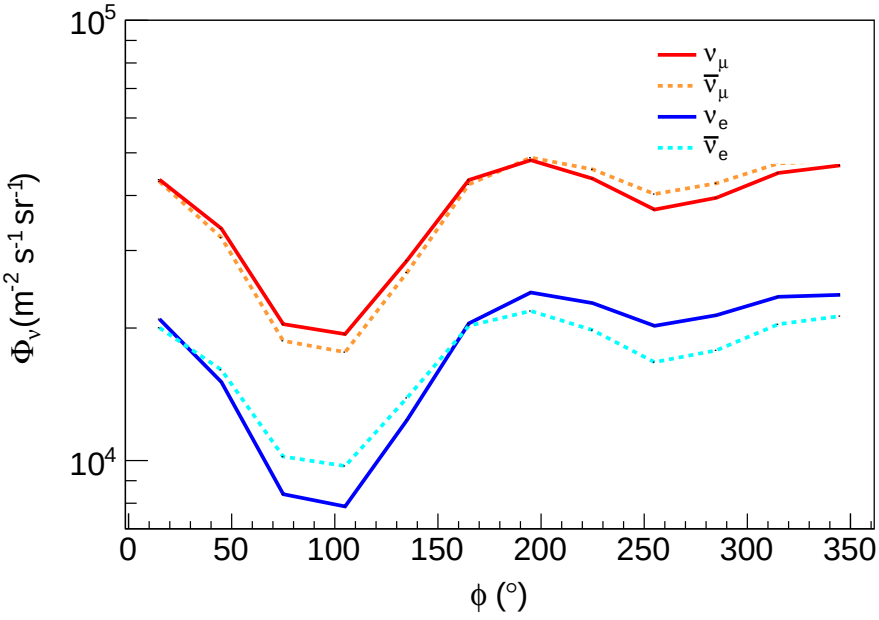

Figure 4.5: The azimuthal angle dependence of the atmospheric neutrino fluxes, averaged over zenith angle bins and summed over entire energy range. In this convention, $\phi = 0$ indicates South, $\phi = 90$ is East and so on.

energy. The ν_μ fluxes are observed to be more than the ν_e fluxes and the trend is the same for their respective antiparticles. This feature holds true irrespective of site's geographical coordinates [21]. From Eq. 4.1, we can see that the ratio of the two flavours:

$$R = \frac{\Phi_{\nu_\mu} + \Phi_{\bar{\nu}_\mu}}{\Phi_{\nu_e} + \Phi_{\bar{\nu}_e}} \approx 2 \tag{4.2}$$

where Φ represents the flux of neutrinos with the subscript denoting its flavour. The flux ratio, using fluxes at Theni, for different flavour combinations are plotted in Fig. 4.2. The flux ratios $\nu_\mu/\bar{\nu}_\mu$ and $\nu_e/\bar{\nu}_e$ reflect the π^+/π^- of the parents pions. Since the majority of the primary cosmic rays are protons, there is an excess of π^+ in general making these ratios more than one. We can see that the ratio in Eq. 4.2 is only approximately true as at high energies muons may not decay before reaching the surface of the earth. However, it is always greater than 2 as can be seen from the figure. The ratio of the ν_μ and $\bar{\nu}_\mu$ fluxes is approximately close to 1 and approaches to a value of 2 for very high energies. The ν_e and $\bar{\nu}_e$ flux ratio has a non-linear behaviour, however, the ratio remains more than 1 for all energies.

Fig. 4.4 show the zenith angle[1] dependence of atmospheric ν_μ, $\bar{\nu}_\mu$, ν_e and $\bar{\nu}_e$ fluxes averaged over all azimuthal angles (ϕ) and summed over entire energy range $E_\nu \in [0.1, 10000]$ GeV. Noticeably, there are large are large up-down asymmetries in the fluxes. It is the low energy neutrinos that mostly contribute to this asymmetry. The asymmetry decreases rapidly for $E_\nu > 3$ GeV and above that $\Phi_\nu(E_\nu, \cos\theta) \approx \Phi_\nu(E_\nu, -\cos\theta)$. At low energies, geomagnetic effects result in a deviation from this equality. At higher energies, any asymmetry in the fluxes of the upward and downward going neutrinos could be attributed to neutrino oscillations and forms the basis of atmospheric neutrino analysis.

Fig. 4.5 shows the azimuthal angle dependence of the atmospheric neutrino fluxes, averaged over zenith angle bins and summed over entire energy range. There is some noticeable East-West asymmetry and it has a complex dependence on azimuthal angle for even energies beyond 10 GeV. This is due to the rigidity cut-off and muon bending in the geomagnetic field [21]. We will discuss

[1]Note that the $\cos\theta$ definition here is opposite to that of ICAL convention as described in Chapter 5.

these features again while comparing Theni and kamioka fluxes.

As mentioned in the previous section, the calculation of atmospheric neutrino fluxes involve precise measurement of cosmic ray spectra, energy spectrum of secondary muons produced due to interaction of cosmic rays with the air nuclei and modelling of several effects such as altitude dependence of interactions in the atmosphere, the geomagnetic effect on the cosmic ray fluxes and the subsequently produced secondaries as well as the latitude and longitudinal dependence of air density profile. Each of these steps introduce an uncertainty in the neutrino flux calculation. We have included these in the form of following uncertainties in our analysis [60, 65, 147]:

- 20% error on flux normalisation [148],
- 10% error on cross-section normalisation [147],
- 5% uncorrelated error on the zenith angle distribution of atmospheric neutrino fluxes, assuming it to be energy independent [60],
- an energy dependent "tilt factor", which parametrizes possible deviations of the energy dependence of the atmospheric fluxes from the simple power law and has been incorporated as per the following prescription given in Ref. [60]. Events using the neutrino fluxes are calculated as per the description in Chapter 5. Two sets of event spectrum are calculated: using the given atmospheric fluxes Φ and another set using the titled Φ_δ fluxes according to

$$\Phi_{delta}(E) = \Phi_0(E)\Big(\frac{E}{E_0}\Big)^{\delta} \simeq \Phi_0(E)\Big(1 + \delta \ln\frac{\mathrm{E}}{\mathrm{E_0}}\Big), \tag{4.3}$$

  where $E = 2$ GeV and δ is 1σ systematic error which we have taken to be 5% for our analysis. The difference between the event rates for the two sets is then included as a tilt error in our analysis. Similar to previous ICAL analysis[2] [65], these uncertainties are incorporated

[2]It should be noted that a detailed study of ICAL systematic uncertainties is under way. For analyses presented in this thesis, we have assumed that the previous set of systematic uncertainties hold for the new flux as well as the extended momentum range. Therefore, these numbers would change when a better estimates on systematic uncertainties are available.

in our statistical analysis, by parametrizing them in terms of a set of variables called "pulls" [60].

4.4 Comparison of Theni and Kamioka Fluxes

Previous simulation and physics studies at ICAL have been carried out using atmospheric neutrinos fluxes calculated for Kamioka site. After Theni fluxes were calculated by Honda et al. [21] and made available publicly, we have used them in our studies. Therefore, it is essential to make a comparison between the atmospheric neutrino fluxes calculated for the Theni and Kamioka site[3].

Fig. 4.6 shows the atmospheric ν fluxes, averaged over all directions, as a function of neutrino energy E_ν for Kamioka and Theni sites. The qualitative features are the same for both the sites. However, we find a difference of flux between the sites by factor $\sim$3 at the low energy end which is due to a large difference of rigidity cut off for these sites. The difference between the fluxes at two sites decreases with the increase in E_ν and above 10 GeV it is very small. The fluxes shown in Fig. 4.6 have been averaged over all seasons. As mentioned earlier, the seasonal variations for fluxes at a given site is insignificant for Theni. For a mid-latitude site such as Kamioka, the variations are slightly noticeable but still not large. For high latitude sites such as South Pole and Pyhasalmi mine, the seasonal variations are rather large (see Figure 4 of Ref. [21] for quantitative details).

Fig. 4.7 shows the zenith angle dependence of atmospheric ν_μ and $\bar{\nu}_\mu$ fluxes averaged over all azmiuthal angles (ϕ) and summed over all energy range $E_\nu \in [0.1, 10000]$ GeV. Larger up-down asymmetry can be seen in the fluxes at Theni site in comparison to Kamioka site. Noticeably, the fluxes at the SK site can be seen to be smaller than that of INO site around $cos\theta$ range -0.4 to -0.8., and where the INO fluxes have a bump structure which can be explained in terms of rigidity cut off and the muon bending at the places where the neutrinos are produced. There are large differences in the atmospheric neutrino fluxes from other sites as well (also see Figure 7 of Ref. [21]). The difference of rigidity cut off at near horizontal directions is primarily responsible

[3] Atmospheric neutrino fluxes have been taken from http://www.icrr.u-tokyo.ac.jp/ mhonda/

for these differences in the fluxes at near horizontal directions. The neutrinos arriving from the near horizontal geomagnetic East directions are the ones strongly affected by the rigidity cut off. For the SK site, rigidity cut off at near vertical directions are not significant. However, for the near horizontal directions at SK site, rigidity cut off affects strongly. This explains the difference of fluxes between SK site and the polar regions but for explaining the difference between Theni and Kamioka site, one needs to consider the muon bending as well. It turns out that the suppression for the ν_μ and $\bar{\nu}_e$ is stronger than $\bar{\nu}_\mu$ and ν_e for the Theni site. For understanding this further, we need to discuss the azimuthal variation of atmospheric neutrinos.

Again, two kinds of effects from the geomagnetic field, the rigidity cut off and the muon bending, have to be considered while discussing the azimuthal dependence of the atmospheric neutrino fluxes. Since the cosmic rays generally carry a positive charge, the geomagnetic field pointed to the North filters the low energy cosmic rays from the East directions. The rigidity cut off reduces neutrinos of all flavors from the East direction at the same rate whereas the effect of muon bending depends on the muon charge. Thus, the geomagnetic field and rigidity cut off affects the μ^+ in the same fashion. Opposite effect is true for μ^-. The muon bending reduces the $\bar{\nu}_\mu$ and ν_e fluxes from the East and ν_μ and $\bar{\nu}_e$ fluxes from the West which is seen as a dip at 90° and 270° azimuthal directions for these fluxes (Fig. 4.8), respectively.

The muon bending suppresses the ν_μ and $\bar{\nu}_e$ fluxes from the West, but enhances them from the East. The rigidity cut off, however, affects strong the same fluxes from the East directions, therefore cancelling the enhancement from the East. Hence the muon bending results in suppression of the ν_μ and $\bar{\nu}_e$ fluxes in Fig. 4.5 and Fig. 4.8. The muon bending affects the $\bar{\nu}_\mu$ and ν_e fluxes in an opposite manner *i.e.*, it enhances the fluxes from the West, but suppresses them from the East. However, the rigidity cut off has a weaker impact for the West directions, and hence the muon bending results in an enhancement of the $\bar{\nu}_\mu$ and ν_e in Fig. 4.5 and Fig. 4.8. The same mechanism is applicable at other at other geographical sites, but in comparison to the the amplitudes of the suppression and enhancement at Theni site, the effects are smaller, and hence is not clearly observable for the Kamioka site. Since the geomagnetic field is almost vertical at the poles, we expect almost no

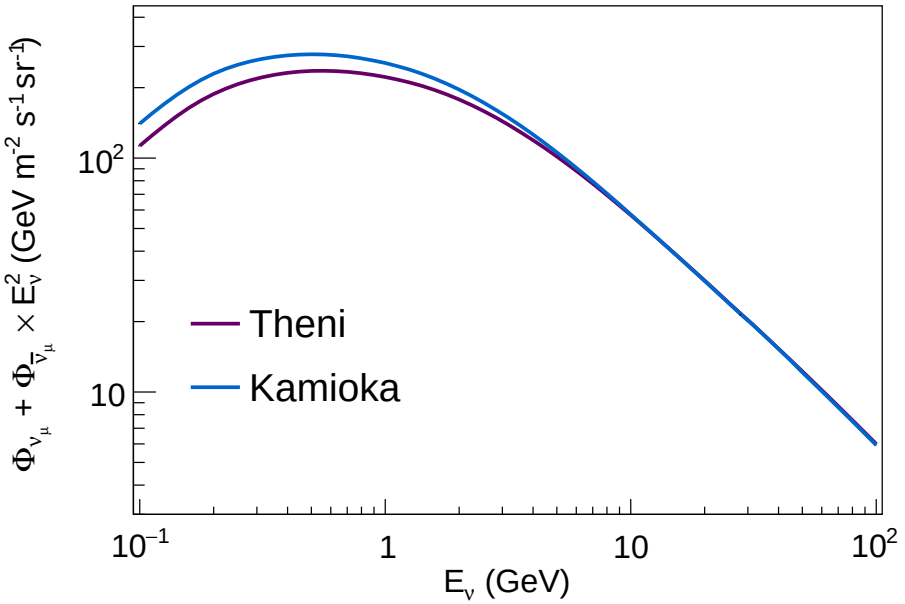

Figure 4.6: Atmospheric ν fluxes, averaged over all directions, as a function of neutrino energy E_ν for Kamioka and Theni sites. The difference between the fluxes at two sites decreases with the increase in E_ν.

azimuthal variation of the atmospheric neutrinos except for the near horizontal directions. The rigidity cut off works very weakly at the poles, and the muon bending works mainly with the residual horizontal component of the geomagnetic field (See Ref. [21] for detailed comparison).

Since the total atmospheric neutrino fluxes at Theni are smaller than that at Kamioka site, we expect a reduction in the total number of muon events calculated with the former fluxes. This, depending on the physics quantity of interest, could deteriorate or improve the expected sensitivity at ICAL. For the dark matter searches, since the atmospheric neutrinos act as a background, we expect an increased in sensitivity.

4.5 Atmospheric neutrinos as a background to indirect detection

The study of atmospheric neutrinos provides a rich insight into the neutrino physics. Besides providing neutrinos and antineutrinos in two distinct flavours, they span energies ranging from a

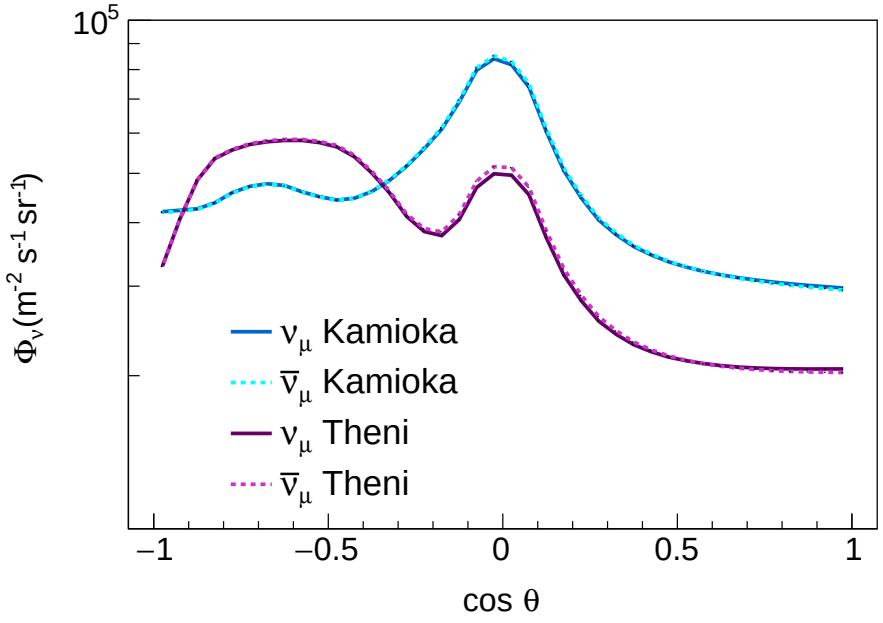

Figure 4.7: The zenith angle dependence of atmospheric neutrino fluxes averaged over all azmiuthal angles (ϕ) and summed over all energy range $E_\nu \in [0.1, 10000]$ GeV. The ν_μ fluxes for Theni (magenta) and Kamioka (azure) are shown. The corresponding $\bar{\nu}_\mu$ fluxes are shown in a lighter shade and dotted lines.

.

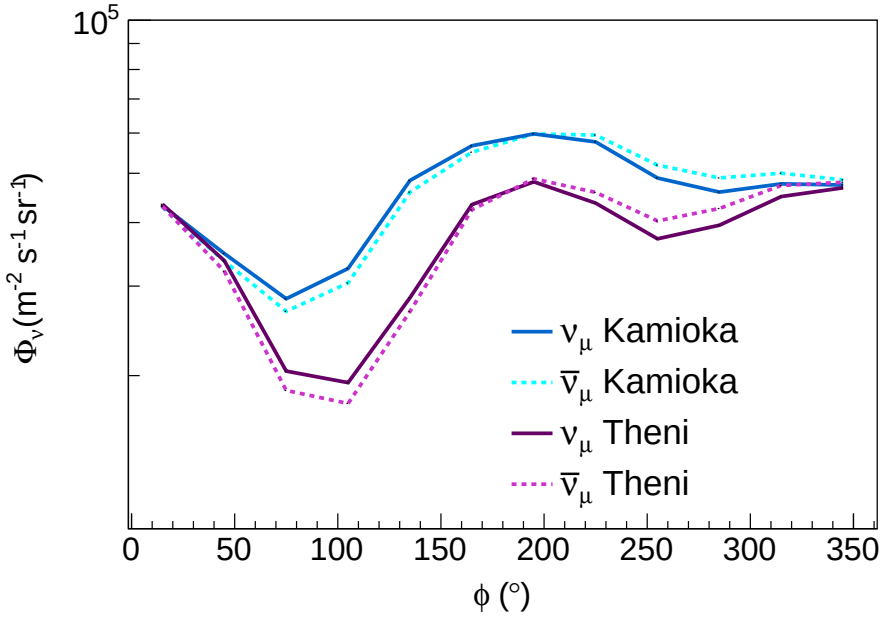

Figure 4.8: The azimuthal angle dependence of atmospheric neutrino fluxes averaged over all zenith angles ($\cos\theta$) and summed over all energy range $E_\nu \in [0.1, 10000]$ GeV. The ν_μ fluxes for Theni (magenta) and Kamioka (azure) are shown. The corresponding $\bar{\nu}_\mu$ fluxes are shown in a lighter shade and dotted lines.

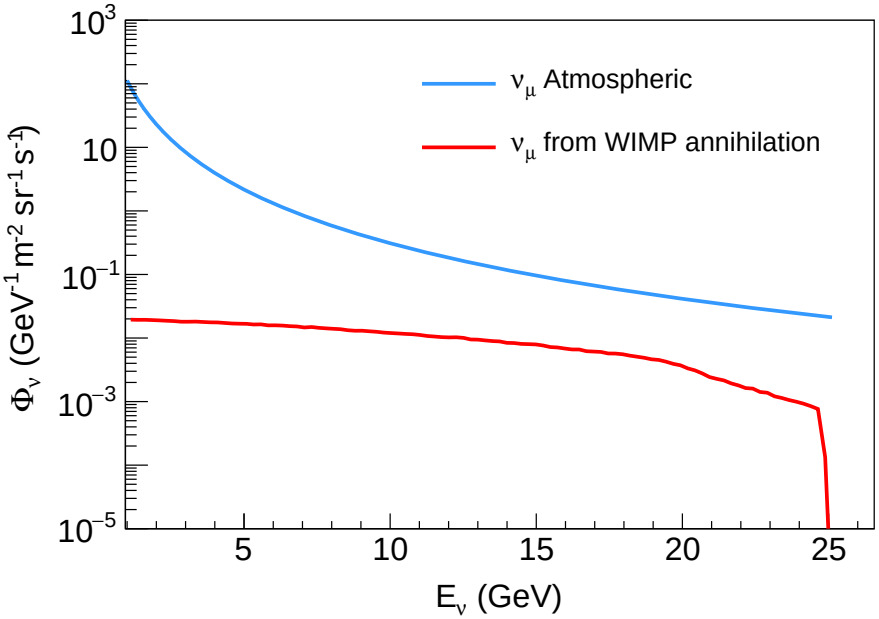

Figure 4.9: Atmospheric neutrinos act as a severe background to the signal neutrinos coming from the WIMP annihilation. The background ν_μ fluxes are shown in azure for the $E_\nu \in [1, 25]$ GeV. The ν_μ fluxes due to WIMP annihilation in the sun for a 25 GeV WIMP and assuming 100% branching ratio for $\tau^+\tau^-$ channel and $\sigma_{SD} = 10^{-39}\mathrm{cm}^2$ and is also shown (red). The signal fluxes are several orders of magnitude lower than the background neutrino fluxes. The signal and the background fluxes have been averaged over all directions.

hundreds of MeV to tens of TeV and beyond. They also provide different baseline (L) and energy E combinations thereby traversing matter of varying densities. By studying them, ICAL can explore oscillation parameters and probe signatures of various new physics in the neutrino sector. In Chapter 9, we describe prospects of detecting non-standard interactions at INO. However, for the majority of the analysis carried out in this thesis, *viz.*, indirect searches of dark matter, atmospheric neutrinos pose a severe background and hence have to be suppressed. The atmospheric neutrino fluxes are several orders of magnitude more than the neutrino fluxes arising due to WIMP annihilation in the sun, the earth or the galactic centre. Fig 4.9 shows the comparison of atmospheric neutrinos and neutrinos arising out of WIMP annihilation in the sun. These fluxes have been averaged over all directions and shown for ν_μ. The other flavours and type of neutrinos follow a similar trend. The signal fluxes are for a 25 GeV WIMP annihilating through $\tau^+\tau^-$ channel, assuming a 100 % branching ratio and a $\sigma_{SD} = 10^{-39}\mathrm{cm}^2$.

We can see, however, that the atmospheric neutrinos differ from the signal neutrinos in terms of spectral shape. The more crucial difference is directionality, which we will discuss in the later chapters, and using this feature we will suppress the atmospheric neutrino background considerably. We will discuss the case of atmospheric neutrino background suppression in detail in Chapters 6, 7 and 8.

Chapter 5

ICAL detector and simulation framework

In this chapter, we describe the ICAL detector and the related simulation framework which has been employed for the analyses presented in this thesis. The organisation of this chapter is as follows. In Section 5.1, we briefly discuss the proposed India-based Neutrino Observatory which will house the ICAL detector. Thereafter, in Section 5.2, we describe the features of ICAL in detail, including its detector geometry in Subsection 5.2.1, magnetic field in Subsection 5.2.2, and resistive plate chambers, which are the building blocks of ICAL, in Subsection 5.2.3. In Section 5.4, we discuss the ICAL simulation scheme, including the event generation scheme as well as muon track reconstruction algorithm. Thereafter, in Section 5.5, we describe the ICAL response to muons and present our results on muon reconstruction and charge identification efficiency, as well as muon momentum and angle resolution. Finally, in Section 5.6, where we layout the prescription on incorporating the ICAL detector response to obtain final events for further analysis.

5.1 India-based Neutrino Observatory

India-based Neutrino Observatory (INO) is a proposed underground research facility to be built in the southern part of India. INO will be located at Bodi West Hills (BWH) near Pottipuram village in Theni district of Tamil Nadu. The site has been chosen considering the geo-technical and environmental aspects of the hill and the adjacent area. The facility would comprise one large

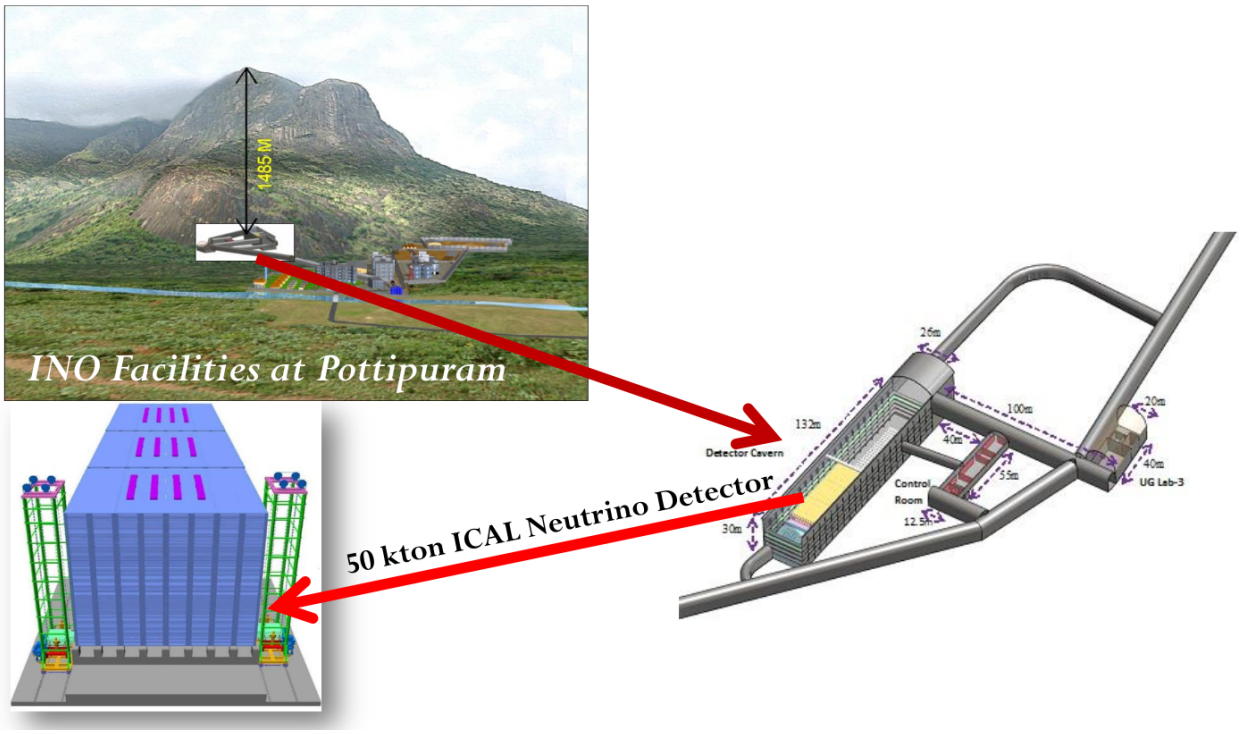

Figure 5.1: The Bodi West Hills (BWH) and the layout of INO facilities. Figure taken from Ref. [14].

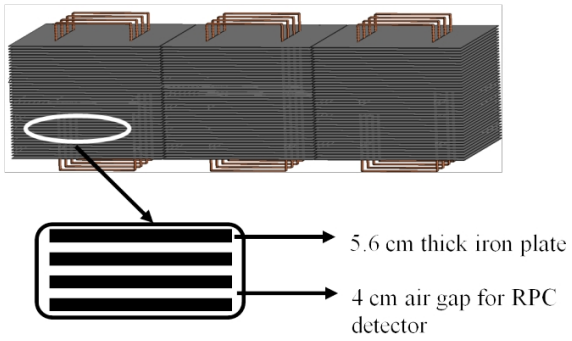

Figure 5.2: The three modules of ICAL detector. Each module dimension is 16 m (L) $\times$ 16 m (W) $\times$ 14.5 m (H). The axis along which the modules will be placed is defined as x-axis in ICAL coordinate system. The remaining traverse axis is labelled as y-axis. The vertical direction is labelled as z-axis. Each of the modules contain two vertical slots cut into it so as to enable the current carrying copper coils to be wound around them. Figure taken from Ref. [14].

and three small laboratory caverns with rock burden of 1000 m or more from all sides and with a vertical overburden of approximately 1300 m (Fig. 5.1). Such a rock burden causes reduction in the cosmic ray muon fluxes significantly and is crucial for the study of neutrino physics in an underground neutrino laboratory.

The main cavern ("UG-Lab 1") would house ICAL detector whose primary goal is to determine neutrino mass hierarchy and performing other precision studies with atmospheric neutrinos. The smaller caverns would house experiments dedicated to neutrinoless double beta decay, direct detection of dark matter, low energy neutrino spectroscopy, etc. In the next section, we describe the detector in detail.

5.2 The Iron Calorimeter

5.2.1 The detector geometry

The ICAL[1] detector will have a modular structure with a total lateral size of 48 m $\times$ 16 m, which is subdivided into three modules having base area of 16 m $\times$ 16 m each, with a gap of 20 cm between the modules. ICAL will have 151 layers of glass resistive plate chambers (RPCs) interspersed with 5.6 cm thick iron plates (Fig. 5.2), making the stack height to be 14.5 m. The vertical spacing between two iron plates is 4 cm, and the iron sheets have steel structures supporting them at every 2 m, in both x and y directions. The RPC units with dimension 1.84 m $\times$ 1.84 m $\times$ 2.5 cm are placed in a grid format between the two iron plates. In order to accommodate the support structures the RPC units have 16 cm horizontal gap between them. There are vertical slots at $x = x_0 + \pm 4$ m (x_0 is the central x value of each module) extending upto $y = \pm 4$ m and cutting through all the layers so as to accommodate the four copper coils that wind around the iron plates. The resultant magnetic field is in $x - y$ direction. The detector weighs $\sim$ 52 kt, excluding the weight of copper coils, and 98% of this weight comes from iron and only 2% from the glass RPCs. The steel support

[1]UG-Lab 1 would accommodate a 50 kt Iron CALorimeter (ICAL) detector and a possible ICAL-II neutrino detector of equal size. Each 50 kt ICAL would comprise three modules with dimensions of 16 m $\times$ 16 m $\times$ 14.5 m (L $\times$ W $\times$ H), so that the total footprint of both the detectors in that case would be 96 m (L) and 16 m (W).

ICAL	
No. of modules	3
Module dimension	16 m $\times$ 16 m $\times$ 14.5 m
Detector dimension	48 m $\times$ 16 m $\times$ 14.5 m
No. of layers	151
Iron plate thickness	5.6 cm
Gap for RPC trays	4.0 cm
Magnetic field	1.5 Tesla
RPC	
RPC unit dimension	1.84 m $\times$ 1.84 m $\times$ 2.5 cm
Readout strip width	3 cm
No. of RPC units/layers/module	64
Total no. of RPC units	2 30,000
No. of electronic readout channels	3.9 $\times$ 10^6

Table 5.1: ICAL at a glance

structures along with the copper coils form the bulk of the dead spaces of the detector. Table 5.1 shows the detector parameter specifications which have been used in the ICAL simulation.

The ICAL coordinate system defines X-direction to be the direction along which the modules are placed and the remaining horizontal transverse direction is labelled as Y-direction. As of now, X is also considered to coincide with South, since the final orientation of the INO cavern has not been decided. The vertically upward direction is labelled as z-axis, and the zenith angle 180° corresponds to $\theta = 0$ in the ICAL convention. The zero of the azimuthal angle ϕ points South. The origin is taken to be the centre of the second module.

5.2.2 The Magnetic Field

Each of the modules contain two vertical slots cut into it so as to enable the current carrying copper coils to be wound around them as shown in the Fig. 5.2. The iron plates would be magnetised to a field strength of about 1.5 T and through simulations it has been estimated that the strength is more than 1 T over at least 85% of the detector volume. This magnetisation gives ICAL a unique capability of charge identification for the oppositely charged particles will bend in the opposite directions in the presence of magnetic field. Particularly, we can distinguish between μ^+ and μ^- produced by $\bar{\nu_\mu}$ and ν_μ charged current interactions with the iron. With around 14000 iron plates

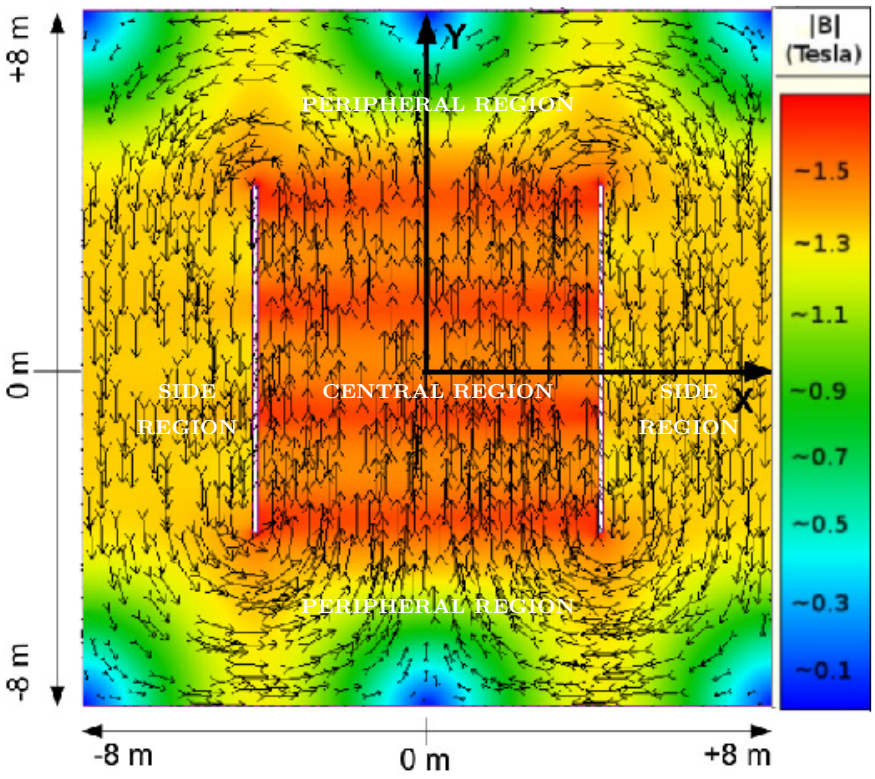

Figure 5.3: Magnetic field map in the central plate of the central module ($z = 0$). The length and the direction of the arrows indicate the strength and the direction of the field respectively. The magnitude is also shown in T in the colour palette. This map is generated using the MAGNET6 [15] software. Figure taken from Ref. [14].

of 2 m $\times$ 4 m area and 5.6 cm thickness, ICAL will be one of the world's largest electromagnet.

The simulation of the magnetic field is done by the collaboration (see Ref. [149] for details) using MAGNET6.26 software [15]. In Fig. 5.4, the magnetic field lines in the central iron plate near the centre of the second module is shown. The arrow direction and length (as well as the shading) indicate the magnetic field direction and the magnitude, respectively. The maximum magnitude of the magnetic field is about 1.5 T. The field direction can be seen to reverse direction on the two sides of the coil slots (beyond $x_0 \pm 4$ m) in the x direction. In the 'central region' of the detector, which is the 8 m $\times$ 8 m square area between the coil slots and in the $x - y$ plane, the field can be seen to be almost uniform in both magnitude ($\sim 10\%$) and direction. In the 'side' region, the region bounded as 4 m $\leq |x| \leq$ 8 m, the magnetic field is nearly uniform but in opposite direction to that of the central region. In the 'peripheral region', the region in the 4 m $\leq |y| \leq$ 8 m range, there is considerable variation in the magnitude and the direction of the magnetic field. However, the simulation results included in this thesis, assume the magnetic field to be uniform over the entire thickness of the iron plates at its each (x, y) position and has been generated for the centre of the iron plate, *viz.*, at $z = 0$. In the 4 cm air gap between the iron plates, the field is taken to be zero since it falls off drastically to several hundreds gauss in these regions in comparison to more than 1 T field strength inside the plates. The magnetic field for the steel support structures has also been taken to be zero as they are non-magnetic in nature. Since the magnetic field strength in the side and peripheral regions are either non-uniform or lower in magnitude and are also marred by edge effects, we restrict our simulation to the central region of the detector (-4 m $\leq x - x_0 \leq$ 4 m and -4 m $\leq y \leq$ 4 m), although the particles generated can subsequently travel outside this region and exit the detector. In our analysis, we have restricted the vertex position of the muons to be $z \leq$ 4 m. It should be noted that this choice (restricting ourselves to the central region), reduces the ICAL fiducial volume to be significantly less than 50 kt. However, for the analyses presented in this thesis, we will assume 50 kt of ICAL fiducial volume, therefore, for 10 years of ICAL running, the total exposure is 500 kt-years. Restricting the Geant4 simulation to the central volume of the ICAL detector where magnetic field is uniform, considerably simplifies the

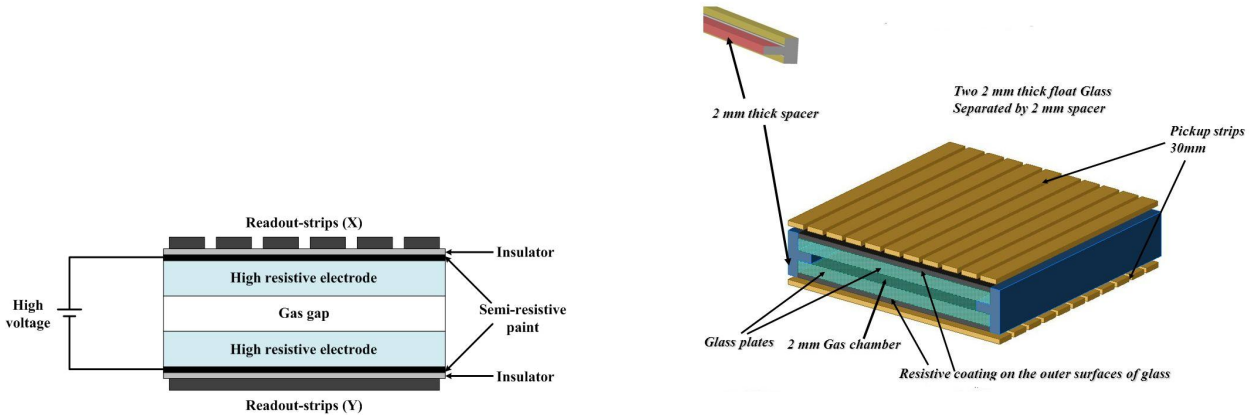

Figure 5.4: Schematic representation of an RPC. Figures taken from Ref. [14]

computation of ICAL's muon response. For the results presented in this thesis, an exposure of 500 kt-years have been assumed which can be achieved by increasing the exposure time suitably to compensate for smaller fiducial volume. Inclusion of the side and peripheral regions in the the simulation of ICAL detector demands careful consideration of magnetic field fringe effects. Such dedicated studies have been done by the other members of the collaboration [150]. Inclusion of simulations from side and peripheral regions would result in worsening the results, as efficiency in the side and peripheral regions are lower than that of central region.

5.2.3 Resistive Plate Chambers

RPC constitutes the active detector element and is made up of sealing two 3 mm thick glass sheets, with a gap of 2 mm between them using plastic edges and spacers. The glass sheets act as a high resistive electrodes and their outer surfaces are coated with a semi-resistive paint in order to apply high voltage electric field across the gas gap. Fig. 5.4 gives a schematic representation of an RPC. The RPCs will be kept in the gaps between the iron layers and will be operated in an avalanche mode at a high voltage of 10 kV. The gap in an RPC is filled with a gas mixture of Freon-R134A, isobutane, and trace amounts of SF_6 gas which flows continually through them. This particular gas mixture was chosen based on the optimisation studies done on glass RPCs being developed for ICAL detector. For operating the RPC detectors in avalanche mode, the optimised gas mixture comprises $C_2H_2F_4$ (1,1,1,2-Tetrafluoroethane and also known as R134A) 95.2% 4.5% Iso-butane

and 0.3% SF_6. Freon-R134A controls the avalanche development in the glass gaps, is slightly electronegative, and serves as the medium for the interaction of incident radiation. Ionisation of the gaseous mixture (predominantly Freon) creates signal ions and electrons. These could recombine and produce UV photons which could then cause spurious pulses elsewhere in the detector. Isobutane can absorb and convert the energy of photons into vibration states. Since Isobutane is a highly inflammable gas, its proportion is the gas mixture is kept below its inflammability limit. SF_6 is a strongly electronegative gas and acts as a quenching medium and reduces the formation of streamers thereby ensuring that the detector remains in avalanche mode of operation. When a charge particles passes through this gaseous mixture, it causes an ionisation and leaves a detectable signal. The gaseous mixture has been optimised so as to keep the signal localised and this location is used to determine the trajectory of the charged particle in the detector. The signal from RPC is collected using pick-up panels made up of copper sheets and foam. A charged particles induces a signal in the 150 micron thick copper sheet which is pasted on the inside on the 5 mm thick foam placed above and below the glass chambers. The foam provides the structural strength and electrical insulation to the RPC units. The copper sheet faces the glass RPC and there are a few layers of mylar sheet between the glass and the copper sheet which is scratched through to create strips of width 1.96 cm. The two copper sheets are places in such a way that their pick-up strips are orthogonal to each other and picks up the x and y location of the charged particle as it traverses the RPC, while the z information is provided by the RPC layer number. The time resolution of $\sim$ 1 ns gives ICAL the capability to distinguish between the upward and downward going particles. Noting down the hit pattern of the charged particles in the RPCs, one could reconstruct the energy as well as the direction of these particles. See Ref. [151] for more details.

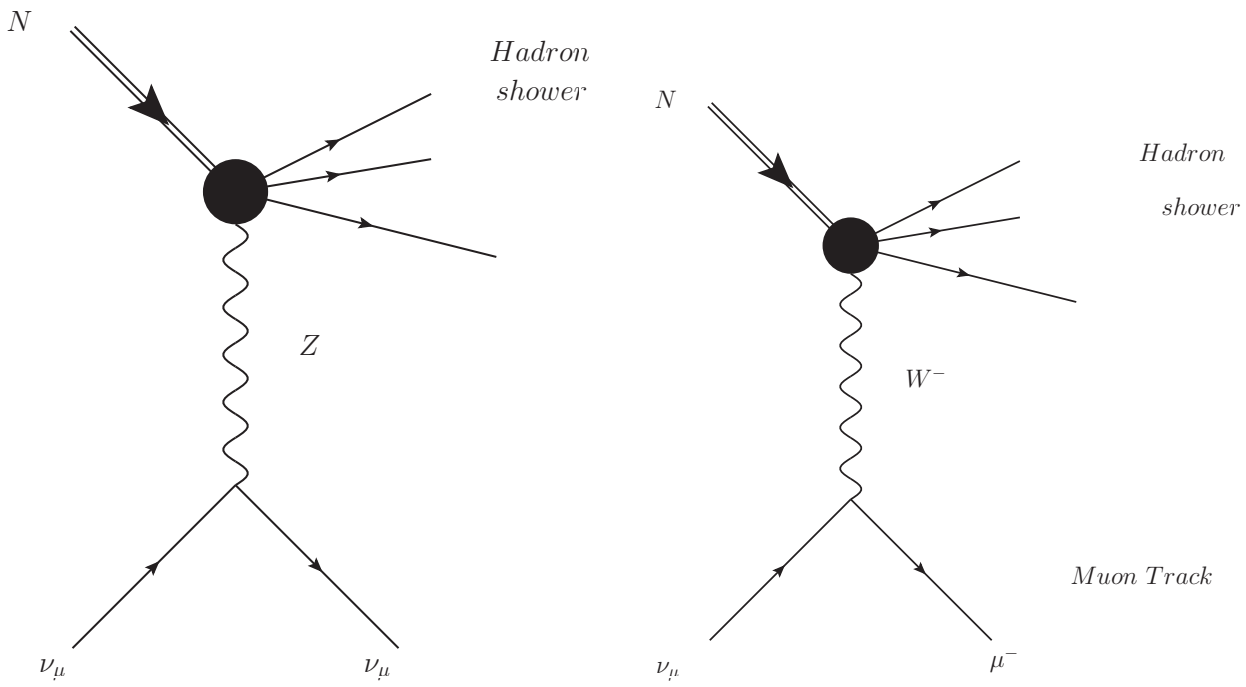

(a) NC events (b) CC events

Figure 5.5: NC and CC events.

5.3 Event generation at ICAL

5.3.1 Neutrino interactions and event generation

The neutrino and antineutrino interactions at ICAL detector are simulated using NUANCE version 3.5 [152] and GENIE version 2.8 [153] event generators. Neutrinos interact weakly with other particles and typical cross section for neutrino interactions is around 6 orders of magnitude smaller than the electromagnetic interactions. In weak interactions, the $W^{\pm}$ and Z^0 bosons are interchanged between quarks and leptons. Depending on the boson exchanged during the process, the neutrino interactions could be of the following two types :

- **Neutral current (NC) interactions** : In this process, Z^0 is exchanged as shown in Fig. 5.5a. The reaction is of the type

$$\nu_l + N \rightarrow \nu_l + N' + ...,$$

where N is a nucleon and N' is the final state nucleon with a modified momentum.

- **Charged current (CC) interactions** : Here, $W^{\pm}$ boson is exchanged and the Feynman diagram is shown in Fig. 5.5b. The reaction involved in this interaction is:

$$\nu_l + N \rightarrow l + N' + ...,$$

where l is a charged lepton of the same flavour as the incident neutrino.

For the work presented in this thesis, the neutrino energies considered are between 1-100 GeV. For this energy range, the following types of NC and CC interactions can take place in the detector :

1. quasi-elastic scattering (QE) for both charged and neutral current neutrino interactions with nucleons, and dominate for sub-GeV neutrino energies,

2. resonant processes (RES) with baryon resonance production for neutrinos between 1-2 GeV energy range,

3. deep inelastic scattering (DIS) processes, with considerable momentum (squared) transfer from the neutrino to the target nuclei, is a dominant mode of scattering in the multi-GeV region.

Enumerated above are the main processes of interest for ICAL detector. In CC neutrino interactions, we have charged leptons in the final state corresponding to the neutrinos in the initial state. In DIS events, usually in addition to the charged lepton and the recoil nucleon in the final state, there could be other particles, mostly pions, produced along with. Resonance interactions produce at most one pion along with the charged lepton. Among the charged leptons produced, electrons (associated with electron neutrino) are get absorbed in the thick iron plates, whereas, tau (associated with the tau neutrino[2] which are produced due to oscillation from other neutrino flavours) decays

[2]The neutrino fluxes due to WIMP annihilation will have strength similar to the muon neutrinos. Tau decay into muons with a branching ratio of $\sim 17\%$ and hence including this will improve the expected sensitivity of ICAL for indirect detection. However, we do not include tau events for the work presented in this thesis.

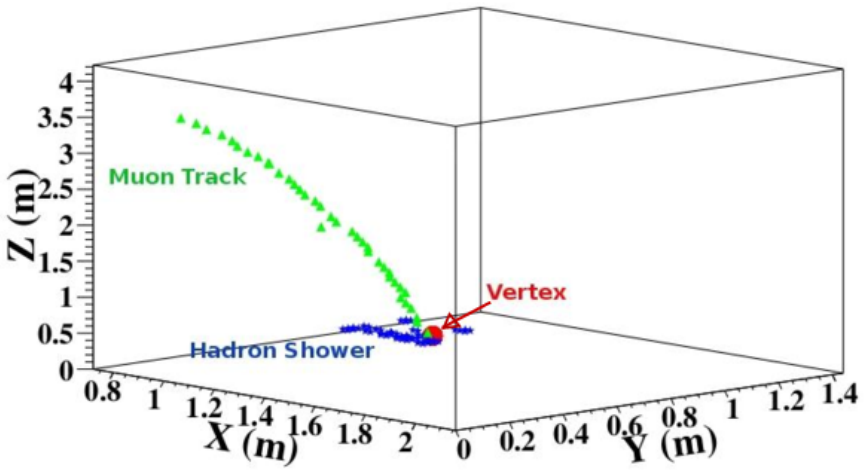

Figure 5.6: Sample track of a neutrino event with a muon track and hadron shower in the ICAL detector, where z = 0 indicates the central layer of the detector. Figure taken from Ref. [14].

to muon because of its short life time. Therefore, only muon (associated with muon neutrino) leaves a clean signature in the form of a track in the ICAL detector. ICAL, being magnetised, can distinguish between muons of opposite charges by bending them in opposite directions. Hadrons interacts via strong force and shower instead of tracks and require special techniques [154] for their momentum reconstruction. Fig. 5.6 shows a typical neutrino CC interaction producing an even with a clean muon track and the associated diffused hadron shower. NC processes are usually difficult to reconstruct as the energy of the final state is mostly contained in the neutrino which is unobservable directly. In order to reconstruct the properties of the incoming neutrino, one measures and reconstructs the momentum and direction of the outgoing muon and from which we reconstruct the momentum and direction of parent neutrino. Adding the information on hadron energy improves the ability of the experiment to reconstruct the energy of the incoming neutrino. Inclusion of hadron events improves the mass hierarchy sensitivity of the experiment as shown in Ref. [154]. However, for the results presented in this thesis, we have performed analyses in terms of muons only.

Both NUANCE and GENIE neutrino event generators have been suitably modified by the INO collaboration. NUANCE contains a simple ICAL geometry, mainly the iron and glass components of the detector. GENIE on the other hand has been provided with a detailed ICAL geometry

comprising 151 layers of glass RPCs, interspersed iron plates, the gaseous mixture and also the plastic components. We have used GENIE for the work on the indirect detection of dark matter presented in Chapters 6, 7 and 8, whereas for the analysis presented in Chapter 9 we have used NUANCE.

The neutrino event generators calculate event rates by integrating different cross sections weighted by the fluxes for all the charged current (CC) and neutral current (NC) channels at each neutrino energy and angle.

5.3.2 Event Reweighting

The event generation in both the cases have been done for 1000 years of ICAL running so as to reduce the Monte-Carlo fluctuations and then scaled down to 10 years at the stage of data analysis. Running neutrino event generators for such large event sample takes a very long time. Running events for different set of oscillation parameters is extremely time consuming and practically impossible. Therefore, we generate events with both the generators for the case of no oscillation and thereafter apply a reweighting algorithm which gives final event sample for a given set of oscillation parameters. The reweighting algorithm works through the following scheme:

A ν_μ event generated with the neutrino event generator is characterised by true energy and true zenith angle for both the muon and the neutrino associated to that event. For each neutrino, with a given true energy and zenith angle, survival oscillation probabilities $P_{\mu\mu}$ and transition oscillation probability $P_{\mu e}$ are calculated numerically for a specified set of oscillation parameters. Thereafter, a random number R is generated between $0-1$ and if $R < P_{\nu_\mu\nu_e}$ the event is classified to be a ν_e event. If $R > P_{\nu_\mu\nu_e} + P_{\nu_\mu\nu_e}$, then it is classified to be a ν_τ event. The case $P_{\nu_\mu\nu_e} \geq R \leq P_{\nu_\mu\nu_e} + P_{\nu_\mu\nu_e}$ signifies that the event has occurred due to ν_μ which has survived. We select such events and use it in our analysis. Such event selection of a statistically large number of event sample yields ν_μ survived sample which follows the ν_μ survival probability to a high precision. Muon events can also arise due to oscillation of ν_e into ν_μ. To calculate such events, we generate events at ICAL with ν_e fluxes but using ν_μ CC interaction cross sections. In order to get the oscillated

events from this sample, we generate another random number S and use a similar scheme as above. If $S < P_{\nu_e\nu_\mu}$, then this event is selected as an "oscillated" ν_μ event. The total ν_μ events at ICAL is the sum total of "survived" and "oscillated" events. Reweighting exercise is similarly applied on $\bar{\nu}_\mu$ events producing μ^+.

5.4 ICAL Simulation Framework

In this section, we describe the ICAL simulation scheme based on Geant4 framework. Fig 5.7 shows the INO simulation and analysis flowchart. We discussed neutrino event generation in the previous section. We will discuss event simulation, digitisation and reconstructed, as incorporated in the ICAL code, in the following subsections.

5.4.1 Event simulation and digitisation

Neutrino interactions within the detector material produces muons and hadrons. The propagation of such particles through the detector volume is simulated using an ICAL code based on Geant4.9.4.p02 [2] framework. The ICAL geometry is provided in form of machine readable gdml files and it includes details of the RPC detector components, the support structure and the gas composition described above. For Geant4 simulations, the pick-up strips are considered as a continuous material, however for signal digitization the strips are considered independently. A charged particle like a muon passing through an RPC produces a signal in the pick up strips whereby they are assigned appropriate x or y values. Also, depending on the RPC layer, z value is assigned and also a time stamp t. The threshold energy for a charged particle to produced an electron-ion pair in the RPC gap is taken to be 30 eV with an average efficiency of 95%. Digitisation is the process that translates the global coordinates of the signals into information of the $X^{th}x$ strip and the $Y^{th}y$ strip at the Z^{th} plane. These digitised signals along with the timestamp are called "hits".

In the horizontal plane, the spatial resolution is of the order of 0.6 cm because of the strip width. In the vertical plane (z direction) the resolution is of the order of 1 mm due to the gas gap

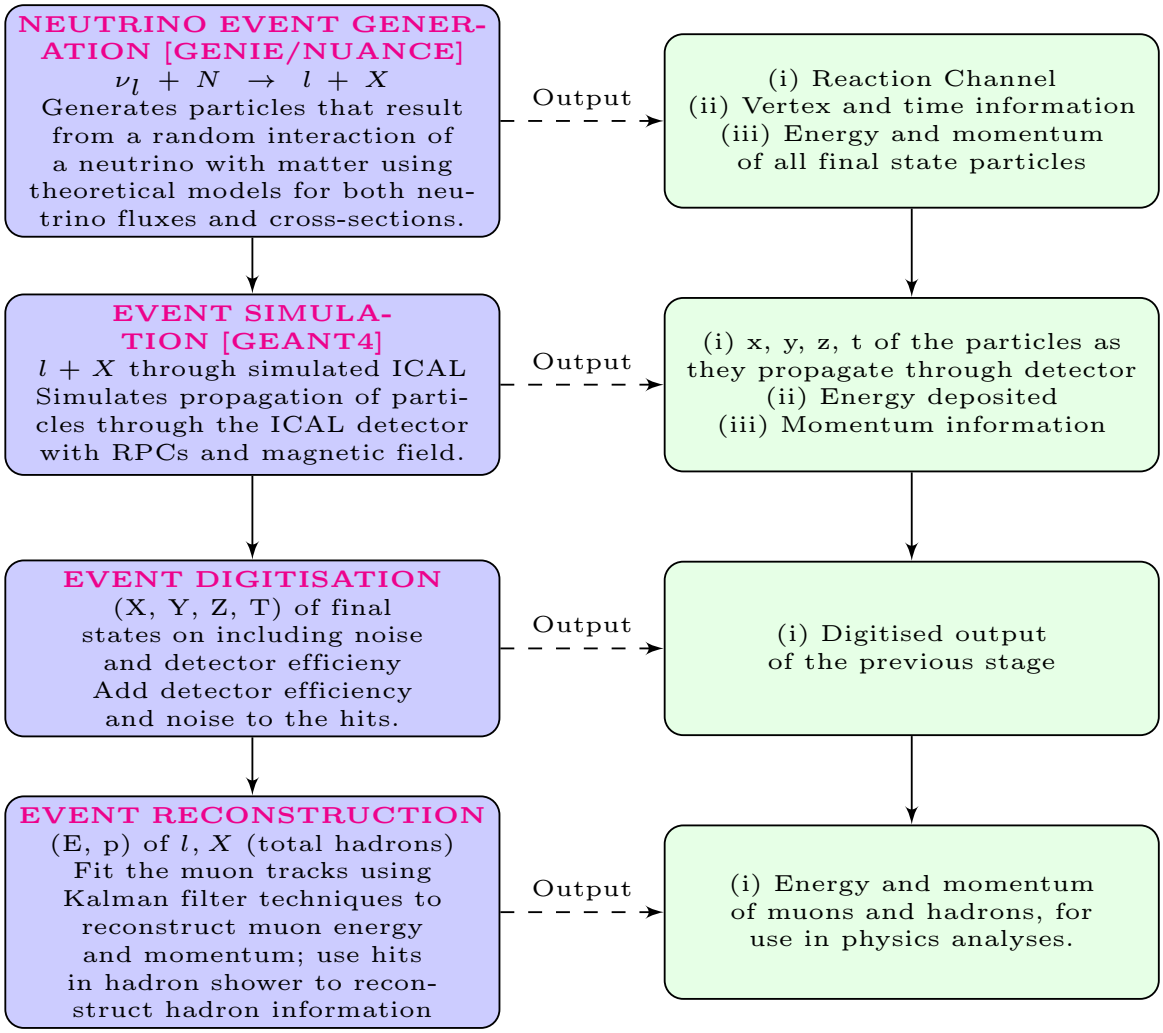

Figure 5.7: The INO simulation and analysis framework.

between the glass plates in the RPCs. X and Y strip informations are independent and all the possible pair of X and Y hits in a plane are combined to form a cluster.

5.4.2 Event reconstruction

Muons, being minimum ionising particle leave a long clean track while traversing through the detector. As muons propagate through layers, the magnetic field causes it to bend and the muon momentum can be determined from the curvature of its trajectory by measuring its path length. The time resolution of RPCs is of the order of a nanosecond and that allows ICAL to distinguish between the upgoing and down going muons. ICAL detector is well suited to muon detection and reconstruction of its properties. Hadrons, however, are difficult to be reconstructed individually since the response of the detector to different hadrons is rather similar. In principle, only an averaged information on the energy and direction of the hadrons can be reconstructed. Also, hadrons due to their interaction nature travel relatively shorter distances in the detector. In this thesis, our focus is on muons. To reconstruct the muon momentum ICAL code uses a track finding algorithm which is followed by a track fitting algorithm that reconstructs both the momentum and charge of the muon using the local magnetic field.

Track finder

This algorithm takes clusters which are the combinations of all possible pairs of nearby X and Y hits in a Z-plane. A 'tracklet' is defined as a set of clusters generated in three successive layers. The track fitting algorithm resorts to simple curve fitting to look for possible tracklets by searching for clusters in three adjacent planes. Due to inefficiency of a particular plane, there could be no hit in that layer and in that case, the track finding algorithm expands it search to next adjoining planes. A typical neutrino CC events consists of a long muon track and a hadron shower near the vertex. Muons leave only 1-2 hits per layer whereas hadrons leave several hits per layer and hence hadron shower separation involves use of the average number of hits per layer in a given event. The algorithm tends to match the end of tracklets to form longer tracks and find the longest possible track through several iterations. The track finding algorithm thus forms muon tracks as an array

of three dimensional clusters. In cases where there are more than two tracks, the longest track is taken to be the muon track. The averaged over X and Y timings in a plane is over to determine the direction (up/down) of the track. Muon tracks which have at least 5 hits in the event are chosen and the clusters in the layer are averaged to one single hit per layer and the corresponding coordinate and timing information is forwarded to track fitter for further analysis. This criterion translates to minimum momentum of 0.4 GeV/c for a nearly vertical muon, below which no track is fitted.

Track fitter

The track fitter is a Kalman-filter based algorithm and is used to fit the tracks based on the curvature of tracks due to the effect of magnetic field. For each track, we take an identifying starting vector $X_0 = (X, Y, dX/dZ, dY/dZ, q/p)$ which contains the coordinate information of the first hit (X, Y, Z) as recorded by the track finder, with the charge-weighted inverse momentum q/p taken to be 0. As the curvature of tracks is negligible in the starting section, the initial direction of the track i.e. the slopes of $dX/dZ, ddY/dZ$ is determined from the first two layers. Using the standard Kalman-filter algorithm, this initial state vector is extrapolated to the next layer. This involves calculation of Kalman gain matrix by making use of the information of the local magnetic field, geometry, composition of the matter through which the particle propagates and the observed cluster position in that layer. In ICAL code, the state prediction is based on the Kalman filter algorithm and the corresponding error propagation is carried out by a propagator matrix [155]. The state extrapolation takes care of process noise due to multiple scattering [156], energy loss in matter, mostly in iron, and in accordance to the Bethe formula [157]. The extrapolated point is then compared to the actual hit position, if any, registered by that layer and then this process undergoes iteration. This iteration also obtains the best fit to the track. Thereafter, the extrapolated track is extrapolated backwards to another half-layer of iron since the interaction would have most likely taken in the iron. This step is needed to determine the vertex of the neutrino interaction and the best fit value of the muon momentum at the vertex is returned as the reconstructed momentum both in terms of energy and direction. The condition $\chi^2/ndf < 10$ for the fits is imposed to qualify as a properly fitted track which are then accepted for analysis. The magnitude of the muon momentum

at the interaction vertex is determined by q/p and the direction is reconstructed using dX/dZ and dY/dZ which yield the zenith (θ) and the azimuthal (Φ) angles of the track. The next section describes in detail the response of ICAL detector to muons.

5.5 ICAL response to muons

The detector efficiencies and resolution functions are needed to simulate the signal and background events in terms of muon reconstructed energy and muon zenith angle. To obtain the ICAL response to muons, simulation of muon events was done on Geant4 framework and the simulated events were then further analysed with ROOT [158] based C++ code. The study of the detector resolutions and efficiencies closely follows the simulation procedure carried out previously by the collaboration [78]. However, the earlier simulation was done for muon energies of up to 20 GeV. In this work we extend the range of muon energy E_μ beyond 20 GeV upto 100 GeV. In our convention, the cosine of the zenith[3] angle $\cos\theta = 1$ represents an upward going muon, whereas $\cos\theta = -1$ indicates a downward going muon. We take 37 E_μ bins of variable bin-width between 1 and 100 GeV, finer bins for low energies and coarser for high energies, and 20 $\cos\theta$ bins. 10,000 muon events are generated for a fixed E_μ and $\cos\theta$, separately for μ^+ and μ^-. The vertices of these events were smeared over the central region (as defined in [78]) of ICAL. In each case, the azimuthal angle (ϕ) was uniformly averaged over the range $-\pi \leq \phi \leq \pi$.

5.5.1 Reconstruction efficiency

Reconstruction efficiency (ε_{rec}) for each $\mu(E_\mu, \cos\Theta)$ event is given by the ratio of total number of events properly reconstructed (η_{rec}) and total number of events generated in the central region of the detector (η_{total}) i.e. $\varepsilon_{rec} = \frac{\eta_{rec}}{\eta_{total}}$. Fig. 5.8 shows the reconstruction efficiencies of the muon events as a function of E_μ for various $\cos\theta$ values. The left and right figures are for μ^- and μ^+, respectively. We can see from the figure how the reconstruction efficiency depends on the true

[3] In many places in the literature this is indeed referred to as the nadir angle, and rightly so. However, we will continue to following the convention adopted in all previous the INO simulation papers.

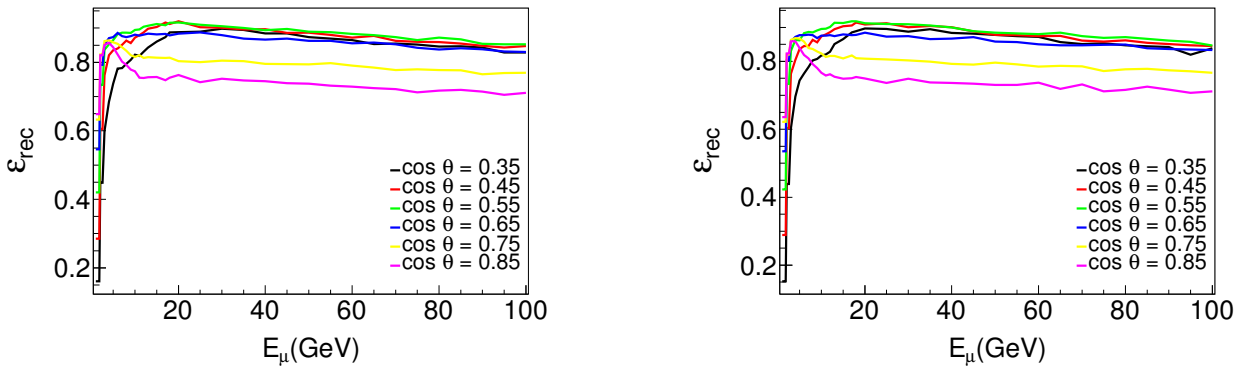

Figure 5.8: LEFT: Reconstruction Efficiency for μ^- at ICAL. RIGHT: Reconstruction efficiency for μ^+ at ICAL

energy and true zenith angle of the muon. The efficiency is seen to initially rise with muon energy, reach a peak at about $E_\mu \sim 10$ GeV, after which it is seen to fall, albeit extremely slowly. The reconstruction efficiency increases for all $\cos\theta$, with an increase of muon momentum from 1 GeV. This is due to the fact that the number of hits increase as the particle crosses more layers. For the slanting angles, there are fewer hits and hence the efficiency at a given momentum is expected to be better for larger values of $\cos\theta$ and the same trend can be seen from Fig. 5.8. However, there is a slight worsening of the efficiency for all angles beyond 10 GeV which is seen as a slow fall in Fig. 5.8. This is due to the selection criterion chosen which dictates that the event should reconstruct exactly one track. At larger muon momenta and large angles, there is a possibility that two portions of a track on either side of a dead space (such as a support structure) are reconstructed as two separate tracks. The reconstruction code is being improved to retrieve such events [155]. With a correct reconstruction, we expect that the efficiency would saturate rather than fall off at high muon momenta.

5.5.2 Charge Identification efficiency

Charge identification efficiency (ε_{CID}) is defined as the ratio of the events with correctly identified charges(η_{CID}) to the total reconstructed (η_{rec}) events: $\varepsilon_{CID} = \frac{\eta_{CID}}{\eta_{rec}}$. Fig. 5.9 shows the CID reconstruction efficiencies of the muon events as a function of E_μ for various $\cos\theta$. Again, the left and right figures are for μ^- and μ^+ respectively. The charge identification efficiency is seen

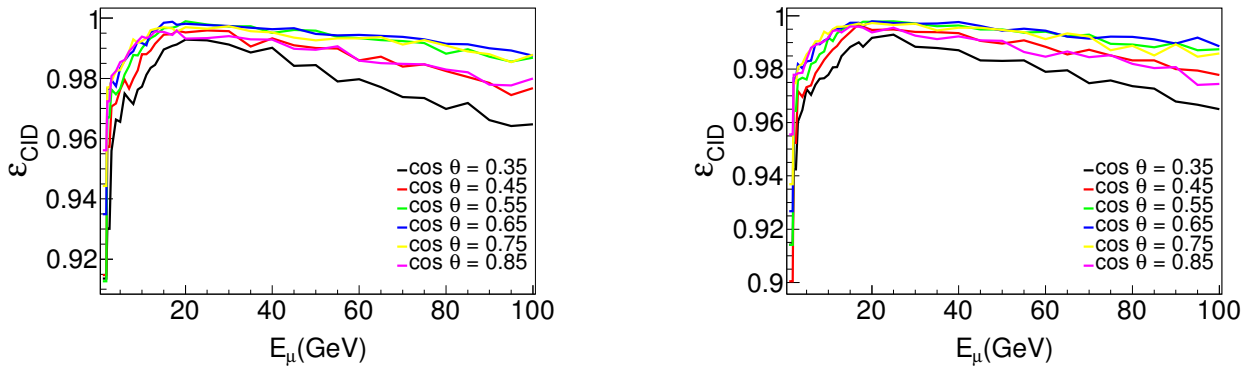

Figure 5.9: LEFT: Charge identification reconstruction efficiency for μ^- at ICAL RIGHT: Charge identification reconstruction efficiency for μ^+ at ICAL

increase until $E_\mu \sim 20$ GeV and thereafter fall. The dependence on the muon zenith angle is again seen to be complicated. Fig. 5.9 reveals that in the energy region of our interest, *i.e.*, $E_\mu = (1-100)$ GeV, the charge identification efficiency in ICAL is better than 96% for all muon zenith angles.

5.5.3 Muon momentum resolution

In order to obtain the muon energy resolutions, the reconstructed momentum distributions for μ^- (and μ^+) are plotted as a function of E_μ for a given true E_μ and true muon $\cos\theta$ value, and then fitted with a Gaussian function to get the σ_E of the distribution. We define the muon energy resolution (σ_E) in terms of width σ'_E of the distribution of the reconstructed energy as $\sigma_E = \sigma'_E/E_\mu$, where E_μ is the true muon energy.

The left panels of Fig. 5.11, Fig. 5.12 and Fig. 5.13 show the reconstructed momentum distribution for true muon $\cos\theta = 0.65$ and true muon energy E_μ = 1, 10 and 100 GeV, respectively. One can clearly see an asymmetric tail in each of these cases. Also, the tail is more pronounced for energies 1 GeV and 100 GeV than 10 GeV case. The distributions in these figures are fitted with two functions - Gaussian probability distribution function and a convolution of Gaussian and Landau probability distribution functions. The fitting by the convolution of Gaussian and Landau function (shown in blue) is seen to be better in terms of χ^2/ndf than fitting the distribution using a pure Gaussian function (shown in red). In the previous studies done by the collaboration [78], the fitting was the convolution of Gaussian and Landau probability distributions for low true mo-

mentum muon events *i.e.* $E_\mu \leq 2$ GeV and for higher true momentum muon events fitting was done with a pure Gaussian function. However, in this work, for the sake of simplicity, the fitting has been done with pure Gaussian functions only for the entire range 1-100 GeV. We do not expect any significant loss in sensitivity due to this simplifying assumption.

It should be noted that the response of the ICAL detector has been averaged over the entire azimuth. This is done for the sake of simplicity. However, for a same zenith angle, $\cos\theta$, muons with different azimuthal angles have different response. The ϕ dependence of the muons is a cumulative consequence of the following: the coil gaps (that are located at $x = x_0 \pm 400$ cm where x_0 is the centre of each module in the x direction); the support structures (which differ in dimensions in the x and y directions); and the orientation of the magnetic field.

To understand the ϕ dependence of muons, let us consider a muon initially directed along the y-axis will experience less bending since its momentum component is in the plane of the iron plates (hence-after referred to as in-plane momentum) is parallel to the magnetic field as can be seen from Fig. 5.6. Further, an upward-going μ^+ in the negative (positive) x direction experiences a force in the positive (negative) z direction. For μ^- the direction of forces will be opposite. This implies that, for the same energy and zenith angles, the muons with $\phi > \pi/2$ traverse more layers than muons with $\phi < \pi/2$ and hence are better reconstructed. This is illustrated in Fig. 5.10 which shows the case of two muons (μ^+), having same energy and zenith angle, injected at the origin along two different azimuth angles. The two muons bends differently, thereby traversing different number of layers and even though they have roughly the same path length, they would exhibit different detector response. This suggests that the momentum resolution is best studied in different azimuthal angle bins as done in Ref. [78] where it has been shown that the fits to the distributions vastly improve in terms of χ^2/ndf. However, taking a simpler approach, in this work while calculating the detector response to muons, we combine events from all azimuthal bins.

The left panel of Fig. 5.14 shows the reconstructed momentum distribution for μ^- for true muon $E_\mu = 25$ GeV and true muon $\cos\theta = 0.85$. The fitted value of σ_E can be read off from the figure. This process is repeated for all values of the true muon energy and true muon zenith

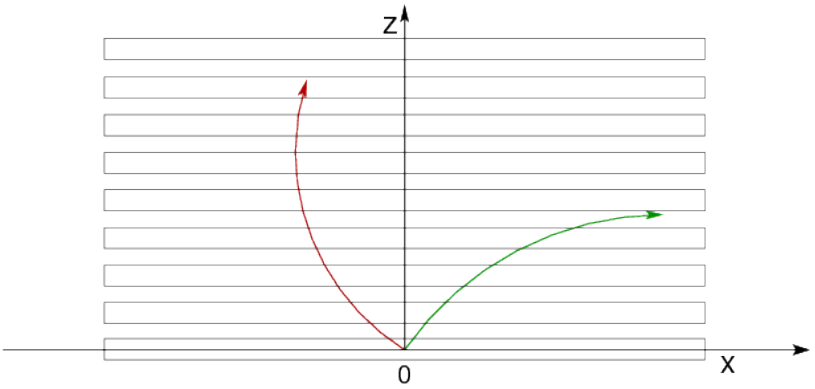

Figure 5.10: Schematic showing tracks for two muons (μ^+) in the $x-z$ plane for the same values of incident muon energy and muon zenith angle, but with $\phi < \pi/2$ (shown in red and has a momentum component in the positive x direction) and other with $\phi > \pi/2$ (shown in green and has a momentum component in the negative x direction). The difference in bending causes the muons to traverse different layers will results in difference in their track reconstruction accuracy, thereby resulting in a ϕ dependence of muon response to the detector.

angle. The left panel of Fig. 5.15 shows the RMS width (which is FWHM/2.35) obtained using Gaussian probability distribution σ'_E for μ^- as a function of true muon energy E_μ and for the full set of values of $\cos\theta$, while the right panel shows the corresponding plots for μ^+. Similarly, the left panel of Fig. 5.16 shows the σ_E for a μ^- as a function of true muon energy E_μ and for the full set of values of $\cos\theta$, while the right panel shows the corresponding plots for μ^+.

From the Fig. 5.16, it can be seen that initially (upto about 6 GeV), the resolution improves with increasing the muon energy. This holds true for all the zenith angles. This is due to the following reason. Starting with small muon energies, with the increase in muon energy, the muons traverse more number of RPC layers, thereby increasing the number of layers and hits. Additionally, the magnetic field bends the tracks appreciably resulting in increase in accuracy of momentum reconstruction leading to an improvement in energy resolution. However, as the particle momentum is increased further, it begins to exit the detector, so that only a partial track is contained in the detector. This consists of relatively straight sections since the radius of curvature increases with momentum, resulting in a poorer fit. This results in worsening of the muon energy resolution with the increase in the input energy. It also seen that the resolution is relatively poor for the muon tracks with smaller $\cos\theta$ than the ones with larger $\cos\theta$ for the entire energy considered. This is

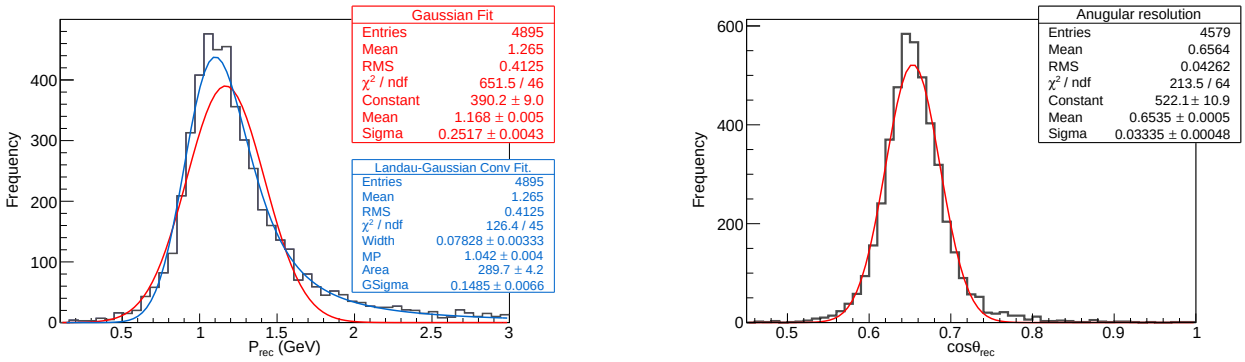

Figure 5.11: LEFT: Reconstructed momentum distribution for μ^- at ICAL. RIGHT: Reconstructed cosine of zenith angle distribution for μ^- at ICAL. Both the distributions are for μ^- with true $E_\mu = 1$ GeV and $\cos\theta = 0.65$.

due to the fact that horizontal muon tracks will have less number of hits in the RPCs than at more vertical angles. This is a consequence of the detector geometry and hence ICAL is not so sensitive to very horizontal muons.

5.5.4 Muon zenith angle resolution

To obtain the muon zenith angle resolution we use a similar procedure. The right panel of Fig. 5.17 shows the reconstructed zenith angle distribution for μ^- for true muon $E_\mu = 25$ GeV and true muon $\cos\theta = 0.85$. The width of the distribution gives $\sigma_{\cos\theta}$ which is extracted from the fit and the steps repeated for all values of true muon energy and true muon zenith angle to get the full table. The left panel of Fig. 5.17 shows the $\sigma_{\cos\theta}$ for μ^- as a function of true muon energy E_μ and for the full set of values of $\cos\theta$, while the right panel shows the corresponding plots for μ^+.

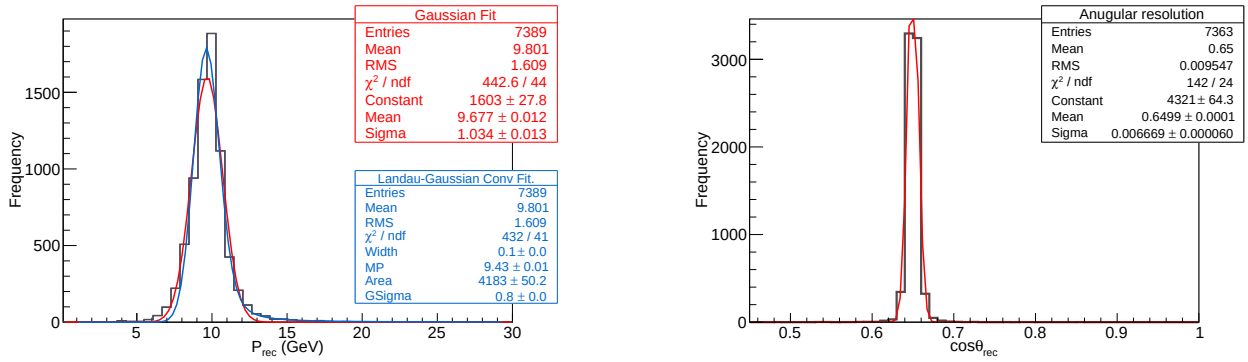

Figure 5.12: LEFT: Reconstructed momentum distribution for μ^- at ICAL. RIGHT: Reconstructed cosine of zenith angle distribution for μ^- at ICAL. Both the distributions are for μ^- with true $E_\mu = 10$ GeV and $\cos\theta = 0.65$.

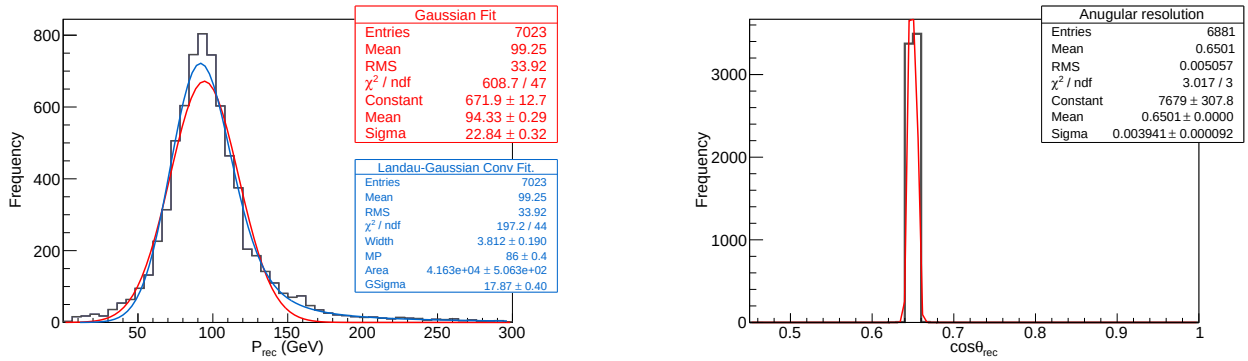

Figure 5.13: LEFT: Reconstructed momentum distribution for μ^- at ICAL. RIGHT: Reconstructed cosine of zenith angle distribution for μ^- at ICAL. Both the distributions are for μ^- with true $E_\mu = 100$ GeV and $\cos\theta = 0.65$.

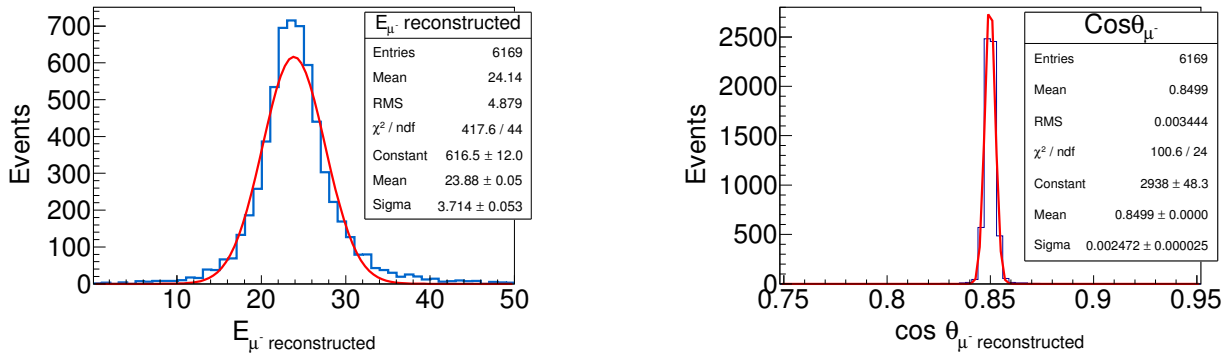

Figure 5.14: LEFT: Reconstructed momentum distribution for μ^- at ICAL. The energy resolution(σ_E) is given by σ'_E/E, where σ'_E is the width obtained by fitting this with Gaussian probability distribution functions. RIGHT: Reconstructed cosine of zenith angle distribution for μ^- at ICAL. Angular resolution is given by $\sigma_{cos\theta}$ which is the width obtained by fitting it with Gaussian probability distribution functions. Both the distributions are for μ^- with true $E_\mu = 25$ GeV and $\cos\theta = 0.85$.

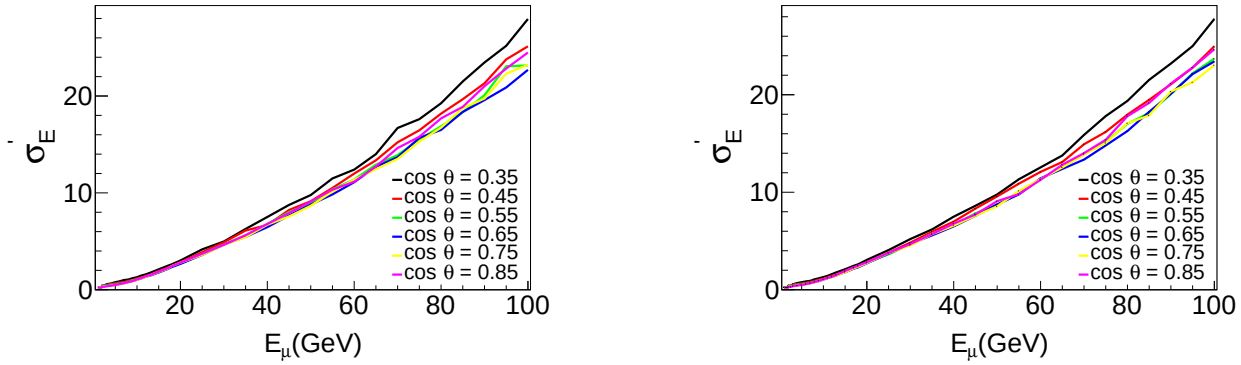

Figure 5.15: LEFT: RMS width for μ^-. RIGHT: RMS width for μ^+ at ICAL

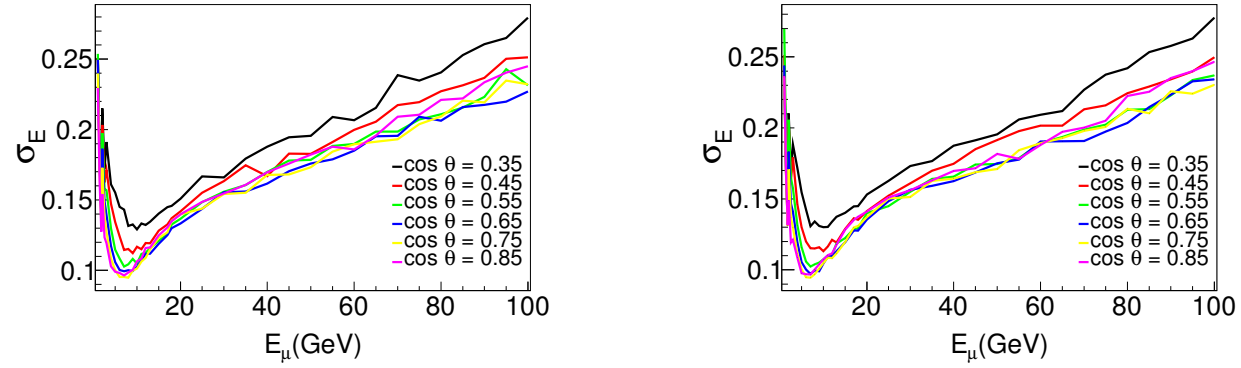

Figure 5.16: LEFT: Momentum resolution for μ^-. RIGHT: Momentum resolution for μ^+ at ICAL

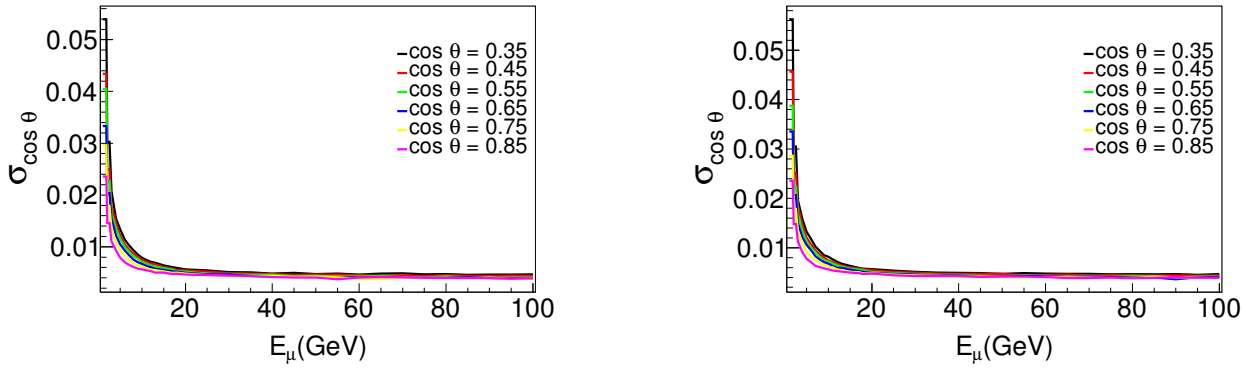

Figure 5.17: LEFT: $\cos\theta$ resolution for μ^- at ICAL. RIGHT: $\cos\theta$ resolution for μ^+ at ICAL

5.6 Folding events with detector efficiency and resolution functions

The raw events, *i.e.*, the events from the generator stage[4], are then folded with detector energy and angle resolutions, as well as, reconstruction and charge identification efficiencies to get the final events. These muons are binned in reconstructed energy and zenith angle bins. The results in Section 5.5 show that the energy and the angle resolutions for the muons are functions of both muon energy and muon zenith angle. Same is true for the charge identification efficiency and reconstruction efficiency. The detector efficiencies obtained as such and shown in Figs. 5.8 and 5.9 are then implemented onto the signal and background events as follows:

$$N_{ij}^{'th} = \mathcal{N} \sum_k \sum_l K_i^k(E_T^k) M_j^l(\cos\Theta_T^l) \left(\varepsilon_{kl}\mathcal{C}_{kl} n_{kl}(\mu^-) + \bar{\varepsilon}_{kl}(1-\bar{\mathcal{C}}_{kl}) n_{kl}(\mu^+)\right) \tag{5.1}$$

where the indices i and j denote the measured energy and zenith angle bin of the muon, $\mathcal{N}$ is the normalisation corresponding to a specific exposure in ICAL, E_T^k and $\cos\Theta_T^l$ are the true (kinetic) energy and true zenith angle of the muon, where the indices k and l denote the true energy and true zenith angle bin of the muon. The quantities $n_{kl}(\mu^-)$ and $n_{kl}(\mu^+)$ are the number of μ^- and μ^+ events in the k^{th} true energy and l^{th} true zenith angle bin, respectively. The quantities ε_{kl} and $\bar{\varepsilon}_{kl}$

[4]These include the events after applying reweighting algorithm or background suppression scheme, whichever is applicable to the data set.

are the reconstruction efficiencies of μ^- and μ^+ respectively for the k^{th} energy and the l^{th} zenith angle bin. $\mathcal{C}_{kl}$ and $\bar{\mathcal{C}}_{kl}$ are the corresponding charge identification quantities.

The muon energy and angle smearing are then implemented by folding in the Gaussian resolution functions K_i^k and M_j^l in Eq. (5.1). These are given as,

$$K_i^k = \int_{E_{L_i}}^{E_{H_i}} dE \frac{1}{\sqrt{2\pi}\sigma_E} \exp\left(-\frac{(E_T^k - E)^2}{2\sigma_E^2}\right) , \tag{5.2}$$

$$M_j^l(\cos\Theta_T^l) = \int_{\cos\Theta_{L_j}}^{\cos\Theta_{H_j}} d(\cos\Theta) \frac{1}{\sqrt{2\pi}\sigma_{\cos\Theta}} \exp\left(-\frac{(\cos\Theta_T^k - \cos\Theta)^2}{2\sigma_{\cos\Theta}^2}\right) , \tag{5.3}$$

where E and $\cos\Theta$ are the measured (kinetic) energy and zenith angle of the muon and the values of σ_E and $\sigma_{\cos\Theta}$ are given in Figs. 5.16 and 5.17, respectively. Similar expressions can be written for the μ^+ events. The folded events are then used for further analysis.

Chapter 6

Searches for DM annihilations in the sun

We calculated neutrino fluxes at ICAL due to annihilation in the sun in Section 3.1. In this chapter, we present prospects of detecting neutrinos at ICAL due to WIMP annihilation in the sun. The neutrinos produced due to WIMP annihilation deep inside the sun, will undergo oscillations, interactions and regeneration as they propagate out of the core. These signal neutrinos, on reaching the detector, interact with the medium and produce corresponding charged leptons.

We carry out a detailed background suppression study in order to reduce the atmospheric neutrino background, which pose a serious background to indirect detection of WIMPs. The other source of neutrinos such as solar neutrinos and terrestrial neutrinos are in MeV range and hence easily distinguishable. There is another source of background where high energy neutrinos are produced in reactions when cosmic rays hit the solar corona. However, this background is of order of a few neutrino events per year [159], and we ignore them for our present analysis. We consider WIMP masses in the range from 3 GeV to 100 GeV and for several annihilation channels, assuming 100 % branching ratio for each. We perform a χ^2 analysis and present exclusion C.L. contours in the WIMP mass - WIMP-nucleon scattering cross-section plane.

The chapter is organised as follows. In Section 6.1, we describe the atmospheric background suppression scheme. We also present the expected event spectrum at ICAL, due to WIMP annihilation through several channel, along with the suppressed atmospheric neutrino background for each case. In Section 6.2, we describe our statistical analysis. We present our main results in Section 6.3

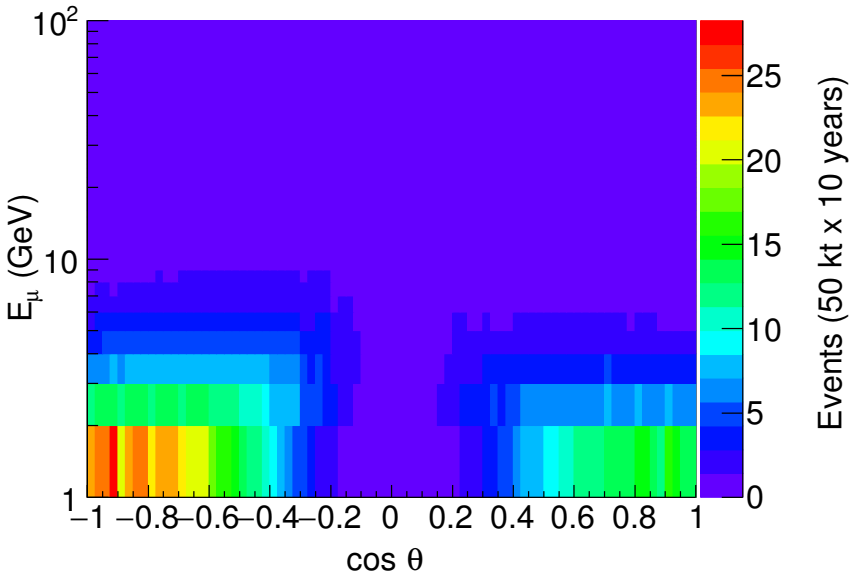

Figure 6.1: The μ^- event distribution at ICAL due to atmospheric neutrino background for 500 kt-years of ICAL exposure. ICAL has zero efficiency for horizontal tracks which is reflected in the bins around $\cos\theta = 0$. Note that $\cos\theta = 1$ represents upward going muons in ICAL convention.

and finally conclude in Section 6.4.

6.1 Atmospheric neutrino background suppression

Using the atmospheric neutrino fluxes for Theni site as shown in Chapter 4 and the event generation prescription from Chapter 5, we generate the expected event spectrum at ICAL. Fig. 6.1 shows the reconstructed μ^- event distribution due to atmospheric neutrino background. These neutrinos have energies similar to those of neutrinos from WIMP annihilation for WIMP masses 3-100 GeV and hence atmospheric neutrino events are indistinguishable from indirect detection events in ICAL. However, there are two features in which the signal neutrinos are different from the atmospheric neutrinos. Firstly, the signal flux, as we had seen in Section 3.1, has an energy dependence that is quite different from the energy dependence of the atmospheric neutrinos which falls sharply as $\sim E_\nu^{-2.7}$. Therefore, an analysis binned in energy should be able to discriminate between the two kinds of events. More importantly, unlike the neutrinos from WIMP annihilation which come from the direction of the sun, the atmospheric neutrinos have a distribution over all zenith and azimuth

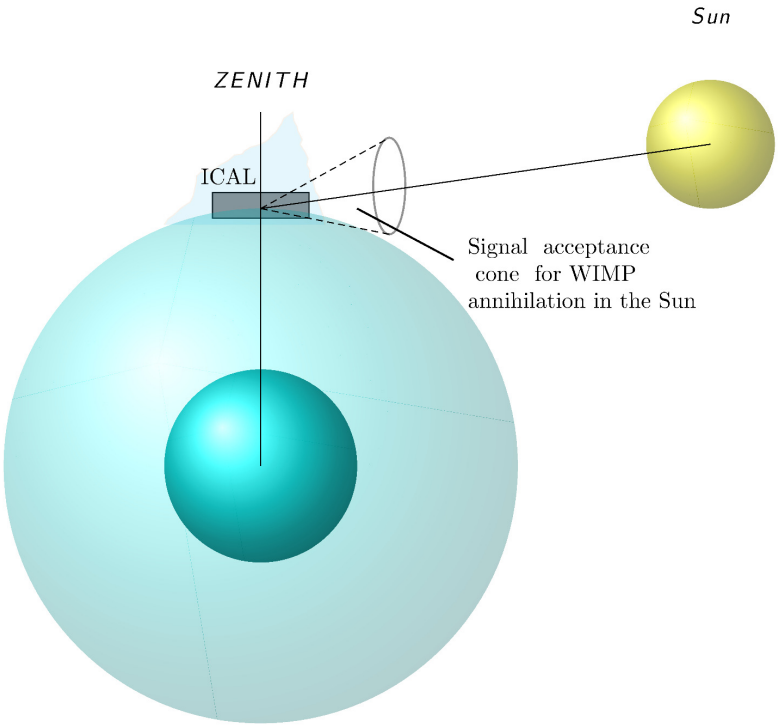

Figure 6.2: The cone regions where signal from the WIMP annihilations are expected for the sun.

angular bins. We can exploit this feature for an effective background suppression. In what follows, we will describe in detail our cone-cut analysis method for suppressing the atmospheric neutrino background.

Since our signal comes only from the sun while the atmospheric neutrino comes from all sides, we accept events only from the direction of the sun. The signal neutrinos will be coming from the direction of the sun and the associated scattered lepton produced at the detector (muon in our case) will make an angle (θ_{ν_μ}) with the parent neutrino. The angle θ_{ν_μ} depends only on the energy of the parent neutrino and the detector medium. Due to finite detector resolution there will be smearing effects and the reconstructed muon direction will be slightly different compared the true direction. However, since muon angle resolution is rather good for ICAL (cf. Section 5.5), we do not apply detector angular resolutions at this stage of background suppression for simplicity. That is to say, we calculate θ_{ν_μ} using the generator level information *i.e.*, using the true direction of

neutrino and the corresponding muon rather than using true direction of neutrino and reconstructed muon direction.

We define cone angle θ_{90} as the half angle of the cone that contains 90 % of the signal muons, the axis of the cone being in the direction of the parent neutrino. The cartoon showing our geometrical cone-cut criteria is given in Fig. 6.2. The higher energy neutrinos will have a narrower cone opening while lower energy ones will have a broader θ_{90}. Since the neutrino energy is determined by the mass of the annihilating WIMP, we expect the neutrino flux from annihilation of heavier WIMP to produce more muons peaked along the direction of the sun and hence have narrower cone angle θ_{90} than neutrino flux produced by lighter WIMP. For the same reason, θ_{90} for the $\tau^+\tau^-$ channel is expected to be smaller than θ_{90} for the $b\bar{b}$ channel. Likewise, among the channels considered, we expect the largest and smallest value of θ_{90} for gg and $\nu\bar{\nu}$ [1] respectively. Using WIMPSIM and GENIE, we calculate θ_{90} for each WIMP mass and for a given annihilation channel in the sun. Fig. 6.3 shows the θ_{90} calculated for the sun as a function of the WIMP mass (m_χ). The different lines correspond to different annihilation channels. For each WIMP mass and annihilation channel, we place θ_{90} cone around the neutrino direction and accept events that fall within this cone. As expected the cone-cut angle θ_{90} is smaller for the $\tau^+\tau^-$ channel compared to the $b\bar{b}$ channel since the former is harder compared to the latter. The θ_{90} for the antineutrinos is seen to be smaller since for the same energy, the μ^+ events from antineutrinos are seen to be more forward peaked compared to the μ^- events coming from neutrinos.

After having applied the cone cut to each of the atmospheric neutrino background events, we have to assure that the events are indeed coming from the direction of the sun. For the case of WIMP annihilation in the sun, the direction of the signal neutrinos is same as the direction of the sun. Since we are using a Monte-Carlo generated data for our analysis, we assign a weight to

[1] The fluxes, the cone-cut angles and hence the expected sensitivities due to $\nu_e\bar{\nu}_e, \nu_\mu\bar{\nu}_\mu and \nu_\tau\bar{\nu}_\tau$ are almost identical. Throughout this chapter, unless otherwise specified by a subscript, we have taken $\nu_\tau\bar{\nu}_\tau$ as the representative of all neutrino flavours and indicated by $\nu\bar{\nu}$.

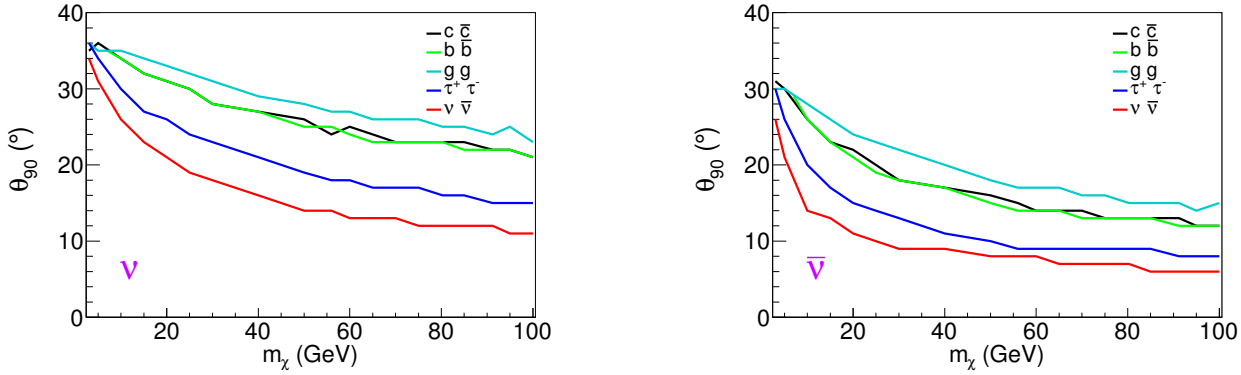

Figure 6.3: 90 % cone-cut values obtained for the sun for neutrinos (LEFT) and antineutrinos (RIGHT) as a function of the WIMP mass m_χ.

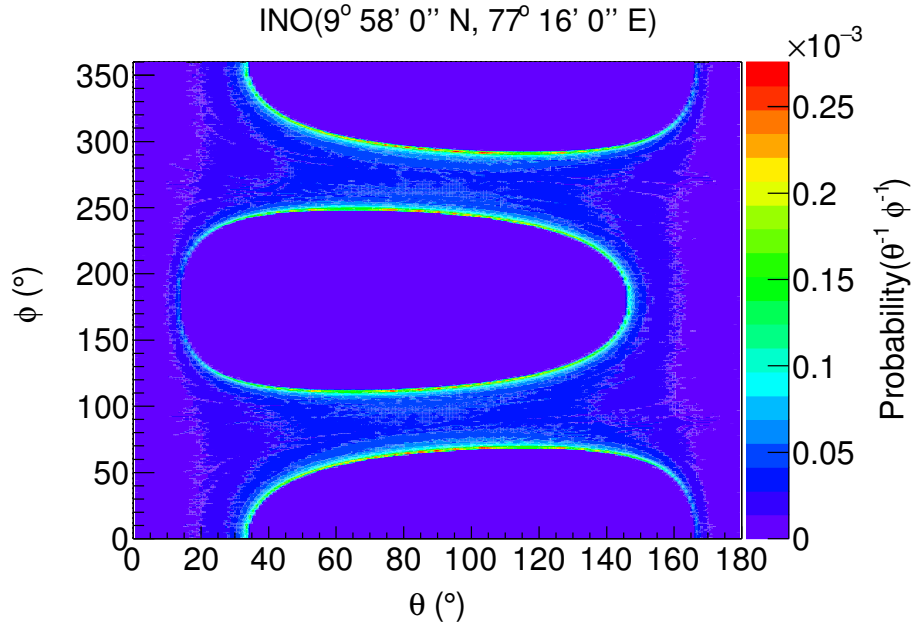

Figure 6.4: The figure shows the probability of solar exposure for each zenith (θ) and azimuthal (ϕ) angle bin for INO's geographical coordinates. Here, $\theta = 180°$ represents zenith. The plot has been obtained through SLALIB routine of WIMPSIM.

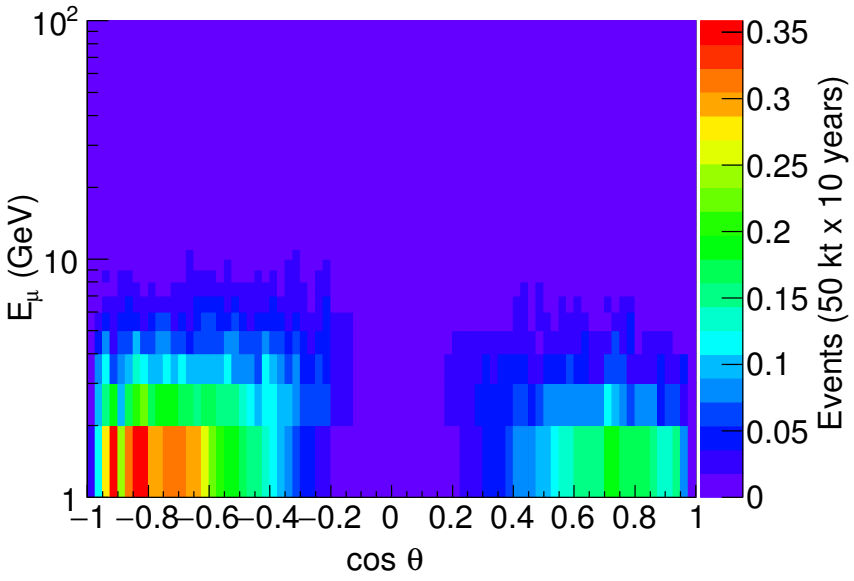

Figure 6.5: The μ^- event distribution at ICAL due to atmospheric background after applying the angular suppression corresponding to a 100 GeV WIMP. $\cos\theta = 1$ represents upward going muons. The plot is for 10 years of ICAL running.

each of the background events, where the weight corresponds to the probability that a particular event has originated from the direction of the sun. We call the probability of the sun exposing a particular zenith and azimuth, for a given latitude and longitude at the earth, as the solar exposure probability. We calculate this using WIMPSIM which uses SLALIB [160] routines. Fig. 6.4 shows the solar exposure probability for the location of INO. The neutrino fluxes arising due to WIMP annihilations in the sun necessarily follow the same angular distribution. The events accepted after this step are the final background events which are shown in Fig. 6.5. The reduced background has been shown for a the cone-cut angle θ_{90} corresponding to a 100 GeV WIMP and the $\tau^+\tau^-$ channel.

To compare our WIMP indirect detection signal with the reduced atmospheric neutrino background in ICAL, we show in Fig. 6.6 the μ^- and μ^+ signal events due to a 25 GeV WIMP annihilating into $\tau^+\tau^-$, $b\bar{b}$, $c\bar{c}$, $b\bar{b}$, $\nu_\mu\bar{\nu}_\mu$, $\nu_\tau\bar{\nu}_\tau$ and gg channels. $\nu_e\bar{\nu}_e$ event spectra is similar to $\nu_\mu\bar{\nu}_\mu$ and $\nu_\tau\bar{\nu}_\tau$ and hence we have not shown it here. Also shown are corresponding reduced atmospheric neutrino background events. In Fig. 6.6a, we show the signal events for the $\tau^+\tau^-$ channel for a 25 GeV WIMP and the atmospheric neutrino background corresponding to the neutrino and antineutrino

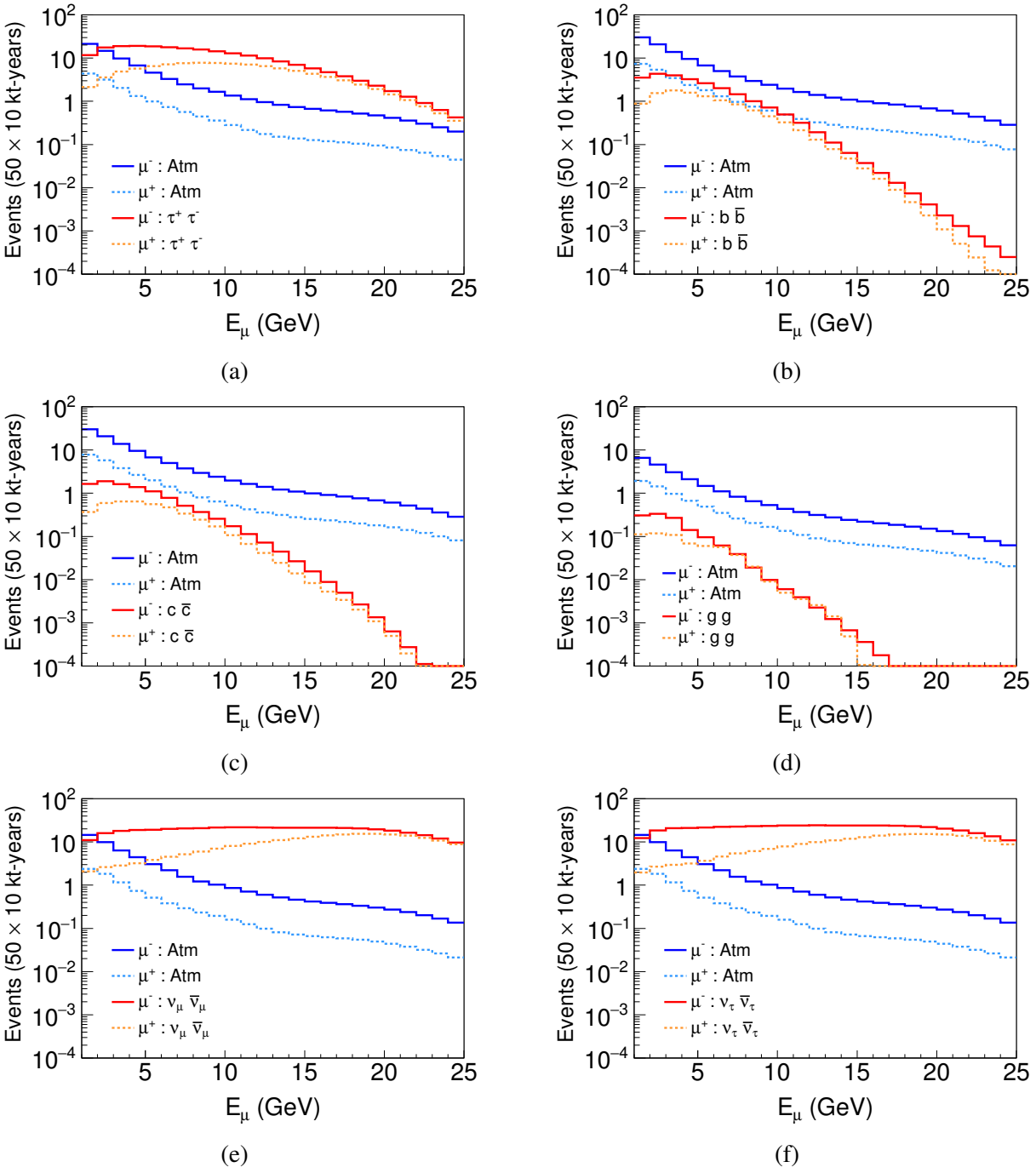

Figure 6.6: The μ^- (red solid lines) and μ^+ (orange dotted lines) event distribution at ICAL due to signal neutrinos arising out of WIMP annihilations in the sun through various annihilation channels. The signal events correspond to neutrino fluxes arising due to SD capture rate. A cross-section of $\sigma_{SD} = 10^{-39}\text{cm}^2$ has been assumed for the signal neutrinos and m_χ is taken as 25 GeV. Also shown are μ^- (blue solid lines) and μ^+ (azure dotted lines) event distributions due the reduced atmospheric neutrino background after applying the cone-cut angular suppression and the solar exposure function suppression.

θ_{90} for this channel and 25 GeV WIMP mass. Like-wise, Fig. 6.6b shows the corresponding events spectra and atmospheric neutrino background expected for the $b\bar{b}$ channel. As noted before, since the neutrino flux from the $\tau^+\tau^-$ channel is higher than the $b\bar{b}$ channel and since it also produces a harder neutrino spectrum, the signal event spectrum is higher for the former as well as harder for both neutrinos as well as antineutrinos. The atmospheric neutrino background too is lower for the $\tau^+\tau^-$ channel since a harder neutrino spectrum gives a smaller θ_{90}, improving the cone-cut background rejection employed in our analysis. Therefore, the signal to background ratio and hence the sensitivity to WIMP is expected to be better for the $\tau^+\tau^-$ channel, as we will see in the following sections. It can be seen from Fig. 6.6c that the fluxes from $c\bar{c}$ are only slightly lower in comparison to $b\bar{b}$, the event distribution follows the similar trend. However, since the θ_{90} values for $c\bar{c}$ and $b\bar{b}$ channels are almost comparable for various WIMP masses, it would be difficult to distinguish between these two channels. The events due to direct annihilation of WIMP into neutrinos give rise to a higher number of event and hence better sensitivity to indirect detection.

6.2 The statistical analysis

We perform a χ^2 analysis to obtain expected sensitivity limits on SD and SI WIMP-nucleon scattering cross-sections for given WIMP masses. We simulate the prospective data at ICAL for no WIMP annihilation and fit it with a theory where WIMP annihilate in the sun to give neutrinos. Therefore, the "data" or "observed" events correspond to only the reduced atmospheric neutrino backgrounds, whereas the "theory" or "predicted" events comprise the sum of the signal events due to WIMP annihilation in the sun as well as the atmospheric neutrino background events. The χ^2 function is defined as:

$$\chi^2 = \chi^2(\mu^-) + \chi^2(\mu^+)\,, \tag{6.1}$$

where

$$\chi^2(\mu^\pm) = \min_{\xi_k^\pm} \sum_{i=1}^{N_i} \sum_{j=1}^{N_j} \left[2\left(N_{ij}^{\rm th}(\mu^\pm) - N_{ij}^{\rm ex}(\mu^\pm) \right) + 2N_{ij}^{\rm ex}(\mu^\pm) \ln\left(\frac{N_{ij}^{\rm ex}(\mu^\pm)}{N_{ij}^{\rm th}(\mu^\pm)} \right) \right] + \sum_{k=1}^{l} \xi_k^{\pm 2}\,, \tag{6.2}$$

$$N_{ij}^{\rm th}(\mu^{\pm}) = N'^{\rm th}_{ij}(\mu^{\pm})\left(1+\sum_{k=1}^{l}\pi_{ij}^{k}\xi_{k}^{\pm}\right)+\mathcal{O}(\xi_{k}^{\pm 2})\,, \tag{6.3}$$

$N'^{\rm th}_{ij}(\mu^{\pm})$ and $N_{ij}^{\rm ex}(\mu^{\pm})$ are the 'predicted' and 'observed' number of $\mu^{\pm}$ events at ICAL respectively. As explained above, in our analysis $N_{ij}^{\rm ex}(\mu^{\pm})$ include only the reduced atmospheric neutrino background events, while $N'^{\rm th}_{ij}(\mu^{\pm})$ include both signal events from WIMP annihilation in the sun as well as the reduced background events from atmospheric neutrinos. The quantities π_{ij}^{k} are the correction factors due to the k^{th} systematic uncertainty, and $\xi_{k}^{\pm}$ are the corresponding pull parameters. Since this is an analysis which looks for signal events above atmospheric neutrino backgrounds, and it is well known that there are substantial systematic uncertainties in the predicted atmospheric neutrino fluxes, we include systematic uncertainties on the atmospheric neutrino background. We include 5 systematic errors on the atmospheric neutrino background: 20 % error on flux normalisation, 10 % error on cross-section, 5 % uncorrelated error on the zenith angle distribution of atmospheric neutrino fluxes and 5 % tilt error. We further include a 5 % overall error to account for detector systematics[2]. The individual contributions from μ^{-} and μ^{+} data samples are calculated by minimising over the pull parameters. These are then added to obtain the χ^2 for a given set of WIMP mass and WIMP-nucleon cross-section.

6.3 Results

We now present our main results on the expected sensitivity of ICAL to indirect detection of dark matter. The 90 % C.L. expected sensitivity from 10 years of running of ICAL is shown in Fig. 6.7 in the $\sigma_{SD} - m_{\chi}$ plane for the spin dependent cross-section. The expected sensitivity assuming 100 % BR in $\nu\bar{\nu}$ (red solid line), $\tau^{+}\tau^{-}$ (red dashed line) and $b\bar{b}$ (red dashed line) channels have been shown. Also shown are limits from other complementary indirect detection experiments: IceCube [161] $\tau^{+}\tau^{-}$ (bottom, light blue and dotted) and $b\bar{b}$ (top, light blue and dotted) channels, Super-Kamiokande (SK) [49] $\tau^{+}\tau^{-}$ (bottom, black) and $b\bar{b}$ (top, black), BAKSAN [162] $\tau^{+}\tau^{-}$

[2]Simulations to estimate the detector systematic uncertainties in ICAL is under way. This number could therefore change when better estimates of this become available.

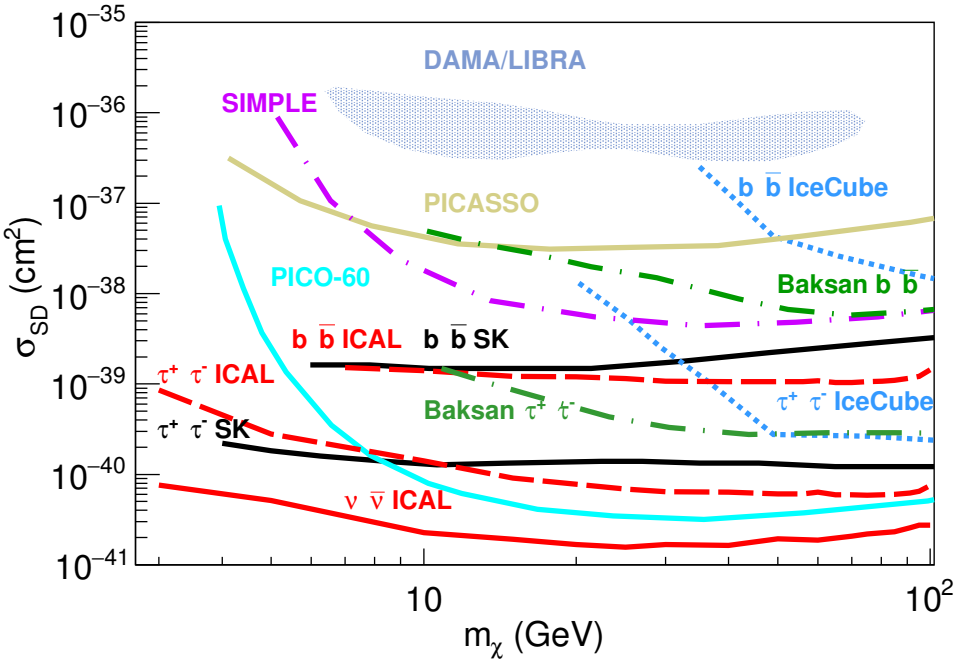

Figure 6.7: The expected 90 % C.L. sensitivity limit on the WIMP-nucleon spin-dependent cross-sections as a function of the WIMP mass. The ICAL expected sensitivity are shown for $\nu\bar{\nu}$ (red solid line), $\tau^+\tau^-$ (red dashed line) and $b\bar{b}$ (red dashed line) channels and for 10 years of running of ICAL. Current 90 % C.L. limits from other indirect detection and direct detection experiments have been shown. Also shown is the region compatible with the claimed signal seen by DAMA/LIBRA.

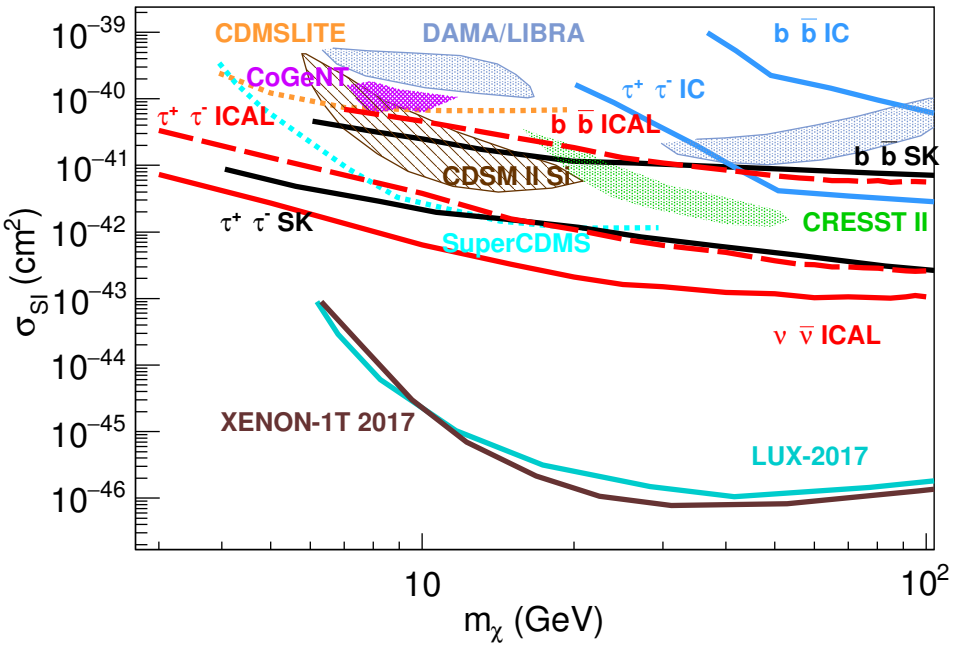

Figure 6.8: The expected 90 % C.L. sensitivity limit on the WIMP-nucleon spin-independent cross-sections as a function of WIMP mass. The expected ICAL sensitivity are shown for $\nu\bar{\nu}$ (red solid line), $\tau^+\tau^-$ (red dashed line) and $b\bar{b}$ (red dashed line) channels and for 10 years of running of ICAL. Current 90 % C.L. limits from other indirect detection and direct detection experiments have been shown. Also shown is the region compatible with the claimed signal seen by DAMA/LIBRA, CoGeNT, CRESSTII and CDMS II Si.

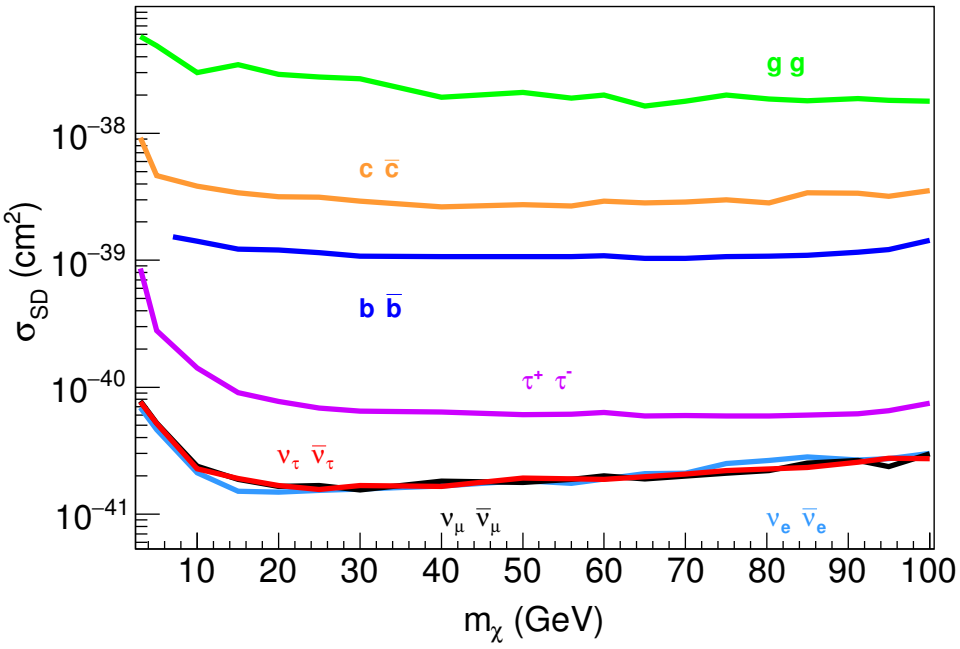

Figure 6.9: The expected 90 % C.L. sensitivity limit for ICAL on the WIMP-nucleon spin-dependent cross-sections as a function of the WIMP mass and for different annihilation channels.

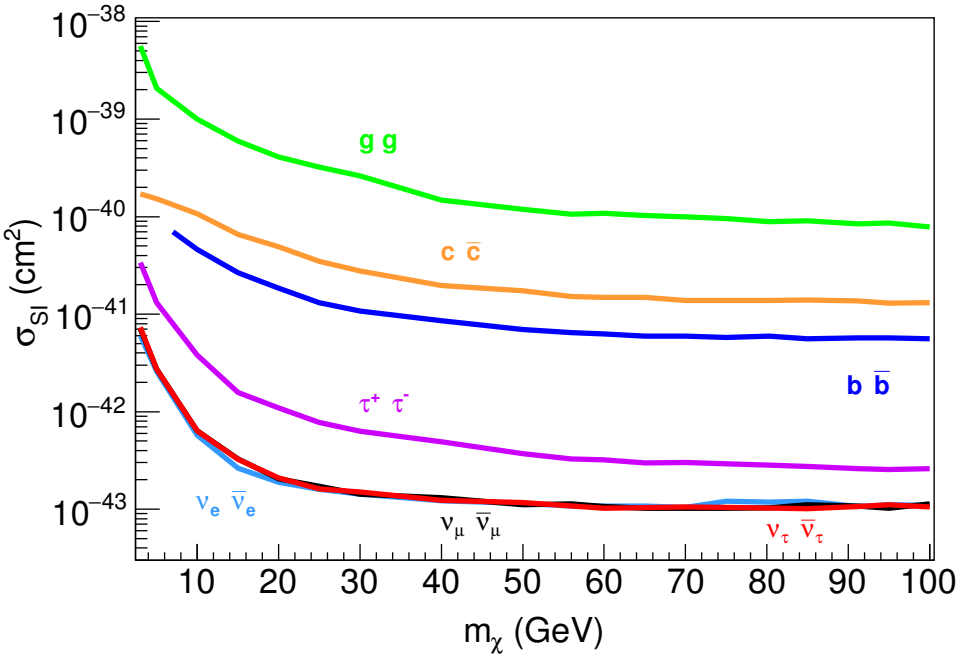

Figure 6.10: The expected 90 % C.L. sensitivity limit for ICAL on the WIMP-nucleon spin-independent cross-sections as a function of the WIMP mass and for different annihilation channels.

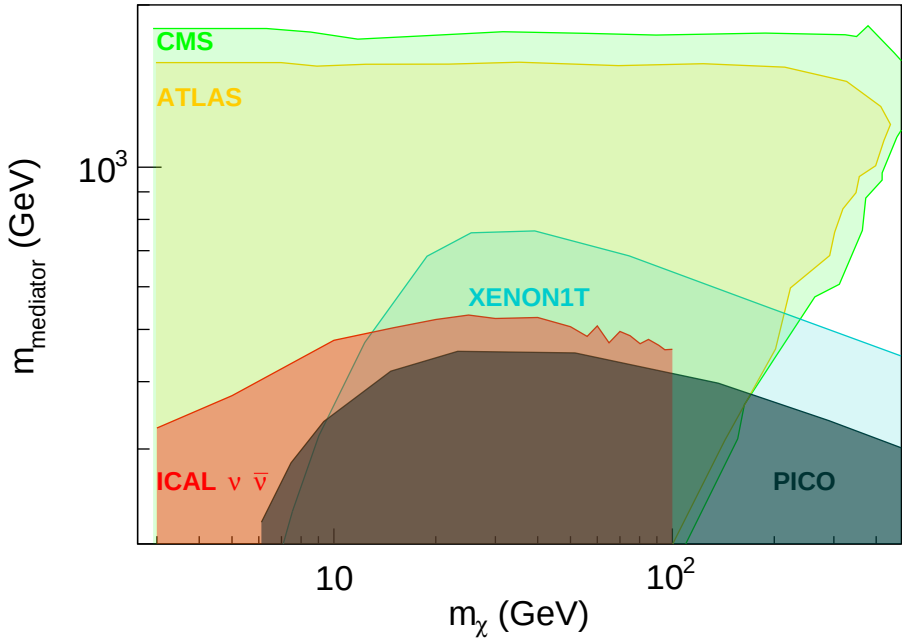

Figure 6.11: The expected 95% C.L. ICAL sensitivity limits in the mediator mass M_{med} vs DM mass m_χ plane for WIMP proton SD scattering. It has been generated following the prescription given by LHCDMWG [16] and using the recommended values of the universal coupling to quarks $g_q = 0.25$ and the mediator coupling to DM $g_\chi = 1.0$ in Eq. 2.19. The red shaded region represents the expected exclusion parameter space at 95 % C.L. for 500kt-years of ICAL exposure and assuming $\chi\chi \rightarrow \nu_\tau\bar{\nu}_\tau$ annihilation channel. Exclusion regions at 95 % C.L. are shown from other experiments for comparison: PICO-60 [17] (blue-gray shaded region), XENON-1T [18] (light blue shaded region), ATLAS [19] (orange shaded region) and CMS [20](green shaded region).

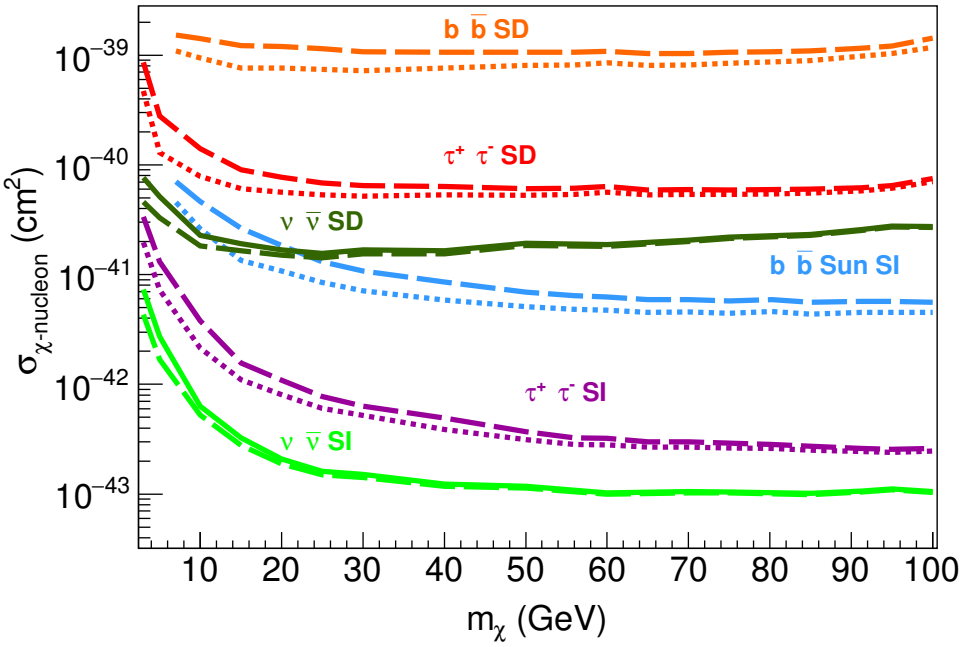

Figure 6.12: The expected 90 % C.L. sensitivity limit for ICAL on the WIMP-nucleon spin-dependent and spin-independent cross-sections as a function of the WIMP mass and for different annihilation channels. The solid lines are the sensitivity limits calculated using detector systematics as described in Sec 6.2. The corresponding dotted lines are without systematics.

(bottom, green dot dashed) and $b\bar{b}$ (top, green dot dashed) channels. For comparison we also show the 90 % C.L. limits from direct detection experiments: PICASSO [163] (brownish-yellow), SIMPLE [164] (violet long dot dashed) and PICO-60 C_3F_8 [17] (cyan solid line). Finally, the blue-gray shaded region is the 3σ C.L. area compatible with the signal claimed by DAMA/LIBRA [37, 38]. We find that the expected sensitivity from 10 years of running of ICAL is comparable[3] to SK for both $\tau^+\tau^-$ and $b\bar{b}$ channels, with ICAL performing a tad better for all WIMP masses greater than 10 GeV. Note that ICAL is expected to be better than all other direct as well as indirect experiments which have placed limits on the WIMP-nucleon spin-dependent scattering cross-section. In particular, the sensitivity of the ICAL experiment is expected to be better than the current limits from IceCube and Baksan. The limits on σ_{SD} from the direct detection experiments, in general, are weaker than those from indirect detection experiments for all ranges of WIMP masses m_χ with

[3]We compared the event spectra for $\tau^+\tau^-$ and atmospheric background as given in Fig. 6.6a with the corresponding signal and background event spectra of Fig. 2 of [165]. Applying the same statistical analysis on both these event sets, the calculated sensitivity limits were found to be comparable.

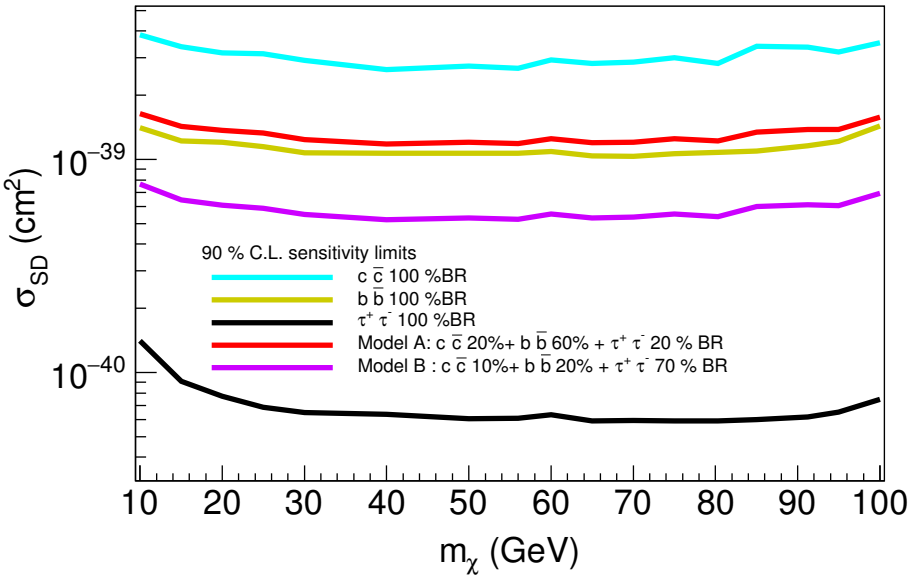

Figure 6.13: Impact of varying branching ratios on the expected 90 % C.L. sensitivity limit at ICAL. The shown limits are for WIMP-nucleon spin-dependent cross-sections as a function of the WIMP mass and for three annihilation channels (same as in Fig. 6.7). Detector systematics have been included. The expected 90 % C.L. sensitivity limit due to toy Models A (red line) and B (violet line) have been shown.

the exception of the limit obtained by PICO-60 C_3F_8. Depending on the choice of model, limits obtained from the collider searches could be very stringent. For instance, see Figure 12(b) of Ref. [166] for ATLAS 95% C.L. exclusion limits in the $\sigma_{SD} - m_\chi$ plane.

The 90 % C.L. expected sensitivity from 10 years of running of ICAL for the spin-independent cross-section is shown in the $\sigma_{SI} - m_\chi$ plane in Fig. 6.8 along with limits from other experiments. We show the expected sensitivity assuming 100 % BR in $\nu_\tau\bar{\nu}_\tau$ (red solid line), $\tau^+\tau^-$ (red dashed line) and $b\bar{b}$ (red dashed line) channels. Also shown are the current limits from earlier and ongoing experiments. For the SI cross-sections, the limits from the direct detection experiments are significantly better than those from the indirect detection experiments. Allowed regions from the direct searches claiming positive signal for dark matter at DAMA/LIBRA [37, 38] is shown by metallic blue shaded region at 3σ C.L., at CoGeNT [42] by violet diagonally cross-hatched region at 90 % C.L., at CRESSTII [41] by the green shaded region at 2σ C.L. and at CDMS II Si [167] by brown hatched region at 90 % C.L. The limits on SI cross-sections from direct detection experiments are shown for SuperCDMS [168] (cyan dotted line), CDMSlite [169] (orange dotted), XENON-1T [25] (brown solid line) and LUX [24] (solid cyan line). The limits from Xenon-1T are currently the best limits on WIMP-nucleon SI cross-sections. Also shown are the less competitive limits from the indirect searches at IceCube [161] for $\tau^+\tau^-$ (cyan solid line) and $b\bar{b}$ (cyan dotted line) channels, and SK [49] for $\tau^+\tau^-$ (dark violet line) and $b\bar{b}$ (light violet line) channels. As for the SD cross-section case, we find that the expected sensitivity of ICAL is comparable to that from SK for both channels and better than the current limits from IceCube. In this case as well, the limits obtained from the collider searches could be very strong, subject to the choice of model. For instance, see Figure 12(a) of Ref. [166] for ATLAS 95% C.L. exclusion limits in the $\sigma_{SI} - m_\chi$ plane. Again, it is worth pointing out that even though the limits on SI case from indirect detection experiments are expected to be poorer than from direct detection experiments, they provide an independent check on the WIMP parameters and can be used as a complementary probe of the WIMP paradigm.

It is interesting to compare the sensitivity of indirect and direct detection experiments to dark matter searches. The sensitivity of an experiment, in a specified WIMP parameter space, depends on the following principle factors. The detection approach (i.e direct or indirect) primarily dictates the sensitivity. For either approach, however, signal detection threshold, signal detection and reconstruction efficiency, the choice of target material, as well as the fiducial volume and exposure, acts in a cumulative manner and determine the sensitivity for a particular experiment. In the case of direct detection experiments (also see Chapter 2), the sensitivity follows an approximate paraboloid curve in the WIMP cross-section vs WIMP mass plane, and features a minimum cross-section representing the greatest sensitivity for the corresponding WIMP mass ($m_{\chi,0}$). The exact position of ($m_{\chi,0}$) is a complex function of detection efficiency and target nuclei mass. Detection efficiency is directly related to technique with which nuclear recoils due to WIMP scattering are detected such as bubble chamber (PICO) or Dual phase liquid time projection chambers (XENON/LUX). It is the target nucleus that decides the dominant mode of scattering of WIMP. PICO-60 used C3F8 as the target which has unpaired nucleons in fluorine resulting in dominant SD WIMP scattering, and for this choice of the target material the corresponding SD sensitivity is maximum for ($m_{\chi,0}$) = 30 GeV which can be seen in Fig. 6.7. In experiments like XENON and LUX, the target is primarily sensitive to SI scattering and for this choice their sensitivity is greatest around $\sim$ 80 GeV WIMP mass. It should be emphasised, however, that these experiments are indeed sensitive to SD scattering. However, since only a smaller fraction of nucleons in the target nuclei contribute to SD scattering, their sensitivity to SD interactions is poorer (see Figure 3 of Ref. [18] for comparison). For the masses below $m_{\chi,0}$, the sensitivity for all the direct experiments decrease because of the drop in detection efficiency. For example, in case of PICO-60 experiment for masses below $m_{\chi,0}$ there is a drop in bubble nucleon efficiency and as we go further down the efficiency drops to zero at detection threshold of a few GeVs. For PICO-60, above $m_{\chi,0}$, the detection efficiency is rather close to 100%. However, there is a drop in sensitivity due to drop in the signal rate which is approximately $\propto 1/m_{\chi}$ which can be inferred from Eq. 2.11. Similarly, trend for other direct detection experiments can be explained. For both approaches, the sensitivity, in general, increases

with an increase in the detector fiducial volume and exposure. For a given indirect detection experiment, among other above mentioned factors, the signal to background ratio, plays a crucial role in determining the sensitivity. However, for a specified annihilation channel and WIMP mass, the sensitivity difference between two experiments is due to difference in the statistics (exposure and fiducial volume of these experiments) as well as the detector systematics that have been considered in each case. Therefore, for same exposure and fixed WIMP mass and annihilation channel, we expected a similar sensitivity from two different experiments. This can be seen while comparing the sensitivity limits from SK and calculated sensitivity from ICAL, as these are for approximately same statistics. For lower WIMP masses, ICAL's reconstruction efficiency is poorer than SK for lower WIMP masses and improves as approach WIMP masses above 10 GeV. This is seen as a crossing over of expected ICAL sensitivity limits over SK limits at around 10 GeV, in both Fig. 6.7 and Fig. 6.8.

Following the prescription given by LHCDMWG [16] and using the recommended values of the universal coupling to quarks $g_q = 0.25$ and the mediator coupling to DM $g_\chi = 1.0$ in Eq. 2.19, we show in Fig. 6.11 the expected 95% C.L. ICAL sensitivity limits in the mediator mass M_{med} vs DM mass m_χ plane for WIMP proton SD scattering. The red shaded region represents the excluded parameter space and the expected sensitivity is shown for 500kt-years of ICAL exposure and assuming $\chi\chi \rightarrow \nu_\tau\bar{\nu}_\tau$ annihilation channel. Exclusion regions at 95% C.L. are shown from other experiments for comparison: PICO-60 [17] (blue-gray shaded region), XENON-1T [18] (light blue shaded region), ATLAS [19](orange shaded region) and CMS [20](green shaded region).

Now we show the expected sensitivity of ICAL to indirect detection due to several WIMP annihilation channels. The 90 % C.L. expected sensitivity from 10 years of running of ICAL is shown in Fig. 6.9 in the $\sigma_{SD} - m_\chi$ plane for the spin dependent cross-section. The green lines are for gg channel, orange lines for $c\bar{c}$, blue for $b\bar{b}$, violet for $\tau^+\tau^-$, azure lines for $\nu_e\bar{\nu}_e$, black for $\nu_\mu\bar{\nu}_\mu$ and red for $\nu_\tau\bar{\nu}_\tau$ channel. Fig. 6.10 presents the 90 % C.L. expected sensitivity from 10 years of running of ICAL for the spin-independent cross-section, shown in the $\sigma_{SI} - m_\chi$ plane for different annihilation channels. The colour coding remains the same. For the reasons described in

3.1, the expected sensitivity limit due to WIMP annihilating into neutrino-antineutrino channels is the strongest and weakest for the gg channel. This holds for both SD and SI case.

In Fig. 6.12 we present the impact of systematic uncertainties in the atmospheric neutrino background on the indirect detection sensitivity of ICAL. The solid lines in this figure show the 90 % C.L. expected sensitivity of ICAL when systematic uncertainties are included. These were the expected limits shown in Figs. 6.7, 6.8, 6.9 and 6.10. The corresponding dashed lines are obtained by switching off the systematic uncertainties in the analysis. The orange lines are for σ_{SD} and $b\bar{b}$ channel, the red lines are for σ_{SD} and $\tau^+\tau^-$ channel, the azure lines are for σ_{SI} and the $b\bar{b}$ channel, the magenta lines are for σ_{SI} and $\tau^+\tau^-$ channel, the dark green lines for σ_{SD} and $\nu\bar{\nu}$ channel and light green lines are for σ_{SI} and $\nu\bar{\nu}$ channel. The impact of the systematic uncertainties for all the channels are seen to be more for lower WIMP masses. This is because the atmospheric neutrinos peak at lower energies and their fluxes fall as roughly $E_\nu^{-2.7}$. Therefore, for lower WIMP masses, since the neutrino spectrum from WIMP annihilation are softer, these get more affected by the uncertainties in the atmospheric neutrino fluxes. The impact of the uncertainties is also seen to be more for the $b\bar{b}$ channel. The reason for this behaviour is again the same. We had seen in section 3.1 that the neutrino spectrum from the $b\bar{b}$ channel is softer. Similarly, the harder channels like $\nu\bar{\nu}$ and $\tau^+\tau^-$ have greater high energetic neutrino content. Therefore, the impact of the atmospheric neutrino background and also the uncertainty on the atmospheric neutrino background affect the softer channels more than the harder channels.

Finally, in Fig. 6.13 we illustrate the impact of varying branching ratios on sensitivity limits. It is clear from Fig. 3.2 that some channels are weaker in comparison to others and would yield a weaker sensitivity to indirect detection as shown in Fig. 6.9 and Fig. 6.10. However, these sensitivity limits are assuming 100% branching ratios for each of the annihilation channel. Therefore, the above sensitivity limit indicates the best limit one would expect at ICAL due to a particular channel considered. In nature, however, we would have a mixture of fluxes from different channels and correspondingly the sensitivity limits would be altered. For a given WIMP

model, the branching ratio of a particular channel would be known and corresponding contribution in terms of neutrino fluxes can be easily calculated. In a framework of a particular model, therefore, the sensitivity due to this mixture of fluxes would get scaled appropriately. To illustrate this point, we consider two toy models and calculate their expected sensitivities at ICAL. We take two toy models restricted to three annihilation channels: Model A which has a following prediction : $BR_{c\bar{c}} : BR_{b\bar{b}} : BR_{\tau^+\tau^-} = 20\% : 60\% : 20\%$ and Model B which predicts $BR_{c\bar{c}} : BR_{b\bar{b}} : BR_{\tau^+\tau^-} = 10\% : 20\% : 70\%$. We see from the Fig. 6.13 that sensitivity due to Model B (violet line) is more than Model A (red line), and it is expected since it has greater contribution from a 'harder' channel which is $\tau^+\tau^-$ in this case. For both the models, sensitivities are indeed bounded by the strongest and the weakest channels which in this particular case are $\tau^+\tau^-$ and $c\bar{c}$ respectively.

6.4 Conclusions

In this chapter, we studied the potential of the ICAL detector to detect the neutrinos from WIMP annihilations in the sun. We performed a study of μ^- and μ^+ events arising at ICAL due to such neutrinos through various WIMP annihilation channels : $\tau^+\tau^-$, $b\bar{b}$, $c\bar{c}$, $b\bar{b}$, $\nu_e\bar{\nu}_e, \nu_\mu\bar{\nu}_\mu, \nu_\tau\bar{\nu}_\tau$ and gg channels. The atmospheric neutrinos come from all directions while the dark matter signal neutrinos only come from the direction of the sun and we used this feature to place an angular cut to effectively reduce the atmospheric neutrino background. We presented the signal and background for various annihilation channels for WIMP mass 25 GeV and $\sigma_{SD} = 10^{-39}$ cm^2. We defined a χ^2 function for the indirect detection sensitivity of ICAL to dark matter and presented the expected sensitivity in the $\sigma_{SD} - m_\chi$ and $\sigma_{SI} - m_\chi$ planes for spin-dependent and spin-independent cross-sections, respectively. The expected 90 % C.L. sensitivity was presented for $\tau^+\tau^-$, $b\bar{b}$, $c\bar{c}$, $b\bar{b}$, $\nu_e\bar{\nu}_e, \nu_\mu\bar{\nu}_\mu, \nu_\tau\bar{\nu}_\tau$ and gg channels for an exposure of 500 kt-yrs of ICAL and with systematic uncertainties on atmospheric neutrino background included in the analysis. For a WIMP mass of 25 GeV, the expected 90 % C.L. limit using the $\tau^+\tau^-$ channel with 500 kt-yrs exposure in ICAL is $\sigma_{SD} < 6.87 \times 10^{-41}$ cm^2 and $\sigma_{SI} < 7.75 \times 10^{-43}$ cm^2 for the spin-dependent and spin-

independent cross-sections, respectively. We also studied the effect of systematic uncertainties on the atmospheric neutrino background.

Chapter 7

Searches for DM annihilations in the earth

In this chapter, we will study the prospect of indirect detection of WIMP at ICAL from their annihilations in the center of the earth. As is well known, the WIMP annihilation cross-section can be related to the WIMP-nucleus scattering cross-section. The WIMP scattering on nucleons can proceed both via Spin Independent (SI) as well as Spin Dependent (SD) process, where the SI cross-section depends on the mass of the nucleus involved while the SD cross-section does not. Therefore, heavier target nuclei offer better sensitivity to SI cross-sections. As a result, the WIMP direct detection experiments, which look for the recoil energy of target nuclei due to WIMPs scattering on them in dedicated terrestrial detectors, are more sensitivity to SI cross-sections owing to their heavier target nuclei. On the other hand, the indirect detection search for WIMP annihilation in the sun is more sensitive to the SD cross-sections since the sun mostly consists of hydrogen. The earth has heavier elements, with only a negligible amount of nuclei with unpaired nucleons, and hence are sensitive to SI cross-sections. While the direct detection experiments continue to be several order of magnitude more sensitive for SI interactions, indirect searches provide a complementary probe to dark matter and are hence interesting. The neutrino fluxes due to WIMP annihilation in the earth core have been presented in Section 3.2. Using the prescription in Chapter 5, we calculate expected signal events at ICAL for a given WIMP mass and the annihilation channel.

The organisation of the chapter is as follows. In Section 7.1, we describe the atmospheric

background suppression scheme. and present the expected event spectrum at ICAL. We define the χ^2 function in Section 7.2, present results on expected sensitivity of ICAL in Section 7.3 and, finally, conclude in Section 7.4.

7.1 Atmospheric neutrino background suppression

Similar to the search in the previous chapter, the major source of background to the indirect searches from WIMP annihilation in the earth is due to the atmospheric neutrinos. However, unlike the neutrinos from WIMP annihilation which come from the direction of the earth core, the atmospheric neutrinos have a distribution over all zenith and azimuth angular bins and is comparatively well studied. We can exploit this feature and use it to suppress the atmospheric background considerably. Other source of neutrinos such a geothermal neutrinos coming from the core direction are in the MeV range and hence are not relevant here. The signal neutrinos, for the case of WIMP annihilation in the earth, will come from the direction of earth core. The signal search region for the WIMP annihilation in the earth is shown in Figure 7.1. These neutrinos on reaching ICAL will interact with the detector iron and produce leptons, muons being the lepton of interest for ICAL. The scattered muon will make an angle ($\theta_{\nu\mu}$) with their parent neutrino, where ($\theta_{\nu\mu}$) is a function of parent ν energy and detector medium. Due to finite detector resolution there will be smearing effects. However, we choose to work with true muon direction rather than the reconstructed muon direction at the stage of background suppression. As we seen in Section 5.5, ICAL has an excellent muon angle resolution for the considered energy range and hence this choice will not affect the final results significantly. We define θ_{90} to be the half angle of the cone that contains 90% of the signal muons, the axis of the cone being in the direction of the earth's core. Harder channels like $\tau^+\tau^-$ with higher energy neutrinos will have a narrower θ_{90} in comparison to softer channels like $b\bar{b}$ with lower energy neutrinos which will have a broader θ_{90}. Likewise, we expect that the ν spectra from annihilation of massive WIMP to have most of the associated muons in a narrower cones than neutrinos by lighter WIMP. Also, the heavier the WIMP, the closer it is to the center

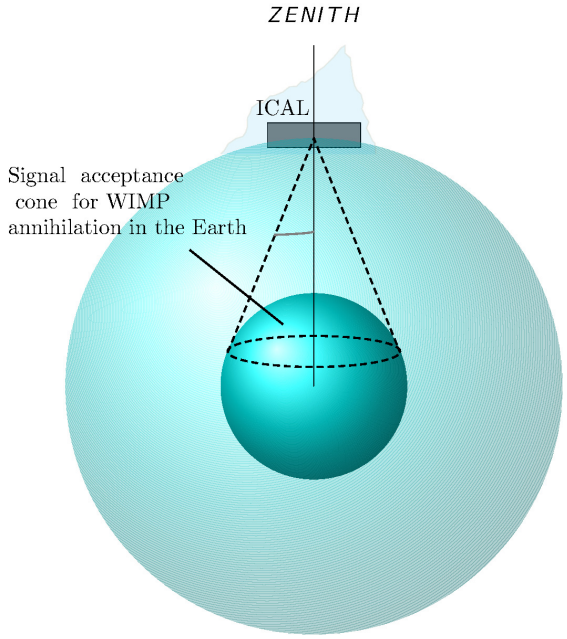

Figure 7.1: The cone regions where signal from the WIMP annihilations are expected for the earth.

of the earth and hence smaller cone opening[1]. Using WIMPSIM and GENIE, we estimate θ_{90} for each WIMP mass and for a given annihilation channel. Figure 7.2 shows the θ_{90} obtained for WIMP annihilation inside earth, as a function of WIMP mass (m_χ), and for different annihilation channels.

The atmospheric neutrino background is then suppressed as follows. For each WIMP mass and annihilation channel, we accept only those muons whose zenith angle are within θ_{90} with respect to the earth core. These atmospheric background events that fall within this cone represents

[1]The captured WIMP settle in the core of the earth with an isothermal distribution at a temperature equal to the core temperature. In order to calculate WIMP annihilation profile for the earth, WIMPSIM uses the expression (Eq. (1) and (2)) described in Ref. [170]. At a distance r from the center of the earth, the annihilation rate per unit volume is proportional to the square of the WIMP number density $n(r)$ and can be written as:

$$n(r) = n(0)e^{-r^2/2r_\chi^2} \tag{7.1}$$

where r_χ can be written as:

$$r_\chi = \left[\frac{3kT}{4\pi G\rho m}\right]^{\frac{1}{2}} = \frac{0.56R_\oplus}{\sqrt{m_\chi/\mathrm{GeV}}} \tag{7.2}$$

where k and G are the Boltzmann and Gravitational constants, respectively, $R_\oplus$ is the radius of the earth, ρ is the density of the earth's center and T is the temperature at the center of the earth.

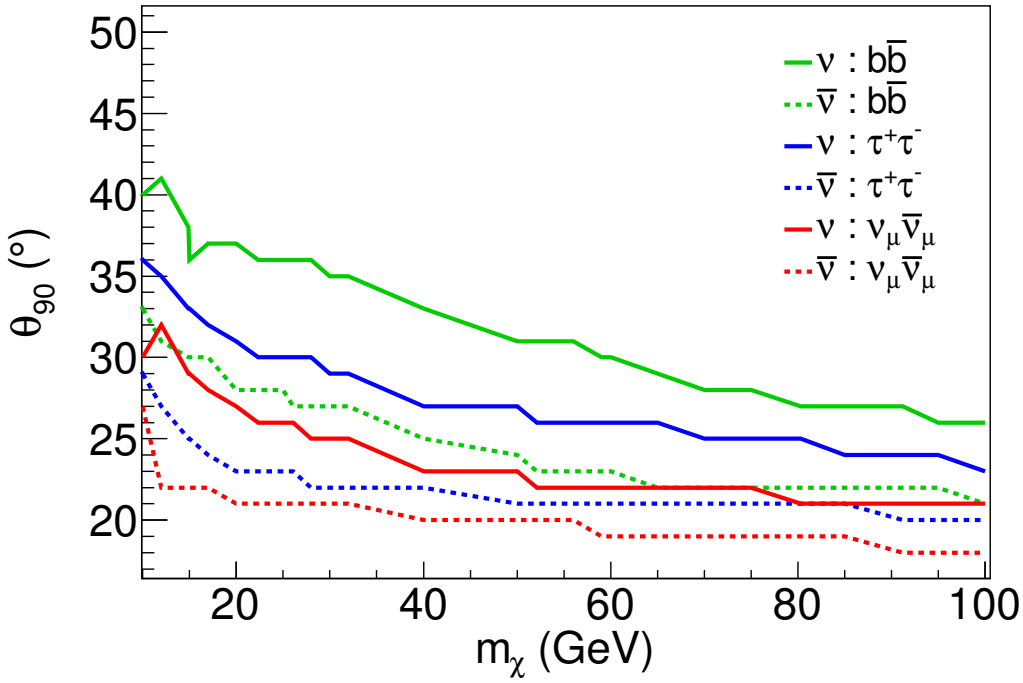

Figure 7.2: 90 % cone cut values obtained for the earth. This is obtained using WIMPSIM and GENIE. A cone angle is estimated such that it contains 90% of the signal events. The solid lines correspond to neutrinos and dashed lines correspond to anti-neutrinos for each of the annihilation channel.

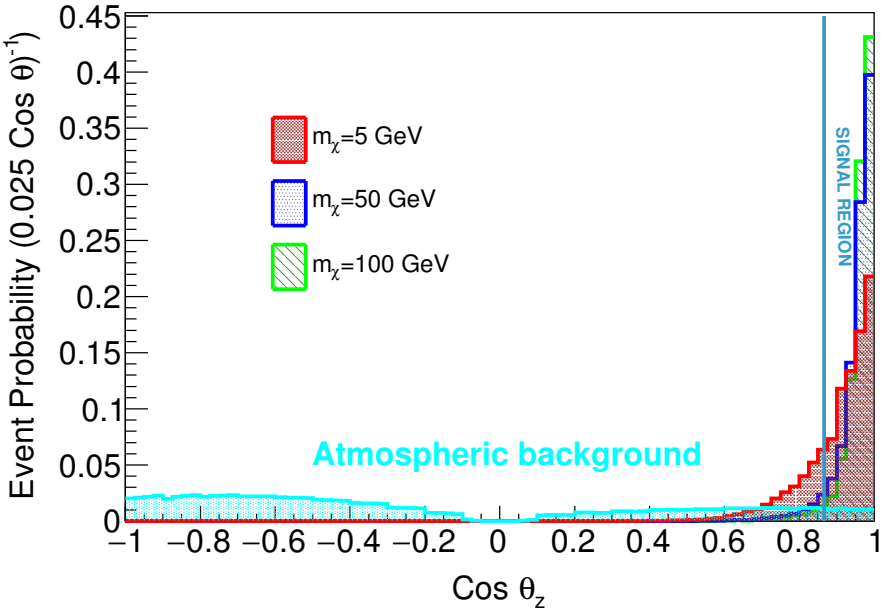

Figure 7.3: Angular probability distribution of reconstructed μ^- at ICAL due to WIMP annihilations in the earth. A comparison for three WIMP masses has been shown and the region where signal is expected is marked. The probability distribution for the unsuppressed atmospheric background is also shown.

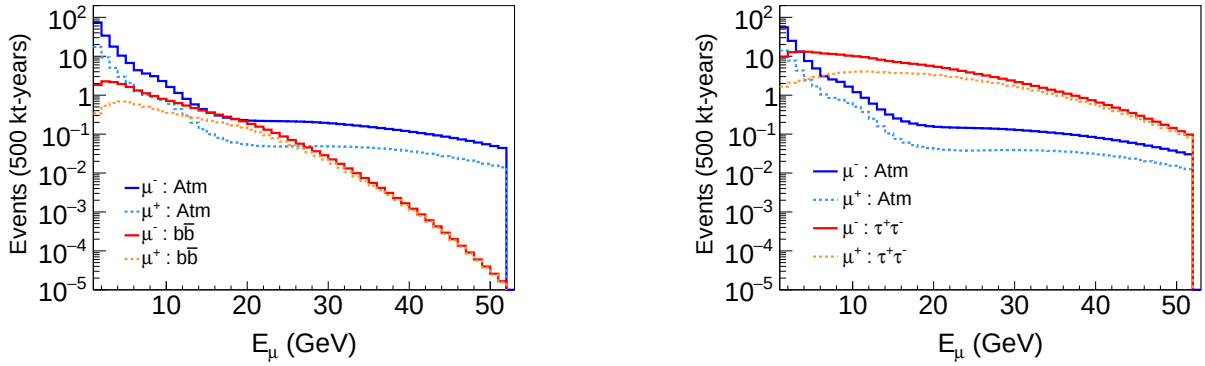

Figure 7.4: Muon event distribution at ICAL due to atmospheric neutrinos and signal neutrinos arising out of a WIMP annihilations in the earth. The plots are for fluxes arising due to SI capture rate. A cross-section of $\sigma_{\rm SI} = 10^{-44}{\rm cm}^2$ has been assumed for the signal neutrinos. The left plot is for the WIMPs annihilating into the channel $b\bar{b}$ while the right plot is for the annihilation channel $\tau^+\tau^-$. A 100 % branching ratio has been assumed for each of the channels. Also shown are the corresponding events coming from the atmospheric background after applying the suppression scheme as described in 7.1. Atmospheric events have been simulated using Honda fluxes at Theni [21]. The softer channel $b\bar{b}$ has more background than the harder channel $\tau^+\tau^-$.

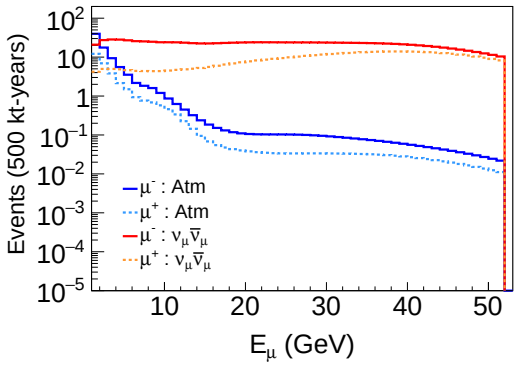

Figure 7.5: Muon event distribution at ICAL due to atmospheric neutrinos and signal neutrinos arising out of a WIMP annihilations in the earth. The plots are for fluxes arising due to SI capture rate. A cross-section of $\sigma_{\rm SI} = 10^{-44}{\rm cm}^2$ has been assumed for the signal neutrinos. The plot is for the WIMPs annihilating into the channel $\nu_\mu\bar{\nu}_\mu$, assuming a 100 % branching ratio. The corresponding events coming from the atmospheric background after applying the suppression scheme as described in 7.1 are also shown. It can be seen that events in this case are more than the $b\bar{b}$ and $\tau^+\tau^-$ channels.

an irreducible background for we can not distinguish them from the neutrinos due to WIMP annihilation in the core. After applying this suppression scheme, we fold the background events with detector resolution and efficiencies as described in Section 5.6 to obtain the final reconstructed and suppressed background events which are then used for χ^2 analysis.

Figure 7.3 shows the angular probability distribution of μ^- due to WIMP annihilations in the earth for the $\tau^+\tau^-$ channel along with the distribution of the (unsuppressed) atmospheric background muon events at ICAL. A comparison for three WIMP masses 5, 50 and 100 GeV has been shown. The above probability distribution, for each of the WIMP mass, has been obtained by normalising the reconstructed μ^- events in each bin by total number of reconstructed μ^- events for that WIMP mass. It can be noted that as WIMP mass increases, the angular probability distribution peaks towards the direction of the core. This is expected because of the reasons discussed above. The signal search is carried out in the region right of the vertical line represents θ_{90}. We draw a line at $\sim 30^\circ$ from the earth center $(\cos\theta = 1)$ just for illustration. The actual values of θ_{90} for each WIMP mass and channel is taken from Figure 7.2 while doing the analysis. Fig. 7.4 shows the signal events due to a 52.14 GeV WIMP annihilating through $\tau^+\tau^-$ and $b\bar{b}$ channels. Also shown

are corresponding suppressed atmospheric background events.

7.2 Statistical Analysis

We perform a χ^2 analysis to obtain expected sensitivity limits on spin independent WIMP nucleon cross section as a function of WIMP masses. We simulate the prospective data at ICAL for the case of no WIMP annihilation and fit it with a theory where WIMP annihilate in the earth to give neutrinos. Therefore, the "data" or "observed" events correspond to only the reduced atmospheric neutrino backgrounds, whereas the "theory" or "predicted" events comprise the sum of the signal events due to WIMP annihilation in the earth as well as the atmospheric neutrino background events. The χ^2 function is defined as:

$$\chi^2 = \chi^2(\mu^-) + \chi^2(\mu^+)\,, \tag{7.3}$$

where

$$\chi^2(\mu^\pm) = \min_{\xi_k^\pm} \sum_{i=1}^{N_i} \sum_{j=1}^{N_j} \left[2\left(N_{ij}^{\rm th}(\mu^\pm) - N_{ij}^{\rm ex}(\mu^\pm) \right) + 2N_{ij}^{\rm ex}(\mu^\pm) \ln\left(\frac{N_{ij}^{\rm ex}(\mu^\pm)}{N_{ij}^{\rm th}(\mu^\pm)} \right) \right] + \sum_{k=1}^{l} \xi_k^{\pm 2}\,, \tag{7.4}$$

$$N_{ij}^{\rm th}(\mu^\pm) = N'^{\rm th}_{ij}(\mu^\pm)\left(1 + \sum_{k=1}^{l} \pi_{ij}^k \xi_k^\pm \right) + \mathcal{O}(\xi_k^{\pm 2})\,, \tag{7.5}$$

$N'^{\rm th}_{ij}(\mu^\pm)$ and $N_{ij}^{\rm ex}(\mu^\pm)$ are the 'predicted' and 'observed' number of $\mu^\pm$ events at ICAL respectively, similar to Chapter 6. The systematics uncertainties included on the background events are same as in Chapter 6.

7.3 Results

We present the expected results on ICAL sensitivity to indirect detection in this section. As mentioned in Section 3.2, for the case of WIMP annihilation in the earth, the spin-independent WIMP

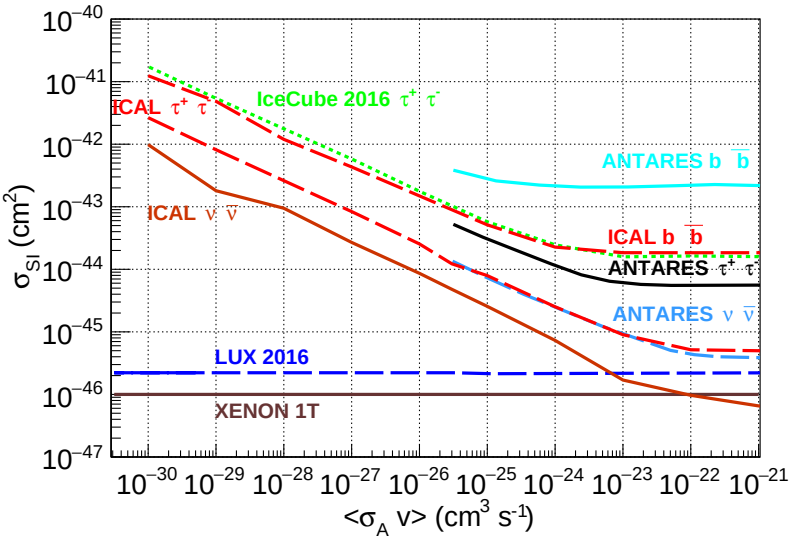

Figure 7.6: The expected 90 % C.L. sensitivity limits on $\sigma_{\rm SI}$ for ICAL as a function of annihilation cross-section $\langle\sigma_{\rm A}v\rangle$ for a 52.14 GeV WIMP annihilating through $\nu_\mu\bar{\nu}_\mu$ (dark orange solid), τ^+ and τ^- (red solid) and $b\,\bar{b}$ (red dashed). Also shown are upper limits at 90 % C.L obtained by various experiments IceCube [22] τ^+ and τ^- (green), ANTARES [23] τ^+ and τ^- (black), $b\,\bar{b}$ (cyan), $\nu_\mu\bar{\nu}_\mu$ (azure), LUX [24] (blue-dashed) and XENON-1T [25] (dark brown solid) have been shown for comparison. For ICAL, systematics have been included.

nucleon cross sections $\sigma_{\rm SI}$ and annihilation rate $\Gamma_{\rm A}$ are related by Eq. (3.4-3.5). The capture rate and the annihilation rate are not in equilibrium, and hence the annihilation rate depends on the $\sigma_{\rm SI}$ as well as on the annihilation cross section $\langle\sigma_{\rm A}v\rangle$. Figure 7.6 shows our expected sensitivity upper limits at 90 % C.L. in the $\sigma_{\rm SI}$ - $\langle\sigma_{\rm A}v\rangle$ plane for a WIMP mass of 50 GeV. As shown in Figure 3.4, the capture rate for the WIMP masses closer to iron mass is greatly enhanced and hence we expect stronger bounds. It is evident that for a 50 GeV WIMP, ICAL seems to put a stronger bound on $\sigma_{\rm SI}$ for a given $\langle\sigma_{\rm A}v\rangle$ for a given annihilation channel such as $\tau^+\,\tau^-$. For the obvious reasons, described in earlier sections, the harder channels $\nu_\mu\bar{\nu}_\mu$ and τ^+ and τ^- give stronger limits in comparison to the softer channel $b\,\bar{b}$.

In Figure 7.7 we present the expected 90 % C.L. sensitivity limits on the WIMP-nucleon SI interaction cross-section as a function of WIMP mass for 500 kt-years of ICAL exposure and compare it with the exclusion limits obtained from various other direct and indirect detection experiments. The direct detection experiment XENON-1T [25] gives the most stringent bound till date. Bounds from indirect searches are, in general, weaker in comparison to direct detection ex-

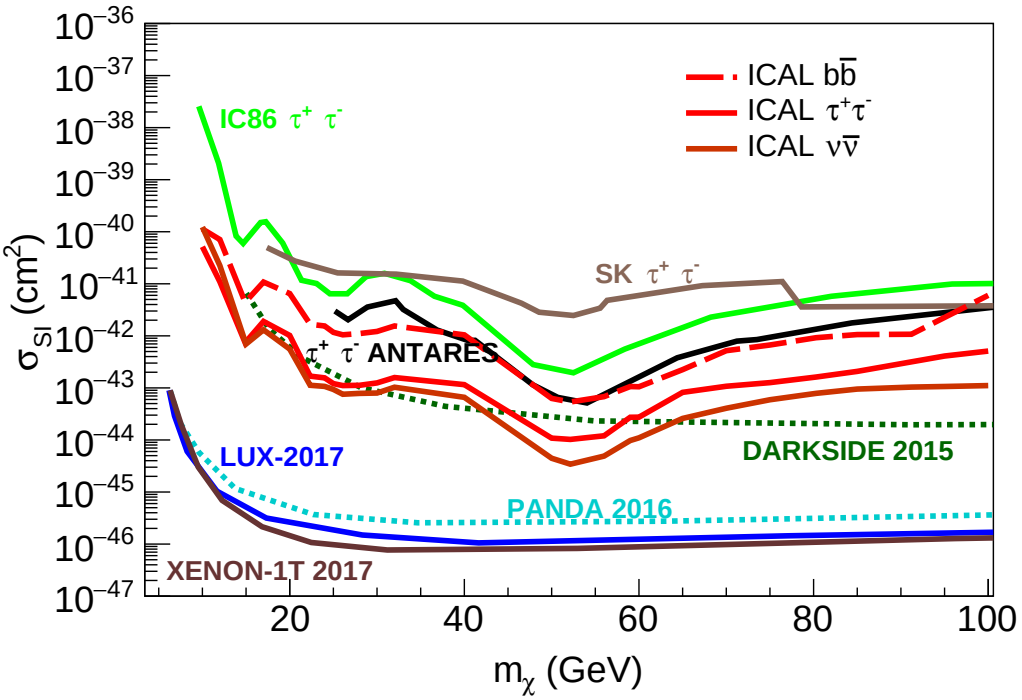

Figure 7.7: The expected 90% C.L. sensitivity limits on $\sigma_{\rm SI}$ as a function of WIMP mass, assuming a WIMP annihilation cross section $\langle\sigma_{\rm A}v\rangle = 3\times10^{-26}\ {\rm cm}^3\ {\rm s}^{-1}$. The displayed sensitivity limits are for the local dark matter density $\rho = 0.3\ {\rm GeVcm}^{-3}$. Among the indirect detection experiments, using neutrinos as a probe, ICAL provides the most stringent bound. The dip around 50 GeV in the limits obtained for Earth WIMP annihilation is a prominent feature in all experiments and is due to resonant capture of WIMPs on Fe. ICAL 90% C.L. sensitivity limits for $\nu_\mu\bar{\nu}_\mu$ (dark orange solid), $\tau^+\tau^-$ (red solid) and $b\ \bar{b}$ (red dashed) channels for WIMP annihilation in the Earth are shown; 90% C.L. upper limits from SK [26] for τ^+ and τ^- (brown), IceCube [22] τ^+ and τ^- (green) and ANTARES [23] τ^+ and τ^- (black). Also, shown are the limits obtained from DARKSIDE [27] (dark green dotted), LUX (blue), XENON-1T [25] (brown solid) and PANDA [28] (cyan dotted).

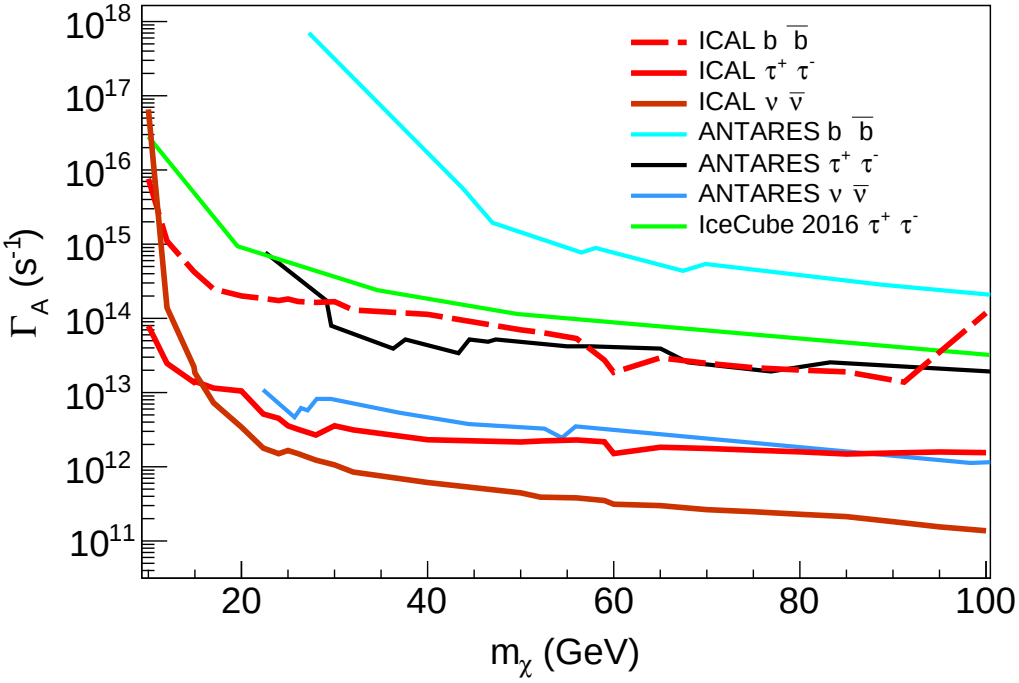

Figure 7.8: The expected 90% C.L. sensitivity limits on the annihilation rate ($\Gamma_{\rm A}$) as function of WIMP mass (m_χ) due to WIMPS annihilating into $\nu_\mu\bar{\nu}_\mu$ (dark orange), $\tau^+\ \tau^-$ (red solid) and $b\ \bar{b}$ (red dashed) with 100% branching ratio each. The limits are for 10 years of ICAL running. For comparison limits from various other experiments have been shown: ANATARES [23] $\tau^+\ \tau^-$ (black), $b\ \bar{b}$ (cyan), $\nu_\mu\bar{\nu}_\mu$ (azure) , and IceCube [22] τ^+ and τ^- for $m_\chi < 50$ GeV and W^+W^- for $m_\chi > 50$ GeV (green). We show these limits for a fixed $\langle\sigma_{\rm A}v\rangle = 3\times10^{-26}{\rm cm}^3{\rm s}^{-1}$.

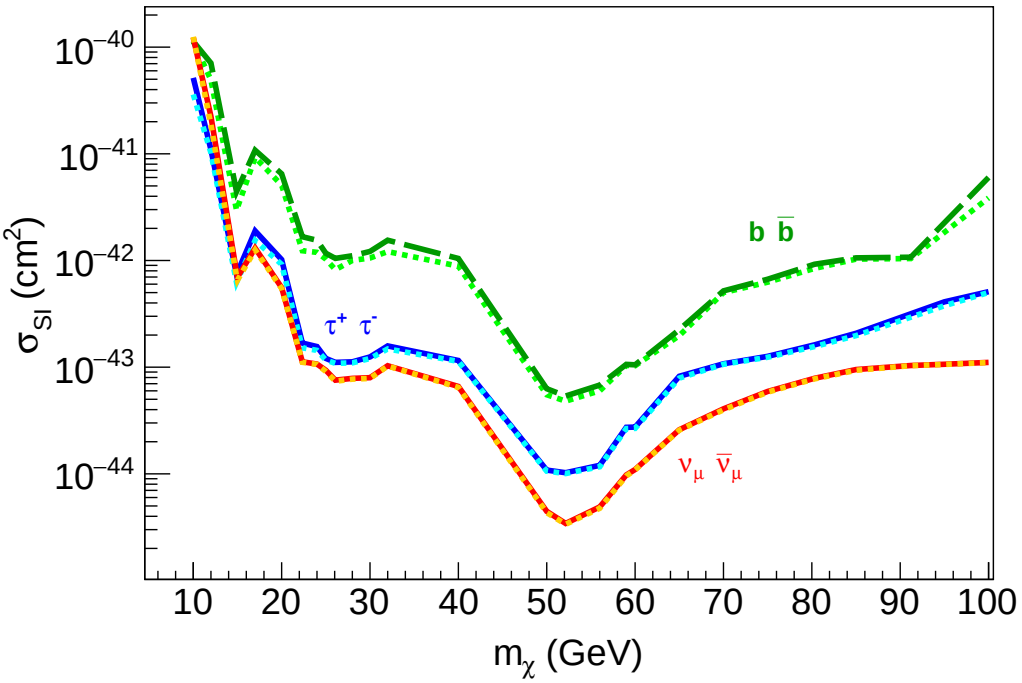

Figure 7.9: The expected 90% C.L. sensitivity limits for WIMP annihilation for different masses and two annihilation channels for WIMP annihilation in the earth are shown. The solid lines are the sensitivity limits calculated using detector systematics as described in Sec 6.2. The corresponding dotted lines are without systematics. The expected sensitivity limits are shown for $\nu_\mu\bar{\nu}_\mu$ in red solid (with systematics) and orange-dotted lines (without systematics), for τ^+ and τ^- are shown in blue solid (with systematics) and azure-dotted lines (without systematics) and for $b\,\bar{b}$ in dark green solid (with systematics) and light green-dotted lines (without systematics). The effect of systematics, as we expect, is to worsen the limits as expected. It can be seen that for the harder channels, the impact of systematics is seen to decrease and for $\nu_\mu\bar{\nu}_\mu$ channel it becomes almost non-negligible.

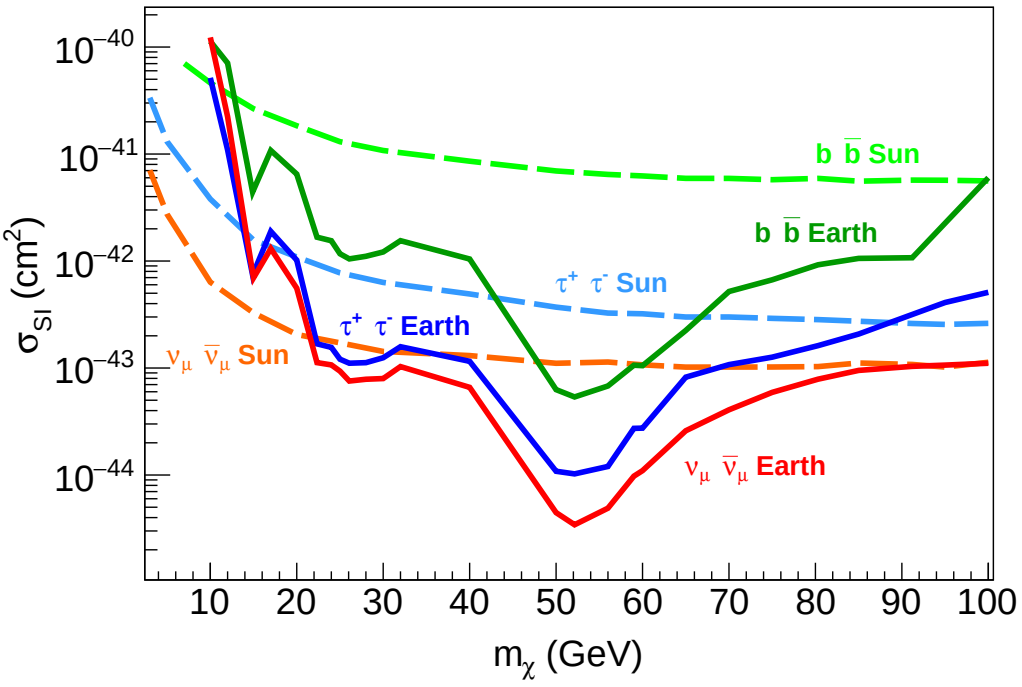

Figure 7.10: The expected 90% C.L. ICAL sensitivity limits on $\sigma_{\rm SI}$ as a function of m_χ for WIMP annihilation in the sun and earth. The expected sensitivity limits for the annihilation in the sun is shown for $\tau^+\ \tau^-$ (light blue dashed), $b\ \bar{b}$ (green dashed), and $\nu_\mu\bar{\nu}_\mu$ (dark orange dashed) with 100% branching ratio each. The expected sensitivity due to WIMP annihilation in the earth for channels $\tau^+\ \tau^-$ (blue solid), $b\ \bar{b}$ (dark green solid) and $\nu_\mu\bar{\nu}_\mu$ (red solid) are shown for comparison. For calculating earth's sensitivity, a WIMP annihilation cross section $\langle\sigma_{\rm A}v\rangle = 3\times10^{-26}{\rm cm}^3{\rm s}^{-1}$ has been assumed.

periments. However, among the neutrino detectors, ICAL seems to give the most stringent bound for the chosen WIMP mass range. For the WIMP masses close to iron mass, there is a resonant capture and hence enhance event rates resulting in a stronger bound.

For calculating sensitivity limits on annihilation rate and $\sigma_{\rm SI}$ in case of the earth, we assume an annihilation cross-section $\langle \sigma_{\rm A} v \rangle = 3 \times 10^{-26} {\rm cm}^3 {\rm s}^{-1}$. As discussed in Chapter 3, we have a relation between the annihilation rate $\Gamma_{\rm A}$ and SI WIMP-nucleon cross-section $\sigma_{\rm SI}$. Using the χ^2 analysis described in Section 7.2, we derive limits on the $\sigma_{\rm SI}$ as a function of WIMP mass m_χ. Using Eq. (3.4-3.5) from Section 3.1, we transported these sensitivity limits from $\sigma_{\rm SI} - m_\chi$ plane to $\Gamma_{\rm A} - m_\chi$ plane. Figure 7.8 shows the expected sensitivity limits at 90 % C.L. calculated on the WIMP annihilation rate for annihilation in the earth through channels $\nu_\mu \bar{\nu}_\mu$, τ^+ and τ^- and $b\ \bar{b}$. Results from other experiments are also shown for comparison[2]. Again, we can see that for chosen WIMP mass range, ICAL presents a stronger bound on the WIMP annihilation rate for a given channel. Again, $\nu_\mu \bar{\nu}_\mu$ bounds are the strongest among the three channels considered.

In Figure 7.9 we present the effect of systematic uncertainties on the expected 90 % C.L. sensitivity limits on the WIMP-nucleon SI interaction cross-section. The dashed lines are the limits calculated while taking only statistical uncertainties. As expected, the effect of systematic uncertainties is to worsen the limits as can be seen from the figure.

Finally, in Fig 7.10, we compare the expected ICAL sensitivity limits due to WIMP annihilation in the sun and earth. The sensitivity limits shown here for the sun are the as in Fig .6.8.

7.4 Summary

The analysis presented in this work is a part of ongoing studies to probe the physics potential of the upcoming ICAL detector. Neutrinos arising out of WIMP annihilations in the earth could be used to probe dark matter signatures. Such searches would be complementary to direct searches for WIMP. We presented a study of prospects of detecting muon events at ICAL arising due to WIMP annihilation in the earth for $\nu_\mu \bar{\nu}_\mu$, $\tau^+ \tau^-$ and $b\ \bar{b}$ annihilation channels. Employing an effective at-

[2]For SK latest preliminary results please see [29].

mospheric background suppression scheme, the expected 90 % C.L. sensitivity limits obtained for SI WIMP-nucleon cross-section for the case for the earth is better than present neutrino detection experiments.

Chapter 8

Searches for DM in the galactic centre

The milky way galaxy is inlaid in a DM halo with a varying density profile, peaking at the centre. At these centres of WIMP concentration, annihilation could happen and, through various annihilation channels, produce Standard Model (SM) particles which subsequently give rise to neutrino fluxes. These neutrinos can escape the interior of galaxy, oscillating along the way, and reach earth where they could produce detectable signal. In this chapter, we study prospects of detecting muons events at ICAL due to WIMP annihilation in the region near galactic center. The number of expected events is related to velocity averaged WIMP annihilation cross section $\langle \sigma v \rangle$ and WIMP mass and hence could be used to constrain these parameters.

Galactic centre (GC) is an extended source unlike other astrophysical sources, such as the sun, which are (nearly) point-like sources. These neutrinos will travel to the ICAL detector and interact with the detector medium to produce a detectable signal, *i.e.*, muons. The searches for muon events arising at ICAL due to WIMP annihilations in the sun and the earth have been considered in chapter 6 and chapter 7, respectively. In this chapter, we consider the events arising at ICAL due to WIMP annihilations in the galactic centre. Prospects of detecting events arising out of WIMP annihilation from the diffused dark matter halo have been done in Ref. [171]. In this chapter which is based on [4], we focus on the annihilations in the centre of milky way galaxy and through a full detector simulation.

For this analysis, we consider WIMP masses (m_χ) between 5 and 100 GeV. The WIMP

annihilation channel considered are $\tau^+\tau^-$, $b\,\bar{b}$, $\mu^+\mu^-$ and $\nu\,\bar{\nu}$. The WIMP annihilation could be into various channels with a branching ratio. However, as discussed in the previous chapters, the branching ratio of these channels depend on a particular WIMP model considered. In order to probe a generic scenario, we choose 100 % branching ratio for each of the annihilation channels and estimate expected sensitivity limits for ICAL.

Several indirect detection experiments have provided limits on the neutrino fluxes arising out of WIMP annihilation in the galactic centre, such as IceCube [30], ANTARES [31], and SK [26]. The organization of this chapter is as follows : In section 8.1 we describe the signal search region and the optimisation scheme for the signal expectation calculations. This is followed by section 8.2 where the atmospheric background suppression scheme is discussed in detail and a comparison of expected signal and the suppressed background is presented for various annihilation channels. Thereafter, in section 8.3, we briefly mention the statistical analysis scheme and present our main results for the search for DM in the GC in the section 8.4 and finally conclude in section 8.5.

8.1 Signal and the background

Fig. 10.1 shows the signal search cone for WIMP annihilation in the galactic centre. The angular separation of produced neutrinos with respect to the galactic centre is denoted by Ψ which is also the angular separation of the parent WIMP with respect to GC (Please refer Fig. 3.6). The neutrinos on reaching ICAL will interact with detector iron and produce muons tracks whose separation with respect to the GC is denoted by Ψ_μ. The scattering angle ($\theta_{\nu\mu}$) of the muons with the parent neutrino is a function of neutrino energy and hence $\theta_{\nu\mu}$ can be mapped to a function of m_χ and annihilation channel. As discussed in chapter 3, the neutrino fluxes for WIMP annihilation in GC, among other factors, depend on velocity averaged WIMP annihilation cross section $\langle\sigma_A\ v\rangle$ and J-Factors $\mathcal{J}(\Delta\Omega)$. The value of Ψ, and hence the corresponding $\Delta\Omega$, has to be chosen such that it yields the maximum sensitivity for that specific WIMP mass, annihilation channel and DM density profile considered. The value of Ψ is chosen as follows. For a specified m_χ, annihilation channel,

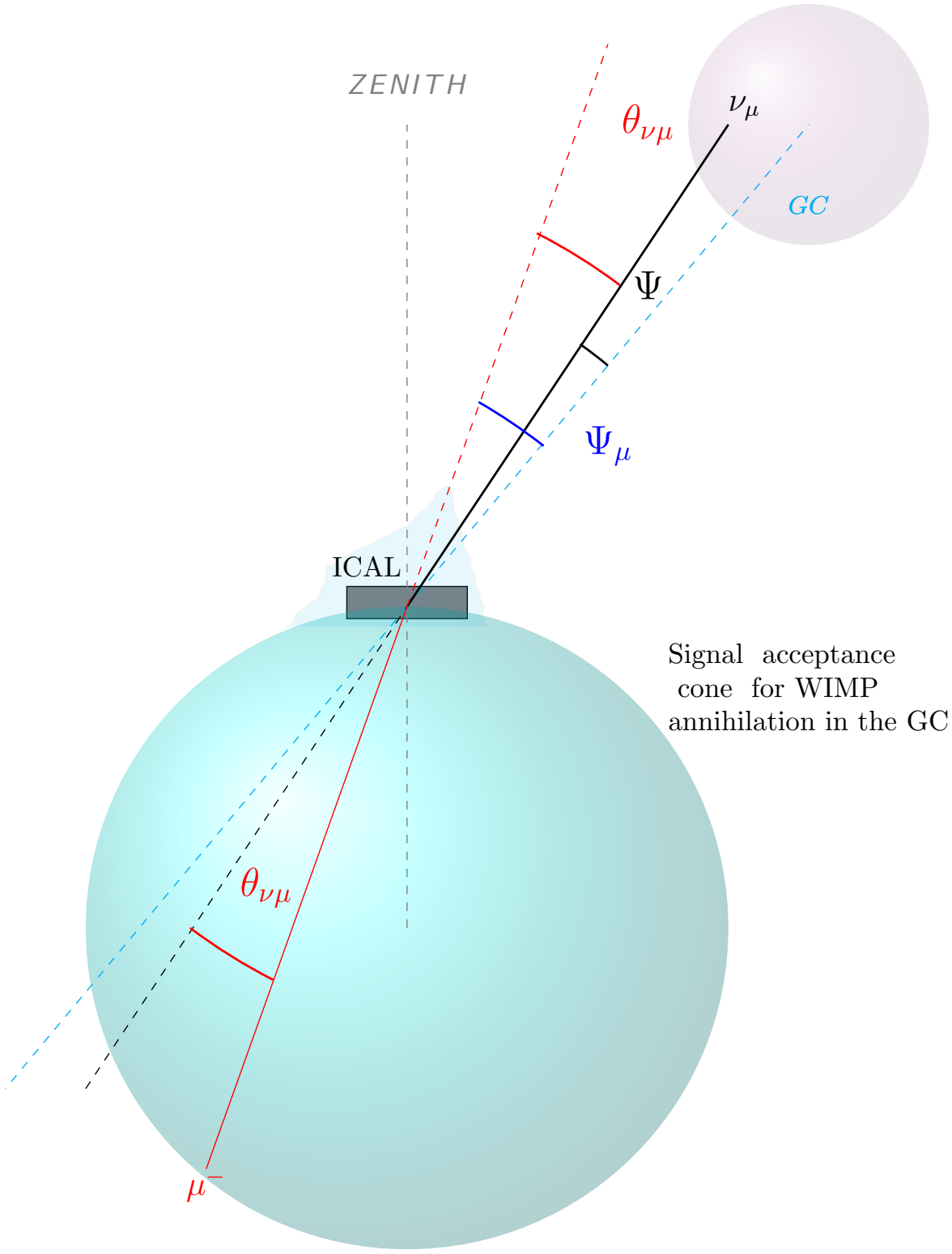

Figure 8.1: The signal search region for the WIMP annihilation in the galactic centre. The figure is not to scale. The angular separation Ψ has to be optimised so as to maximise the ICAL sensitivity to this search.

DM density profile and an benchmark value of $\langle \sigma_A \, v \rangle$, signal neutrino fluxes are calculated using Eq. 3.14. For the other values of $\langle \sigma_A \, v \rangle$, the events are scaled linearly and then used for further statistical analysis. For calculating the background events, we use the cone acceptance criterion similar to the approach used in Chapter 6. We choose Ψ_μ value to be equal to Ψ, and then using this as a cone half angle, accept the background events within the solid cone given by solid angle $\Delta\Omega = 2\pi(1 - \cos\Psi_\mu)$. It is to be noted that Ψ and Ψ_μ are related by $\theta_{\nu\mu}$ by the equation:

$$\Psi_\mu = \Psi \pm \theta_{\nu\mu}. \tag{8.1}$$

The value of $\theta_{\nu\mu}$ depends on the energy of the parent neutrino and has a probability distribution with $\theta_{90} \sim 35^\circ$ for m_χ = 5 GeV. By choosing, $\Psi = \Psi_\mu$ for accepting the signal and the background, we are choosing only the signal and background events which are essentially coming from the direction of parent neutrino. This approximation is valid for high energy neutrinos as their associated muons are essentially in the same direction, but for the low energy neutrinos this angle can be quite large as shown in Section 6.1. Therefore, a better analysis would require optimisation over both Ψ and Ψ_μ. However, choosing a single Ψ parameter, we substantially reduce the computation involved. Also, Ψ_μ is the only observable for our case, as Ψ reconstruction depends on the muon information, *i.e.*, Ψ_μ itself. For a given Ψ_μ (and hence Ψ) the background and the signal events are generated and used for the statistical analysis. $\mathcal{J}(\Delta\Omega)$ involved in the WIMP annihilation fluxes are calculated for various Ψ values shown in Fig. 8.2[1].

8.2 Atmospheric neutrino background suppression

The atmospheric neutrinos pose a severe background to the searches of annihilation in the GC, similar to the previous Chapters 6 and 7. We follow the same approach, as was done for the case of

[1]The value of Ψ should be optimised for various WIMP masses, annihilation channels, and DM density profiles. However, for the sake of computational simplicity, we calculate signal and background for set of Ψ values shown in Fig. 8.2 and quote expected ICAL sensitivity and leave optimisation for a later work. The Ψ values used in this analysis are taken from Table 1 of Ref. [31] for masses 25, 50, 90 and 100 GeV. For intermediate masses, Ψ value is interpolated and for m_χ < 25 GeV, Ψ value is obtained through extrapolation.

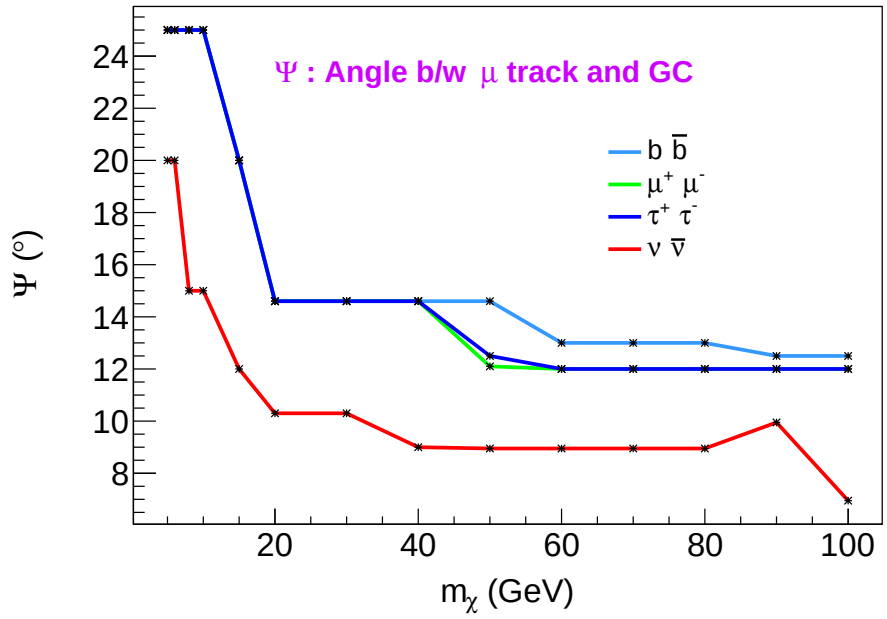

Figure 8.2: The Ψ_μ values as a function of m_χ used for the analysis in this work.

the sun (Section 6.1) to handle the background. As mentioned in the previous section, we accept the signal and the background events that fall within a solid angle of cone $\Delta\Omega = 2\pi(1 - \cos\Psi_\mu)$. The signal neutrinos are, by definition, from the galactic centre region, such that the axis of the signal acceptance cone coincides with the angular direction $\Psi_\mu = 0$[2]. In a running experiment, only the background events whose Ψ_μ fall within this acceptance cone and accepted for analysis. Since we are dealing with Monte-Carlo generated data, we assign a probability that a particular background event has originated from the direction of the galactic centre. In order to apply this probability, or in other words assign a weight to the background events we do the following. The position of galactic centre remains approximately fixed in terms of the equatorial coordinates. However, in terms of the horizontal coordinates, it keeps changing. We track the motion of the galactic centre (approximated by the position of Sagittarius A*) with the help of Stellerium[3] and PyAstronomy[4]and record it's visibility at ICAL's coordinates in terms of zenith and azimuthal angles. The recorded values are stored in a histogram and then normalised by the total number of recorded values to yield what we

[2]Hereafter, $\Psi_\mu = \Psi$, unless stated otherwise, will be assumed throughout this chapter.
[3]http://stellarium.org/
[4]https://github.com/sczesla/PyAstronomy

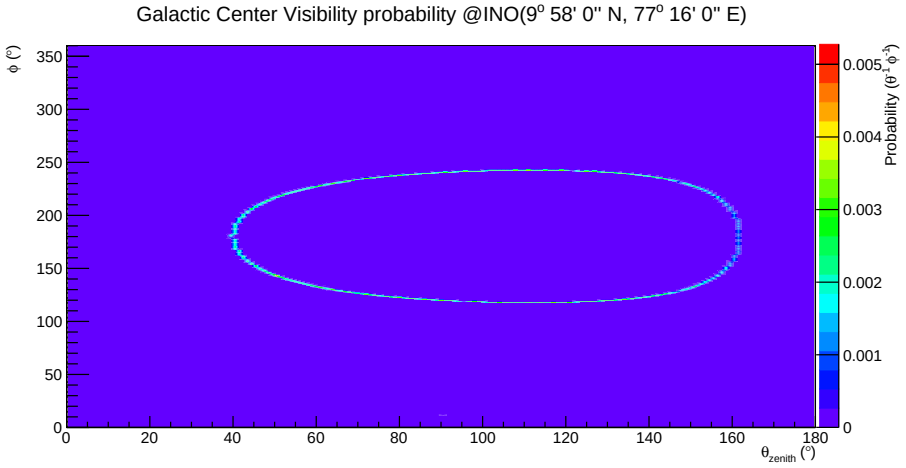

Figure 8.3: The galactic centre exposure function in terms of horizontal coordinates θ and ϕ.

call as "galactic exposure probability". The galactic exposure probability in terms of zenith angle θ and azimuth angle ϕ is shown in Fig. 8.3. It can be seen that for INO's geographical coordinates, the galactic centre remains between directions $\phi = 120°$ and $\phi = 240°$. In the vertical direction, the visibility of G.C. is more pronounced and varies between $\theta = 40°$ and $\theta = 160°$. Using the GC's visibility (or exposure) from this distribution, we assign a probability to a background event which is 'signal like', *i.e.*, the background events coming from the direction of GC and having energies less than m_χ, as such background events are indistinguishable from the signal events due to WIMP annihilation. As done in the previous chapters, we do this background suppression at the neutrino generator stage rather than at the reconstruction stage in order to simplify our analysis. We proceed as follows : We take a background event which has an energy and angle information given by GENIE output and assign a cone to this event, such that the axis of the cone coincides with the muon direction and cone half angle is given by the appropriate Ψ_μ. On this cone surface, we calculate the galactic exposure integral probability which corresponds to the probability of the given background event having come from the direction of galactic centre region. This probability is assigned as a weight to the background muon event and is carried forward for further steps which include event reconstruction and statistical analysis.

Now we present plots which represent the expected signal and the suppressed background events at ICAL for 500 kt-year of iron mass. Using the prescription in the chapter 5, we generate

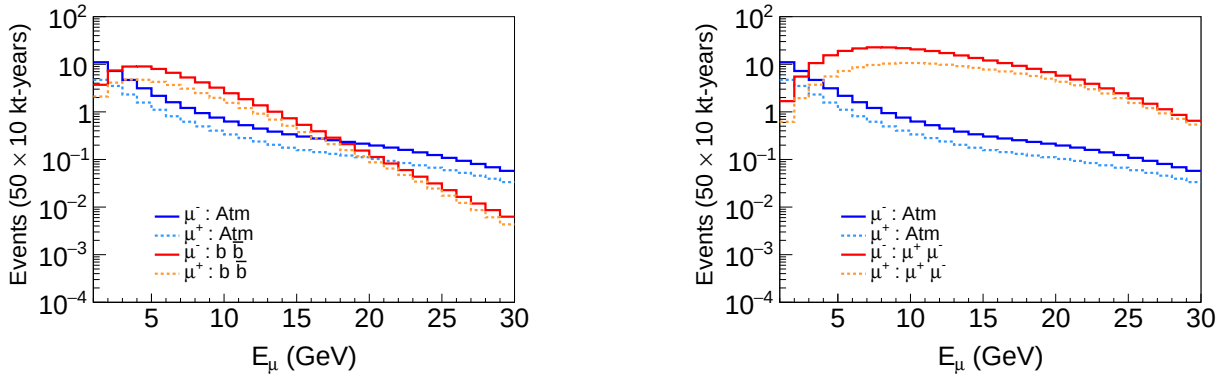

Figure 8.4: μ^- event distribution at ICAL due to annihilation of 30 GeV WIMP in GC and the corresponding suppressed atmospheric neutrino background. The signal μ^- events corresponding to channels $b\bar{b}$ (LEFT) and $\mu^+\mu^-$ (RIGHT) have been shown in red. The μ^+ events for the channels are shown in dotted orange lines. μ^- and μ^- events for the suppressed atmospheric background is shown in solid blue and light blue dotted lines for both the channels. These events are for 50 $\times$ 10 kt-years of ICAL exposure and signal expectation is assuming $\langle\sigma_A\, v\rangle = 5 \times 10^{-21}\mathrm{cm}^3\mathrm{s}^{-1}$ and NFW density profile.

events for the signal and background cases separately. Fig. 8.4 and Fig. 8.5 show the muon events at ICAL due to annihilation of 30 GeV WIMP for $b\ \bar{b}$, $\mu^+\mu^-$, $\tau^+\tau^-$ and $\nu_\mu\bar{\nu}_\mu$ channels and assuming NFW DM density profile. The signal neutrino fluxes are calculated using [7] for different annihilation channels as discussed in Section 3.3. Also shown are the corresponding suppressed background using the prescription described above.

The signal events shown in these figures correspond to a rather large value of $\langle\sigma_A v\rangle = 5 \times 10^{-21}\mathrm{cm}^3\mathrm{s}^{-1}$. The events for BURKERT profile are less than NFW for the same value of assumed parameters. Therefore, the expected sensitivity to indirect searches for WIMP annihilation in the GC is more for NFW than BURKERT and we will see that it is indeed the case in the results section. For the case of the EINASTO density profile, the events are marginally smaller and hence not shown here for brevity.

For obtaining each of the event distributions, a 100% branching ratio was considered. The solid red lines represent the neutrino events and orange dotted lines are for antineutrino events. For the chosen values of $\langle\sigma_A v\rangle$, the signal events are below the suppressed background events for a few GeVs and then go above the background thereafter. This feature, as shown in Figs. 8.4 and 8.5, is true for all the channels except $b\bar{b}$ for which the events fall below the background around

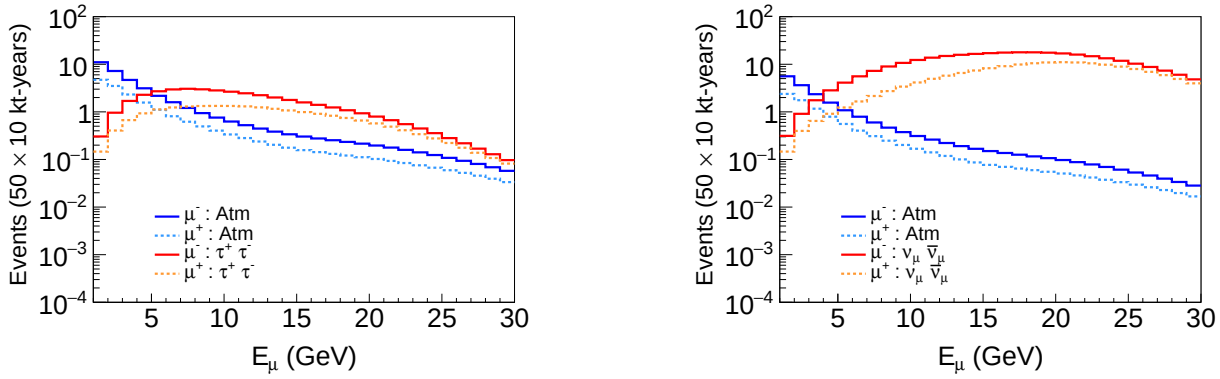

Figure 8.5: μ^- event distribution at ICAL due to annihilation of 30 GeV WIMP for $\tau^+\tau^-$ (LEFT) and $\nu_\mu\bar{\nu}_\mu$ (RIGHT) channels. The colour convention, detector exposure parameter values are same as in Fig. 8.4.

20 GeV. Among the four channels, $\nu_\mu\bar{\nu}_\mu$ channel produces the hardest neutrino (and antineutrino) spectra. It can also be noted that the corresponding background events are less for this channel in comparison to others. The reason is same as we have discussed earlier chapters. The neutrino channel give a harder neutrino spectra and hence the produced muons will have a smaller scattering angle and a narrow background acceptance cone, which is manifested in a smaller value of Ψ_μ. In nature, however, we expect WIMP to annihilate through a mixture of these channels and hence the corresponding event spectra would be modified.

8.3 Statistical Analysis

We proceed with the statistical analysis similar to the previous chapters. We perform a χ^2 analysis to obtain expected sensitivity limits on velocity averaged WIMP annihilation cross section $\langle\sigma_A\, v\rangle$ for given WIMP masses. We simulate the prospective data at ICAL for no WIMP annihilation and fit it with a theory where WIMP annihilate in the GC to give neutrinos. Therefore, the "data" or "observed" events correspond to only the reduced atmospheric neutrino backgrounds, whereas the "theory" or "predicted" events comprise the sum of the signal events due to WIMP annihilation in the GC as well as the atmospheric neutrino background events. The χ^2 function is defined as:

$$\chi^2 = \chi^2(\mu^-) + \chi^2(\mu^+)\,, \tag{8.2}$$

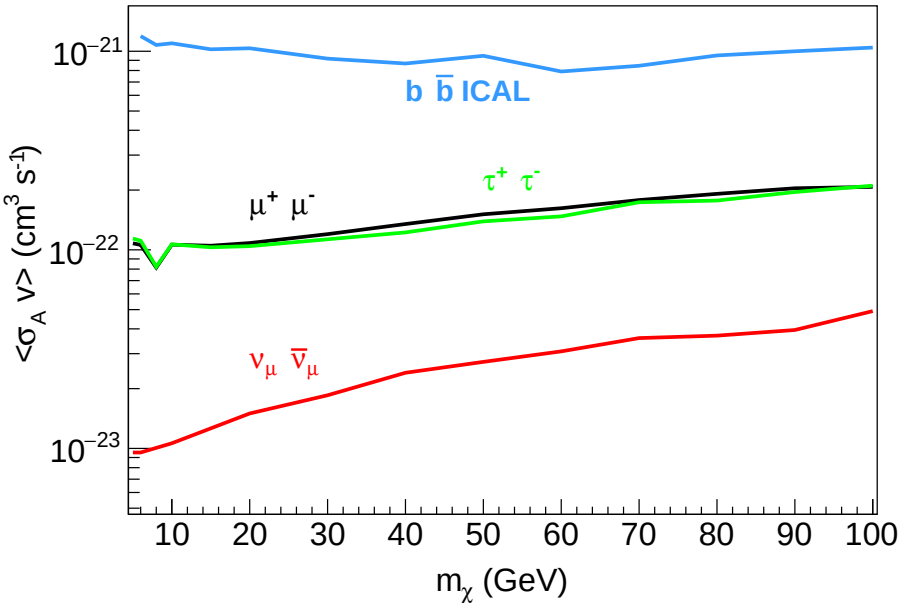

Figure 8.6: The 90% C.L. expected ICAL sensitivity for $\langle\sigma_A v\rangle$ as a function of m_χ for $b\bar{b}$ (light blue), $\mu^+\mu^-$ (black), $\tau^+\tau^-$ (green) and $\nu_\mu\bar{\nu_\mu}$ (red) annihilation channels. The shown result is assuming 100 % branching ratio for each annihilation channel and NFW DM density profile. This is for 50 $\times$ 10 kt-years of ICAL exposure and systematic uncertainties have been considered.

where

$$\chi^2(\mu^\pm) = \min_{\xi_k^\pm} \sum_{i=1}^{N_i} \sum_{j=1}^{N_j} \left[2\left(N_{ij}^{\rm th}(\mu^\pm) - N_{ij}^{\rm ex}(\mu^\pm) \right) + 2N_{ij}^{\rm ex}(\mu^\pm) \ln\left(\frac{N_{ij}^{\rm ex}(\mu^\pm)}{N_{ij}^{\rm th}(\mu^\pm)} \right) \right] + \sum_{k=1}^{l} \xi_k^{\pm 2}\,, \quad (8.3)$$

$$N_{ij}^{\rm th}(\mu^\pm) = N'^{\rm th}_{ij}(\mu^\pm)\left(1 + \sum_{k=1}^{l} \pi_{ij}^k \xi_k^\pm \right) + \mathcal{O}(\xi_k^{\pm 2})\,, \quad (8.4)$$

$N'^{\rm th}_{ij}(\mu^\pm)$ and $N_{ij}^{\rm ex}(\mu^\pm)$ are the 'predicted' and 'observed' number of $\mu^\pm$ events at ICAL respectively, similar to the previous chapters. The systematics uncertainties included here are same as in Section 6.2.

8.4 Expected sensitivity for ICAL

Now, we present the main results for the expected sensitivity of ICAL for WIMP annihilation in the GC. Fig. 8.6 shows the 90% C.L. expected sensitivity limits on $\langle\sigma_A v\rangle$ as a function of

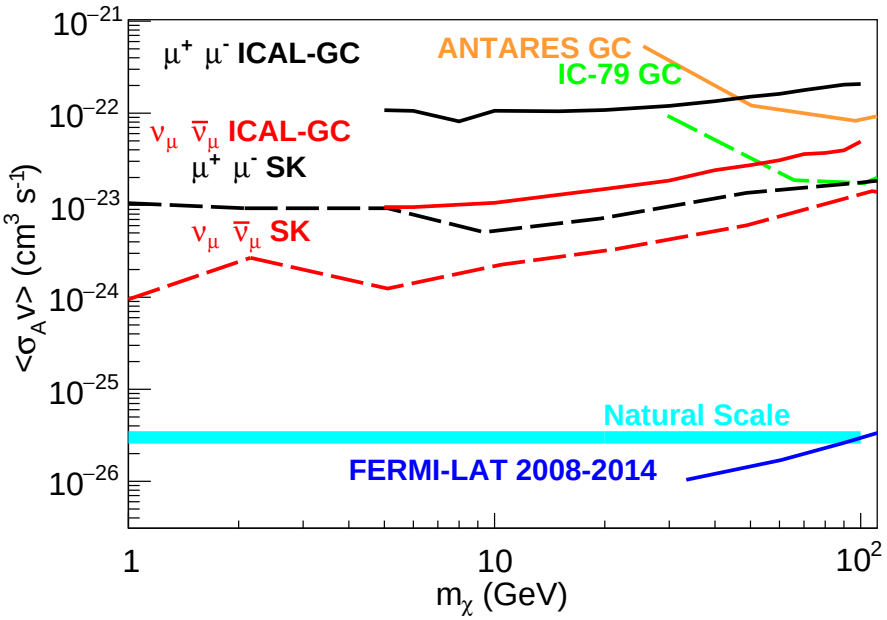

Figure 8.7: The 90% C.L. expected ICAL sensitivity for $\langle\sigma_A v\rangle$ as a function of m_χ assuming 100% branching ratio each for the channels $\mu^+\mu^-$ (black solid line) and $\nu_\mu\bar{\nu_\mu}$ (red solid) for 50 $\times$ 10 kt-years of ICAL exposure and assuming NFW density profile. The 90 % C.L. upper limit obtained by other experiments are also shown : SK [29] are shown for $\mu^+\mu^-$ (black dashed line) and $\nu_\mu\bar{\nu_\mu}$ (red dashed), IceCube [30] for channel $\tau^+\tau^-$ (green) and ANTARES [31] for $\tau^+\tau^-$ (brownish yellow) channel. The observed e^+ e^- excesses and the interpretations of them as dark matter self annihilations, limit obtained by FERMI-LAT [32] (blue) is also shown. The thick cyan line represents the natural scale for which WIMP is a thermal relic from the early universe.

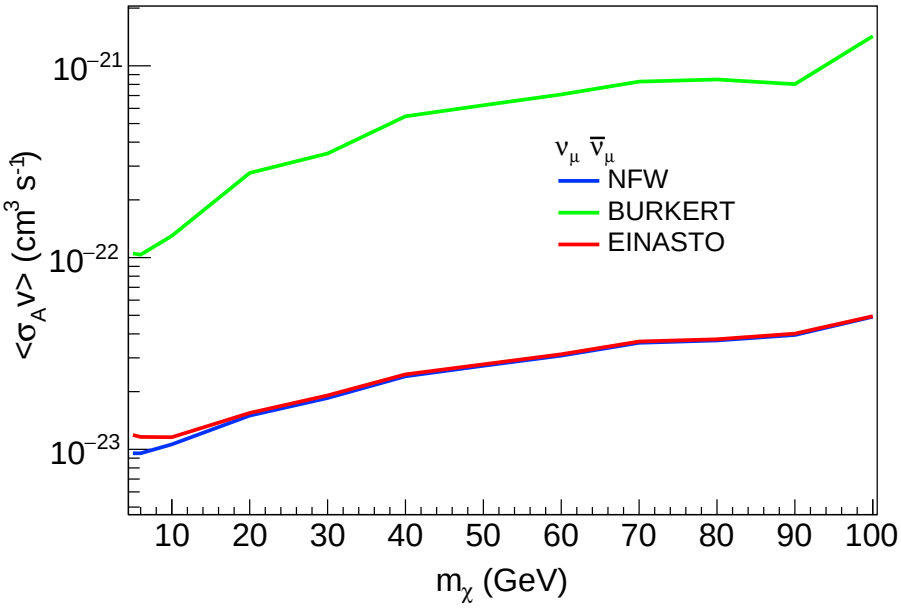

Figure 8.8: The 90% C.L. expected ICAL sensitivity for $\langle\sigma_A v\rangle$ as a function of m_χ assuming 100% branching ratio for $\nu_\mu\bar{\nu_\mu}$ channel and for 50 $\times$ 10 kt-years of detector exposure are shown for NFW (blue). EINASTO (red) and BURKERT (green) dark matter density density profiles.

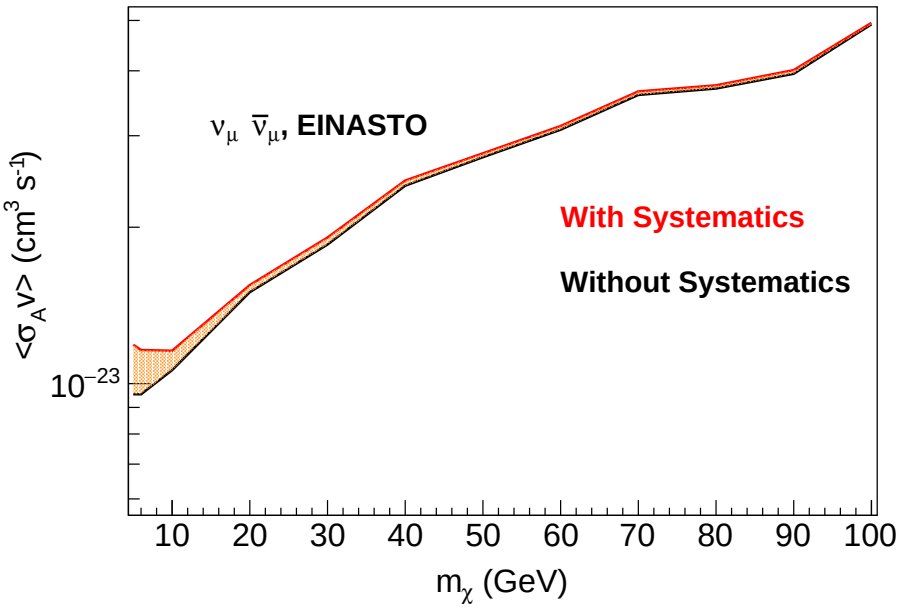

Figure 8.9: The 90% C.L. expected ICAL sensitivity for $\langle\sigma_A v\rangle$ as a function of m_χ assuming 100% branching ratio for $\nu_\mu\bar{\nu_\mu}$ channel, for 50 $\times$ 10 kt-years of detector exposure and EINASTO dark matter density density profile. The result considering systematic uncertainties (red solid line) and with only statistical uncertainties (black solid line) are shown and the area in the between has been shaded for visual clarity.

m_χ for 500 kt-years of detector exposure. The expected sensitivity are obtained assuming NFW DM density profile. It can be seen that for the reasons described earlier, the expected sensitivity limits for $\nu_\mu\bar{\nu_\mu}$ (red) annihilation channel is the best and $b\bar{b}$ (light blue) channels is the worst. The annihilation of WIMP through the leptonic channels like $\mu^+\mu^-$ (black) and $\tau^+\tau^-$ (green) channels give comparable bounds. Since the harder channel has higher energy neutrinos than that of $b\ \bar{b}$ channel, the expected sensitivity limits for these channels are better. For each of the channels, we observe that the expected sensitivity decreases with the increase in WIMP mass. This is mainly because the signal fluxes decreases with the increasing WIMP mass as seen by Eq. 3.14 in Chapter 6. With the increase in WIMP mass, we accept fewer background events as smaller Ψ_μ values needed for larger m_χ values (and the hence the narrower acceptance cone), the decrease in signal fluxes dominates which results in an overall decrease in the sensitivity.

In Fig. 8.7, the 90% C.L. expected sensitivity for $\langle\sigma_A v\rangle$ as a function of m_χ assuming 100% branching ratio each for the channels are shown again and compared with the existing experimental limits in this WIMP mass region. The annihilation channels $\mu^+\mu^-$ and $\nu_\mu\bar{\nu}_\mu$ are shown in solid black and red lines, respectively. The ICAL limits are for 500 kt-years of detector exposure and assuming NFW density profile. The 90 % C.L. upper limit obtained by other experiments are also shown for comparison. The 90% C.L. upper limit obtained by SK [29] are shown for $\mu^+\mu^-$ (black dashed line) and $\nu_\mu\bar{\nu_\mu}$ (red dashed) channels. The SK limits have been obtained for the search for DM induced diffused neutrinos in the Milky Way galaxy. The trend is similar to the expected ICAL sensitivity limits. The expected sensitivity of ICAL for $\langle\sigma_A v\rangle$ are found to be an order of magnitude worse than that of SK for the corresponding channels. Several factors could be at play. The signal expectation calculated for ICAL are using PPPC4DMID [7], whereas SK uses DarkSUSY [172] for signal expectation calculation. It has been found that PPPC4DMID fluxes gives more conservative limits in comparison to DarkSUSY[5]. Also, the signal to background

[5]Preliminary expected sensitivity limits calculated using WIMPSIM gives results which are comparable to SK for the same detector exposure. A detailed analyses is under way to understand this further. However, for the results presented in this thesis we restrict ourselves to the fluxes calculated by Cirelli et al. [7] Also see Ref. [173], where a comparison between different DM flux calculating packages has been done.

optimisation could be improved further. For a very simple analysis [6] done for an iron detector using DM induced neutrino fluxes see [171]. Also shown are the much weaker 90% C.L. upper limits on $\langle \sigma_A v \rangle$ for $\tau^+\tau^-$ channel for IceCube [30] (green) and ANTARES [31] (brownish yellow). The observed e^+ e^- excesses by FERMI-LAT [32] satellite and its interpretations as dark matter self annihilations, the shown limit (blue) have been obtained. The natural scale for which WIMP is a thermal relic from the early universe is also indicated by a thick cyan coloured line. Depending on the choice of model, corresponding limits obtained from the collider searches could be very stringent. For instance, see Figure 12(c) of Ref. [166] for ATLAS 95% C.L. exclusion limits.

In Fig. 8.8, we compare the expected 90 % C.L. ICAL sensitivity limits for various DM density profiles. The expected results for NFW (blue) and EINASTO (red) profiles are almost the same, except for the region below 10 GeV. The expected sensitivity limits for BURKERT are worse than EINASTO and NFW as it predicts less concentration of DM in the galactic centre and hence lower signal expectation.

Finally, in Fig. 8.9, we show the effect of systematic uncertainties on the expected sensitivity limits. The 90% C.L. expected sensitivity for $\langle \sigma_A v \rangle$ as a function of m_χ, assuming 100% branching ratio for $\nu_\mu \bar{\nu_\mu}$ channel and for for 500 kt-years of detector exposure is presented with systematic uncertainties included (solid red line) and without systematics (solid black line) for EINASTO dark matter density profile. The area in the between has been shaded for visual clarity. It can be seen that the effect of uncertainty is negligible for this DM profile except for the lower WIMP masses. This is easy to understand with the following reasoning. The systematic uncertainty has been applied only on the background and we see that the background suppression improves as the m_χ increases, and hence the effect of systematic uncertainties decrease with the increase in m_χ. This trend can be seen in case of other DM density profiles as well.

[6] The analysis done in [171] does not make use of realistic ICAL detector characteristics and hence is a not a realistic result.

8.5 Conclusions

In this chapter, we discussed the prospect of detecting neutrino fluxes due to WIMP annihilation in the G.C. The 90% C.L. expected sensitivity for ICAL in the $\langle\sigma_A v\rangle$ - m_χ parameter space was presented for $b\bar{b}$, $\mu^+\mu^-$, $\tau^+\tau^-$ and $\nu_\mu\bar{\nu_\mu}$ WIMP annihilation channels assuming 100 % branching ratio each. Among the channels considered, the 90% C.L. expected sensitivity limits for $\nu_\mu\bar{\nu_\mu}$ channel and NFW profile was found to be the most stringent. ICAL expected sensitivity was found to be better than the current limits from indirect detection experiments like IceCube and ANTARES for the range of $m_\chi \in (5, 100)$ GeV. The experimental limits obtained by SK are better than the corresponding ICAL sensitivity limits by more than an order of magnitude. A comparison of expected sensitivity for various DM density profiles was also presented. Also shown was the effect of systematics on the expected sensitivity for a given DM density profile and an annihilation channel in Fig 8.9. With a better Ψ_μ optimisation scheme for the signal expectation calculation and background suppression, ICAL expected sensitivity can be improved further.

Chapter 9

Neutrino Physics with Non-Standard Interactions at INO

9.1 Introduction

In this chapter, we will study in detail the impact of NSI on the atmospheric neutrino signal in the ICAL detector at INO. We analyse the prospective data at ICAL in terms of the measured muon energy and muon angle through a binned χ^2 analysis. ICAL is expected to also measure the energy deposited in the associated hadron shower. Inclusion of the hadron energy information improves the energy reconstruction of the events and hence in general improves the sensitivity of ICAL [66]. We have not included the hadron energy information in this work. This is being studied in a follow-up work by the INO collaboration.

For this work, we use the Nuance neutrino event generator with the ICAL detector geometry for generating muons from atmospheric neutrinos. The ICAL energy and angle resolutions and reconstruction and charge identification efficiencies are obtained from the Geant4-based detector simulation code developed for ICAL as described in Chapter 5. We generate muon events in the range (1-100) GeV and show the increase in the sensitivity to NSI parameters with the increase of the neutrino energy, and hence the muon energy, as was pointed out in Ref. [55]. We will quantify the extent of modification in the expected muon signal at ICAL in the presence of NSI. Using that

we will study the expected limits that ICAL could impose on NSI parameters if there is no evidence of NSI in the data. If on the other hand the NSI parameters are large enough, we would see a signal of new physics in the ICAL data. We give the lower limit on the NSI parameters which is needed in order to allow their discovery in ICAL at any given C.L.. Likewise, the presence of NSI could change the sensitivity of ICAL to other neutrino oscillation parameters. In particular, we will show how the NSI parameters alter the mass hierarchy sensitivity in this class of experiments and present the revised sensitivity limits.

The chapter is organised as follows. In Section 9.2, we discuss the neutrino oscillation probabilities in the presence of NSI. In particular, we study the impact of NSI on the difference in the probabilities between the NH and IH cases. In Section 9.3, we describe the simulation techniques, and the statistical analysis procedure. We present our main results in Section 9.4. All results are shown for 500 kt-year of data in ICAL. Subsection 9.4.1 is devoted to study the impact of NSI on the mass hierarchy sensitivity of ICAL. In Subsections 9.4.2, 9.4.3, and 9.4.4, we discuss the expected constraints on NSI parameters, the expected lower limit allowing for discovery of NSI, and the allowed areas in NSI parameters space, respectively. We end in Section 9.5 with our conclusions.

9.2 Impact of NSI on Oscillation Probabilities

As outlined in the introduction, an extension of the Standard Model of particle physics in its gauge sector and/or particle sector is likely to give rise to additional (effective) interactions between Standard Model particles. In particular, in this work, we are concerned with such interactions experienced by the neutrinos when they propagate inside earth matter. This effective term in the Lagrangian is of the form [174–177]

$$\mathcal{L}_{\text{NSI}} = -2\sqrt{2}G_F\epsilon^{fC}_{\alpha\beta}(\overline{\nu_\alpha}\gamma^\mu P_L\nu_\beta)(\overline{f}\gamma_\mu P_C f)\,, \tag{9.1}$$

where f is a fermion, $P_C = (1 \pm \gamma_5)/2$ ($C = R, L$) are the chiral projection operators, G_F is the Fermi constant, and $\epsilon^{fC}_{\alpha\beta}$ are the corresponding NSI parameters. Since earth matter is made up of the first generation fermions only, the NSI parameters corresponding to e, u, and d are the only ones which contribute towards modifying the neutrino propagation inside the earth. For the neutral-current NSI what is relevant is the sum $\epsilon^{f}_{\alpha\beta} = \epsilon^{fL}_{\alpha\beta} + \epsilon^{fR}_{\alpha\beta}$. Furthermore, since only the incoherent sum of the NSI contributions is important, we combine the NSI effects coming from $\epsilon^{e}_{\alpha\beta}$, $\epsilon^{u}_{\alpha\beta}$, and $\epsilon^{d}_{\alpha\beta}$ as

$$\epsilon_{\alpha\beta} = \sum_{f=e,u,d} \frac{n_f}{n_e} \epsilon^{f}_{\alpha\beta} \,, \tag{9.2}$$

where n_f is the number density of the fermion f and we have normalised the effective contribution to the number density of electrons in earth.[1] While, in principle, the NSI parameters are complex[2], we consider only values which have phases either 0 and π. Throughout this work, we will use this assumption. Note that we sometimes refer to the NSI parameters as $\epsilon_{\alpha\beta}$ for simplicity, even though we work with only the real values of these parameters.

Each of the NSI parameters has been constrained from existing data. The corresponding model-independent upper bounds at 90 % C.L. are [180]

$$|\epsilon_{\alpha\beta}| < \begin{pmatrix} 4.2 & 0.33 & 3.0 \\ 0.33 & 0.068 & 0.33 \\ 3.0 & 0.33 & 21 \end{pmatrix} , \tag{9.3}$$

where we have arranged the parameters in the form of a matrix with the rows and columns corresponding to $\{e, \mu, \tau\}$. Note that only the NSI parameter $\epsilon_{\mu\mu}$ is well constrained in this phenomenological approach, while constraints on all other NSI parameters are rather loose. In particular, large values of ϵ_{ee}, $\epsilon_{e\tau}$, and $\epsilon_{\tau\tau}$ are still allowed. These bounds are generally referred to in the litera-

[1] Note that the convention followed in defining the NSI parameters is crucial to interpret the actual constraints on them from a given experiment and there are some places in the literature where a different convention has been followed (see Ref. [178] for a discussion).

[2] The complex phases of NSI parameters can affect the discovery reach of CP violation in a complicated manner as shown in Ref. [179]. The complex phases can indeed introduce contributions to CP violations. Restricting the NSI parameters to real values, we have considered a simpler scenario.

ture as indirect bounds as these bounds on parameters affecting neutrino oscillations come from non-neutrino experiments. The only[3] neutrino experiment that has provided bounds on (some) of these parameters that are better than these indirect bounds is the SK experiment, which puts direct bounds on the NSI parameters $|\epsilon_{\mu\tau}|$ and $|\epsilon_{\tau\tau} - \epsilon_{\mu\tau}|$ in the framework of the so-called two-flavor hybrid model. From the combined SK I and SK II data sets, the 90 % C.L. upper bounds are given by [51, 178]

$$|\epsilon_{\mu\tau}| < 0.033\,, \quad |\epsilon_{\tau\tau} - \epsilon_{\mu\mu}| < 0.147\,. \tag{9.4}$$

The MINOS experiment has also used its data to set the following bound $-0.2 < \epsilon_{\mu\tau} < 0.07$ at 90 % C.L. [181]. However, this bound is weaker than the one set by SK.

In what follows, we will work with the exact three-flavor neutrino oscillation probabilities and consider the following ranges for the relevant NSI parameters:[4]

$$\begin{aligned} -0.3 < \quad & \epsilon_{e\mu} \quad < 0.3\,, \\ -0.5 < \quad & \epsilon_{e\tau} \quad < 0.5\,, \\ -0.04 < \quad & \epsilon_{\mu\tau} \quad < 0.04\,, \\ -0.15 < \quad & \epsilon_{\tau\tau} \quad < 0.15\,, \end{aligned} \tag{9.5}$$

while for the oscillation parameters we assume the following true values:

$$\begin{aligned} \sin^2\theta_{12} = 0.31\,, \quad \sin^2\theta_{23} = 0.5\,, \quad \sin^2 2\theta_{13} = 0.1\,, \\ \Delta m^2_{21} = 7.5 \times 10^{-5}\ \mathrm{eV}^2\,, \quad |\Delta m^2_{31}| = 2.4 \times 10^{-3}\ \mathrm{eV}^2\,, \quad \delta_{\mathrm{CP}} = 0\,. \end{aligned} \tag{9.6}$$

The NSI parameter(s), if present, will alter the neutrino oscillation probabilities. Oscillo-

[3] Experimental constraints on the NSI parameters using from data from IceCube Deep Core became available at a much later date [52] and hence this chapter will not refer to this.

[4] We choose a smaller range than the current 90 % C.L. allowed range in Eq. (9.3), since outside these ranges the χ^2 corresponding to the ICAL data is already large.

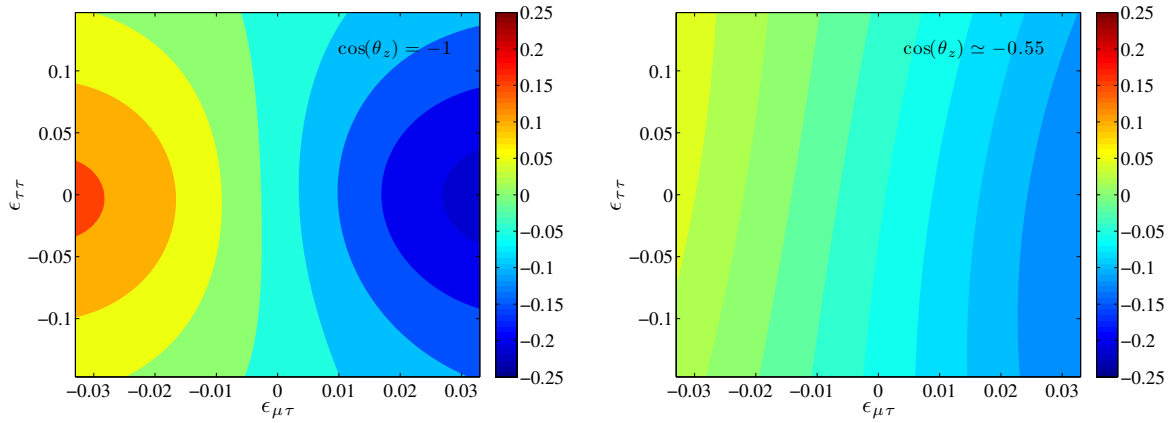

Figure 9.1: The relative probability difference $A^{\mathrm{MH}}_{\mu\mu}$ as a function of the NSI parameters $\epsilon_{\mu\tau}$ and $\epsilon_{\tau\tau}$ for $\cos\theta = -1$ (left panel) and $\cos\theta = -0.55$ (right panel). Please note the scale of the colorbars to the right of each panel. The following values of the neutrino parameters have been used: $\theta_{12} = 34°$, $\theta_{13} = 9.2°$, $\theta_{23} = 45°$, $\delta = 0$ (no leptonic CP-violation), $\Delta m^2_{21} = 7.5 \cdot 10^{-5}\,\mathrm{eV}^2$, and $\Delta m^2_{31} = +2.4 \cdot 10^{-3}\,\mathrm{eV}^2$ (normal neutrino mass hierachy). All NSI parameters, except $\epsilon_{\mu\tau}$ and $\epsilon_{\tau\tau}$, have been set to zero.

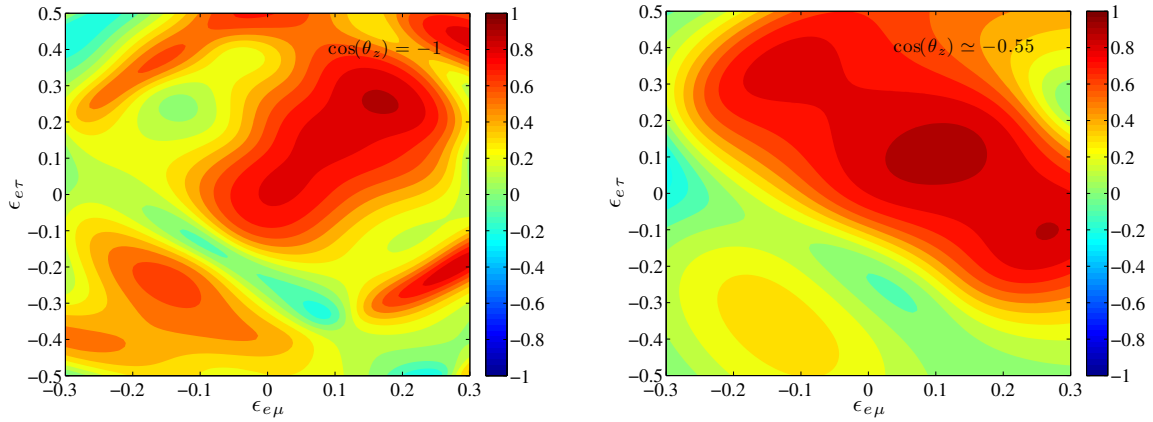

Figure 9.2: The relative probability difference $A^{\mathrm{MH}}_{\mu e}$ as a function of the NSI parameters $\epsilon_{e\mu}$ and $\epsilon_{e\tau}$ for $\cos\theta = -1$ (left panel) and $\cos\theta = -0.55$ (right panel). The neutrino parameter values used are the same as in Fig. 9.1, except that $\epsilon_{e\mu}$ and $\epsilon_{e\tau}$ are non-zero, while all other NSI parameter values have been set to zero.

grams showing the impact of NSI on the neutrino oscillation probabilities have appeared vastly in the literature. The muon neutrino survival probability $P_{\mu\mu}$ is affected most by the parameters $|\epsilon_{\mu\tau}|$ and $|\epsilon_{\tau\tau} - \epsilon_{\mu\mu}|$, while the transition probability $P_{e\mu}$ depends on $|\epsilon_{e\mu}|$ and $|\epsilon_{\mu\tau}|$. This dependence can be used to discover NSI parameters using neutrino oscillation data or constrain them.

It is also known that the dependence of the neutrino oscillation probabilities on NSI parameters is different for the NH and IH cases. Indeed, since measurement of the neutrino mass hierarchy is one of the prime goals of the INO experiment, it is pertinent to ask how the mass hierarchy sensitivity of the experiment alters in the presence of NSI. For the mass hierarchy determination, what matters is the difference in the oscillation probabilities between NH and IH. Therefore, it is appropriate to ask how the difference in the probabilities between NH and IH changes in presence of NSI. In order to show the impact of NSI on the mass hierarchy sensitivity, we present in Figs. 9.1 and 9.2 the contours of the relative difference $A^{\rm MH}_{\alpha\beta}$ between the neutrino oscillation probabilities $P_{\alpha\beta}$ (including NSI) corresponding to NH and IH. We define the relative probability difference $A^{\rm MH}_{\alpha\beta}$ as follows (*cf.* the definition of the total CP-asymmetry in Ref. [182])

$$A^{\rm MH}_{\alpha\beta}(\theta_z) = \frac{\Delta P^{\rm MH}_{\alpha\beta}(\theta_z)}{\Sigma P^{\rm MH}_{\alpha\beta}(\theta_z)} = \frac{\int \Delta P^{\rm MH}_{\alpha\beta}(E,\theta_z)\,{\rm d}E}{\int \Sigma P^{\rm MH}_{\alpha\beta}(E,\theta_z)\,{\rm d}E}\,, \tag{9.7}$$

where

$$\begin{aligned}
\Delta P^{\rm MH}_{\alpha\beta}(E,\theta_z) &= P^{\rm NH}_{\alpha\beta}(E,\theta_z) - P^{\rm IH}_{\alpha\beta}(E,\theta_z)\,,\\
\Sigma P^{\rm MH}_{\alpha\beta}(E,\theta_z) &= P^{\rm NH}_{\alpha\beta}(E,\theta_z) + P^{\rm IH}_{\alpha\beta}(E,\theta_z)\,,
\end{aligned}$$

$P^{\rm NH}_{\alpha\beta}$ and $P^{\rm IH}_{\alpha\beta}$ being the $\nu_\alpha \to \nu_\beta$ oscillation probability for NH and IH, respectively. In each case, we calculate $A^{\rm MH}_{\alpha\beta}$ for a particular zenith angle θ_z, while the energy dependence is integrated out in the range (1-100) GeV.

In Fig. 9.1, we show the relative probability difference $A^{\rm MH}_{\mu\mu}$ in the $\epsilon_{\mu\tau}$-$\epsilon_{\tau\tau}$ plane, keeping $\epsilon_{e\mu}$ and $\epsilon_{e\tau}$ fixed at zero.[5] The probabilities are calculated numerically within the full three-generation oscillation paradigm, using the PREM [183] density profile for the earth matter. We compute this for two benchmark zenith angles of $\cos\theta_z = -1$ and -0.55 corresponding to neutrino baseline lengths of $L = 12742$ km and $L = 7000$ km, respectively. The colors represent the contours corresponding to the values of $A^{\rm MH}_{\mu\mu}$ shown in the colorbar. The (0,0) point in the $\epsilon_{\mu\tau}$-$\epsilon_{\tau\tau}$ plane

[5]Here and throughout the rest of this work, we keep $\epsilon_{\mu\mu} = 0$.

corresponds to neutrino oscillations without NSI (*i.e.* standard neutrino oscillations). At all other points, NSI are included in the model, and this can be observed to alter the mass hierarchy sensitivity parameter $A^{\rm MH}_{\mu\mu}$. Note that for standard oscillations we have $A^{\rm MH}_{\mu\mu} \sim -5\%$. This small relative difference is what the atmospheric neutrino experiments observing ν_μ are exploiting to determine the neutrino mass hierarchy. When the NSI parameters are switched on, $A^{\rm MH}_{\mu\mu}$ changes. The relative difference $A^{\rm MH}_{\mu\mu}$ is seen to increase for $\epsilon_{\mu\tau} < 0$ and decreases further to larger negative values for $\epsilon_{\mu\tau} > 0$. However, since for the hierarchy measurement what is relevant is the absolute difference $|A^{\rm MH}_{\mu\mu}|$, we will later see that for all $|\epsilon_{\mu\tau}| > 0$, the hierarchy sensitivity increases as long as all the parameters are kept fixed between the NH and IH cases. The change in $A^{\rm MH}_{\mu\mu}$ with $|\epsilon_{\mu\tau}|$ is seen to be in the same direction for both the zenith angles shown, though its magnitude is seen to be larger for $\cos\theta_z = -1$ case. The change in $A^{\rm MH}_{\mu\mu}$ with $\epsilon_{\tau\tau}$ is less pronounced. In particular, for the $\cos\theta_z = -0.55$ case, the dependence on $\epsilon_{\tau\tau}$ is marginal. Even for the $\cos\theta_z = -1$ case, the dependence of $A^{\rm MH}_{\mu\mu}$ on $\epsilon_{\tau\tau}$ for $\epsilon_{\tau\tau} = 0$ is negligible. For larger values of $|\epsilon_{\tau\tau}|$, the role of $|\epsilon_{\tau\tau}|$ is to reduce the overall change in $A^{\rm MH}_{\mu\mu}$ due to NSI, and this happens for both positive and negative $\epsilon_{\tau\tau}$.

In order to understand the change of the probability difference as a function of the NSI parameters, we can series expand the neutrino oscillation probabilities in orders of the NSI parameters and keep only the first-order terms. The expression for the difference in the muon neutrino survival probability between NH and IH, keeping only leading-order terms in NSI parameters and neglecting the standard matter effects, is given by [184–186]

$$\begin{aligned}\Delta P^{\rm MH}_{\mu\mu} \simeq \quad & -2{\rm Re}(\epsilon_{\mu\tau})\sin 2\theta_{23}\left(\sin^2 2\theta_{23}\frac{AL}{2E}\sin\frac{|\Delta m^2_{31}|L}{2E} + 4\cos^2 2\theta_{23}\frac{A}{|\Delta m^2_{31}|}\sin^2\frac{|\Delta m^2_{31}|L}{4E}\right) \\ & +(|\epsilon_{\mu\mu}| - |\epsilon_{\tau\tau}|)\sin^2 2\theta_{23}\cos 2\theta_{23}\left(\frac{AL}{2E}\sin\frac{|\Delta m^2_{31}|L}{2E} - 4\frac{A}{|\Delta m^2_{31}|}\sin^2\frac{|\Delta m^2_{31}|L}{4E}\right) \end{aligned} \quad (9.8)$$

where $A = 2\sqrt{2}G_F n_e E$. Note that Eq. (9.8) depends only on the parameters ${\rm Re}(\epsilon_{\mu\tau})$ and $|\epsilon_{\mu\mu}| - |\epsilon_{\tau\tau}|$ to leading order. Dependence on $\epsilon_{e\mu}$ and $\epsilon_{e\tau}$ appear only at higher orders, which can be neglected unless these parameters are taken to be large. Therefore, in Fig. 9.1, we show the relative probability difference for the survival channel in the $\epsilon_{\mu\tau}$-$\epsilon_{\tau\tau}$ plane keeping the other NSI param-

eters at zero. For $\epsilon_{\tau\tau} = 0$, the expression clearly shows that $|\Delta P^{\rm MH}_{\mu\mu}|$, and hence $|A^{\rm MH}_{\mu\mu}|$, grows with $|\epsilon_{\mu\tau}|$ and flips sign when the sign of $\epsilon_{\mu\tau}$ changes. The quantity $A^{\rm MH}_{\mu\mu}$ is positive for $\epsilon_{\mu\tau} < 0$ and negative for $\epsilon_{\mu\tau} > 0$. This agrees fairly well with the exact results shown in Fig. 9.1. The impact of $\epsilon_{\tau\tau}$ on the other hand is more involved. Using Eq. (9.8), we note that for any given large value of $\epsilon_{\mu\tau}$, we should have the highest possible $|A^{\rm MH}_{\mu\mu}|$ for $\epsilon_{\tau\tau} = 0$, and since the dependence on this parameter comes in the form of $|\epsilon_{\tau\tau}|$, we should have lower $|A^{\rm MH}_{\mu\mu}|$ on both sides of $\epsilon_{\tau\tau} = 0$. On the other hand, for $\epsilon_{\mu\tau} = 0$, the $\Delta P^{\rm MH}_{\mu\mu}$ obtains contribution only from the second term, and there is a relative sign between the two terms in the parentheses. As a result for $\epsilon_{\mu\tau} = 0$ we do not expect large contribution to $\Delta P^{\rm MH}_{\mu\mu}$ from NSI. These features can be observed in the exact result in Fig. 9.1.

In Fig. 9.2, we present the $A^{\rm MH}_{e\mu}$ contours in the $\epsilon_{e\mu}$-$\epsilon_{e\tau}$ plane with $\epsilon_{\mu\tau}$ and $\epsilon_{\tau\tau}$ fixed at zero. The probability $P_{e\mu}$ depends crucially on the NSI parameters $\epsilon_{e\mu}$ and $\epsilon_{e\tau}$ at leading order, and hence, NSI bring significant change to $|A^{\rm MH}_{e\mu}|$. In this case, the corresponding analytic expression is complicated and we refer the reader to Ref. [184] for a related expression for the approximate formula. However, the exact results shown in the figure tell us that the presence of the NSI parameters $\epsilon_{e\mu}$ and $\epsilon_{e\tau}$ could bring substantial change to the mass hierarchy sensitivity of atmospheric neutrino experiments. In fact, $\epsilon_{e\mu}$ and $\epsilon_{e\tau}$ could either increase or decrease the mass hierarchy sensitivity compared to what we expect from standard oscillations.

9.3 Event Spectrum at INO

Since earth matter effects develop only in either the neutrino or the antineutrino channel for a given mass hierarchy, the charge identification capability gives ICAL an edge to better observe the earth matter effects, and hence, the neutrino mass hierarchy. The capability of this experiment to help discover the mass hierarchy has been studied before by the INO collaboration using information on muon energy and angle in Ref. [65] and using both the muon energy and angle information as well as hadron energy information in Ref. [66]. In this work, we only use the muon energy and

angle information and quantify the change in the mass hierarchy sensitivity of ICAL in presence of NSI. We also study the prospects of constraining or discovering the NSI parameters with the muon event sample.

For calculating the predicted number of μ^- and μ^+ events in ICAL, we use the same prescription as in the earlier chapters[6]. The unoscillated events are calculated using the Nuance event generator modified for ICAL. The oscillation probabilities, with and without NSI effects, are implemented through a re-weighting algorithm as discussed in Chapter 5. Finally, the muon reconstruction efficiency, charge identification efficiency, and muon energy and angular resolutions are folded in as described in Chapter 5 (See Refs. [65, 66, 68, 70, 154] for more details). The new ingredient in the simulations performed for this work is that while all the earlier INO works used muon sample in the energy range (1-11) GeV, we consider in this work a much larger energy range of (1-100) GeV.

This event sample is then binned in energy and zenith angle bins as follows. For the zenith angle we have 20 equal size bins in the $\cos\theta_z$ range $(-1,1)$. For the energy, we take variable bin sizes to ensure that there are reasonable number of events in each bin. Between muon energies (1-10) GeV, we take 9 energy bins of size 1 GeV, and between (10-100) GeV, we take 3 energy bins of size 30 GeV.

The predicted events are then analysed by a statistical procedure identical to the one used in the earlier chapters. A χ^2 function is defined as

$$\chi^2 = \chi^2(\mu^-) + \chi^2(\mu^+)\,, \tag{9.9}$$

where

$$\chi^2(\mu^\pm) = \min_{\xi_k^\pm} \sum_{i=1}^{N_i}\sum_{j=1}^{N_j}\left[2\left(N_{ij}^{\rm th}(\mu^\pm) - N_{ij}^{\rm ex}(\mu^\pm)\right) + 2N_{ij}^{\rm ex}(\mu^\pm)\ln\left(\frac{N_{ij}^{\rm ex}(\mu^\pm)}{N_{ij}^{\rm th}(\mu^\pm)}\right)\right] + \sum_{k=1}^{l}\xi_k^{\pm 2}, \tag{9.10}$$

[6]However, unlike other projects included in thesis, this work makes use of NUANCE event generator in conjunction with Kamioka fluxes.

$$N_{ij}^{\rm th}(\mu^{\pm}) = N'^{\rm th}_{ij}(\mu^{\pm})\left(1+\sum_{k=1}^{l}\pi_{ij}^{k}\xi_{k}^{\pm}\right) + \mathcal{O}(\xi_{k}^{\pm 2})\,, \tag{9.11}$$

$N'^{\rm th}_{ij}(\mu^{\pm})$ and $N_{ij}^{\rm ex}(\mu^{\pm})$ being the predicted and 'observed' number of $\mu^{\pm}$ events in ICAL, respectively, π_{ij}^{k} the correction factors due to the k^{th} systematic uncertainty, and $\xi_{k}^{\pm}$ the corresponding pull parameters. Similar to previous analyses, we include 5 systematic uncertainties. The individual contributions from μ^{-} and μ^{+} data samples are calculated by minimising Eq. (9.10) over the pull parameters. These are then added [*cf.* Eq. (9.10)] to obtain the χ^2 for a given set of oscillation (and NSI) parameters. This resultant χ^2 is then marginalised over the oscillation parameters, and when applicable, over the NSI parameters. We assume for the oscillation parameters the true values given in Eq. (9.6) and marginalise our χ^2 over their current 3σ ranges. We include priors defined as

$$\chi^2_{\rm prior} = \left(\frac{p_{\rm true}-p}{\sigma_p}\right)^2, \tag{9.12}$$

where $p_{\rm true}$ is the assumed true value of the parameter p and σ_p the 1σ error on it. We include priors on $|\Delta m^2_{31}|$, $\sin^2\theta_{23}$, and $\sin^2 2\theta_{13}$ with 1σ errors of 1 %, 2 %, and 0.005, respectively [187, 188]. For the NSI parameters, the χ^2 is marginalised over their range given in Eq. (9.5). For all results presented in this work, we use 500 kton-year of statistics in ICAL. We next define the different χ^2 that we compute in this work for the different physics studies we perform.

Sensitivity to Neutrino Mass Hierarchy: To find the sensitivity of ICAL to the neutrino mass hierarchy, we compute the χ^2 according to Eqs. (9.9) and (9.10), where $N_{ij}^{\rm ex}(\mu^{\pm})$ correspond to the right hierarchy and $N'^{\rm th}_{ij}(\mu^{\pm})$ correspond to the wrong hierarchy. The $\Delta\chi^2_{\rm MH}$ thus obtained is then marginalised over the oscillation and NSI parameters. We do this for different assumed true values of the NSI parameters.

Bounds on NSI parameters: In the event that there is no signal for NSI in the ICAL data, one will be able to give upper bounds on the NSI parameters at a given C.L. In order to find the expected sensitivity of ICAL to constrain the NSI parameters, we compute the χ^2 by generating $N_{ij}^{\rm ex}(\mu^{\pm})$ for

standard oscillations (with all NSI parameters set to zero) and fitting this with $N'^{\rm th}_{ij}(\mu^{\pm})$ computed with non-zero NSI parameters. The corresponding $\Delta\chi^2_{\rm S}$, where S stands for sensitivity, obtained after marginalising over oscillation gives a measure of the sensitivity reach of ICAL to NSI.

Discovery of NSI parameters: If on the other hand, one finds a signal of NSI in the ICAL data, this would be a discovery of NSI, and hence, physics beyond the Standard Model. Of course, the NSI parameters in this case have to be above a certain value to be able to produce a discoverable signal at ICAL. We find this lower limit on the NSI parameters needed to be discovered at ICAL for a given C.L. by generating $N^{\rm ex}_{ij}(\mu^{\pm})$ with NSI and fitting this with $N'^{\rm th}_{ij}(\mu^{\pm})$ corresponding to standard oscillations. The corresponding $\Delta\chi^2_{\rm D}$ obtained after marginalising over oscillation gives a measure of the discovery reach of ICAL to NSI.

Precision on NSI parameters: Finally, for a given set of NSI parameters, one can use the ICAL data to produce C.L. contours in the NSI parameter space. We will show these contours at the 68 %, 95 %, and 99 % C.L. in the $\epsilon_{\mu\tau}$-$\epsilon_{\tau\tau}$ and $\epsilon_{e\mu}$-$\epsilon_{e\tau}$ planes. For this, we will generate $N^{\rm ex}_{ij}(\mu^{\pm})$ for a certain set of NSI parameters and fit it with all values of the NSI parameters in the given plane while marginalising over the oscillation parameters.

9.4 Expected Results from INO

We now present our main results. We first show the impact of NSI on the mass hierarchy sensitivity of ICAL, which is the main goal of the experiment. We next give the sensitivity reach of this experiment in constraining NSI parameters. Subsequently, we quantify the NSI discovery potential at INO. Finally, we briefly discuss with what precision the NSI parameters could be measured at INO if they were indeed above the discovery limit.

9.4.1 Impact of NSI on Mass Hierarchy Sensitivity

We noted in Figs. 9.1 and 9.2 that the difference in the oscillation probabilities between NH and IH changes in the presence of NSI. Since the mass hierarchy sensitivity is defined in terms of the

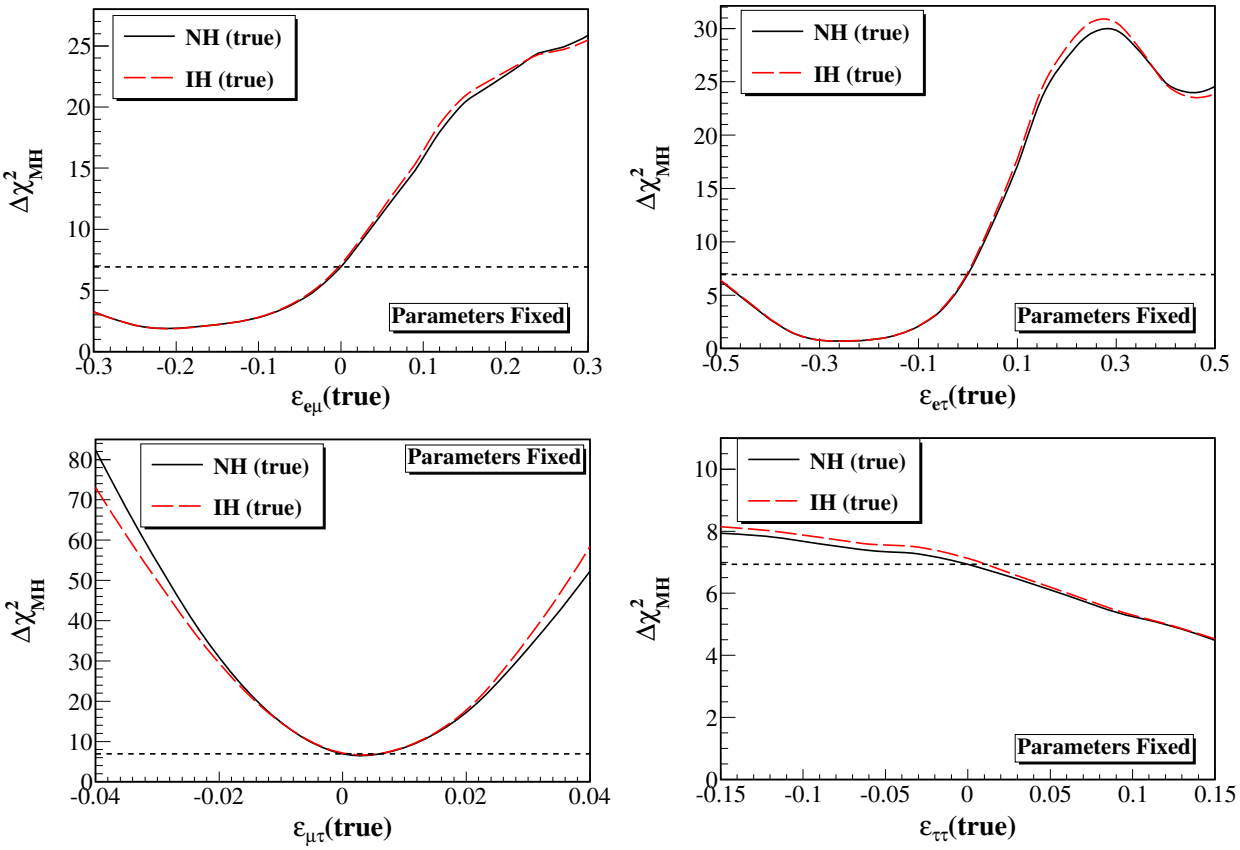

Figure 9.3: The $\Delta\chi^2_{\rm MH}$, giving the expected mass hierarchy sensitivity from 10 years of running of ICAL, as a function of the true value of NSI parameters. We keep only one $\epsilon_{\alpha\beta}$(true) to be non-zero at a time, while others are set to zero. The $\Delta\chi^2$ is obtained as explained in the text. However, the resultant $\Delta\chi^2$ is *not* marginalised over the oscillation parameters as well as NSI parameters.

difference in the event distribution for NH and IH, it is therefore expected that the mass hierarchy sensitivity of the experiment would change in the presence of NSI. The mass hierarchy sensitivity for standard oscillations using only the muon events in ICAL is given in Ref. [65]. We revisit the mass hierarchy sensitivity in ICAL in the presence of NSI parameters and show our results in Figs. 9.3 and 9.4. The $\Delta\chi^2_{\rm MH}$ corresponds to the difference in χ^2 of the fit with the wrong and the right hierarchy as a function of the true value of the NSI parameter. For the sake of simplicity, we take only one non-zero NSI parameter in the data at a time. For instance, the black curves in the top-left panels of Figs. 9.3 and 9.4 are obtained as follows. The data are generated for NH and a given true value of $\epsilon_{e\mu}$ (shown as the x-axis). The oscillation parameters in data are taken from Eq. (9.6) and all other NSI parameters are set to zero. This is then fitted with a theory

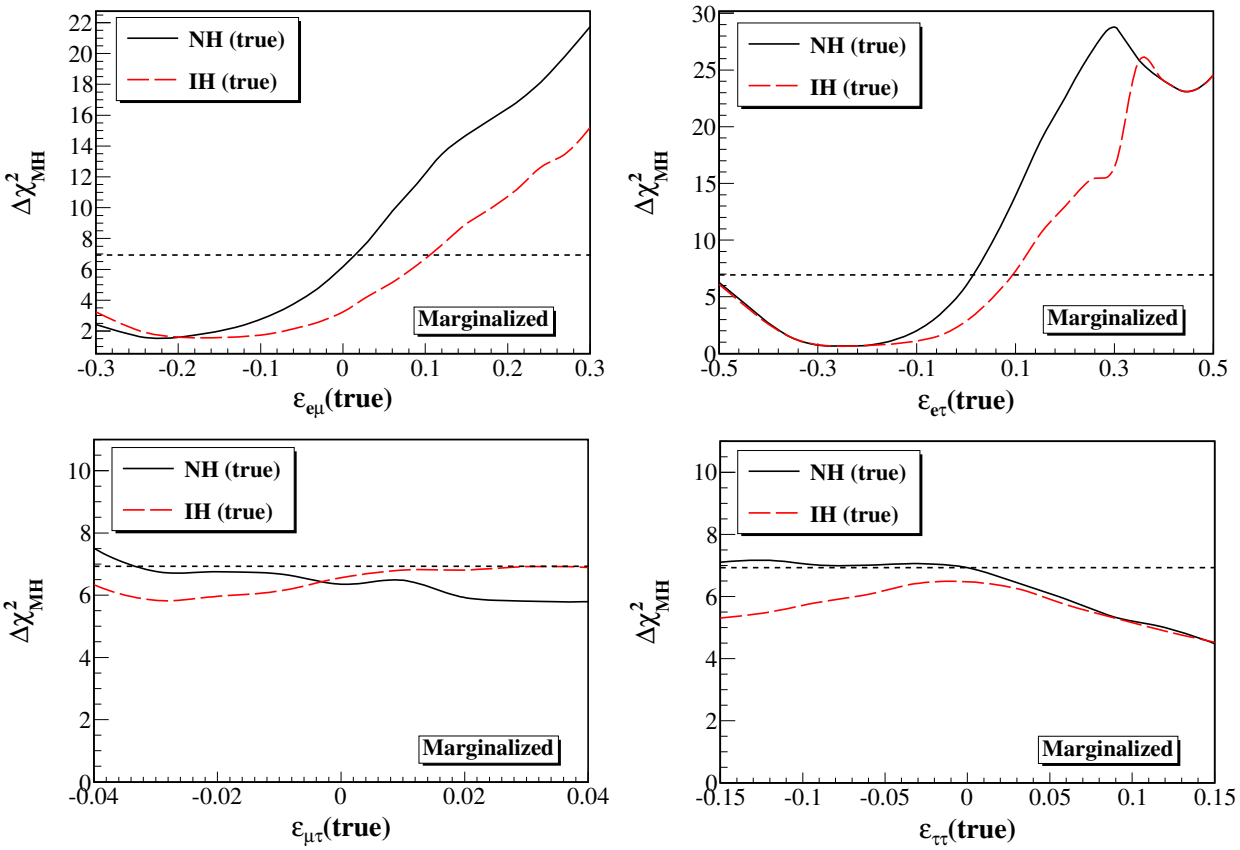

Figure 9.4: The $\Delta\chi^2_{\rm MH}$, giving the expected mass hierarchy sensitivity from 10 years of running of ICAL, as a function of the true value of NSI parameters. We keep only one $\epsilon_{\alpha\beta}$(true) to be non-zero at a time, while others are set to zero. The $\Delta\chi^2$ is obtained after marginalisation over the oscillation parameters as well as NSI parameters as explained in the text.

prediction corresponding to IH. In Fig. 9.3, we present the $\Delta\chi^2_{\rm MH}$ obtained when all oscillation and NSI parameters in the fit are fixed at their assumed true values. In Fig. 9.4, we marginalise the $\Delta\chi^2$ over the oscillation parameters $|\Delta m^2_{31}|$, $\sin^2\theta_{23}$, and $\sin^2 2\theta_{13}$ with priors. The $\Delta\chi^2_{\rm MH}$ is also marginalised over the NSI parameter which is taken as non-zero in the data, while the other NSI parameters are kept fixed at zero. For instance, in the top-left panel, the $\Delta\chi^2$ is marginalised over $\epsilon_{e\mu}$, while the other NSI parameters are kept fixed at zero. In all cases, the $\Delta\chi^2_{\rm MH}$ is marginalised over the oscillation parameters $|\Delta m^2_{31}|$, $\sin^2\theta_{23}$, and $\sin^2\theta_{13}$ with priors included as described in the previous section. The other panels are also obtained in a similar way.

The horizontal black dashed lines in the four panels of Figs. 9.3 and 9.4 show the mass hierarchy sensitivity expected in ICAL for the case when there are no NSI considered in either

the data or the fit. A comparison of this with the black solid and red dashed curves in the figure reveals that presence of NSI in the data could change the mass hierarchy sensitivity of ICAL. In particular, we see that the $\Delta\chi^2_{\rm MH}$ changes sharply with the true value of $\epsilon_{e\mu}$ and $\epsilon_{e\tau}$. In presence of NSI, we note that the $\Delta\chi^2_{\rm MH}$ increases for $\epsilon_{e\mu}({\rm true}) \gtrsim 0$ and $\epsilon_{e\tau}({\rm true}) \gtrsim 0$, while it decreases for $\epsilon_{e\mu}({\rm true}) \lesssim 0$ and $\epsilon_{e\tau}({\rm true}) \lesssim 0$, compared to what is expected for standard oscillations.

These features can be understood from Figs. 9.1 and 9.2. Since the NSI parameters $\epsilon_{e\mu}$ and $\epsilon_{e\tau}$ mainly affect the appearance channel $P_{e\mu}$, we refer to Fig. 9.2 to understand the upper panels of Figs. 9.3 and 9.4. The (0,0) point of Fig. 9.2 refers to standard oscillations and gives the mass hierarchy sensitivity shown by the black dashed lines in Figs. 9.3 and 9.4. If we stay on $\epsilon_{e\tau} = 0$ and change $\epsilon_{e\mu}$, we note from the left panel ($\cos\theta_z = -0.55$) of Fig. 9.2 that for $\epsilon_{e\mu} \lesssim 0$ $|A^{\rm MH}_{e\mu}|$ decreases, while for $\epsilon_{e\mu} \gtrsim 0$ it increases. This is less clear in the core-crossing bin, however, since the largest mass hierarchy sensitivity at ICAL comes from zenith angle bins close to $\cos\theta_z = -0.55$, this feature stays in the final $\Delta\chi^2_{\rm MH}$.

The effect of $\epsilon_{\tau\tau}$ on the mass hierarchy sensitivity is seen to be less severe from the bottom-right panels of Figs. 9.3 and 9.4. This NSI parameter affects the muon neutrino survival channel the most. Figure 9.1 reveals that the impact of $\epsilon_{\tau\tau}$ on $|A^{\rm MH}_{\mu\mu}|$ (when $\epsilon_{\mu\tau} = 0$) is very small for both the core-crossing and the $\cos\theta_z = -0.55$ bin. The impact of $\epsilon_{\mu\tau}$ on the mass hierarchy sensitivity is more interesting and has been discussed in Refs. [55–57]. For $\epsilon_{\tau\tau} = 0$, we see that $|A^{\rm MH}_{\mu\mu}|$ could change up to 20 % for the core-crossing bin and a few percent for the $\cos\theta_z = -0.55$ bin, as we change $\epsilon_{\mu\tau}$. Note that for standard oscillation $|A^{\rm MH}_{\mu\mu}|$ is already a very small number, and hence, the relative change of $|A^{\rm MH}_{\mu\mu}|$ due to $\epsilon_{\mu\tau}$ is significant. This is reflected in the bottom-left panel of Fig. 9.3, where we see a large increase in $\Delta\chi^2_{\rm MH}$ with $\epsilon_{\mu\tau}$. However, once we marginalise over oscillation and $\epsilon_{\mu\tau}$ in the fit, this increase is washed out and we obtain no significant impact of $\epsilon_{\mu\tau}$ on $\Delta\chi^2_{\rm MH}$ in the bottom-left panel of Fig. 9.4.

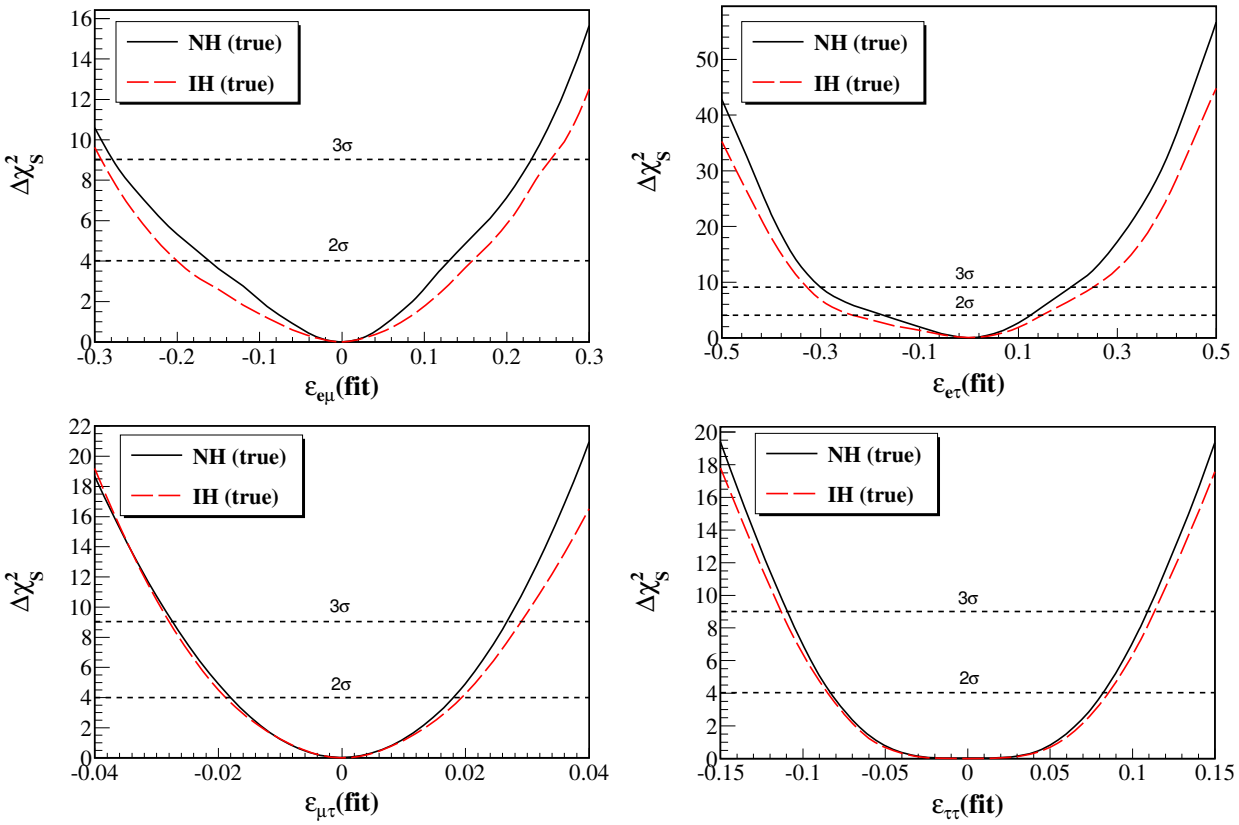

Figure 9.5: The $\Delta\chi^2_S$, giving the sensitivity reach of 10 years of ICAL data in constraining the NSI parameters in the event that the data show no signal of any new physics, as a function of the fit value of NSI parameters. We keep only one $\epsilon_{\alpha\beta}$(true) to be non-zero at a time, while others are set to zero. The $\Delta\chi^2_S$ has been marginalised over the oscillation parameters and NSI parameters as explained in the text.

9.4.2 Expected Bounds on NSI

In Fig. 9.5, we present the expected sensitivity reach of ICAL in constraining NSI parameters. The figure shows the expected sensitivity for each of the NSI parameters $\epsilon_{e\mu}$ (top-left panel), $\epsilon_{e\tau}$ (top-right panel), $\epsilon_{\mu\tau}$ (bottom-left panel), and $\epsilon_{\tau\tau}$ (bottom-right panel). This figure is obtained as follows. We use as data the event distribution at ICAL corresponding to standard oscillations by setting all NSI parameters to zero. This is then fitted with the predicted event distribution which includes one non-zero NSI parameter at a time, and the corresponding $\Delta\chi^2_S$ calculated. In Fig 9.5, we show this $\Delta\chi^2_S$ as a function of the NSI parameter that is allowed to be non-zero in the fit. The $\Delta\chi^2_S$ is marginalised over the oscillation parameters $|\Delta m^2_{31}|$, $\sin^2\theta_{23}$, and $\sin^2 2\theta_{13}$. Priors on

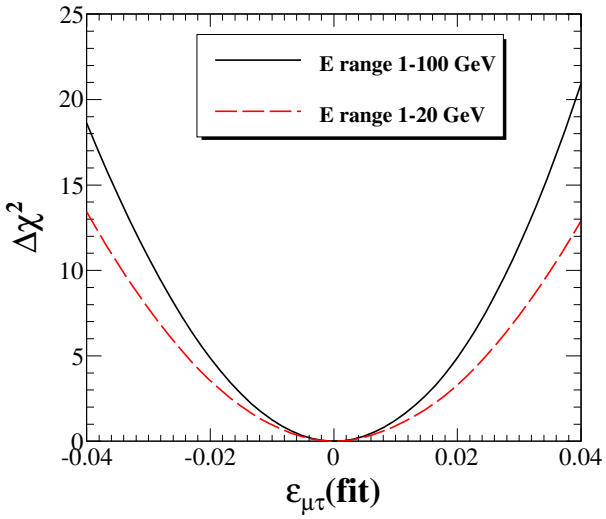

Figure 9.6: The improvement in the expected bounds on NSI from increasing the considered muon energy range from 20 GeV to 100 GeV in the analysis. We show this only for the NSI parameters $\epsilon_{\mu\tau}$.

the three oscillation parameters were included as described in the previous section. The resultant $\Delta\chi^2_{\rm S}$ shows little change as a result of marginalisation over them. The black solid curves are obtained when the data are considered corresponding to NH, while the red dashed curves are for data corresponding to IH. We keep the hierarchy fixed to its assumed true value in the fit.

The expected sensitivity for IH is only marginally worse than that for NH. At the 90 % (3σ) C.L., the expected bounds on the NSI parameters from 500 kton-years of statistics in ICAL for NH can be read from the figure as

$$\begin{aligned}
-0.119\ (-0.3) &< \epsilon_{e\mu} < 0.102\ (0.2)\,, \\
-0.127\ (-0.27) &< \epsilon_{e\tau} < 0.1\ (0.23)\,, \\
-0.015\ (-0.027) &< \epsilon_{\mu\tau} < 0.015\ (0.027)\,, \\
-0.073\ (-0.109) &< \epsilon_{\tau\tau} < 0.073\ (0.109)\,.
\end{aligned}$$

For the IH case, the bounds are comparable and can be read from the figure.

In Fig. 9.6, we show the improvement that we obtain in the sensitivity reach of ICAL to

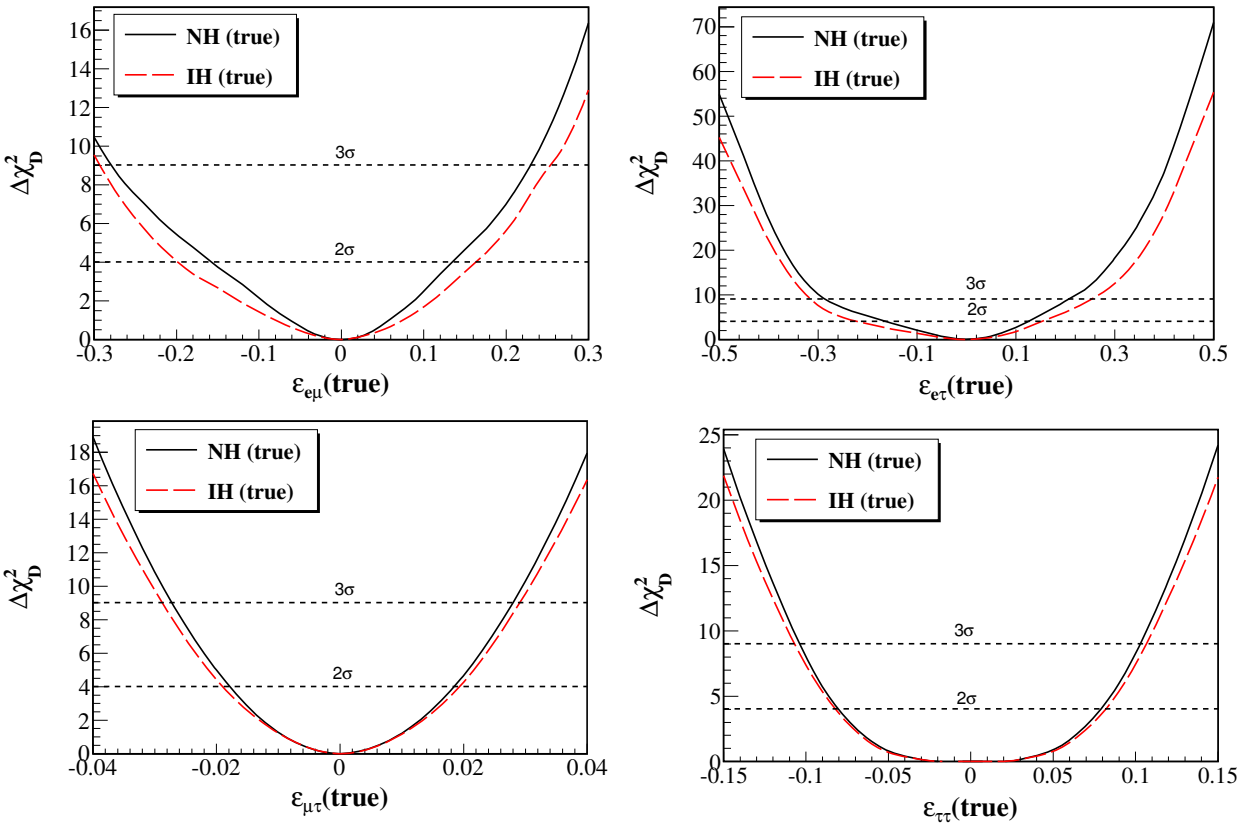

Figure 9.7: The $\Delta\chi^2_{\rm D}$, giving the discovery potential of 10 years of ICAL data in observing NSI, as a function of the true value of NSI parameters. We keep only one NSI parameter to be non-zero at a time, while others are set to zero. The $\Delta\chi^2_{\rm D}$ has been marginalised over the oscillation parameters as explained in the text.

the NSI parameters when we increase the muon energy range considered in the analysis from 20 GeV (red dashed curve) to 100 GeV (black solid curve). The 3σ bound on $\epsilon_{\mu\tau}$ improves from $-0.033 < \epsilon_{\mu\tau} < 0.033$ to $-0.027 < \epsilon_{\mu\tau} < 0.027$, when we increase the muon energy from 20 GeV to 100 GeV in the data.

9.4.3 Discovery Reach for NSI Parameters

In the previous section, we looked at how well ICAL will be able to constrain NSI parameters if its data were consistent with just standard oscillations. Next, we take the complementary view and ask ourselves that if NSI parameters were indeed non-zero, at what C.L. would ICAL be able to tell them apart from standard oscillations. In other words, we are looking for the limiting true values of

the NSI parameters above which the data at ICAL would be a signal for NSI at a certain C.L. For that, we now consider data for various (assumed) true values of the NSI parameters and fit them with a predicted event spectrum corresponding to standard oscillations and compute the resultant $\Delta\chi^2_{\rm D}$. We present this in Fig. 9.7. For simplicity, we consider only one non-zero NSI parameter at a time in the data. We marginalise over the oscillation parameters $|\Delta m^2_{31}|$, $\sin^2\theta_{23}$, and $\sin^2\theta_{13}$ with priors imposed on each one of them as discussed before. The black solid curves correspond to the case for NH, while the red dashed curves are for IH. We keep the hierarchy to be the same in the theory as in the data. The figure shows the expected $\Delta\chi^2_{\rm D}$ for the discovery of each of the NSI parameters $\epsilon_{e\mu}$ (top-left panel), $\epsilon_{e\tau}$ (top-right panel), $\epsilon_{\mu\tau}$ (bottom-left panel), and $\epsilon_{\tau\tau}$ (bottom-right panel). While the nature of the curves are very similar to the ones we had in Fig. 9.5, the values of the $\Delta\chi^2_{\rm D}$ are different. With 500 kton-years of data, the ICAL experiment will be able to give a signal of NSI at the 90 % (3σ) C.L. for NH if

$$\begin{aligned}
\epsilon_{e\mu} &< -0.116\ (-0.28), \qquad \epsilon_{e\mu} > 0.105\ (0.2)\,, \\
\epsilon_{e\tau} &< -0.12\ (-0.29), \qquad \epsilon_{e\tau} > 0.102\ (0.23)\,, \\
\epsilon_{\mu\tau} &< -0.015\ (-0.027), \qquad \epsilon_{\mu\tau} > 0.015\ (0.028)\,, \\
\epsilon_{\tau\tau} &< -0.07\ (-0.104), \qquad \epsilon_{\tau\tau} > 0.07\ (0.103)\,.
\end{aligned}$$

The corresponding limiting values for IH are similar, as can be seen from the figure.

9.4.4 Precision on NSI Parameters

In Figs. 9.8 and 9.9, we show the projected C.L. area in the NSI parameter space allowed after 10 years of running of the ICAL experiment. In Fig. 9.8, we show these for the case where we assume that there are no NSI, or in other words, when the assumed true values of the NSI parameters are taken as zero, shown by the black dots in the figure. The black dotted, blue dashed, and red solid contours show the 68 %, 95 % and 99 % C.L. in two-dimensional NSI planes. The contours are marginalised over the oscillation parameters after including priors that are described above. The

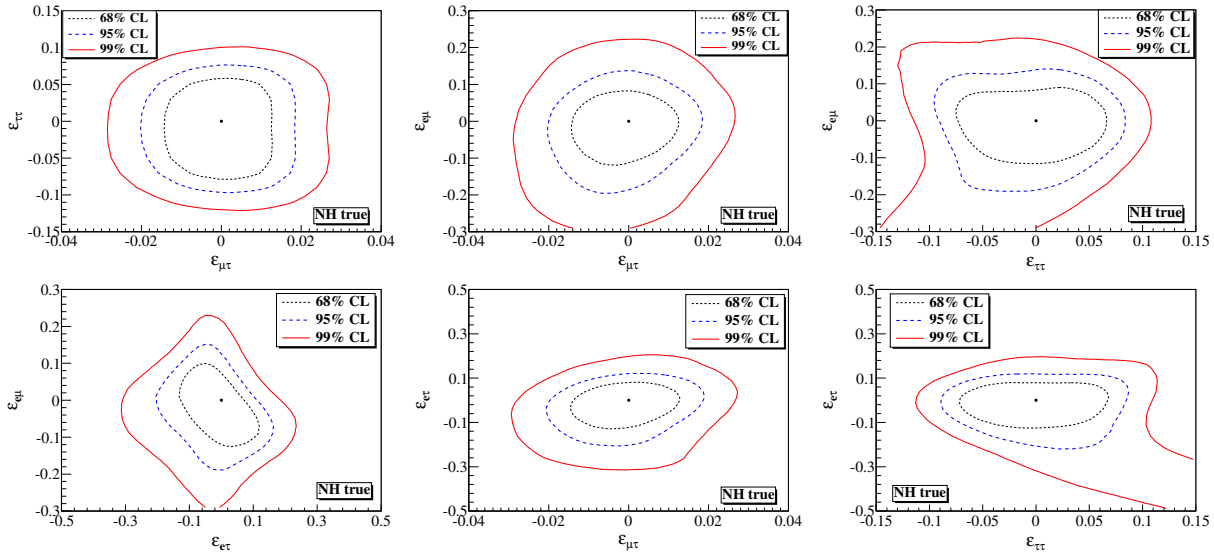

Figure 9.8: The expected C.L. contours in the given NSI parameter plane. The other NSI parameters are set to zero. The NH has been assumed to be true. The black dots show the points where the data were generated, which are for no NSI in this case.

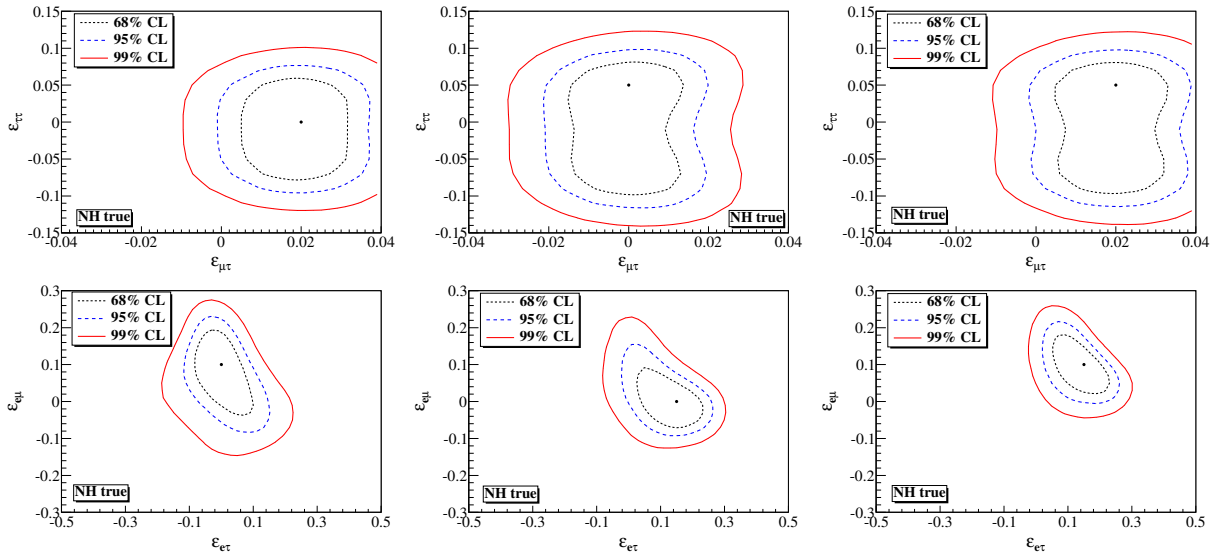

Figure 9.9: The expected C.L. contours in the given NSI parameter plane. The other NSI parameters are set to zero. The upper panels are drawn in the $\epsilon_{\mu\tau} - \epsilon_{\tau\tau}$ plane, while the lower panels are drawn in the $\epsilon_{e\tau} - \epsilon_{e\mu}$ plane. The black dots show the points where the data were generated.

NSI parameters other than the ones appearing in the two-dimensional plane are kept fixed at zero. NH is assumed for all plots. The corresponding contours for the IH case are very similar and we do not repeat them for brevity.

In Fig. 9.8, we show the C.L. contours for the case where we assume the true values of the NSI parameters to be non-zero. The upper panels show the C.L. in the $\epsilon_{\mu\tau}$-$\epsilon_{\tau\tau}$ plane when the true values of $(\epsilon_{\mu\tau}, \epsilon_{\tau\tau})$ are taken as (0.02,0), (0,0.075), and (0.02,0.075) for the left, middle, and right panels, respectively. These assumed true points are shown by black dots in the plots. The values $\epsilon_{e\mu}$ and $\epsilon_{e\tau}$ are assumed to be zero in both the data as well as in the fit, and we do not show the contours in planes involving these parameters. The lower panels are similar to the upper panels except that now we show the C.L. in the $\epsilon_{e\tau}$-$\epsilon_{e\mu}$ plane when the true values of $(\epsilon_{e\tau}, \epsilon_{e\mu})$ are taken as (0,0.1), (0.15,0), and (0.15,0.1) for the left, middle, and right panels, respectively. For these panels, the values $\epsilon_{\mu\tau}$ and $\epsilon_{\tau\tau}$ are assumed to be zero in both the data as well as in the fit. Again, the figures are for NH, however, the ones for IH are similar and we do not present them for brevity.

9.5 Conclusions

We probe in this work the impact of NSI parameters on the expected signal at ICAL and the physics conclusions that one can draw out of it. The neutral-current NSI if present, could alter the propagation of atmospheric neutrinos inside the earth matter changing the signal at ICAL. This change due to NSI can be used to study the NSI parameters. On the other hand, one needs to estimate how much the potential of ICAL to standard physics gets modified in the presence of NSI. In this work, we have taken both these considerations into account and studied the physics potential of ICAL in presence of NSI.

Measurement of the neutrino mass hierarchy is the primary goal of the ICAL atmospheric neutrino experiment. We showed how the difference in the neutrino oscillation probabilities between NH and IH change in presence of NSI. We defined the relative probability difference $A^{\rm MH}_{\alpha\beta}$ for the oscillation channel $\nu_\alpha \to \nu_\beta$ and showed the oscillograms for $A^{\rm MH}_{\mu\mu}$ and $A^{\rm MH}_{e\mu}$, the two oscillation channels relevant for the atmospheric neutrinos in ICAL. These oscillograms (and all other results

shown in this paper) were obtained from an exact numerical calculation of the three-generation neutrino oscillation probabilities using the PREM profile for the earth matter density [183]. The oscillograms show that the relative difference $A_{\mu\mu}^{\rm MH}$ changes significantly with $\epsilon_{\mu\tau}$ compared to its Standard Model value, while $A_{e\mu}^{\rm MH}$ is seen to vary sharply with the values of $\epsilon_{e\mu}$ and $\epsilon_{e\tau}$. The impact of the NSI parameter $\epsilon_{\tau\tau}$ is seen to be less important.

We next simulated μ^- and μ^+ events in the ICAL detector in presence of NSI and defined a χ^2 function, including energy and zenith angle correlated as well as uncorrelated systematic uncertainties, to give C.L. predictions for the estimated sensitivity of ICAL.[7] The χ^2 is marginalised over the NSI parameters and the oscillation parameters $|\Delta m^2_{31}|$, $\sin^2\theta_{23}$, and $\sin^2 2\theta_{13}$ after putting priors on them. Using this we presented the change in $\Delta\chi^2_{\rm MH}$ if NSI was assumed to be a certain true value in Nature. We showed that the $\Delta\chi^2_{\rm MH}$ increases rapidly for $\epsilon_{e\mu}$(true)>0 and $\epsilon_{e\tau}$(true)>0, while it decreases for $\epsilon_{e\mu}$(true)<0 and $\epsilon_{e\tau}$(true)<0 compared to what we expect for standard oscillations. This behavior can be understood from the oscillograms we showed. The impact of the NSI parameter $\epsilon_{\tau\tau}$ is small, however, the $\Delta\chi^2_{\rm MH}$ could vary significantly with $\epsilon_{\mu\tau}$.

We next showed the potential of ICAL in discovering or constraining NSI. If the case that ICAL was consistent with no NSI in the data, we presented the expected upper limit on the NSI parameters. At the 90 % (3σ) C.L. we have for the NH the limits

$$\begin{aligned}
-0.119\ (-0.3) &< \epsilon_{e\mu} < 0.102\ (0.2)\,,\\
-0.127\ (-0.27) &< \epsilon_{e\tau} < 0.1\ (0.23)\,,\\
-0.015\ (-0.027) &< \epsilon_{\mu\tau} < 0.015\ (0.027)\,,\\
-0.073\ (-0.109) &< \epsilon_{\tau\tau} < 0.073\ (0.109)\,.
\end{aligned}$$

The limits for IH are similar. Compared to the current 90% C.L. bounds given in Eqs. (9.3) and (9.4) the expected bounds from ICAL are promising. We next considered the case where the data

[7] It has been shown that the inclusion of hadron energy information in the analysis of ICAL data improves the mass hierarchy sensitivity of ICAL. The impact of the hadron energy information on the sensitivity of ICAL to NSI is being studied in an independent work.

at ICAL is consistent with NSI and we gave the expected statistical significance with which ICAL will rule out the theory with no NSI. We calculated the range of the NSI parameters that would lead to 90% (3σ) C.L. discovery of NSI at ICAL. Finally, we presented the C.L. contours in the two-parameter NSI planes, for different choices of true values of the NSI parameters.

Chapter 10

Summary and outlook

The WIMP paradigm could be a solution to the observed dark matter abundance of the universe. Considering this scenario to be true, WIMPs would be gravitationally captured by celestial bodies like the sun and earth and eventually accumulate in their cores where, as well as in other regions of preponderance such as the GC, they would annihilate into standard model particle-antiparticle pairs. Among the final state annihilation products, the neutrinos would manage to escape the point of production and reach the detector on earth, carrying with them, the vital information of the parent WIMPs. The neutrinos on reaching detector interacts with the detector material and by studying the products of interaction such as the charged leptons, we can, in principle, reconstruct the properties of the annihilating WIMPs. In this thesis, the prospect of detecting neutrinos from WIMP annihilations in the sun, earth and GC with ICAL detector was explored. This work is a part of ongoing studies to probe the physics potential of the ICAL detector.

In order to analyse the indirect signal for WIMP masses up to 100 GeV, dedicated ICAL detector simulation were performed using the Geant4-based ICAL detector code to obtain the detector and charge identification efficiencies as well as the muon energy and angle resolution functions. We presented our results on the ICAL detector response for higher energy muon in Chapter 5. The simulations presented in this thesis are an extension of the detector simulations performed by the INO collaboration [78], where the detector response was simulated for muon energies up to 25 GeV. All analyses presented in this thesis makes use of the results presented in

Chapter 5 for muon energies up to 100 GeV.

We simulated the expected event spectrum for the dark matter signal using the event generator GENIE, suitably modified to include the ICAL detector geometry. The GENIE output is given in terms of true energy and true zenith angle of the muon and is for a 100 % efficient ideal detector. The detector and charge identification efficiencies as well as muon energy and zenith angle resolutions are functions of both true muon energy and true muon zenith angle. We first fold these events with detector efficiency and charge identification efficiency with the ICAL muon response presented in Chapter 5. Next, in order to simulate the events in bins of measured muon energy and muon zenith angle, we fold them with the muon energy resolution functions and muon zenith angle resolution functions. The muon events after this stage represents the prospective data at ICAL for 500 kt-year exposure. All results shown in this thesis were obtained from an exact numerical calculation of the three-generation neutrino oscillation probabilities using the PREM profile for the earth matter density [183].

The atmospheric neutrinos pose a serious background to the signal neutrinos due to WIMP annihilation. However, the atmospheric neutrinos come from all directions whereas the dark matter signal neutrinos only come from the direction of source. The signal direction corresponds to the direction of the sun for solar WIMPs, the direction of the earth's core for the terrestrial WIMPs and from the angular position of GC with respect to the detector for the annihilation in the galactic centre region. This feature is what we use to place an angular cut to effectively reduce the atmospheric neutrino background.

Searches for the WIMP annihilation in the sun was presented in Chapter 6. A study of μ^- and μ^+ events arising at ICAL due to WIMP annihilation was presented for the following annihilation channels : $\tau^+\tau^-$, $b\bar{b}$, $c\bar{c}$, $b\bar{b}$, $\nu_e\bar{\nu}_e, \nu_\mu\bar{\nu}_\mu, \nu_\tau\bar{\nu}_\tau$ and gg. For the case of solar WIMPs, we first performed a generator-level simulation to find the opening angle between the signal neutrinos and the direction of the sun such that 90 % of the signal events were accepted. We presented these 90 % cone-cut angles θ_{90} as a function of the WIMP mass. Heavier WIMPs produce higher energy neutrinos and hence have smaller cone-cut angles. This 90 % cone-cut criteria was then implemented

on the atmospheric neutrino background, wherein the event was accepted or rejected depending on whether its zenith angle lied inside or outside the cone defined by θ_{90}. Since the cone-cut angle θ_{90} was found to be different for different WIMP mass, the atmospheric neutrino events accepted for the analysis was also different for different WIMP masses. Finally, since the sun spends a specific amount of time on a given zenith angle, we obtained the exposure function of the sun at the INO site and weighted the accepted atmospheric neutrino events with this exposure function to get the final reduced atmospheric neutrino background events as a function of the WIMP mass. We showed that the cone-cut acceptance method reduces the atmospheric neutrino background by a factor of ~ 100. We presented the signal and background for $\tau^+\tau^-$, $b\bar{b}$, $c\bar{c}$, $\nu_e\bar{\nu}_e, \nu_\mu\bar{\nu}_\mu, \nu_\tau\bar{\nu}_\tau$ and gg channels for WIMP mass 25 GeV and $\sigma_{SD} = 10^{-39}$ cm^2 and showed that for the $\tau^+\tau^-$ and $\nu\bar{\nu}$ channels the signal is above the background for most part of the spectrum. For higher WIMP masses, the signal to background ratio were better.

We defined a χ^2 function for the indirect detection sensitivity of ICAL to dark matter and presented the expected sensitivity in the $\sigma_{SD} - m_\chi$ and $\sigma_{SI} - m_\chi$ planes for spin-dependent and spin-independent cross-sections, respectively. The expected 90 % C.L. sensitivity was presented for $\tau^+\tau^-$, $b\bar{b}$, $c\bar{c}$, $\nu_e\bar{\nu}_e, \nu_\mu\bar{\nu}_\mu, \nu_\tau\bar{\nu}_\tau$ and gg channels for an exposure of 500 kt-yrs of ICAL and with systematic uncertainties on atmospheric neutrino background included in the analysis. For a WIMP mass of 25 GeV, the expected 90 % C.L. limit using the $\tau^+\tau^-$ channel with 500 kt-yrs exposure in ICAL is $\sigma_{SD} < 6.87 \times 10^{-41}$ cm^2 and $\sigma_{SI} < 7.75 \times 10^{-43}$ cm^2 for the spin-dependent and spin-independent cross-sections, respectively. The effect of systematic uncertainties on the atmospheric neutrino background was also studied.

Similarly, in Chapter 7, we presented a study on the prospects of detecting muon events at ICAL due to WIMP annihilation in the earth core. We simulated events arising due to $\tau^+\tau^-$ and $b\bar{b}$ annihilation channels and WIMP masses $m_\chi \in [10, 100]$ GeV. Evaporation could be significant for masses below 10 GeV, resulting in a lower expected signal rates, and hence we have not considered energies below 10 GeV. Unlike the case of the sun, the signal neutrinos for this case originate only from the fixed zenith direction *viz.*, the direction of earth's core, which makes the background

suppression algorithm slightly easier. Similar to the solar WIMP analysis, θ_{90} was defined as a cone cut criterion. However, in this case, θ_{90} represents the cone half angle containing 90 % of the signal events with the axis of cone being fixed in the direction of earth's centre. This cone-cut criterion was used to suppress background and the atmospheric neutrinos coming from the direction of earth's core represents an irreducible background. We presented the expected event spectrum for $\tau^+\tau^-$ and $b\bar{b}$ channels and corresponding suppressed background with 500 kt-years of ICAL exposure. Using these expected events, χ^2 was calculated for indirect detection sensitivity and presented the expected sensitivity.

Due to resonant capture of WIMPs close to abundant iron nuclei, the annihilation rate is greatly enhanced resulting in an increased sensitivity for WIMP mass around 50 GeV. Unlike the case of sun, equilibrium between the capture rate and annihilation rate has not reached in the earth, due to which the capture rate has a dependence on $\langle\sigma_A v\rangle$ besides σ_{SI}. We presented the expected sensitivity upper limits at 90 % C.L. in the σ_{SI} - $\langle\sigma_A v\rangle$ plane for a WIMP mass of 50 GeV. Thereafter, we presented ICAL sensitivity in the $\sigma_{SI} - m_\chi$ plane for spin-independent cross-sections, assuming $\langle\sigma_A v\rangle = 3\times10^{-26}\mathrm{cm}^3\mathrm{s}^{-1}$. The 90 % C.L. sensitivity limits for ICAL, assuming 100% branching ratio for each channel, are : $\sigma_{SI} = 1.02 \times 10^{-44}$ cm^2 for the $\tau^+\tau^-$ channel and $\sigma_{SI} = 5.36 \times 10^{-44}$ cm^2 for the $b\ \bar{b}$ channel, which is stronger than present bounds from other indirect detection experiments. The sensitivity limits from $\sigma_{SI} - m_\chi$ plane were transported to $\Gamma_A - m_\chi$ plane and presented for the two considered annihilation channels. A comparison of ICAL's sensitivity to σ_{SI} for the searches in the sun and earth was also presented.

Subsequently, in Chapter 8, we explored the prospect of detecting neutrino fluxes due to WIMP annihilation in GC. Background suppression followed a scheme similar to that of solar WIMP analysis. An acceptance cone with a cone-half angle Ψ was constructed, as a function of WIMP mass and annihilation channel. Ψ, the angular separation of the muon track with GC, is analogous to θ_{90} in the case of the sun. A galactic exposure function containing information regarding galactic centre's visibility as a function of zenith and azimuthal angles was obtained and was used to assign weight to the background events to ensure that they are in the acceptance cone.

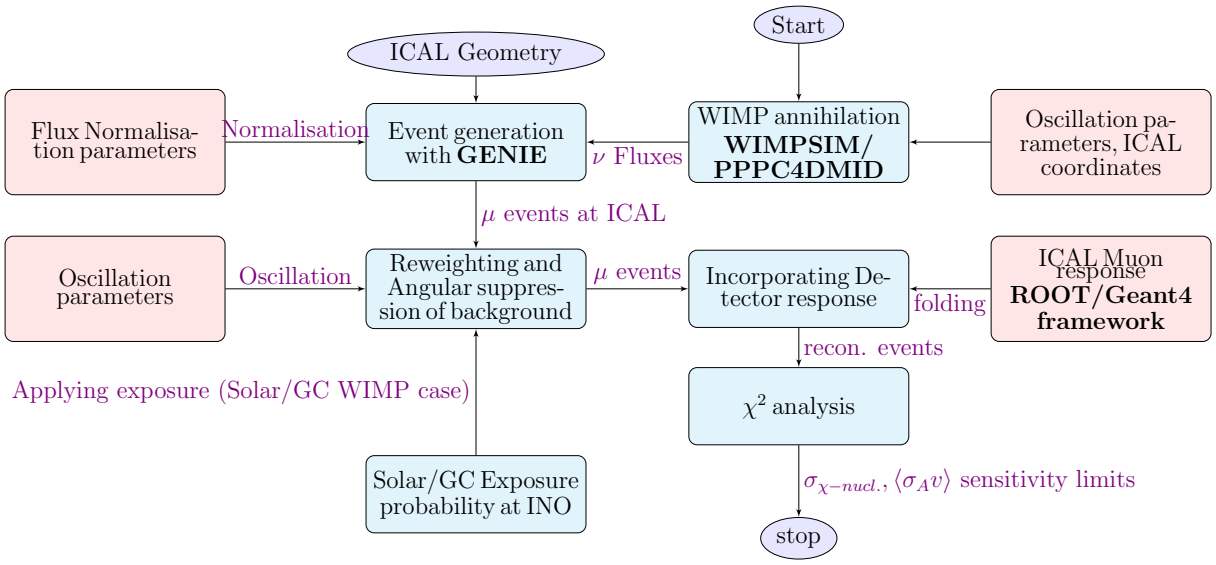

Figure 10.1: The simulation and analysis involved in the indirect searches for WIMP annihilation with ICAL.

The expected event spectrum at ICAL for different annihilation channels and WIMP masses were presented and used to calculated expected ICAL sensitivity. The 90% C.L. expected sensitivity for ICAL in the $\langle\sigma v\rangle$ - m_χ parameter space was presented for $b\bar{b}$, $\mu^+\mu^-$, $\tau^+\tau^-$ and $\nu_\mu\bar{\nu_\mu}$ WIMP annihilation channels assuming 100 % branching ratio each. Among the channels considered, the 90% C.L. expected sensitivity limits for $\nu_\mu\bar{\nu_\mu}$ channel and NFW profile was found to be the most stringent. ICAL expected sensitivity was found to be better than other indirect detection experiments like IceCube and ANTARES for the range of $m_\chi \in (5, 100)$ GeV. The experimental limits obtained by SK are better than the corresponding ICAL sensitivity limits by more than an order of magnitude. A comparison of expected sensitivity for various DM density profiles was also presented. Also shown was the effect of systematics on the expected sensitivity for a given DM density profile and an annihilation channel. With a better optimisation scheme for the signal expectation calculation and background suppression, ICAL expected sensitivity could be improved further. Fig. 10.1 summarises the simulation and analysis involved in the indirect searches for WIMP annihilation with ICAL.

Finally, in Chapter 9 we studied ICAL's sensitivity to probe signatures of neutral current NSI

and its effect on the physics potential of the detector. We defined the relative probability difference $A^{\rm MH}_{\alpha\beta}$ for the oscillation channel $\nu_\alpha \to \nu_\beta$. We showed the oscillograms for $A^{\rm MH}_{\mu\mu}$ and $A^{\rm MH}_{e\mu}$, the two oscillation channels relevant for the atmospheric neutrinos in ICAL, from which we concluded that the relative difference $A^{\rm MH}_{\mu\mu}$ changes significantly with $\epsilon_{\mu\tau}$ compared to its SM value, while $A^{\rm MH}_{e\mu}$ is seen to vary sharply with the values of $\epsilon_{e\mu}$ and $\epsilon_{e\tau}$. The NSI parameter $\epsilon_{\tau\tau}$ is seen to have only a mild impact. We simulated μ^- and μ^+ events in the ICAL detector in presence of NSI and χ^2 was calculated. The change in $\Delta\chi^2_{\rm MH}$ was presented assuming NSI to be have a certain true value in nature. We found that the $\Delta\chi^2_{\rm MH}$ increases rapidly for $\epsilon_{e\mu}$(true)> 0 and $\epsilon_{e\tau}$(true)> 0, while it decreases for $\epsilon_{e\mu}$(true)< 0 and $\epsilon_{e\tau}$(true)< 0 compared to what we expect for standard oscillations. The impact of the NSI parameter $\epsilon_{\tau\tau}$ is small, however, the $\Delta\chi^2_{\rm MH}$ could vary significantly with $\epsilon_{\mu\tau}$.

This was followed by the discussion of the potential of ICAL in discovering or constraining NSI. If the case that ICAL was consistent with no NSI in the data, we presented the expected upper limit on the NSI parameters at the 90 % (3σ) C.L.. Compared to the current 90% C.L. bounds given in Eqs. (9.3) and (9.4) the expected bounds from ICAL are promising. We next considered the case where the data at ICAL is consistent with NSI and we gave the expected statistical significance with which ICAL will rule out the theory with no NSI. We calculated the range of the NSI parameters that would lead to 90% (3σ) C.L. discovery of NSI at ICAL. Finally, we presented the C.L. contours in the two-parameter NSI planes, for different choices of true values of the NSI parameters. In the presence of NSI, the signal and background event spectrum at ICAL would be modified thereby affecting ICAL's sensitivity to indirect searches. However, in this thesis we have not considered this study.

In conclusion, with an effective atmospheric neutrino background suppression scheme, the expected 90 % C.L. sensitivity limits from about 10 years of running of ICAL for SD and SI WIMP-nucleon scattering cross-sections due to WIMP annihilation in the sun and earth are competitive to the most stringent bounds till date. The expected ICAL sensitivity on $\langle\sigma_A v\rangle$ due to WIMP annihilation in GC are also promising. The other experiments like SK, ORCA and PINGU

will also offer competing limits for the lighter WIMP masses. Also, bounds obtained on SI cross sections from direct detection experiments are already very stringent and getting stronger. Similarly, strong limit on $\langle \sigma_A v \rangle$ comes from photon search limits from observation of dwarf spheroidals by Fermi-LAT [32]. Nevertheless, detectors like ICAL offer complementary approach using neutrinos and hence the study carried out in this thesis should be useful.

Despite an extensive search program encompassing direct, indirect and collider detection experiments, there has been no conclusive signature of WIMP detection. So far, the WIMP paradigm is being scrutinised through several ultra advanced technologies and with more experimental data we could have a clearer picture of the nature of dark matter. ICAL is expected to play a role in this quest for the search of dark matter. The present time is super exciting and the coming decade will (hopefully) stand witness to new discoveries.

References

[1] S. Choubey, A. Ghosh and D. Tiwari, *Prospects of Indirect Searches for Dark Matter at INO*, *JCAP* **1805** (2018) 006, [1711.02546].

[2] GEANT4 collaboration, S. Agostinelli et al., *GEANT4: A Simulation toolkit*, *Nucl. Instrum. Meth.* **A506** (2003) 250–303.

[3] D. Tiwari, S. Choubey and A. Ghosh, *Prospects of indirect searches for dark matter annihilations in the earth with ICAL@INO*, 1806.05058.

[4] S. Choubey and D. Tiwari, *Hunting for dark matter in the galactic centre with INO*, in preparation.

[5] C. Combet, A. Charbonnier and D. Maurin, *Introducing CLUMPY: A public code for gamma-ray emission from dark matter annihilation in the galaxy*, in *Cosmic rays for particle and astroparticle physics. Proceedings, 12th ICATPP Conference, Como, Italy, October 7-8, 2010*, pp. 590–595, 2011, DOI.

[6] J. F. Navarro, C. S. Frenk and S. D. M. White, *The Structure of cold dark matter halos*, *Astrophys. J.* **462** (1996) 563–575, [astro-ph/9508025].

[7] M. Cirelli, G. Corcella, A. Hektor, G. Hutsi, M. Kadastik, P. Panci et al., *PPPC 4 DM ID: A Poor Particle Physicist Cookbook for Dark Matter Indirect Detection*, *JCAP* **1103** (2011) 051, [1012.4515].

[8] S. Choubey, A. Ghosh, T. Ohlsson and D. Tiwari, *Neutrino Physics with Non-Standard Interactions at INO*, *JHEP* **12** (2015) 126, [1507.02211].

[9] A. Riotto, *Particle cosmology*, in *High-energy physics. Proceedings, 5th CERN-Latin-American School, Recinto Quirama, Colombia, March 15-28, 2009*, 2010, 1010.2642, http://inspirehep.net/record/872740/files/arXiv:1010.2642.pdf.

[10] K. Freese, *Status of Dark Matter in the Universe*, *Int. J. Mod. Phys.* **1** (2017) 325–355, [1701.01840].

[11] PLANCK collaboration, P. A. R. Ade et al., *Planck 2015 results. XIII. Cosmological parameters*, *Astron. Astrophys.* **594** (2016) A13, [1502.01589].

[12] M. A. Deliyergiyev, *Recent Progress in Search for Dark Sector Signatures*, *Open Phys.* **14** (2016) 281–303, [1510.06927].

[13] P. Ciafaloni, M. Cirelli, D. Comelli, A. De Simone, A. Riotto and A. Urbano, *On the Importance of Electroweak Corrections for Majorana Dark Matter Indirect Detection*, *JCAP* **1106** (2011) 018, [1104.2996].

[14] ICAL collaboration, S. Ahmed et al., *Physics Potential of the ICAL detector at the India-based Neutrino Observatory (INO)*, *Pramana* **88** (2017) 79, [1505.07380].

[15] I. Corp., *Electromagnetic field simulation software*, http://www.infolytica.com/en/products/magnet.

[16] G. Busoni et al., *Recommendations on presenting LHC searches for missing transverse energy signals using simplified s-channel models of dark matter*, 1603.04156.

[17] PICO collaboration, C. Amole et al., *Dark Matter Search Results from the PICO-60 C_3F_8 Bubble Chamber*, *Phys. Rev. Lett.* **118** (2017) 251301, [1702.07666].

[18] XENON collaboration, E. Aprile et al., *Constraining the spin-dependent WIMP-nucleon cross sections with XENON1T*, 1902.03234.

[19] ATLAS collaboration, M. Aaboud et al., *Search for dark matter and other new phenomena in events with an energetic jet and large missing transverse momentum using the ATLAS detector*, *JHEP* **01** (2018) 126, [1711.03301].

[20] CMS collaboration, A. M. Sirunyan et al., *Search for new physics in final states with an energetic jet or a hadronically decaying W or Z boson and transverse momentum imbalance at* $\sqrt{s} = 13$ TeV, *Phys. Rev.* **D97** (2018) 092005, [1712.02345].

[21] M. Honda, M. Sajjad Athar, T. Kajita, K. Kasahara and S. Midorikawa, *Atmospheric neutrino flux calculation using the NRLMSISE-00 atmospheric model*, *Phys. Rev.* **D92** (2015) 023004, [1502.03916].

[22] ICECUBE collaboration, M. G. Aartsen et al., *First search for dark matter annihilations in the Earth with the IceCube Detector*, *Eur. Phys. J.* **C77** (2017) 82, [1609.01492].

[23] ANTARES collaboration, A. Albert et al., *Search for Dark Matter Annihilation in the Earth using the ANTARES Neutrino Telescope*, *Phys. Dark Univ.* **16** (2017) 41–48, [1612.06792].

[24] LUX collaboration, D. S. Akerib et al., *Results from a search for dark matter in the complete LUX exposure*, *Phys. Rev. Lett.* **118** (2017) 021303, [1608.07648].

[25] XENON collaboration, E. Aprile et al., *First Dark Matter Search Results from the XENON1T Experiment*, 1705.06655.

[26] SUPER-KAMIOKANDE collaboration, S. Desai et al., *Search for dark matter WIMPs using upward through-going muons in Super-Kamiokande*, *Phys. Rev.* **D70** (2004) 083523, [hep-ex/0404025].

[27] DARKSIDE collaboration, P. Agnes et al., *First Results from the DarkSide-50 Dark Matter Experiment at Laboratori Nazionali del Gran Sasso*, *Phys. Lett.* **B743** (2015) 456–466, [1410.0653].

[28] PANDAX-II collaboration, A. Tan et al., *Dark Matter Results from First 98.7 Days of Data from the PandaX-II Experiment*, *Phys. Rev. Lett.* **117** (2016) 121303, [1607.07400].

[29] SUPER-KAMIOKANDE collaboration, K. Frankiewicz, *Dark matter searches with the Super-Kamiokande detector*, *J. Phys. Conf. Ser.* **888** (2017) 012210.

[30] ICECUBE collaboration, M. G. Aartsen et al., *Search for Dark Matter Annihilation in the Galactic Center with IceCube-79*, *Eur. Phys. J.* **C75** (2015) 492, [1505.07259].

[31] ANTARES collaboration, S. Adrian-Martinez et al., *Search of Dark Matter Annihilation in the Galactic Centre using the ANTARES Neutrino Telescope*, *JCAP* **1510** (2015) 068, [1505.04866].

[32] FERMI-LAT collaboration, M. Ackermann et al., *Dark matter constraints from observations of 25 Milky Way satellite galaxies with the Fermi Large Area Telescope*, *Phys. Rev.* **D89** (2014) 042001, [1310.0828].

[33] I. Esteban, M. C. Gonzalez-Garcia, M. Maltoni, I. Martinez-Soler and T. Schwetz, *Updated fit to three neutrino mixing: exploring the accelerator-reactor complementarity*, *JHEP* **01** (2017) 087, [1611.01514].

[34] G. Bertone, D. Hooper and J. Silk, *Particle dark matter: Evidence, candidates and constraints*, *Phys. Rept.* **405** (2005) 279–390, [hep-ph/0404175].

[35] G. Jungman, M. Kamionkowski and K. Griest, *Supersymmetric dark matter*, *Phys. Rept.* **267** (1996) 195–373, [hep-ph/9506380].

[36] B. Bellazzini, Y. Grossman, I. Nachshon and P. Paradisi, *Non-Standard Neutrino Interactions at One Loop*, *JHEP* **06** (2011) 104, [1012.3759].

[37] DAMA collaboration, R. Bernabei et al., *First results from DAMA/LIBRA and the combined results with DAMA/NaI*, *Eur. Phys. J.* **C56** (2008) 333–355, [0804.2741].

[38] C. Savage, G. Gelmini, P. Gondolo and K. Freese, *Compatibility of DAMA/LIBRA dark matter detection with other searches*, *JCAP* **0904** (2009) 010, [0808.3607].

[39] KIMS collaboration, H. S. Lee et al., *Limits on WIMP-nucleon cross section with CsI(Tl) crystal detectors*, *Phys. Rev. Lett.* **99** (2007) 091301, [0704.0423].

[40] R. Bernabei et al., *First model independent results from DAMA/LIBRA-phase2*, 1805.10486.

[41] G. Angloher et al., *Results from 730 kg days of the CRESST-II Dark Matter Search*, *Eur. Phys. J.* **C72** (2012) 1971, [1109.0702].

[42] CoGeNT collaboration, C. E. Aalseth et al., *Results from a Search for Light-Mass Dark Matter with a P-type Point Contact Germanium Detector*, *Phys. Rev. Lett.* **106** (2011) 131301, [1002.4703].

[43] T. Schwetz and J. Zupan, *Dark Matter attempts for CoGeNT and DAMA*, *JCAP* **1108** (2011) 008, [1106.6241].

[44] C. Kelso, D. Hooper and M. R. Buckley, *Toward A Consistent Picture For CRESST, CoGeNT and DAMA*, *Phys. Rev.* **D85** (2012) 043515, [1110.5338].

[45] CMS collaboration, A. M. Sirunyan et al., *Search for new physics in events with a leptonically decaying Z boson and a large transverse momentum imbalance in proton–proton collisions at* $\sqrt{s}$ *= 13 TeV*, *Eur. Phys. J.* **C78** (2018) 291, [1711.00431].

[46] LHCb collaboration, R. Aaij et al., *Search for Higgs-like bosons decaying into long-lived exotic particles*, *Eur. Phys. J.* **C76** (2016) 664, [1609.03124].

[47] MiniBooNE DM collaboration, A. A. Aguilar-Arevalo et al., *Dark Matter Search in Nucleon, Pion, and Electron Channels from a Proton Beam Dump with MiniBooNE*, *Phys. Rev.* **D98** (2018) 112004, [1807.06137].

[48] BELLE II collaboration, W. Altmannshofer et al., *The Belle II Physics Book*, 1808.10567.

[49] SUPER-KAMIOKANDE collaboration, K. Choi et al., *Search for neutrinos from annihilation of captured low-mass dark matter particles in the Sun by Super-Kamiokande*, *Phys. Rev. Lett.* **114** (2015) 141301, [1503.04858].

[50] ICECUBE collaboration, M. G. Aartsen et al., *Search for annihilating dark matter in the Sun with 3 years of IceCube data*, 1612.05949.

[51] SUPER-KAMIOKANDE collaboration, G. Mitsuka et al., *Study of Non-Standard Neutrino Interactions with Atmospheric Neutrino Data in Super-Kamiokande I and II*, *Phys. Rev.* **D84** (2011) 113008, [1109.1889].

[52] ICECUBE collaboration, M. Aartsen et al., *Search for Nonstandard Neutrino Interactions with IceCube DeepCore*, *Phys. Rev.* **D97** (2018) 072009, [1709.07079].

[53] T. Ohlsson, H. Zhang and S. Zhou, *Effects of nonstandard neutrino interactions at PINGU*, *Phys. Rev.* **D88** (2013) 013001, [1303.6130].

[54] A. Esmaili and A. Yu. Smirnov, *Probing Non-Standard Interaction of Neutrinos with IceCube and DeepCore*, *JHEP* **06** (2013) 026, [1304.1042].

[55] S. Choubey and T. Ohlsson, *Bounds on Non-Standard Neutrino Interactions Using PINGU*, *Phys. Lett.* **B739** (2014) 357–364, [1410.0410].

[56] I. Mocioiu and W. Wright, *Non-standard neutrino interactions in the mu-tau sector*, *Nucl. Phys.* **B893** (2015) 376–390, [1410.6193].

[57] A. Chatterjee, P. Mehta, D. Choudhury and R. Gandhi, *Testing nonstandard neutrino matter interactions in atmospheric neutrino propagation*, *Phys. Rev.* **D93** (2016) 093017, [1409.8472].

[58] O. Yasuda, *Constraints on non-standard flavor-dependent interactions from Superkamiokande and Hyperkamiokande*, *PoS* **NUFACT2014** (2015) 045, [1502.01440].

[59] N. Fornengo, M. Maltoni, R. Tomas and J. W. F. Valle, *Probing neutrino nonstandard interactions with atmospheric neutrino data*, *Phys. Rev.* **D65** (2002) 013010, [hep-ph/0108043].

[60] M. C. Gonzalez-Garcia and M. Maltoni, *Atmospheric neutrino oscillations and new physics*, *Phys. Rev.* **D70** (2004) 033010, [hep-ph/0404085].

[61] A. Friedland, C. Lunardini and M. Maltoni, *Atmospheric neutrinos as probes of neutrino-matter interactions*, *Phys. Rev.* **D70** (2004) 111301, [hep-ph/0408264].

[62] A. Friedland and C. Lunardini, *A Test of tau neutrino interactions with atmospheric neutrinos and K2K*, *Phys. Rev.* **D72** (2005) 053009, [hep-ph/0506143].

[63] M. C. Gonzalez-Garcia, M. Maltoni and J. Salvado, *Testing matter effects in propagation of atmospheric and long-baseline neutrinos*, *JHEP* **05** (2011) 075, [1103.4365].

[64] F. J. Escrihuela, M. Tortola, J. W. F. Valle and O. G. Miranda, *Global constraints on muon-neutrino non-standard interactions*, *Phys. Rev.* **D83** (2011) 093002, [1103.1366].

[65] A. Ghosh, T. Thakore and S. Choubey, *Determining the Neutrino Mass Hierarchy with INO, T2K, NOvA and Reactor Experiments*, *JHEP* **04** (2013) 009, [1212.1305].

[66] M. M. Devi, T. Thakore, S. K. Agarwalla and A. Dighe, *Enhancing sensitivity to neutrino parameters at INO combining muon and hadron information*, *JHEP* **10** (2014) 189, [1406.3689].

[67] A. Ajmi, A. Dev, M. Nizam, N. Nayak and S. U. Sankar, *Improving the hierarchy sensitivity of ICAL using neural network*, 1510.02350.

[68] T. Thakore, A. Ghosh, S. Choubey and A. Dighe, *The Reach of INO for Atmospheric Neutrino Oscillation Parameters*, *JHEP* **05** (2013) 058, [1303.2534].

[69] L. S. Mohan and D. Indumathi, *Pinning down neutrino oscillation parameters in the 2?3 sector with a magnetised atmospheric neutrino detector: a new study*, *Eur. Phys. J.* **C77** (2017) 54, [1605.04185].

[70] D. Kaur, M. Naimuddin and S. Kumar, *The sensitivity of the ICAL detector at India-based Neutrino Observatory to neutrino oscillation parameters*, *Eur. Phys. J.* **C75** (2015) 156, [1409.2231].

[71] D. Kaur, Z. A. Dar, S. Kumar and M. Naimuddin, *Search for the differences in atmospheric neutrino and antineutrino oscillation parameters at the INO-ICAL experiment*, *Phys. Rev.* **D95** (2017) 093005, [1703.06710].

[72] S. P. Behera, A. Ghosh, S. Choubey, V. M. Datar, D. K. Mishra and A. K. Mohanty, *Search for the sterile neutrino mixing with the ICAL detector at INO*, *Eur. Phys. J.* **C77** (2017) 307, [1605.08607].

[73] A. Chatterjee, R. Gandhi and J. Singh, *Probing Lorentz and CPT Violation in a Magnetized Iron Detector using Atmospheric Neutrinos*, *JHEP* **06** (2014) 045, [1402.6265].

[74] N. Dash, V. M. Datar and G. Majumder, *Sensitivity of the INO-ICAL detector to magnetic monopoles*, *Astropart. Phys.* **70** (2015) 33–38, [1406.3938].

[75] N. Dash, V. M. Datar and G. Majumder, *Sensitivity for detection of decay of dark matter particle using ICAL at INO*, *Pramana* **86** (2016) 927–937, [1410.5182].

[76] D. Aristizabal Sierra, N. Rojas and M. H. G. Tytgat, *Neutrino non-standard interactions and dark matter searches with multi-ton scale detectors*, *JHEP* **03** (2018) 197, [1712.09667].

[77] S. V. Demidov, *Non-standard interactions and neutrinos from dark matter annihilation in the Sun*, *JCAP* **1802** (2018) 001, [1711.00911].

[78] A. Chatterjee, K. K. Meghna, K. Rawat, T. Thakore, V. Bhatnagar, R. Gandhi et al., *A Simulations Study of the Muon Response of the Iron Calorimeter Detector at the India-based Neutrino Observatory*, *JINST* **9** (2014) P07001, [1405.7243].

[79] G. Bertone and D. Hooper, *A History of Dark Matter*, *Submitted to: Rev. Mod. Phys.* (2016) , [1605.04909].

[80] F. Zwicky, *Die Rotverschiebung von extragalaktischen Nebeln*, *Helv. Phys. Acta* **6** (1933) 110–127.

[81] Y. Sofue and V. Rubin, *Rotation curves of spiral galaxies*, *Ann. Rev. Astron. Astrophys.* **39** (2001) 137–174, [astro-ph/0010594].

[82] K. G. Begeman, A. H. Broeils and R. H. Sanders, *Extended rotation curves of spiral galaxies: Dark haloes and modified dynamics*, *Mon. Not. Roy. Astron. Soc.* **249** (1991) 523.

[83] M. Bartelmann and P. Schneider, *Weak gravitational lensing*, *Phys. Rept.* **340** (2001) 291–472, [astro-ph/9912508].

[84] E. van Uitert, H. Hoekstra, T. Schrabback, D. G. Gilbank, M. D. Gladders and H. K. C. Yee, *Constraints on the shapes of galaxy dark matter haloes from weak gravitational lensing*, *Astron. Astrophys.* **545** (2012) A71, [1206.4304].

[85] L. A. Moustakas and R. B. Metcalf, *Detecting dark matter substructure spectroscopically in strong gravitational lenses*, *Mon. Not. Roy. Astron. Soc.* **339** (2003) 607, [astro-ph/0206176].

[86] D. Harvey, R. Massey, T. Kitching, A. Taylor and E. Tittley, *The non-gravitational interactions of dark matter in colliding galaxy clusters*, *Science* **347** (2015) 1462–1465, [1503.07675].

[87] WMAP collaboration, G. Hinshaw et al., *Nine-Year Wilkinson Microwave Anisotropy Probe (WMAP) Observations: Cosmological Parameter Results*, *Astrophys. J. Suppl.* **208** (2013) 19, [1212.5226].

[88] B. Carr, F. Kuhnel and M. Sandstad, *Primordial Black Holes as Dark Matter*, *Phys. Rev.* **D94** (2016) 083504, [1607.06077].

[89] LIGO SCIENTIFIC, VIRGO collaboration, B. P. Abbott et al., *Observation of Gravitational Waves from a Binary Black Hole Merger*, *Phys. Rev. Lett.* **116** (2016) 061102, [1602.03837].

[90] R. D. Peccei and H. R. Quinn, *CP Conservation in the Presence of Instantons*, *Phys. Rev. Lett.* **38** (1977) 1440–1443.

[91] ADMX collaboration, S. J. Asztalos et al., *A SQUID-based microwave cavity search for dark-matter axions*, *Phys. Rev. Lett.* **104** (2010) 041301, [0910.5914].

[92] S. Dodelson and L. M. Widrow, *Sterile-neutrinos as dark matter*, *Phys. Rev. Lett.* **72** (1994) 17–20, [hep-ph/9303287].

[93] K. Abazajian, G. M. Fuller and M. Patel, *Sterile neutrino hot, warm, and cold dark matter*, *Phys. Rev.* **D64** (2001) 023501, [astro-ph/0101524].

[94] M. Milgrom, *A Modification of the Newtonian dynamics as a possible alternative to the hidden mass hypothesis*, *Astrophys. J.* **270** (1983) 365–370.

[95] T. Appelquist, H.-C. Cheng and B. A. Dobrescu, *Bounds on universal extra dimensions*, *Phys. Rev.* **D64** (2001) 035002, [hep-ph/0012100].

[96] M. Blennow, H. Melbeus and T. Ohlsson, *Neutrinos from Kaluza-Klein dark matter in the Sun*, *JCAP* **1001** (2010) 018, [0910.1588].

[97] P. Gondolo and G. Gelmini, *Cosmic abundances of stable particles: Improved analysis*, *Nucl. Phys.* **B360** (1991) 145–179.

[98] A. Biswas, S. Choubey and S. Khan, *Galactic gamma ray excess and dark matter phenomenology in a $U(1)_{B-L}$ model*, *JHEP* **08** (2016) 114, [1604.06566].

[99] J. Edsjo and P. Gondolo, *Neutralino relic density including coannihilations*, *Phys. Rev.* **D56** (1997) 1879–1894, [hep-ph/9704361].

[100] G. Steigman, B. Dasgupta and J. F. Beacom, *Precise Relic WIMP Abundance and its Impact on Searches for Dark Matter Annihilation*, *Phys. Rev.* **D86** (2012) 023506, [1204.3622].

[101] R. W. Schnee, *Introduction to dark matter experiments*, in *Physics of the large and the small, TASI 09, proceedings of the Theoretical Advanced Study Institute in Elementary Particle Physics, Boulder, Colorado, USA, 1-26 June 2009*, pp. 775–829, 2011, 1101.5205, DOI.

[102] V. A. Bednyakov and F. Simkovic, *Nuclear spin structure in dark matter search: The Finite momentum transfer limit*, *Phys. Part. Nucl.* **37** (2006) S106–S128, [hep-ph/0608097].

[103] G. Duda, A. Kemper and P. Gondolo, *Model Independent Form Factors for Spin Independent Neutralino-Nucleon Scattering from Elastic Electron Scattering Data*, *JCAP* **0704** (2007) 012, [hep-ph/0608035].

[104] T. Marrodán Undagoitia and L. Rauch, *Dark matter direct-detection experiments*, *J. Phys.* **G43** (2016) 013001, [1509.08767].

[105] HAWC collaboration, A. Albert et al., *Search for Dark Matter Gamma-ray Emission from the Andromeda Galaxy with the High-Altitude Water Cherenkov Observatory*, *JCAP* **1806** (2018) 043, [1804.00628].

[106] HAWC collaboration, A. U. Abeysekara et al., *A Search for Dark Matter in the Galactic Halo with HAWC*, *JCAP* **1802** (2018) 049, [1710.10288].

[107] MAGIC collaboration, M. L. Ahnen et al., *Indirect dark matter searches in the dwarf satellite galaxy Ursa Major II with the MAGIC Telescopes*, *JCAP* **1803** (2018) 009, [1712.03095].

[108] P. Picozza et al., *PAMELA: A Payload for Antimatter Matter Exploration and Light-nuclei Astrophysics*, *Astropart. Phys.* **27** (2007) 296–315, [astro-ph/0608697].

[109] GAPS collaboration, C. J. Hailey et al., *Antideuteron based dark matter search with GAPS: Current progress and future prospects*, *Adv. Space Res.* **51** (2013) 290–296.

[110] A. Albert et al., *Recommendations of the LHC Dark Matter Working Group: Comparing LHC searches for heavy mediators of dark matter production in visible and invisible decay channels*, 1703.05703.

[111] S. Arrenberg et al., *Working Group Report: Dark Matter Complementarity*, in *Proceedings, 2013 Community Summer Study on the Future of U.S. Particle Physics: Snowmass on the Mississippi (CSS2013): Minneapolis, MN, USA, July 29-August 6, 2013*, 2013, 1310.8621, http://lss.fnal.gov/archive/preprint/fermilab-conf-13-574-ae.shtml.

[112] M. Pato, O. Agertz, G. Bertone, B. Moore and R. Teyssier, *Systematic uncertainties in the determination of the local dark matter density*, *Phys. Rev.* **D82** (2010) 023531, [1006.1322].

[113] F. Calore, N. Bozorgnia, M. Lovell, G. Bertone, M. Schaller, C. S. Frenk et al., *Simulated Milky Way analogues: implications for dark matter indirect searches*, *JCAP* **1512** (2015) 053, [1509.02164].

[114] L. Bergstrom, T. Bringmann and J. Edsjo, *Complementarity of direct dark matter detection and indirect detection through gamma-rays*, *Phys. Rev.* **D83** (2011) 045024, [1011.4514].

[115] C. Arina, G. Bertone and H. Silverwood, *Complementarity of direct and indirect Dark Matter detection experiments*, *Phys. Rev.* **D88** (2013) 013002, [1304.5119].

[116] F. Ferrer, A. Ibarra and S. Wild, *A novel approach to derive halo-independent limits on dark matter properties*, *JCAP* **1509** (2015) 052, [1506.03386].

[117] M. Blennow, J. Herrero-Garcia and T. Schwetz, *A halo-independent lower bound on the dark matter capture rate in the Sun from a direct detection signal*, *JCAP* **1505** (2015) 036, [1502.03342].

[118] J. Kopp, *Collider Limits on Dark Matter*, in *Proceedings, 46th Rencontres de Moriond on Electroweak Interactions and Unified Theories: La Thuile, Italy, March 13-20, 2011*, pp. 411–416, 2011, 1105.3248, http://lss.fnal.gov/archive/2011/conf/fermilab-conf-11-219-t.pdf.

[119] G. Bertone, D. G. Cerdeno, M. Fornasa, R. Ruiz de Austri and R. Trotta, *Identification of Dark Matter particles with LHC and direct detection data*, *Phys. Rev.* **D82** (2010) 055008, [1005.4280].

[120] G. Bertone, D. G. Cerdeno, M. Fornasa, L. Pieri, R. Ruiz de Austri and R. Trotta, *Complementarity of Indirect and Accelerator Dark Matter Searches*, *Phys. Rev.* **D85** (2012) 055014, [1111.2607].

[121] M. Pato, L. Baudis, G. Bertone, R. Ruiz de Austri, L. E. Strigari and R. Trotta, *Complementarity of Dark Matter Direct Detection Targets*, *Phys. Rev.* **D83** (2011) 083505, [1012.3458].

[122] D. N. Spergel and W. H. Press, *Effect of hypothetical, weakly interacting, massive particles on energy transport in the solar interior*, *Astrophys. J.* **294** (1985) 663–673.

[123] A. Gould, *WIMP Distribution in and Evaporation From the Sun*, *Astrophys. J.* **321** (1987) 560.

[124] L. M. Krauss, M. Srednicki and F. Wilczek, *Solar System Constraints and Signatures for Dark Matter Candidates*, *Phys. Rev.* **D33** (1986) 2079–2083.

[125] K. Griest and D. Seckel, *Cosmic Asymmetry, Neutrinos and the Sun*, *Nucl. Phys.* **B283** (1987) 681–705.

[126] A. Gould, *Cosmological density of WIMPs from solar and terrestrial annihilations*, *Astrophys. J.* **388** (1992) 338–344.

[127] G. B. Gelmini, P. Gondolo and E. Roulet, *Neutralino dark matter searches*, *Nucl. Phys.* **B351** (1991) 623–644.

[128] O. Mena, S. Palomares-Ruiz and S. Pascoli, *Reconstructing WIMP properties with neutrino detectors*, *Phys. Lett.* **B664** (2008) 92–96, [0706.3909].

[129] M. Cirelli, N. Fornengo, T. Montaruli, I. A. Sokalski, A. Strumia and F. Vissani, *Spectra of neutrinos from dark matter annihilations*, *Nucl. Phys.* **B727** (2005) 99–138, [hep-ph/0506298].

[130] M. Blennow, J. Edsjo and T. Ohlsson, *Neutrinos from WIMP annihilations using a full three-flavor Monte Carlo*, *JCAP* **0801** (2008) 021, [0709.3898].

[131] J. Edsjo, *WimpSim Neutrino Monte Carlo*, http://www.fysik.su.se/edsjo/wimpsim.

[132] J. Edsjo, *NuSigma neutrino interaction Monte Carlo*, http://www.fysik.su.se/edsjo/wimpsim.

[133] T. Sjostrand, S. Mrenna and P. Z. Skands, *PYTHIA 6.4 Physics and Manual*, *JHEP* **05** (2006) 026, [hep-ph/0603175].

[134] A. Gould, *Resonant Enhancements in WIMP Capture by the Earth*, *Astrophys. J.* **321** (1987) 571.

[135] K. Choi, C. Rott and Y. Itow, *Impact of the dark matter velocity distribution on capture rates in the Sun*, *JCAP* **1405** (2014) 049, [1312.0273].

[136] W. J. G. de Blok, *The Core-Cusp Problem*, *Adv. Astron.* **2010** (2010) 789293, [0910.3538].

[137] V. Bonnivard, M. Hutten, E. Nezri, A. Charbonnier, C. Combet and D. Maurin, *CLUMPY : Jeans analysis, gamma-ray and neutrino fluxes from dark matter (sub-)structures*, *Comput. Phys. Commun.* **200** (2016) 336–349, [1506.07628].

[138] L. Hernquist, *An Analytical Model for Spherical Galaxies and Bulges*, *Astrophys. J.* **356** (1990) 359.

[139] J. F. Navarro, C. S. Frenk and S. D. M. White, *A Universal density profile from hierarchical clustering*, *Astrophys. J.* **490** (1997) 493–508, [astro-ph/9611107].

[140] A. Burkert, *The Structure of dark matter halos in dwarf galaxies*, *IAU Symp.* **171** (1996) 175, [astro-ph/9504041].

[141] J. F. Navarro, E. Hayashi, C. Power, A. Jenkins, C. S. Frenk, S. D. M. White et al., *The Inner structure of Lambda-CDM halos 3: Universality and asymptotic slopes*, *Mon. Not. Roy. Astron. Soc.* **349** (2004) 1039, [astro-ph/0311231].

[142] V. Springel, J. Wang, M. Vogelsberger, A. Ludlow, A. Jenkins, A. Helmi et al., *The Aquarius Project: the subhalos of galactic halos*, *Mon. Not. Roy. Astron. Soc.* **391** (2008) 1685–1711, [0809.0898].

[143] SDSS collaboration, X. X. Xue et al., *The Milky Way's Circular Velocity Curve to 60 kpc and an Estimate of the Dark Matter Halo Mass from Kinematics of 2400 SDSS Blue Horizontal Branch Stars*, *Astrophys. J.* **684** (2008) 1143–1158, [0801.1232].

[144] F. Bonnarel, P. Fernique, O. Bienayme, D. Egret, F. Genova, M. Louys et al., *The aladin interactive sky atlas*, astro-ph/0002109.

[145] KASCADE collaboration, T. Antoni et al., *KASCADE measurements of energy spectra for elemental groups of cosmic rays: Results and open problems*, *Astropart. Phys.* **24** (2005) 1–25, [astro-ph/0505413].

[146] M. Boezio and E. Mocchiutti, *Chemical Composition of Galactic Cosmic Rays with Space Experiments*, *Astropart. Phys.* **39-40** (2012) 95–108, [1208.1406].

[147] R. Gandhi, P. Ghoshal, S. Goswami, P. Mehta, S. U. Sankar and S. Shalgar, *Mass Hierarchy Determination via future Atmospheric Neutrino Detectors*, *Phys. Rev.* **D76** (2007) 073012, [0707.1723].

[148] T. K. Gaisser and M. Honda, *Flux of atmospheric neutrinos*, *Ann. Rev. Nucl. Part. Sci.* **52** (2002) 153–199, [hep-ph/0203272].

[149] S. P. Behera, M. S. Bhatia, V. M. Datar and A. K. Mohanty, *Simulation Studies for Electromagnetic Design of INO ICAL Magnet and its Response to Muons*, *IEEE Trans. Magnetics* **51** (2015) 4624, [1406.3965].

[150] R. Kanishka, K. K. Meghna, V. Bhatnagar, D. Indumathi and N. Sinha, *Simulations Study of Muon Response in the Peripheral Regions of the Iron Calorimeter Detector at the India-based Neutrino Observatory*, *JINST* **10** (2015) P03011, [1503.03369].

[151] B. Satyanarayana, *Design and Characterisation Studies of Resistive Plate Chambers,PhD thesis, Department of Physics, IIT Bombay, PHY-PHD-10-701, 2009*, .

[152] D. Casper, *The Nuance neutrino physics simulation, and the future*, *Nucl. Phys. Proc. Suppl.* **112** (2002) 161–170, [hep-ph/0208030].

[153] C. Andreopoulos et al., *The GENIE Neutrino Monte Carlo Generator*, *Nucl. Instrum. Meth.* **A614** (2010) 87–104, [0905.2517].

[154] A. Ghosh and S. Choubey, *Measuring the Mass Hierarchy with Muon and Hadron Events in Atmospheric Neutrino Experiments*, *JHEP* **10** (2013) 174, [1306.1423].

[155] K. Bhattacharya, A. K. Pal, G. Majumder and N. K. Mondal, *Error propagation of the track model and track fitting strategy for the Iron CALorimeter detector in India-based neutrino observatory*, *Comput. Phys. Commun.* **185** (2014) 3259–3268, [1510.02792].

[156] J. Marshall, *A study of muon neutrino disappearance with the MINOS detectors and the NuMI neutrino beam*, *PhD. Thesis, Univ. of Cambridge* (2008) .

[157] H. Bethe and J. Ashkin, *Experimental Nuclear Physics, Ed. E. Segr, J. Wiley, New York* (1953) 253.

[158] R. Brun and F. Rademakers, *ROOT: An object oriented data analysis framework*, *Nucl. Instrum. Meth.* **A389** (1997) 81–86.

[159] J. Edsjo, J. Elevant, R. Enberg and C. Niblaeus, *Neutrinos from cosmic ray interactions in the Sun*, 1704.02892.

[160] P. T. Wallace, "SLALIB: A Positional Astronomy Library." Astrophysics Source Code Library, Mar., 2014.

[161] ICECUBE collaboration, M. G. Aartsen et al., *Search for dark matter annihilations in the Sun with the 79-string IceCube detector*, *Phys. Rev. Lett.* **110** (2013) 131302, [1212.4097].

[162] M. M. Boliev, S. V. Demidov, S. P. Mikheyev and O. V. Suvorova, *Search for muon signal from dark matter annihilations inthe Sun with the Baksan Underground Scintillator Telescope for 24.12 years*, *JCAP* **1309** (2013) 019, [1301.1138].

[163] PICASSO collaboration, S. Archambault et al., *Constraints on Low-Mass WIMP Interactions on* ^{19}F *from PICASSO*, *Phys. Lett.* **B711** (2012) 153–161, [1202.1240].

[164] M. Felizardo et al., *Final Analysis and Results of the Phase II SIMPLE Dark Matter Search*, *Phys. Rev. Lett.* **108** (2012) 201302, [1106.3014].

[165] S. K. Agarwalla, M. Blennow, E. Fernandez Martinez and O. Mena, *Neutrino Probes of the Nature of Light Dark Matter*, *JCAP* **1109** (2011) 004, [1105.4077].

[166] ATLAS collaboration, G. Aad et al., *Search for new phenomena in final states with an energetic jet and large missing transverse momentum in pp collisions at $\sqrt{s}$ =8 TeV with the ATLAS detector*, *Eur. Phys. J.* **C75** (2015) 299, [1502.01518].

[167] CDMS collaboration, R. Agnese et al., *Silicon Detector Dark Matter Results from the Final Exposure of CDMS II*, *Phys. Rev. Lett.* **111** (2013) 251301, [1304.4279].

[168] SUPERCDMS collaboration, R. Agnese et al., *Search for Low-Mass Weakly Interacting Massive Particles with SuperCDMS*, *Phys. Rev. Lett.* **112** (2014) 241302, [1402.7137].

[169] SUPERCDMS collaboration, R. Agnese et al., *Search for Low-Mass Weakly Interacting Massive Particles Using Voltage-Assisted Calorimetric Ionization Detection in the SuperCDMS Experiment*, *Phys. Rev. Lett.* **112** (2014) 041302, [1309.3259].

[170] J. Edsjo and P. Gondolo, *WIMP mass determination with neutrino telescopes*, *Phys. Lett.* **B357** (1995) 595–601, [hep-ph/9504283].

[171] A. Khatun, R. Laha and S. K. Agarwalla, *Indirect searches of Galactic diffuse dark matter in INO-MagICAL detector*, 1703.10221.

[172] P. Gondolo, J. Edsjo, P. Ullio, L. Bergstrom, M. Schelke and E. A. Baltz, *DarkSUSY: Computing supersymmetric dark matter properties numerically*, *JCAP* **0407** (2004) 008, [astro-ph/0406204].

[173] G. Bélanger, J. Da Silva, T. Perrillat-Bottonet and A. Pukhov, *Limits on dark matter proton scattering from neutrino telescopes using micrOMEGAs*, *JCAP* **1512** (2015) 036, [1507.07987].

[174] L. Wolfenstein, *Neutrino Oscillations in Matter*, *Phys. Rev.* **D17** (1978) 2369–2374.

[175] Y. Grossman, *Nonstandard neutrino interactions and neutrino oscillation experiments*, *Phys. Lett.* **B359** (1995) 141–147, [hep-ph/9507344].

[176] Z. Berezhiani and A. Rossi, *Limits on the nonstandard interactions of neutrinos from e+ e- colliders*, *Phys. Lett.* **B535** (2002) 207–218, [hep-ph/0111137].

[177] S. Davidson, C. Pena-Garay, N. Rius and A. Santamaria, *Present and future bounds on nonstandard neutrino interactions*, *JHEP* **03** (2003) 011, [hep-ph/0302093].

[178] T. Ohlsson, *Status of non-standard neutrino interactions*, *Rept. Prog. Phys.* **76** (2013) 044201, [1209.2710].

[179] Z. Rahman, A. Dasgupta and R. Adhikari, *The Discovery reach of CP violation in neutrino oscillation with non-standard interaction effects*, *J. Phys.* **G42** (2015) 065001, [1503.03248].

[180] C. Biggio, M. Blennow and E. Fernandez-Martinez, *General bounds on non-standard neutrino interactions*, *JHEP* **08** (2009) 090, [0907.0097].

[181] MINOS collaboration, P. Adamson et al., *Search for flavor-changing non-standard neutrino interactions by MINOS*, *Phys. Rev.* **D88** (2013) 072011, [1303.5314].

[182] K. Dick, M. Freund, M. Lindner and A. Romanino, *CP violation in neutrino oscillations*, *Nucl. Phys.* **B562** (1999) 29–56, [hep-ph/9903308].

[183] A. M. Dziewonski and D. L. Anderson, *Preliminary reference earth model*, *Phys. Earth Planet. Interiors* **25** (1981) 297–356.

[184] J. Kopp, M. Lindner, T. Ota and J. Sato, *Non-standard neutrino interactions in reactor and superbeam experiments*, *Phys. Rev.* **D77** (2008) 013007, [0708.0152].

[185] N. C. Ribeiro, H. Minakata, H. Nunokawa, S. Uchinami and R. Zukanovich-Funchal, *Probing Non-Standard Neutrino Interactions with Neutrino Factories*, *JHEP* **12** (2007) 002, [0709.1980].

[186] T. Kikuchi, H. Minakata and S. Uchinami, *Perturbation Theory of Neutrino Oscillation with Nonstandard Neutrino Interactions*, *JHEP* **03** (2009) 114, [0809.3312].

[187] S. K. Agarwalla, S. Prakash and W. Wang, *High-precision measurement of atmospheric mass-squared splitting with T2K and NOvA*, 1312.1477.

[188] S. K. Agarwalla, S. Choubey and S. Prakash, *Probing Neutrino Oscillation Parameters using High Power Superbeam from ESS*, *JHEP* **12** (2014) 020, [1406.2219].